Three Dimensional CFD Modeling of Secondary Flow in River Bends and Confluences

By

Rawaa Shaheed

Thesis submitted

in partial fulfillment of the requirements for the

Doctorate in Philosophy degree in Civil Engineering

Department of Civil Engineering

Faculty of Engineering

University of Ottawa

بسم الله الرحمن الرحيم

((وما توفيقي الا بالله عليه توكلت واليه انيب))

" And my success can only come from Allah.
In Him I trust, and unto Him I return. "
[Hud:88]

صدق الله العظيم

To…

The spirit of my parents …

My Lovely Husband Bashar…

Brother, Sisters…and all My Family…

With my Love…

Acknowledgements

The path to completion of this journey is not easy and can be characterized by both difficulties and accomplishments.

First and foremost, I want to express my gratitude to "Allah" for giving me the courage and knowledge necessary to achieve my objectives and complete this effort.

It is a pleasure for me to express my gratitude to everyone who contributed to the success of this thesis, especially my supervisor, lovely husband, family, friends, and thesis committee defense.

I would like to extend my sincere thanks and gratitude to my supervisor Dr. Majid Mohammadian for his continuous support and generosity during the duration of the research.

Special thanks to the committee members, Prof. Tedros Ghobrial, Prof. Hossein Bonakdari, Prof. Xin Liu and Prof. Hamidreza Shirkhani for providing precious suggestions and comments on my thesis.

Bashar, my lovely husband, I am very appreciative of your faithful support, endless love, patience, and encouragement.

My beloveds, brothers, sisters, and the rest of my family, I am happy to report that the objective I had been working for over the past few years has been accomplished. I know you have been there for me in spirit, and I will never forget your prayers and encouragement.

My thanks and appreciation to the General Commission for Irrigation and Reclamation Projects, one of the formations of the Ministry of Water Resources in Iraq for their support and assistance.

The author is also extremely grateful for scholarships and bursaries provided from the University of Ottawa and Ontario Graduate Scholarship (OGS).

Finally, I would like to thank all my friends and everyone who supported me during this phase of my life.

Abstract

Rivers are considered as one of the most important surface water resources on the earth. During the time, most of the rivers on the earth experienced evolution and changes. River bends and confluences are one of the common cases in most rivers. There is a significant impact of the flow on the cross-sectional profile of river bends and confluences.

Secondary currents are one of the important features that characterize flow in river bends and confluences. In such currents, fluid particles follow a helical path instead of moving nearly parallel to the axis of the channel. The local imbalance between the vertically varying centrifugal force and the cross-stream pressure gradient results in generating the secondary flow and raising a typical motion of the helical flow. Several studies, including experimental or mathematical, have been conducted to examine flow characteristics in curved open channels, river meanders, or confluences. In this research, the influence of secondary currents is studied on the elevation of water surface and the hydraulic structures in channel bends and confluences by employing a 3D OpenFOAM numerical model.

The research implements a 3D OpenFOAM numerical model to simulate the horizontal distribution of the flow. In addition, the progress in unraveling and understanding the bend and confluent dynamics is discussed. The finite volume method in OpenFOAM software is used to simulate and examine the behavior of the secondary current. Thereafter, a comparison between the experimental data and a numerical model is conducted. Two sets of experimental data are used as the dataset for these two experiments are complete and validated; the data provided by Rozovskii (1961) for a sharply curved channel, and the dataset provided by Shumate (1998) for a confluent channel.

Two solvers in OpenFOAM software were selected to solve the problem regarding the experiment: InterFoam and PisoFoam. InterFoam is a transient solver for incompressible flow that is used with open channel flow with Free Surface Model. PisoFoam is a transient solver for incompressible flow that is used with closed channel flow and Rigid-Lid Model. Various turbulence models (i.e., Standard k-ε, Realizable k-ε) are applied in the numerical model to assess the accuracy of turbulence models in predicting the behavior of the flow. The accuracies of various turbulence models are examined and discussed.

Table of Contents

List of Tables

List of Figures

List of Abbreviations and Symbols

B	Channel width (m)
g	Acceleration of gravity (m/s^2)
h	Flow depth (m)
H	Bottom elevation (m)
n	Manning's roughness coefficient
P	Pressure (N/m^2)
Q	Flow discharge (m^3/s)
Q_m	Main channel discharge (m^3/s)
Q_b	Branch channel discharge (m^3/s)
q_1	Flow discharge per unit width in the x direction (m^3/s)
q_2	Flow discharge per unit width in the y directions (m^3/s)
r	Radius of curvature for the outer bank (m)
ri	Radius of curvature for the inner bank (m)
t	Time (sec)
U	Depth averaged velocity magnitude (m/s)
U	Mean flow velocity (m/s)
U_i	Depth averaged velocity in *i*-direction (m/s)
$\hat{u}_1$	Velocities at the water surface in excess of mean velocity in the x-direction (m/s)
$\hat{u}_2$	Velocities at the water surface in excess of mean velocity in the y-direction (m/s)
$u_i(z)$	Vertical distribution of *i*-component velocity (m/s)
$\overline{u_i u_j}$	Reynolds stress tensor
u, v, w	Velocity in the *x*, *y*, *z* direction, respectively (m/s)
x, *y*, *z*	Coordinates
μ	viscosity ($N.s/m^2$)
v	Kinematic eddy viscosity (m^2/s)
ρ	Water density (kg/m^3)
ρ	Mass density (kg/m^3)
ρ_w	Density of water (kg/m^3)

ρ_a	Density of the air (kg/m^3)
τ_{ij}	Vertically averaged total turbulent shear stress in the ij-direction (N/m^2)
τ_{bi}	Bed shear stress (N/m^2)
z_m	Mean flow depth (m)

Acronyms

RAS	Reynolds-Averaged Simulation
LES	Large Eddy Simulation
ADV	Acoustic Doppler Velocimeter
CFD	Computational Fluid Dynamics
RANS	Reynolds-Averaged Navier-Stokes
ADCP	Acoustic Doppler Current Profile
DAM	Depth-Averaged Method
FSM	Free Surface Model
RLM	Rigid-Lid Model
FVM	Finite Volume Method
FDM	Finite Difference Method
FEM	Finite Element Method
VOF	Volume Of Fluid
ASM	Algebraic Stress Models
RSM	Reynolds Stress Models
SST	Shear Stress Transport
CPU	Central Processing Unit

Chapter 1. Introduction and objectives

1.1. Introduction

Rivers are a crucial component of the natural world. Their actions affect a wide range of interests, including aesthetics, navigation, and the production of power and water. The one-way flow of water, which offers a continuously renewing supply, a quick way to remove waste, and a valuable source of electricity, is one of the key draws for locals. These characteristics are also essential for the variety of aquatic organisms that live in the riverine habitat (Boon, 1992). Rivers can potentially endanger people and properties through floods, droughts, pollution, and erosion. Rivers, whether they are a resource or a hazard, are important from a political, social, and economic standpoint in addition to their physical importance. Rivers serve as both transportation and erosive forces, carrying water and material from the land's surface to the oceans. They offer the pathways that transport extra precipitation to the marine store, completing the hydrological cycle on a global scale. Rivers have created and are still creating a wide variety of network and channel structures because of the transportation and erosive functions they provide. It's critical to realize that rivers naturally evolve over time, changing both their form and structure. In order to roughly predict how riverbanks will erode, great effort has been put forward to derive correlations between flow patterns, bank features, and velocity profiles. Rivers naturally alter their morphology to balance the stream's ever-changing environmental demands. This kind of alteration frequently leads to phenomena like meandering rivers (Figure 1.1) and confluences (Figure 1.2) (Kinghton, 1998).

a. Immortal Tigris River in Baghdad, Iraq b. A curved river in northern Alberta, Canada

Figure 1.1: An example of river bends

a. Confluence of Tigris and Euphrates in Qurna, Iraq

b. Confluence between Rhone and Drome Rivers, France

Figure 1.2: An example of river confluences

In a river, the flow velocity is greatest when the flow is slowed down by the least amount of bottom friction. As a result, the water's velocity tends to be at its highest away from the channel's bed and toward its center, where the banks have the least impact. The term "thalweg" refers to the route taken by the flow that moves the fastest. Due to the centrifugal forces acting on the water from the turn in meandering rivers, the thalweg impacts the outside bank of the curve. The material outside the bank can be eroded and moved downstream by the energy of this swiftly moving water. On the interior of the bank, the water is moving slowly but with very little energy. The cross-section along the river's longitudinal profile experiences an uneven distribution of shear stress as a result of this velocity pattern (Figure 1.3). The concave bank (outside the bank of the meandering curve) typically experiences erosion, while the convex bank typically experiences accretion (inside of the meander bend). Because the water is not moving quickly enough and has insufficient energy to support the suspended silt that it had transported from upstream, accretion happens. A point bar is created when the suspended sediment is deposited inside the meander bend. Additionally, certain areas of the bank are neutral and don't seem to be eroding or degrading. Rivers move their position and change the shape of their planform throughout time because of the pattern of erosion and accretion along rivers and the variable distribution of shear stress along rivers (Kinghton, 1998). Shear stress is not the same on the walls and the bed because of the different velocity profile.

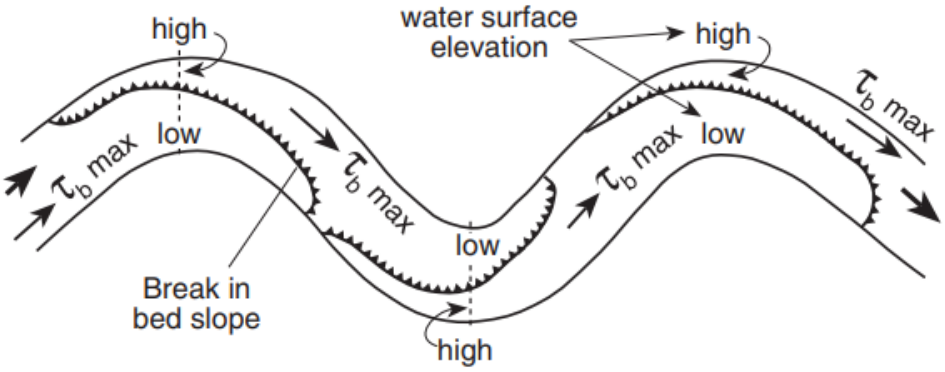

Figure 1.3: Shear stress distribution along a meandering river (from Kinghton 1998, after Dietrich, 1987)

The water and sediment provided by tributaries causes rivers to modify their morphology in the downstream direction at river confluences. The impact is not one-way, though. A way of integrating networks and channels is through the interactions of tributaries with the mainstream. The mainstream acts as the tributary's base level, much like the channel does in relation to the hillslope and shifts in its vertical or horizontal location might cause the tributary to adjust (Schumm and Hadley, 1957). The main valley's incision lowers the base level for tributary streams, which causes the beds of those streams to deteriorate. This deterioration starts at the junctions and moves upwards due to head cut migration. The main valley receives material from this bed erosion along the tributaries, where it builds up and slows down the degrading process. A fresh phase of main-valley incision doesn't start until the gradient is severe enough, at which point the cycle is repeated. It takes a mechanism to start the initial incision, and under the right conditions, river regulation might be that mechanism. According to Germanoski and Ritter (1988), bed degradation beneath a dam caused highly rapid downcutting along rivers that entered near to the dam. The incision also caused bank instability and channel widening. At tributary junctions, the addition of water and sediment can lead to changes in the downstream channel as well as the confluence itself. According to the geometry of the planform, confluences could be symmetrical (Y-shaped) or asymmetrical as depicted in Figure 1.4. The symmetrical example happens when two linked channels produce a new channel downstream (Mosley, 1976), but the asymmetrical case happens when tributaries join to the main channel laterally (Ludeña, 2015).

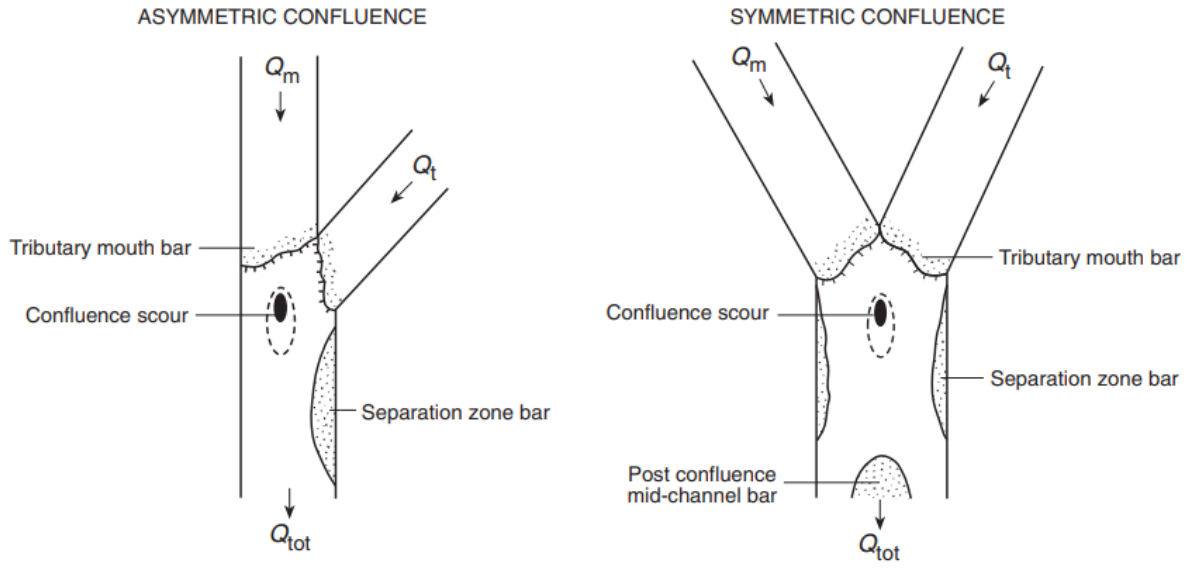

Figure 1.4: Bed morphology developed at channel confluences, indicating the major depositional and erosional elements within symmetric and asymmetric confluences (from Kinghton 1998, after Bristow et al., 1993). Where Qm is the mainstream discharge; Qt is the tributary discharge; Qr is the discharge ratio $= Qt/Qm$.

Several parameters characterize the river confluences like the angle of junction, symbolized by α, and the discharge ratio between the tributary and main channel discharges (Q_r) and momentum flux ratios (M_r), as shown below:

$$Q_r = \frac{Q_t}{Q_m} \tag{1- 1}$$

$$M_r = \frac{\rho Q_t U_t}{\rho Q_m U_m} \tag{1- 2}$$

where Q is the flow discharge, U is the mean flow velocity, and ρ is the water density.
The sub-indexes t, and m indicate to the tributary and the main channel, respectively.

1.1.1. River Bends

River meanders are important surface characteristics of the earth. In their alluvial plane, most rivers naturally tend to follow a curving path. Straight river reaches are rare in the absence of human interference; instead, a dynamic, ever-changing state predominates. This typical bend flow pattern causes variations in the flow and sedimentologic properties in a bend, both in time and space, depending on the flow stage, with ramifications for the environment such as biodiversity, society

such as navigability, and safety such as flooding. The ground is constantly changed by the meandering movement, which also revitalizes the floodplain. The inside of these meandering flows typically has a shallow section, represented by a point bar, and the outside typically has a deep region, represented by a pool. This cross-sectional pattern is a result of the intricate process of riverbed erosion and sedimentation, whose dynamic nature makes it extremely challenging to control river flow given the various demands made on a river flow. In contrast to the outer bank, where the loss of land puts the property at risk and results in the loss of fertile soil, the inner bank's developing vegetation during low flow stages stabilizes the point bar and is crucial to accretion. Additionally, the cross-sectional shape of a river affects its navigability and may necessitate expensive dredging operations in order to sustain the advancement of economic activity. The dynamic meander belt also provides a significant capacity for retention during flood occurrences. Finding a balance between these challenges and opportunities is difficult in river management and engineering (Van Balen, 2010).

1.1.2. Secondary Flow in River Bends

Channel bends have substantially more intricate flow characteristics than straight sections. One of the key characteristics of flows at bends is the existence of the secondary flow. Due to the primary flow velocity's vertical variation, secondary flow is caused by an imbalance between the centrifugal force across the depth and the transverse water surface gradient force. In other words, there is an inward flow along the bed and an outward flow close to the water's surface because the inward pressure gradient near the bed outweighs the centrifugal force. The secondary flow is the name given to this circulatory flow pattern (Lien et al., 1999).

Secondary flow, also known as helical flow, affects sediment movement, changes the topography of the bar-pool bed around the bend, and redistributes velocity. Problems with river restoration, navigability, water quality, and infrastructures like bridge piers and abutments require accurate estimates of the velocity distribution and bed topography (Blanckaert and Graf, 2004).

Schematically, the flow through a curved river reach can be drawn as in Figure 1.5, which illustrates the typical profiles of the velocity components, the structure of the secondary flow and the superelevation of the free surface, due to curvature effects. The streamwise flow velocity in rivers is greatest in the highest part of the water column as a result of the existence of this free surface. The fluid is propelled outward the strongest in the highest part of the water column because of the

centripetal influences acting directly on this streamwise velocity. The flow near the bottom is directed toward the inner bank of the curve because of mass conservation. As a result, the bend's cross-sectional plane experiences a secondary flow motion that also has an impact on the main flow. The streamwise velocities are often largest on the outer half of the curve as a result of this mechanism, also known as differential advection, which has significant effects on the morphology of alluvial beds in river bends. A stronger attack on the river's outer bank results from the high flow velocity in the outer part of the curve. As a result, the outer bank may experience erosion and undermining (Van Balen, 2010).

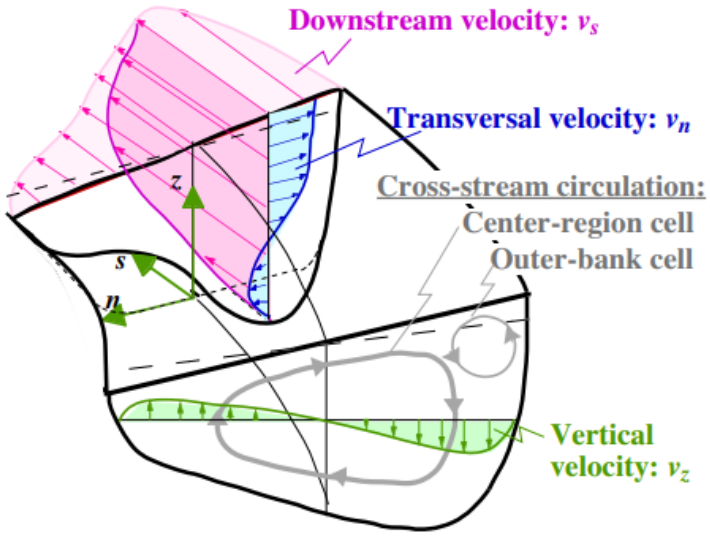

Figure 1.5: Definition sketch of curved open-channel flow and cross-stream circulation (Graf and Blanckaert, 2002)

Along with the traditional helical motion (center-region cell), the outer-bank cell is a weaker, smaller counter-rotating circulation cell that is frequently seen close to the outer bank and is thought to be crucial to the mechanisms involved in bank erosion (Blanckaert and De Vriend, 2004).

1.1.3. River Confluences

The main channel and several tributaries are typical features of natural rivers. A confluence is a term used to describe the point when a tributary meets the main channel. A common occurrence in many hydraulic engineering issues is the confluence of two streams. Natural river networks, water treatment plants, and fish passage conveyance systems are typical examples. Confluence hydrodynamics is extremely complex because there are so many variables influencing the flow

characteristics there. Size, form, slope, and the angle between two channels are examples of geometry variables, which make up one category of variables. There are probably numerous combinations of these elements. The flow attributes, which include geometric, material, kinematic, dynamic, and thermodynamic characteristics, make up the second set of parameters (Baghlani and Talebbeydokhti, 2013).

Confluence features are known to be dependent on the flow dynamics, sediment transport, and bed morphological changes that occur in fluvial networks. In confluence channels, six hydrodynamic zones are distinguished by Best's (1987) conceptual model: flow deflection, flow stagnation, flow separation, maximum velocity, shear layer, and flow recovery (Figure 1.6 for asymmetrical confluences and Figure 1.7 for symmetrical confluences). A deviation of both streams at their intersection causes the flow stagnation zone, which is characterized by an increase in pressure and flow depth and a decrease in flow velocities and shear stresses. In the stagnation zone, the velocity is low and deposit occurs at this area. Due to the flow detaching from the inner wall in the post-confluence channel and its reattachment farther downstream, the tributary's shift in direction creates a zone of flow separation with horizontal recirculation (Best and Reid, 1984). The separation zone's design is crucial because it establishes the post-confluence channel's effective width and acts as an area of reduced pressure and recirculating flow, which encourages sediment buildup. At the contracted cross-section next to the separation zone, the maximum velocity zone is seen downstream of where the flows converge. Shear layers are generated at the intersection of the zones of maximum velocity and flow separation. They are characterized by high shear stresses and turbulence intensities, as well as the existence of well-organized flow structures (Boyer et al., 2006, De Serres et al., 1999).

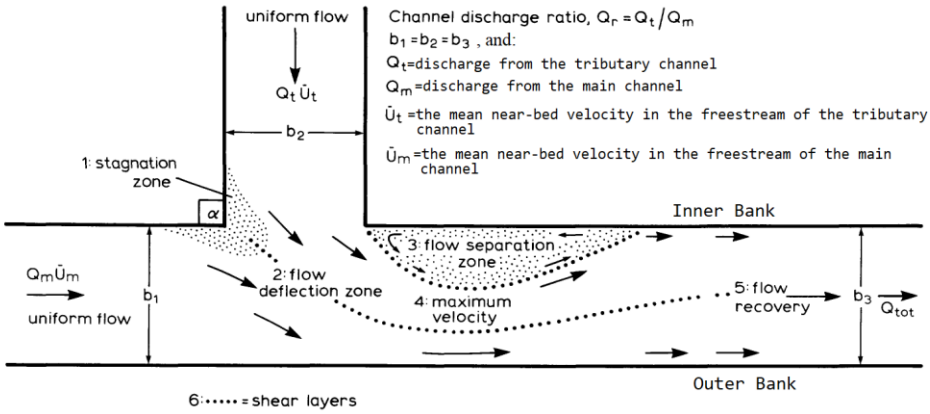

Figure 1.6: A model of flow dynamics at river channel Asymmetrical confluences (Best, 1987)

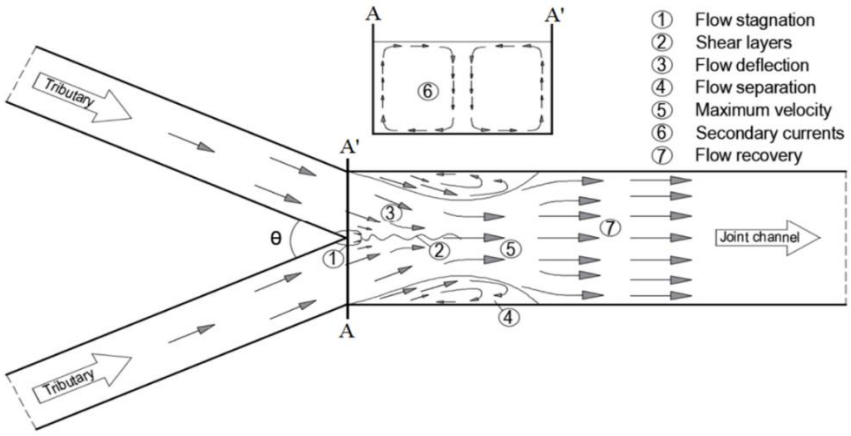

Figure 1.7: Flow elements in symmetrical confluences (Alizadeh and Fernandes, 2021 adapted from Riley and Rhoads, 2012)

In the post confluence channel, the flow recovers toward a straight shear flow as the shear layer widens laterally and fades (Leite Ribeiro et al., 2012). The three-dimensional flow at river confluences is frequently characterized by the existence of helical flow cells. There has been much discussion on the nature and characteristics of these cells for a very long time (Rhoads and Kenworthy, 1995; Lane et al., 2000; Weber et al., 2001). The characteristics of the confluence determine whether or not these cells exist, how many there are, and how intense they are. The interaction between flow, sediment transport, and morphology further complicates processes in alluvial river confluences (Leite Ribeiro et al., 2012).

1.1.4. Secondary Flow in River Confluences

As the tributary's flow enters the main river, the flow direction changes. Due to this change, the centrifugal force induces an opposing surface radial flow to that of the deflection and the bottom inward current. As shown in Figure 1.8, the secondary current of the main channel flow, in contrast, rotates in the opposite direction of the secondary flow in the branch channel. The combining of the branch and main channel flows in this instance causes the tributary channel to set up a shearing action to the main flow, which subsequently results in the evolution of two surface flows. The skewing of the shear plane rather than the vertical is caused by the effects of the relative magnitudes of consolidated flows and the profile of the non-uniform vertical velocity. The interface between counter rotating vortexes is called shear plane. The non-uniform vertical velocity profile has produced a three-dimensionality in the new amalgamated flow. Looking downstream, a secondary vortex with a clockwise rotation was visible near the internal bank at the downstream end of the main channel (Barkdoll, 2003). Another secondary vortex emerges and rotates against the secondary flow of the branch channel at the opposite bank (external bank) of the main channel downstream. Finally, and mostly as a result of the fluid viscosity, the secondary currents of the two channels gradually diminish in the direction of the river (Song et al., 2012).

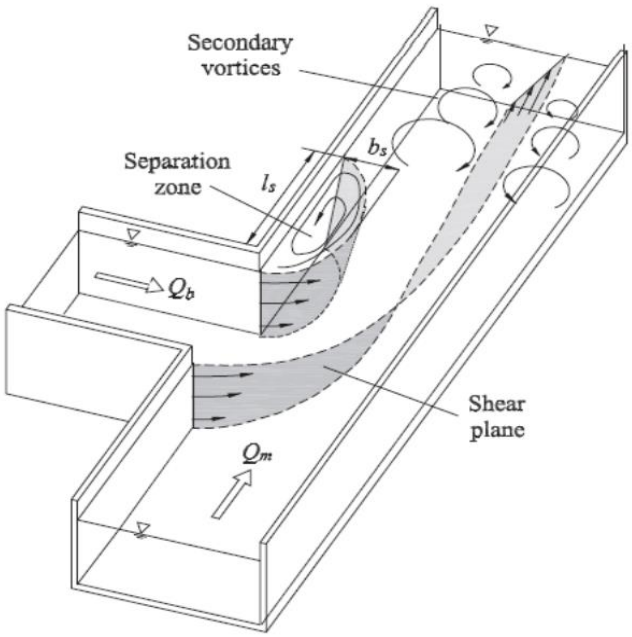

Figure 1.8: The structure of secondary flow in confluent channel (from Song et al., 2012 after Weber et al., 2001)

1.1.5. Mechanism of Flow in River Confluences

Some features characterize the flow in the confluent channels according to the previous studies, which can be summarized as follows (Weerakoon, 1990):

- There exist two oppositely circulating secondary flow cells. The secondary flow of the branch channel that occurs near the internal bank of the main channel could be more intense than the ones of the main channel near the external bank of the main channel (see Figure 1.8) because of the higher curvature experienced by the branch channel flow.
- At the corner of the junction's inner bank, the superelevation of the free surface appears because of the balancing centrifugal forces connected with the cells of the secondary flow.
- The recirculation zone appears near the inner bank of the main channel directly after the junction due to the separation of the accelerated branch channel flow from the wall and forming a steep pressure drop. Then a strong counter flow happens forming a recirculation zone.
- Away from the water surface, the recirculation zone size becomes smaller. This could be because of the entrainment by the secondary flow and is distinguished in the confluences of deep water.
- Transfer of momentum to the recirculation region is appeared by vortices which ascend with the secondary flow.
- The mixing resulting from the gradient of lateral velocity in the shear layer is related to the vortices at the interface, especially, the vortices that arose in the corner of the inner bank. However, this is not robust compared to the scattering produced by the secondary flow.
- In the light of former research, these mentioned features might increase with the increasing confluence angle and discharge ratio.

1.1.6. Open Channel flow

The flow having an open surface or free surface that is in contact with the atmosphere is referred to as an "open channel flow." It may be constructed, such as canals, flumes, spillways, culverts, and weirs, or natural, such as rivers, streams, floodplains, and estuaries. Since closed channels are filled with fluid, there is no free surface there. In these types of channels, the fluid is propelled by pressure

forces, whereas in open channels, it is propelled by gravity forces. The fundamental force balance is between friction and gravity. Based on the channel shape, discharges and water depths can be estimated. The fluid in these cases is often water, the channel is large, and the flow is turbulent. Since the free surface is typically at atmospheric pressure, it is treated under a constant pressure. The flow at the open channel bed complies with the no-slip requirement. The velocity always changes across the channel sections because of friction in the open channel along the border. The maximum velocity often occurs in the middle of the plane, about 20% below the surface. The primary cause of such is a resistance at the air/water interface caused by secondary currents flowing from the edges towards the centre. However, the maximum velocity occurs near the surface in the wide and shallow channels, with a velocity profile that is roughly logarithmic from the bottom to the surface (Herreras and Izarra, 2013).

1.1.7. Free Surface Flows Model

1.1.7.1. Numerical Simulation of Free Surface Flows

In most situations, it is considered that the numerical methods are either incompressible or compressible. The velocity and pressure over the full domain could be met by either the incompressible Navier-Stokes equations or the compressible Euler equations. Techniques that combine an incompressible liquid and a compressible gas have also been thought of. Incompressible liquids should use the Navier-Stokes equations, whereas compressible gases should use the Euler's equations. Numerous numerical techniques can be used to solve free surface flows, particularly when precisely defining the motion of the free surface. When the liquid domain displacement in fluid-structure interactions is small, for instance, Lagrangian methods or Arbitrary-Lagrangian-Eulerian (ALE) methods are mostly used. Additionally, using Eulerian methods, a new unknown has been added to the entire cavity to track the liquid presence. To ensure that the problem is well-posed, this additional unknown necessitates the use of an additional equation. Pseudo-concentration methods, level set methods, and Volume of Fluid (VOF) methods are the three most used Eulerian techniques. The free boundary in the level set method is defined by a level line of a smooth function. This additional function generally satisfies a Hamilton- Jacobi equation. In addition, the free boundary is determined by a level set of a smooth function in the pseudo-concentration method. This additional function satisfies an advection equation. In the VOF methods, the fluid characteristic function follows the fluid domain. In the liquid, this function has value of one, zero

in the gas, and jumps over the interface. It satisfies an advection equation. Despite rigorously conserving the fluid mass, it is difficult to compute the curvature due to the lack of regularity of the characteristic function. It is well-adapted to problems with changes in the topology of the domain, or cavity filling. Mixed VOF and level set methods conjugate the smoothness character of the level sets and the mass conservation (Caboussat, 2003).

1.1.7.2. A Comparison between the Free Surface Model (FSM) and Rigid-Lid Model (RLM)

One must first understand how both are modelled in order to distinguish between the Free Surface Model, which is used to simulate open channel flow, and the Rigid Lid Model, which is used to simulate closed channel flow. In the rigid-lid model, only the water flow is considered as illustrated in Figure 1.9, however in the Free Surface Model, both air and water fluxes are taken into account in the simulation, allowing for a deformed interface. In the past 20 years, there has been a huge increase in the study of rigid-lid models for numerical modelling of curved channel flow. Hodskinson and Ferguson simulated the flow separation in a heavily curved channel using the rigid-lid model in 1998. They achieved good agreement with the flow velocity measurements. (Hodskinson and Ferguson, 1998). Using curved channel, Blanckaert et al. carried out a study in 2009. This study used a rigid-lid model with a 3D LES (Large Eddy Simulation) and RANS (Reynolds Averaged Navier-Stokes) CFD models. It also includes field measurements, laboratory trials, and numerical simulations. They came to the conclusion that the use of the 3D LES model for simulating the flow hydrodynamics for the experiments was successful, and that the use of the 3D RANS code for simulating the flow hydrodynamics was successful in the case of a mobile bed but frequently worse in the case of a horizontal bed (Blanckaert et al., 2009). According to Booij's 2003 study, which used shallow curved free surface flows, the basic characteristics of major and secondary flows could be produced using RANS computations, whereas shear stresses and other flow properties could be accurately reconstructed by 3D LES (Booij, 2003b).

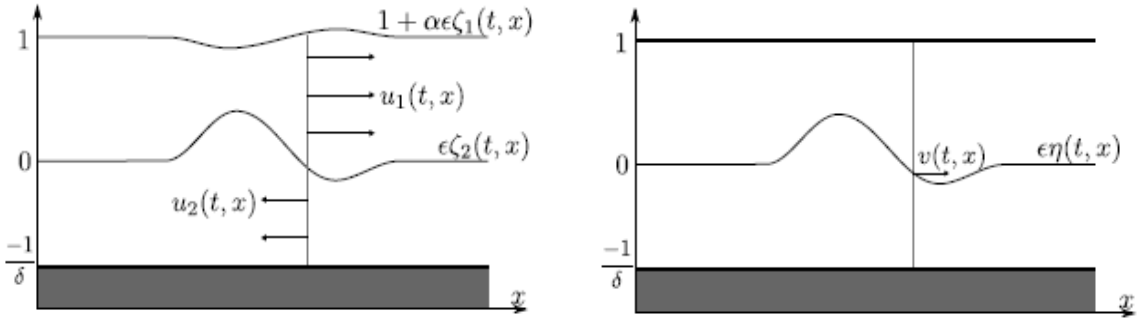

a- Free surface model. b- Rigid-lid model.

Figure 1.9: The domain in the two different models (Duchêne, 2014)

1.2. Thesis objectives

This project involves numerical simulation of two cases including curved channels and confluences. The link between the two cases is the presence of strong secondary flows. To obtain accurate predictions for river curves, 3D numerical models may be thought of as being helpful. These models rely on the complicated spiral flow motion in the river curve combined with three-dimensional flow features. However, the lengthy computation times and potential numerical instability are significant issues that most 3D models experience (Song et al., 2012). This motivates the investigation of more commonly used and more stable turbulence models such as kepsilon and realizable kepsilon. In this study, a 3D OpenFOAM numerical model is used as it has several turbulence models and it has VOF for free surface to investigate the impacts of secondary currents on the hydraulic structures and water surface elevation in curved channels and confluences. Thus, the following objectives are intended to be accomplished through the current research:

- Select the appropriate numerical model to simulate the flow behavior at river bends and confluences.
- Examine and compare various turbulence models within the numerical model to identify the most precise ones and optimal parameters.
- Considering the emphasis on velocity and water depth, compare the numerical results with extensive experimental and numerical data that have been gathered by other researchers.

1.3. Contributions and Novelty of the Thesis

1.3.1. Contributions

Paraphrase objectives like a paragraph does not bullet items.

Several journal articles based on the results of this thesis have been released. This thesis contains four chapters based on these articles.

1. Rawaa Shaheed, Abdolmajid Mohammadian, and Xiaohui Yan (2021) A Review of Numerical Simulations of Secondary Flows in River Bends. Water journal, 13, 884. https://doi.org/10.3390/w13070884.Hjgjkh.
2. Rawaa Shaheed, Xiaohui Yan, and Abdolmajid Mohammadian (2021) Review and Comparison of Numerical Simulations of Secondary Flow in River Confluences. Water journal, 13, 1917. https://doi.org/10.3390/w13141917.Jhlkj.
3. Shaheed R, Mohammadian A, Gildeh HK (2018) A comparison of standard k–ε and realizable k–ε turbulence models in curved and confluent channels. Environmental Fluid Mechanics, 19:543-568. https://doi.org/10.1007/s10652-018-9637-1.
4. Rawaa Shaheed, Abdolmajid Mohammadian, and Xiaohui Yan (2022) Numerical Simulation of Turbulent Flow in Bends and Confluences Considering Free Surface Changes Using the Volume of Fluid Method. Water journal, 14, 1307. https://doi.org/10.3390/w14081307.

The following paper was not included in this thesis because it was presented at a conference.

1. Shaheed R, Mohammadian A, Gildeh HK (2016) 3D Numerical Modelling of Secondary Current in the Shallow River Bends and Confluences. International Symposium on Outfall Systems,2016, May 10-13, 2016, Ottawa, Canada.

1.3.2. Novelty of the Thesis

- The research will implement the 3D OpenFOAM numerical model to simulate the horizontal distribution of flow in curved rivers. In addition, the progress in unravelling and understanding the bend dynamics will be considered.
- Comparing rigid lid and free surface for both bends and confluences to know if the rigid lid which is easier and more stable and accurately solved this problem. Taking in consideration that for the cases when the water surface variation is very large, rigid lid is not accurate.

- Several turbulence models will be studied and evaluated to determine the best numerical models that could predict the secondary current properties in the river bends and confluences with higher level of accuracy.
- In the model evaluation task, the experimental data and simulated results will be compared with the ultimate objective of determining the simplest and most accurate methods of predicting the velocity distribution and secondary flows in river bends and confluences.
- Consequently, this study will impact the design of river engineering works and will help in solving river engineering problems.

1.4. Thesis organization

This thesis is structured as a collection of technical papers with six chapters as follows:

Chapter 2 "A Review of Numerical Simulations of Secondary Flows at River Bends," the first technical paper, is presented in this chapter. The principles of secondary flow, the governing equations and boundary conditions for numerical simulations, and earlier numerical research on river bend flows are all thoroughly reviewed in this chapter. Most significantly, it examines different numerical simulation techniques and the effectiveness of various turbulence models in simulating the flow at river bends and comes to the conclusion that the key challenge is choosing the right model for each instance of turbulent flow. The current study covers recent developments in numerical modelling of secondary flow and highlights the major difficulties, which can help shape future research. This chapter was published in Water journal, (2021), 13, 884.

Chapter 3 "Review and Comparison of Numerical Simulations of Secondary Flow in River Confluences", the second technical publication, is described in this chapter. Since the flow characteristics at river junctions are thought to be turbulent and three-dimensional, the hydrodynamics of flows in confluences are now frequently simulated using three-dimensional models to properly represent the flow structures. For this goal, several numerical models have been suggested, and a number of turbulence models have been employed to simulate the flows at confluences. Different turbulence models have been applied to the numerical model to forecast flows, and the results have been compared with other data such as field, laboratory, and experimental data to evaluate the correctness of the turbulence models. Finding a suitable model for each instance of turbulent flow and for various sorts of confluences was the goal of these investigations. The effectiveness of turbulence models for confluences is examined in this work for

several numerical simulation techniques. This chapter was published in Water Journal, (2021),13,1917.

Chapter 4 "A comparison of standard k-ε and realizable k-ε turbulence models in curved and confluent channels" is the title of the third technical article described in this chapter. To simulate how secondary currents affect water velocity in channel bends and confluences, a 3D OpenFOAM numerical model is used. The finite volume method is used to mimic the behavior of these currents (FVM). The experimental data of a confluent channel and a steeply curved channel were utilized to compare the numerical outcomes and assess the model's applicability. A rigid lid approach is used in this paper. Two turbulence models (standard k–ε and realizable k–ε) were used in the current study to compare how well different models performed in forecasting the behavior of these secondary flows. The precision of the standard and realizable k–ε turbulence models were assessed and discussed. This chapter was published in Environmental Fluid Mechanics Journal, (2018),19:543-568.

Chapter 5 "Numerical Simulation of Turbulent Flow in Bends and Confluences Considering Free Surface Changes Using the Volume of Fluid Method" is the title of the fourth technical paper described in this chapter. Using three-dimensional (3D) numerical models, the effect of secondary flows on the flow velocity in open channel bends and confluences was studied. In this investigation, the standard k-ε and the realizable k-ε turbulence models were used, together with the Reynolds-averaged Navier-Stokes equation system as the governing equations. The volume of fluid free-surface tracking approach was used in this study to simulate free surface displacements. Utilizing experimental data from a confluent channel and a steeply curved channel, the numerical models were assessed and validated. The two turbulence models' accuracy was assessed and discussed. This chapter was published in Water Journal, (2022),14, 1307.

Chapter 6 efforts that have been made to build upon the work from the preceding chapters are summarized and concluded in this chapter. Additionally, it offers guidance on how the study might going forward and makes suggestions for additional research.

Chapter 2. A Review of Numerical Simulations of Secondary Flows in River Bends

Abstract

River bends are one of the common elements in most natural rivers, and secondary flow is one of the most important flow features in the bends. The secondary flow is perpendicular to the main flow and has a helical path moving towards the outer bank at the upper part of the river cross-section, and towards the inner bank at the lower part of the river cross-section. The secondary flow causes a redistribution in the main flow. Accordingly, this redistribution and sediment transport by the secondary flow may lead to the formation of a typical pattern of river bend profile. It is important to study and understand the flow pattern in order to predict the profile and the position of the bend in the river. However, there are a lack of comprehensive reviews on the advances in numerical modeling of bend secondary flow in the literature. Therefore, this study comprehensively reviews the fundamentals of secondary flow, the governing equations and boundary conditions for numerical simulations, and previous numerical studies on river bend flows. Most importantly, it reviews various numerical simulation strategies and performance of various turbulence models in simulating the flow in river bends and concludes that the main problem is finding the appropriate model for each case of turbulent flow. The present review summarizes the recent advances in numerical modeling of secondary flow and points out the key challenges, which can provide useful information for future studies.

Keywords: river bends; secondary flow; numerical model; flow field

---

[2] This chapter has been published as Rawaa Shaheed, Abdolmajid Mohammadian, and Xiaohui Yan (2021) A Review of Numerical Simulations of Secondary Flows in River Bends. Water journal, 13, 884. https://doi.org/10.3390/w13070884.

2.1. Introduction

Rivers rarely run-on straight paths, and most of them run on a curved route. The flow patterns on river bends are very complicated and have special characteristics. Basically, flow patterns in river bends are affected by certain factors such as the centrifugal force caused by the flow curvature and the vertically varying velocity, the cross-sectional stress, in addition to the pressure gradient in the radial direction due to the lateral slope of the water's surface. All these factors create a flow called secondary flow (Ghobadian and Mohammadi, 2011), which may significantly affect the primary flow motion and, in turn, affect pollutant dispersion and sediment transport. Therefore, it is important to predict and estimate the flow behavior of river bends for proper design of nearby hydraulic structures, environmental and ecological assessments, and sound planning of inhabitation projects. Flow patterns and characteristics in river bends have been widely studied due to the major significance of this subject. The secondary flow, according to Rozovskii (1961) and De Vriend (1979,1980), is a helical path moving toward the outer bank at the upper part of the river and moving toward the inner bank at the lower part of the river. Thus, a slight deviation occurs on the shear force, which follows the same direction as the local flow near the bed. This deviation is from the direction of the mean flow (Engelund and Skovgaard, 1973).

The flow in river bends can be studied using either physical or numerical methods. Several experimental and laboratory studies were performed to investigate the flow features in river bends (Blanckaert and Graf, 2001; Booij, 2003a; Reinauer and Hager, 1997; Roca et al., 2007; Tominaga and Nagao, 2000). These studies aimed to collect data on flow variables in channel bends and analysis of the results. The parameters studied in the papers include the flow velocity components, the secondary flow cells including the outer bank cells, etc. These studies have provided the knowledge base for understanding bend flows. However, the requirements of cost and time for the physical tests motivated the researchers to discover more flexible and inexpensive tools to examine flow behavior, which is represented by the numerical models.

The accurate simulation of the flow in curved channels requires a 3D hydrodynamic model. The flow field in curved channels was simulated by several 3D models, which were developed by researchers such as De Vriend, 1980; Shimizu et al., 1990; Wang and Hu, 1990. In addition, two-dimensional (2D) models were applied by other researchers to simulate the flow in curved channels (Hsieh and Yang, 2003; Ikeda and Nishimura, 1986; Molls and Chaudhry, 1995). At straight channels, or when the effect of the curvature is small, the secondary flows are mainly produced by

the non-homogeneity and anisotropy of turbulence (Wang and Cheng, 2006), so there is no significant effect from the secondary flow in many practical cases. According to Chang (1971) and Fischer (1969), the transverse mixing caused by the secondary flow in curved channels is much stronger than that in straight channels. Some researchers (Booij, 2003a; Kang and Choi, 2006; Khosronejad et al., 2007) indicated that there is a limited capability to predict the secondary flow by isotropic turbulence models such as the k-ε model. Thus, the study of flow around bends typically requires higher-order turbulence models such as Reynolds Stress Models (RSM) and Large Eddy Simulation (LES) (Booij, 2003a; Luo and Razinsky, 2009; W. van Balen et al., 2009), especially when the bend of the channel is of a sharp type (Marriott, 1999; W. van Balen et al., 2009; J. Zeng et al., 2008). The distribution of helical flow strength and its changes along channels were first studied by Mosonyi and Gotz (1973). They showed that the strength changes of the secondary flow can well describe the flow itself. Additionally, the existence of the second cycle of the secondary flow near the internal bend, which happens only at the channel of (bed width/water depth) <10, was reported by them for the first time. The finite difference method was used by Leschziner and Rodi (1979) to apply their three-dimensional numerical model to calculating flow in strongly curved open channels (180◦ bend with straight inlet and outlet reaches) with a rectangular cross-section. The standard k-ε model was employed in their study to produce the correct eddy–viscosity distribution in a wide range of flow situations. The transverse surface slope and velocity field in the curved channel were predicted and presented. The results obtained from the employed model were judged to be satisfactory for all major flow phenomena. There is a lack of comprehensive reviews on the advances in numerical modeling of bend secondary flow in the literature. Therefore, this study aims to review some of the previous studies that used numerical models to simulate the secondary flow in river bends. The main motivation of this review is to assess these numerical models used in simulations and choose a suitable numerical model to simulate the behavior of the flow in the river bends from the researcher's point of view. The main point of this review is to determine the choice of the model dimension (i.e., 2D or 3D), selection of a turbulent model (RANS, LES, etc.), and application in different channel geometries (single curved channel or meandering).

This paper is organized as follows: Section 2 deals with the secondary flow in river bends. Section 3 covers boundary conditions, and Section 4 reviews the numerical studies on river bends including different kinds of bends in different situations and some effects of secondary flows in these rivers.

Section 5 is the discussion. Section 6 is the critical review and future research needs. Finally, the conclusions complete the study.

2.2. Secondary Flow in River Bends

2.2.1. Mechanism of Secondary Flow

Given the importance of secondary flow in river bends, and its significant effects on the main flow particularly, and on the bottom configuration of the river generally, it is important to study these effects in river bends and take them into consideration in the design of river engineering works. The secondary flow is a helical path moving towards the outer bank of the river in the upper part and towards the inner bank of the river in the lower part of the cross-section, as shown in Figure 2.1.

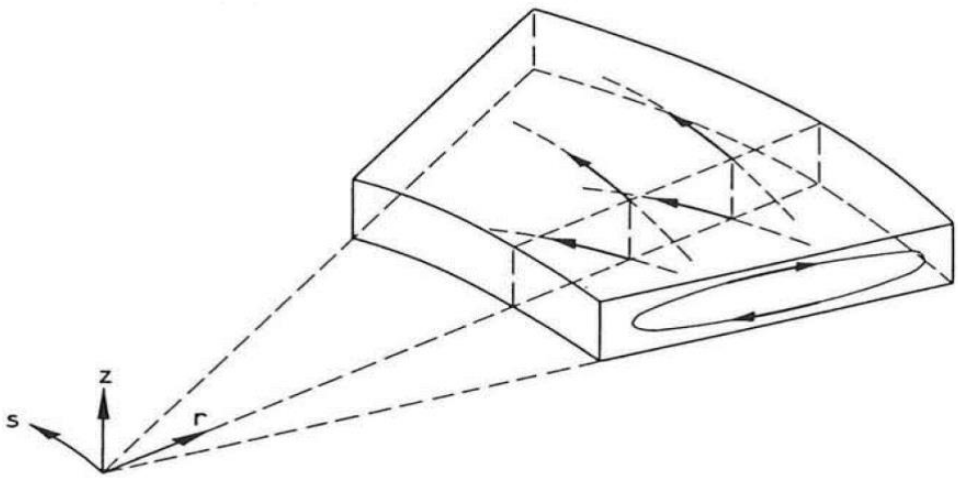

Figure 2.1: The mechanism of secondary flow (Jansen, 1994)

The main flow of the curved channel is affected by the redistribution of the velocity. The velocity increases near the outer bank of the channel and decreases near the inner bank of the channel (H. De Vriend, 1980). As the river enters the bend, the flow particles are affected by the acceleration due to centrifugal force. Accordingly, the flow particles tend to move towards the external wall of the river. Then, an increase in the water level occurs near the outside wall and decreases near the inside wall. Non-uniform pressure distribution is generated in the cross-section due to the slope of the free surface. This pressure increases near the external wall. Due to the difference between the small vertical accelerations and the high gravitational acceleration, there is a distribution of the

hydrostatic pressure over the vertical. Subsequently, there is approximate equality in the pressure gradient in the radial direction over the vertical. Thus, the magnitude of the longitudinal velocities is equal at all points in the vertical direction and the centrifugal accelerations are completely counterbalanced by the centripetal acceleration. Due to the viscosity forces, there is a non-uniform distribution of the longitudinal velocity, which, in turn, causes a non-uniform distribution of the centrifugal acceleration. Accordingly, the velocity and the centrifugal acceleration increase near the flow surface and decrease near the bottom. The helical movement that is vertical to the main flow occurs because of the imbalance between the separate points in a vertical direction as shown in Figure 2.2.

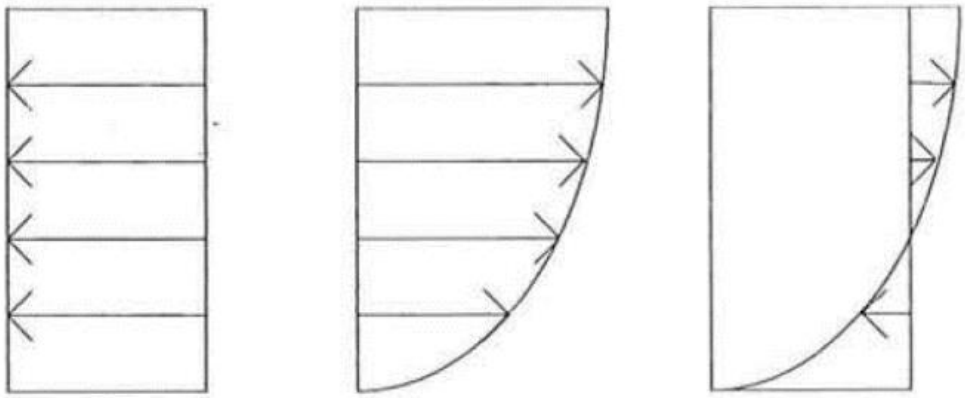

1. Influence of centripetal acceleration | 2. Influence of centrifugal acceleration | 3. Result of the superposition of curves 1 and 2

Figure 2.2: Centripetal and centrifugal acceleration (Jongbloed, 1996)

The movement of the helical path depends on the centrifugal acceleration, which means it is directed towards the outer bank at the upper part of the river as the centrifugal acceleration increases and towards the inner bank at the lower part of the river as the centrifugal acceleration decreases at this area. As the flow enters the bend, the free surface slope must be built up. Therefore, there is a negative pressure gradient near the internal wall and another positive pressure gradient close to the external wall (Jongbloed, 1996). At the exit of the bend, there is a positive pressure gradient near the interior wall and a negative one close to the exterior wall. The free surface slope decreases towards the bend exit until it may gradually become zero at the end of the bend.

2.2.2. Secondary Flow Cells

There are two regions that could be found in the bend of the curved channel: the center region cell and the outer bank cell. The center region cell is the classical helical or spiral motion of the secondary flow that moves toward the outer bank at the upper part of the river and moves toward the inner bank at the lower part of the river. The center region cell results from the interaction of the centrifugal force, the pressure gradient resulting from the inclined water level, and the roughness of the bed (Rozovskii, 1961). The outer bank cell is a counterrotating eddy at the outer bank of the channel (Bathurst et al., 1977). The outer bank cell is mainly caused by turbulence anisotropy and is a key feature of bend flow, and it has been found that the proximity of the water surface and the outer bank can affect its generation and characteristics (Blanckaert, 2009, 2011). The outer bank cell is usually smaller and weaker than the center region cell. However, it should not be underestimated because it could be strongest in the sharp channel bends, and it has a stabilizing effect on the erosion of the outer bank and the mixing abilities in this region (Graf and Blanckaert, 2002). This is shown in Figure 2.3.

2.2.3. Velocity Redistribution

The flow distribution is nearly symmetric in straight channels, but the main velocity of the flow in channel bends is significantly affected by the secondary flow, and accordingly, a considerable redistribution occurs with respect to the main velocity. The flow particles that are close to the free surface are transported towards the outer bank of the river affected by the secondary flow. The core of the high-velocity region is near the inner bend at the bend entrance due to the potential vortex effect (J. Zeng et al., 2008)and gradually shifts towards the outer bank due to secondary flow caused by the combined effects of pressure gradients and centrifugal forces. The velocity and momentum of these particles are larger compared to the ones in the outer bank. Thus, an increase occurs in the velocity of the outer bank region. The process is just the opposite near the bed of the river, where the flow particles with smaller velocity and momentum move towards the inner bank of the river, causing a low velocity at this area. The vertical convective transport of main flow momentum is significant at the area close to the sidewalls, while it is almost negligible near the central part of the river. The main reason for the velocity increase near the outer bank and reduction near the inner bank is vertical convection, while outward lateral interaction is due to radial convection (Jongbloed,

1996). The effect of secondary flow on the main flow is explained in Figure 2.4, where the streamlines represent the secondary flow and the isovels represent the main flow velocity.

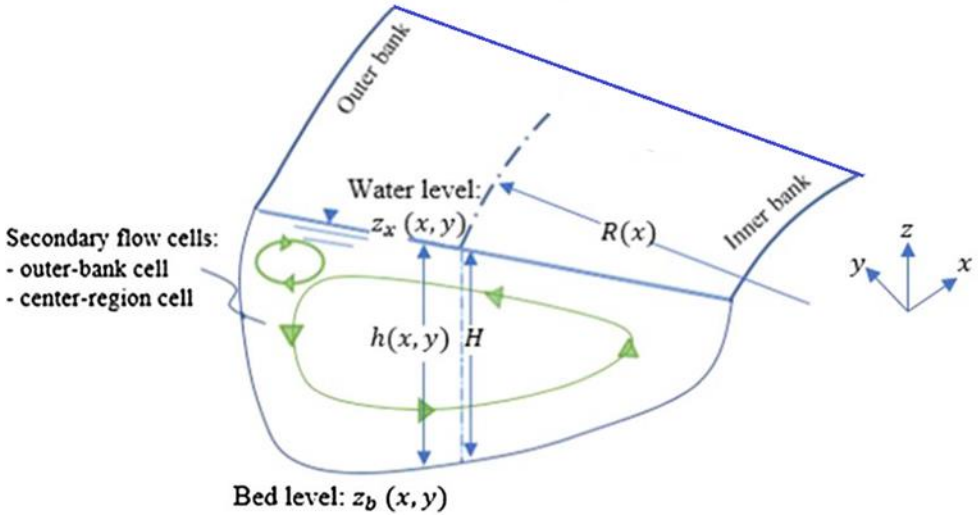

Figure 2.3: Secondary flow cells (based on Blanckaert (2011))

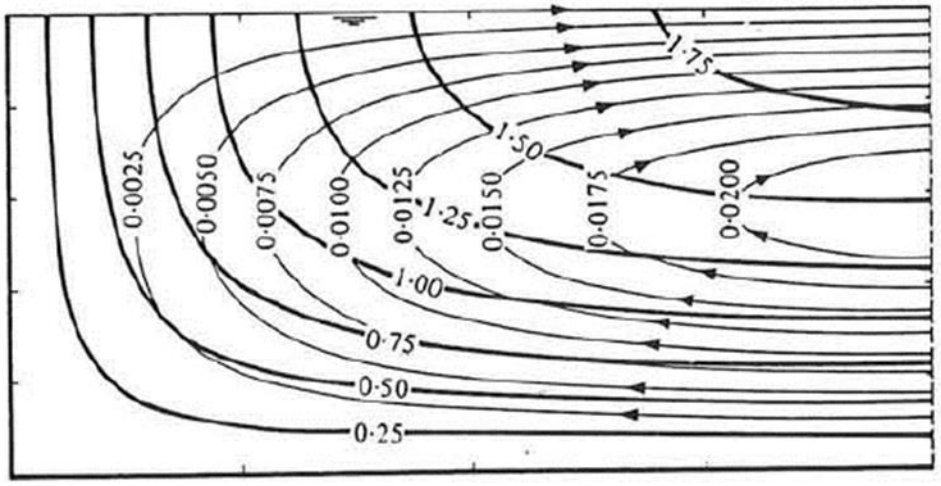

Figure 2.4: Main-flow isovels (———) and secondary-flow streamlines (⟶) in the inner wall region of a shallow channel (d/B = 0.1) (H. De Vriend, 1980)

Figure 2.4 presented above shows that the variance of velocities along the streamlines of the secondary flow near the bed of the river is not significant. The difference increases towards the inner bank, and then streamlines are almost vertical to the isovels near the surface of the river. There are some factors that affect the secondary flow, such as the distance between the isovels (the local main velocity gradient), the secondary flow strength, and the sine of the angle of intersection

between the main flow isovels and the streamlines of the secondary flow. Note that the effect of the secondary flow in the wall district will be comparatively stronger in the upper part of the section where the velocity gradient is of the same order of magnitude throughout the vertical. As a result, the main velocity profile becomes flatter near the surface, which is confirmed by experimental research (Jongbloed, 1996). On the other hand, the longitudinal velocity component at the entry of a bend and in the early part of the internal wall area increases, accompanied by a steep fall of the free surface. In addition, extreme velocity is found at the free surface at this place in the cross section (Booij and Tukker, 1996). It is noticed that the maximum velocity at the end of a 180° curved bend shifts outward—the outer part of the cross-section due to the redistribution of the main velocity (De Vriend, 1980), while the opposite situation is found at the outside wall area at the entry of a bend. Note that the longitudinal velocities decrease due to a positive pressure gradient.

2.2.4. Mathematical Description of the Main Flow and Secondary Circulation

The differential equations, which include the continuity equation and Reynolds-Averaged Navier–Stokes system, can be used to describe the three-dimensional incompressible fluid flow. For uniformity, these equations can be rewritten as below:

Conservation of mass:

$$\nabla . U = 0 \tag{2-1}$$

The momentum equations:

$$\frac{\partial \rho U}{\partial t} + \nabla . (\rho UU) = \nabla . T + \rho g - \nabla p \tag{2-2}$$

where U is the velocity vector; ρ is the density; g is the gravity acceleration; p is the pressure; T is the viscous stress tensor.

2.3. Boundary Conditions

The previous section introduced the mechanisms of secondary flow, the secondary flow cells, the velocity redistribution, and the governing equations. To simulate bend flows, certain boundary conditions should be applied, and the present section introduces the typical boundary condition setup. There are four main kinds of boundaries for the numerical models that should be considered, namely: walls, free surface, inlet, and outlet.

2.3.1. Wall Boundaries

As the velocities at the wall are equal to zero and have large gradients in the vicinity, a very small grid distance should be used at this position. Thus, the high-Reynolds number model is no longer viable, and therefore, the first grid-point is defined at some distance from the wall (Jongbloed, 1996). Considering the effect of the viscous shear stresses or the turbulent shear stresses or both, it is recommended to separate the near-wall area into three regions (Booij, 1992): wall region, buffer layer region, and the turbulent boundary layer. At the wall region, the turbulent shear stresses can be abandoned (the so-called viscous sublayer). A buffer layer region comes next to the wall region where neither of the viscous shear stresses nor the turbulent shear stresses can be abandoned. The third region, the turbulent boundary layer, is distinguished where the viscous shear stresses can be abandoned. Accordingly, the boundary conditions and the first grid point should preferably be positioned in the last zones (Pezzinga, 1990). The boundary conditions for k (turbulent kinetic energy) and ε (turbulent energy dissipation rate) can be found using the following equations (Jongbloed, 1996):

$$k = \frac{u_*^2}{\sqrt{c_\mu}} \tag{2-3}$$

$$\varepsilon = \frac{u_*^3}{k\, y} \tag{2-4}$$

where u_* is shear velocity, c_μ is a model constant ($\cong 0.09$), and y is the distance to the wall.

Flow variation properties at the area close to the solid walls and bed are steep. To simulate the wall effect and estimate the turbulence parameters at this area, the wall function method is employed (Rodi, 1984). With the wall function, a fairly coarse grid is used in the area close to the wall. It is also considered to be an economical method of turbulent flow modeling (Jian and McCorquadale, 1998). Below are some of the turbulence equations for some models that use the wall function approach (Wilcox, 1998):

$$\omega = \frac{k_p^{1/2}}{(\beta_0^*)^{1/4}\kappa\delta_{np}} \tag{2-5}$$

$$\varepsilon = \frac{(\beta_0^*)^{3/4} k_p^{3/2}}{\kappa\delta_{np}} \tag{2-6}$$

$$k = \frac{\rho(\beta_0^*)^{3/4} k_p^{3/2} u_p^+}{\delta_{np}} \tag{2-7}$$

where δ_{np} = distance from the solid boundary to the center of the closest element; k_p = turbulence kinetic energy at the closest cell to the wall; and u_p^+ = defined as follows:

$$u_p^+ = \begin{cases} y_p^+ \; for: y_p^+ \le y_0^+ \\ \frac{1}{\kappa}\ln\left(E y_p^+\right), for: y_p^+ > y_0^+ \end{cases} \tag{2-8}$$

where $y_p^+ = \delta_{np} u_* / v$ and y_0^+=11.53 (Melaaen, 1990) and E is related to the roughness Reynold number $k_s^+ = u_* k_s / v$ as follows (Wu et al., 2000):

$$E = \exp[\kappa(B - \Delta B)] \tag{2-9}$$

where $k_s =$ equivalent roughness height of bed; B = additive constant = 5.2; ΔB = roughness function of the roughness Reynold number, which is calculated by (Cebeci and Bradshaw, 1977):

$$\Delta B = \begin{cases} 0.0 \; k_s^+ < 2.25 \\ \left[B - 8.5 + \frac{1}{\kappa} ln k_s^+\right] sin[0.4258(ln k_s^+ - 0.811)] \; 2.25 < k_s^+ < 90 \\ B - 8.5 + \frac{1}{\kappa} ln k_s^+ \; k_s^+ \ge 90 \end{cases} \tag{2-10}$$

The equivalent roughness height k_s quantified the influence of roughness elements.

2.3.2. Free Surface

For bend flow, the rigid-lid approximation is often adopted. The rigid-lid approximation is used when the Froude number is small, and a frictionless flat plane is assumed (Leschziner and Rodi, 1979). This approximation for this fictitious rigid lid does not neglect the changes in surface elevation but these changes are taken into account in an indirect manner. Accordingly, non-zero pressure gradients in the radial and vertical directions are expected at the boundary, which would result in some errors because the superelevated regions are implicitly considered hydrodynamically passive. However, experiments conducted by Mcguirk and Rodi (1977) showed that the error associated with this approximation does not exceed approximately 10% of the total channel depth (Mcguirk and Rodi, 1977). Therefore, the following assumptions at the free surface can be formulated (Jongbloed, 1996):

- Vertical velocities are zero;
- The derivative in the vertical direction of the radial and longitudinal velocities are zero.

On the water surface, in absence of wind, the boundary conditions for the turbulence parameters are:

- $\varepsilon = 0$
- $k = 0$

For the free surface, the turbulent kinetic energy and net fluxes of horizontal momentum are set as zero. The pressure normal to the surface is set to atmospheric, velocity is set to zero, and the dissipation rate is calculated from the relation given by (Rodi, 1993):

$$\varepsilon = k^{3/2}/(0.43h) \text{ at } z = z_s$$

where h = local water depth.

2.3.3. Inlet

Determining the distributions of velocities and the parameters of the turbulence across the boundary of the inlet is likely not possible in practice. Therefore, most of these distributions are estimated based on physical reasoning. The experimental distribution of k is rarely available and the ε-distribution can only be obtained indirectly from measurements of other turbulent quantities (Leschziner and Rodi, 1979). To smooth out the boundary conditions from the positions of interest, the boundaries must lie at a distance long enough for the flow if the errors caused by the assumptions for the boundary conditions cannot be neglected (Jongbloed, 1996). Below are some of the turbulence equations for some models that are used at the inlet:

$$K_{in} = \frac{3}{2}(U_{in}T_i)^2 \; ; \; \varepsilon_{in} = \frac{9}{100}\frac{K_{in}^{2/3}}{\ell} \; ; \; \omega_{in} = \frac{\varepsilon_{in}}{K_{in}} \; ; \; \ell = 0.07L \qquad (2\text{-}11)$$

where K_{in} = inlet turbulent kinetic energy; ε_{in} = inlet turbulent kinetic dissipation rate; U_{in} = average inlet velocity; T_i = intensity of turbulence; and L and ℓ = characteristic length of channel and length scale of the flow field, respectively.

2.3.4. Outlet

The discussion in the previous section can be used to determine the outlet boundary conditions. If the outlet boundary is far enough away, a zero gradient boundary condition may be employed for most variables.

2.4. Advantages and Disadvantages of Various Numerical Methods

Examples of the widely used turbulence modeling approaches include direct numerical simulation (DNS), Reynolds-averaged numerical simulation (RANS), RSM (Reynolds Stress Model), large eddy simulation (LES), and detached eddy simulation (DES). DNS is the most reliable approach, but its computational costs are super high and are, thus, not further discussed in this paper. The other turbulence modeling approaches are discussed in the present section.

2.4.1. RANS Modeling

For RANS models, the standard k−ε turbulence model (Versteeg and Malalasekera, 2007) is considered to be relatively simpler. A very good performance can be achieved from the k-ε model in many cases as the model is well established. The model has also been extensively validated. However, it is considered more expensive than some other turbulence models, such as the mixing length model. The performance of the k-ε model may not be satisfactory in some cases, such as unconfined flows, flows with large extra strains, rotating flows, and flows driven by the anisotropy of normal Reynolds stresses. The realizable k-ε model has been found to be more precise than some other models (e.g., the standard k-ε model) in predicting flows such as discrete flows and flows with complicated secondary flow features (Gildeh, 2013). The blending function drives the standard k−ω model in close wall regions and drives the k-ε family models in areas further from the surface. These differences make the SST model more accurate for a greater variety of flows than the standard k-ω model (Menter, 1994).

2.4.2. RSM Modeling

RSM models may be considered as a subcategory of RANS models while they are computationally more expensive. According to Davidson (2011), the advantages of RSMs could be summarized as follows: (1) the ability of RSM to respond effectively to any sudden change in the main strain; (2) modelling is not necessarily required for the production terms, which are used to explain many phenomena; and (3) the transport equations, which contain the main physical mechanisms that derive the evolution of turbulence such as production, redistribution, turbulent transport, viscous diffusion, and dissipation, are solved without assuming any behavior for Reynolds stresses. However, implementing the RSMs is considered to be a challenging task due to their complexity and CPU (central processing unit) time consumption. Additionally, the numerical analyses of RSMs

are very sensitive to influencing factors because of the small stabilizing of the second order derivatives of the momentum equations.

2.4.3. LES Modeling

Compared with the two-equation turbulence models (e.g., k-ε, k-ω), LES is typically more expensive in terms of computational costs. However, when comparing the computational cost with the accuracy of LES models, its efficiency, and other features with regard to computational time, can also be reasonable and worthy. This type of turbulence model can be more universally used since it overcomes the issues associated with using small eddies, such as tending to be more isotropic and less dependent on geometry. However, it is more computationally expensive since it needs finer grid densities for LES models than most RANS models. Although the large CPU costs for high-Re flows can be reduced by using a coarse near-wall mesh coupled with wall functions, the discretization schemes should be carefully designed to obtain more accurate results (Cable, 2009).

2.4.4. DES Modeling

The DES model is a cross between the LES and RANS approaches. It is quite beneficial to combine the RANS modeling approach with the LES approach if the usage of LES models is computationally unaffordable. Typically, the DES method is much less expensive than the LES approach but more expensive than the RANS. In regions where large turbulence scales play a dominant role, the LES model based on the sub-grid model by the DES model is used. In areas where viscous impacts predominate, such as near-wall areas, the RANS model is used (Shur et al., 1999).

2.5. Research on River Bends Flows and Key Findings

The previous sections have introduced the fundamentals of secondary flow, governing equations, and boundary conditions. Previous researchers have conducted numerical studies on river bend flows based on these fundamentals and configurations. This section reviews and discusses some of these studies and their key findings. The reviewed papers were mainly selected based on their research focuses, and they are classified into four categories: secondary flow in the curved channel; secondary flow and pollutant dispersion; secondary flow and sediment transport; and secondary flow in bend over topography.

2.5.1. Secondary Flow in a Curved Channel

In this section, some previous numerical research studies on secondary flow in channel bends were discussed, taking into account different bend geometries, and different models of turbulence. Then, each numerical model was examined and evaluated. Table 2.1 summarizes these numerical research studies and their key findings.

Table 2.1: Summary of selected studies about secondary flow in curved channels used in Section 2.5.1.

Shape of Channel	Numerical Model	Key Findings	Reference
S-shape with two identical 90° reverse bends	Standard k-ε low-Reynolds number k-ω	k-ω model is better than the k-ε model in simulating the transverse velocities, which form the secondary flow phenomenon.	(Khosronejad et al., 2007)
U-shaped mildly curved channel having a U-shape	Depth-averaged 2D numerical model	Generally, there was an agreement between the simulated and measured surface elevations at the inner, outer bank, and centerline.	(Duan, 2004)
U-shaped sharply curved channel in 180° bend	Depth-averaged 2D numerical model	There is good agreement between the simulated and measured results.	(Duan, 2004)
A channel in 90° bend	low-Reynolds number k-ω, k-ε (realizable), k-ε (RNG) and LES models	The performance of k-ε (RNG), k-ω and k-ε (realizable) models was good in simulating the flow in the bend, while the LES model has not shown its capability in simulating the flow in channel bends, especially after the curve.	(Ghaneeizad et al., 2010)
A channel in 90° bend	k-ε (RNG)	The results of the comparison between the numerical model and the experimental data indicated that there is an acceptable level of agreement.	(Gholami et al., 2014)
The flume of two successive 180° bends	RANS including (standard k-ε, standard k-ω) and LES	Both RANS simulation and LES model performed well in predicting the primary and an outer bank secondary cell at the peak of the bend.	(Stoesser et al., 2010)
The flume of two successive 180° bends	Standard k-ε model, and the non-linear k-ε model	The two models showed the counter-clockwise secondary cell inherited from the first bend, while only the non-linear k-ε model showed the counter-rotating secondary cell of the previous bend, which is coincident with the higher primary velocities.	(Fraga et al., 2012)
U-shaped sharply curved channel in 180° bend	Standard k–ε model and the realizable k–ε model	The standard k–ε model performed better than the realizable k-ε model.	(Shaheed et al., 2018)

Shape of Channel	Numerical Model	Key Findings	Reference
A channel in 135° bend with side slopes	Standard k-ε, (RNG) k-ε, realizable k-ε, k-ω, and (SST) k-ω)	The realizable k-ε model was the best in capturing the outer bank cells among the tested models.	(Yan et al., 2020)
A mild 180°bend with a rectangular section and rotating annular flumes	LES and RANS (k-ε model)	The outer bank cell was reproduced well by the LES computations, unlike the RANS computations.	(Booij, 2003a)

The standard k-ε model and the low-Reynolds number k-ω model were used by Khosronejad et al. (2007) to simulate the flow in a channel bend. To validate the hydrodynamic model results, the experimental data of Ghanmi (1999) were used. In this experiment, an S-shaped flume with two identical 90◦ reverse bends connected by a straight channel segment was used. The geometric parameters of the flume include the length of the straight channel segment (3.5 m), the rectangular channel cross-section (0.5 m wide and 0.4 m depth), and the inner radius of each channel bend (R0 = 1.25 m). The characteristics and flow conditions considered in the experiment were as follows: the channel boundary was made with aluminum covered with a sand layer with a median diameter, d_{50}, of 2 mm, the discharge was 0.023 m3/s, the flow depth was h = 0.15 m, the mean inflow velocity was U = 0.3 m/s, and 2D velocities (longitudinal and transverse) were measured with a laser Doppler anemometer at 20 flume sections. The boundary conditions applied in this analysis included: inlet, outlet, free surface, and wall. At each section, three verticals were measured with five points for each vertical as shown in Figure 2.5. The results showed that the supreme velocity at the bend happens near the inner bank and moves toward the opposite bank as the outlet of the bend is approached. The streamwise velocity component differs from zero at or close to the bed to a maximum value when approaching the water surface. This situation is expected because it represents frictional effects. Based on the previous point, it can be intuitively concluded that the centrifugal force is greatest near the water surface and decreases with depth. The flow vectors near the bed are directed towards the inner bank and at the free surface towards the outer bank. The analysis showed that the mean absolute errors of the k-ω model (10.4%) are lower than the k-ε model (12.6%) in simulating the transverse velocities. Although the difference is relatively low, it could be concluded that the k-ω model is better than the k-ε model in simulating the transverse velocities which form the secondary flow phenomenon (Falcon, 1984).

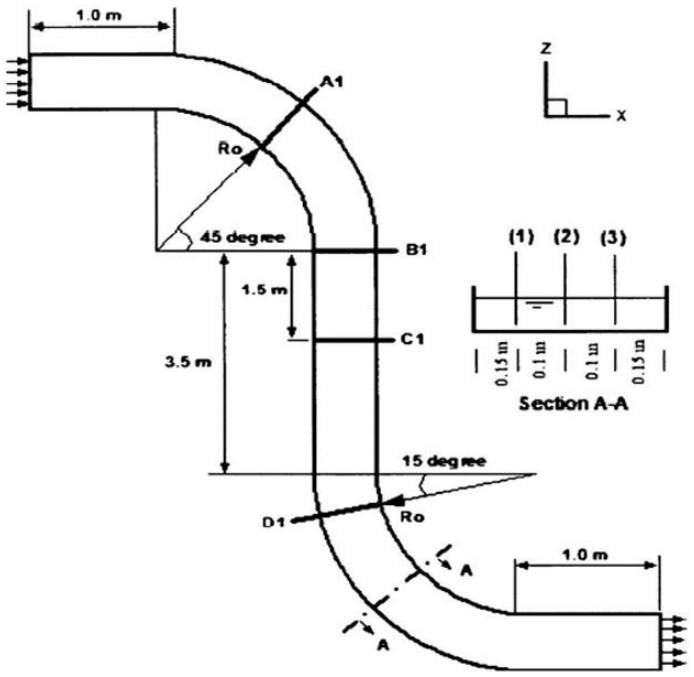

Figure 2.5: S-shaped channel used in Ghanmi's (1999) study from top view and characteristics of sections, which are used to compare calculated and measured data (Reproduced from Khosronejad et al. (2007) with permission from ASCE)

The experiment of De Vriend (1979) was used by Duan (2004) to simulate the flow in a mildly curved channel. The channel comprised a 1.7-m-wide flume having a U-shaped ground plan, with vertical sidewalls and horizontal bottom. The radius of curvature of the flume axis in the bend was 4.25 m, and the length of both straight upstream and downstream was about 6.0 m. The ratio of radius of curvature to channel width was 3.5. The discharge at the inlet was 0.0671 m3/s, the averaged velocity was 0.202 m/s, and the averaged flow depth was 0.1953 m. The boundary condition of the upstream was the inflow unit discharge, and for the downstream was the measured flow depth. By including the dispersion terms, a depth-averaged 2D numerical model was used to simulate the flow in this curved flume, taking into account that various sets of longitudinal and secondary flow profiles for governing equations in Cartesian coordinates were used to derive the dispersion terms. The simulated velocity vector field using a 2D numerical model and surface elevation in shaded color are shown in Figure 2.6. As can be observed in this figure, the higher velocity is directed towards the inner bank of the bend, while the lower velocity is directed towards the outer bank of the bend. The main reason behind the increase in velocity at the inner bank is the transverse convection of momentum induced by the secondary flow. However, the effect of the

secondary flow in the mild bend is very weak because the radius of channel curvature is much larger than the width of the channel. Furthermore, in the bend, the surface water level increases at the outer bank and decreases at the inner bank. The centrifugal force is the main reason behind the increased flow at the outer bank. Generally, there was an agreement between the simulated and measured surface elevations at the inner, outer bank, and the centerline (Duan, 2004).

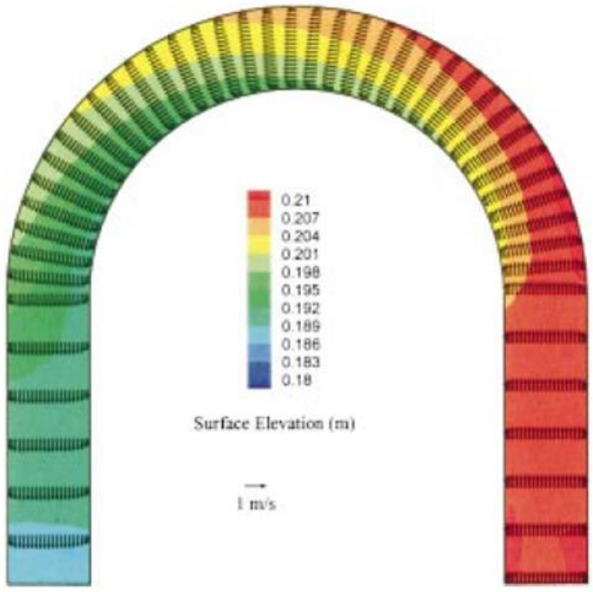

Figure 2.6: Surface elevation and velocity vector field (Reproduced from Duan (2004) with permission from ASCE)

The experiment of Rozovskii (1961) was used by Duan (2004) to apply the depth-averaged 2D numerical model by including the dispersion terms 2D numerical model in a sharply curved open channel. It consisted of a 180° curved reach with a 6-m-long straight approach and a 3-m-long straight exit. The ratio of mean radius of curvature to width was 1.0. The width of the channel was 1.7 m. The cross-section of the channel was rectangular. Water depth at the downstream end was 0.053 m, and the discharge was 0.0123 m3/s. The surface elevation and velocity distribution are shown in Figure 2.7 below. There is an acceleration in the longitudinal flow close to the outer bank of the upstream part of the bend and a deceleration in the flow velocity near the outer bank. The surface elevation increased at the outer bank and decreased at the inner bank. There was good agreement between the simulated and measured results. The impact of secondary flow was observed on the depth-averaged flow distribution and water surface elevations, which became more visible

with the increasing of the channel curvature. Due to the transverse bed slope in natural rivers, the velocity of secondary flow near the bed is higher. There is a significant role of the secondary flow in transporting bedload and suspended load in the transverse direction (Duan et al., 2001). Obviously, a 3D model is more accurate than that of a depth-averaged model. However, the depth-averaged two-dimensional model with the dispersion terms according to this study was capable of simulating the hydrodynamic flow in meandering channels. As the secondary flow could not be taken into account in the depth-averaged turbulence model, the Schmidt number that correlates mass dispersion with turbulent diffusion can be adjusted as a calibration parameter. Finally, the accuracy of the 2D approach is still limited according to the results, and more measurements for calibration and verification are needed to obtain more accurate results.

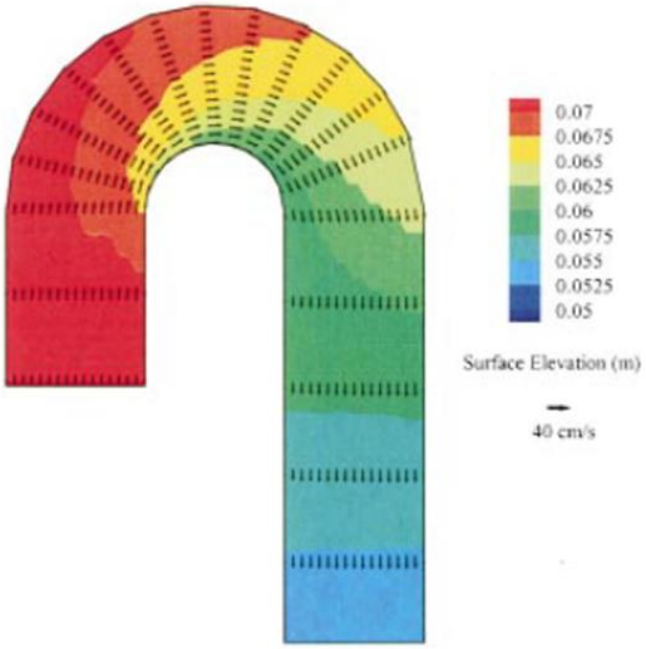

Figure 2.7: Surface elevation and velocity distribution (Reproduced from Duan (2004) with permission from ASCE)

The channel of a 90 bend was used by Ghaneeizad et al. (2010) to study the flow in a curved channel. The width of this channel was 0.4 m, the discharge was 13.55 lit/s, and the depth was 9 cm. The flow is subcritical, and the velocity on subcritical flows is at a high range. The boundary conditions were as follows: pressure-inlet, pressure-outlet, symmetry, and wall for the inlet, outlet, upper surface, and channel wall, respectively. Some turbulence models are used to simulate the flow in this channel including k-ω, k-ε (realizable), k-ε (RNG), and LES. Then, the simulated results

are compared with the measured ones, and the ability of each model is examined with respect to flow analysis. Accordingly, the k-ε (RNG) model showed good performance in simulating the flow in the bend, and k-ω and k-ε (realizable) did not noticeably differ from the k-ε (RNG) model. However, LES has not shown its capability in simulating the flow in channel bends, especially after the curve (Ghaneeizad et al., 2010).

The same channel of a 90° bend used by Ghaneeizad et al. (2010) was also used by Gholami et al. (2014) to study the flow patterns in a strongly curved open channel bend via the k-ε (RNG) model to predict the turbulence, and the volume of fluid (VOF) method to simulate the water's free surface. The channel is shown in Figure 2.8 below. The inlet-water boundary was set as a velocity inlet. The free surface boundary was set as the pressure-inlet condition on which atmospheric pressure was assumed. The boundary at the downstream outlet was defined as a pressure-outlet condition, and wall functions were used to estimate the effect of walls. The water surface is uniform before and after the bend, while along the bend and because of the centrifugal force, a transversal slope occurs on the water's surface. The higher velocity appeared near the inner bank along the bend while the lower velocity appeared near the outer bank. This pattern was reversed after the bend. The results of the comparison between the numerical model and the experimental data indicated that there is an acceptable level of agreement. Major secondary flows and minor ones (near the water surface and in the outer wall) with two opposite rotation directions are formed in the numerical model. The flow pattern is impacted by these two secondary flows, which stay after the bend of the channel for some distance. As the flow in the bend is affected by secondary flows, the velocity increases accordingly in the area close to the bed, more than that near the water surface. Additionally, the higher velocity depth gradations cause an increase in the shear stress.

The flume data by Siebert (1982) were used by Stoesser et al. (2010) to simulate the flow in meandering open channels by using steady Reynolds-Averaged Navier–Stokes equations (RANS) using an isotropic turbulence closure, and Large Eddy Simulation (LES). The Reynolds stress term was modeled by the standard k-ε turbulence model or by the standard k-ω turbulence model, respectively. The flume consisted of two successive 180 bends joined by a 0.5 m-long straight cross-over section. There was a 4 m-long straight inlet before the first bend and a 2 m-long outlet. The channel's section was a rectangle of 0.25 m in width. For the boundary conditions, the mass-flux was kept constant to obtain a pressure gradient between the upstream and downstream sections of the domain. For the bed and side walls, a smooth boundary with the no-slip condition was used,

and for the water's surface, a fixed rigid lid with zero gradients for all variables was used. The results showed that the higher momentum moves from the inner bank of the channel at the entrance of the bend towards the outer bank near the bend exit. Both the LES and the RANS calculations agreed well with the measurements and there is no significant difference between them. The higher velocity appears near the inner bank of the channel at the beginning of the bend, and then it moves towards the outer bank due to the centripetal forces acting in the previous bend. The maximum velocity is predicted well by the LES under the free surface. Additionally, the moving of higher velocity towards the inner bank of the channel at the beginning of the bend is predicted well by both RANS simulations. However, the suppression of the maximum streamwise velocity below the water surface is absent. Both RANS simulation and the LES model agreed well with the experiment in predicting the primary cell and an outer bank secondary cell at the peak of the bend. However, the RANS code failed to predict the persistence of the outer bank cell until the exit of the bend. The results also showed a good agreement between RANS and LES in the comparison of the computed bed and side-wall shear stresses.

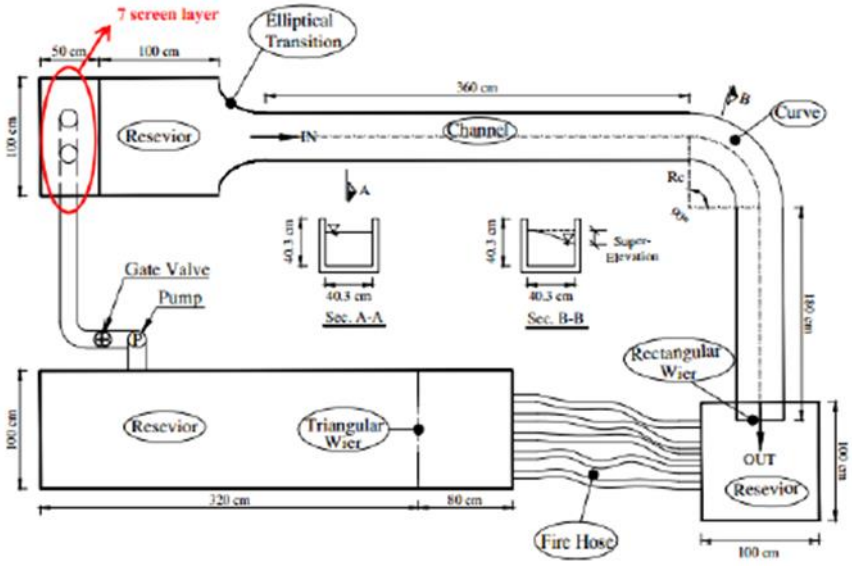

Figure 2.8: Characteristics of geometrical setup (Gholami et al., 2014)

The same flume data by Siebert (1982) were also used by Fraga et al. (2012) to simulate the flow in open channel bends. Two types of models were used in this simulation to solve the unsteady Reynolds-Averaged Navier–Stokes equations (RANS). The first one was an isotropic turbulence closure (standard k-ε model), and the second one was a nonlinear k-ε model which takes into

account anisotropic effects. The boundary conditions were considered as: open boundaries, wall and free surface. The results were compared with the LES data from Stoesser et al. (2010) who used the same flume to simulate the flow by using the steady Reynolds-Averaged Navier–Stokes equations (RANS) with an isotropic turbulence closure, and Large Eddy Simulation (LES). Both models were similar to the LES model, which showed the shift of high-energy momentum from the inner bank to the outer bank. The flow moved under the effect of centripetal forces towards the outer wall and momentum was concentrated there at the first bend. As the flow reaches the second bend, the higher momentum is still under the impact of centripetal forces and moving towards the inner bank, which represents the outer bank of the first bend. Then, along the second bend, the higher momentum moves towards the outer bank of channel due to the centripetal forces. The streamwise velocity is affected by the secondary flow as well. The highest streamwise velocity is located at some depth under the free surface instead of on the surface itself. The higher primary velocity is located at some depth under the free surfaces of outer bank because of the centripetal forces. All three models are in agreement regarding the typical features of meandering channels. Additionally, all three models showed that the counter-clockwise secondary cell was inherited from the first bend, while only the non-linear k-ε and LES models showed the counter-rotating secondary cell of the previous bend, which is coincident with the higher primary velocities. However, the non-linear k-ε model's main secondary cell shape clearly differentiates it from the LES model.

The channel of Rozovskii (1961) was used by Shaheed et al. (2018) to simulate the flow in a closed curved channel. It consisted of a straight approach channel with a length of 6 m followed by a 180 bend with a mean radius of 0.8 m and an outlet section of 3 m. The channel cross-section was a 0.8 m wide rectangle as shown in Figure 2.9 below. Four boundary conditions were applied in this case that include: the inlet and the outlet of the channel, the walls (including side walls and bottom), and the surface of the channel (symmetry). The simulation was performed using the OpenFOAM model and pisoFoam solver, mostly used for incompressible and turbulent flows in closed channel cases (also referred to as the Rigid-lid Model, or RLM).

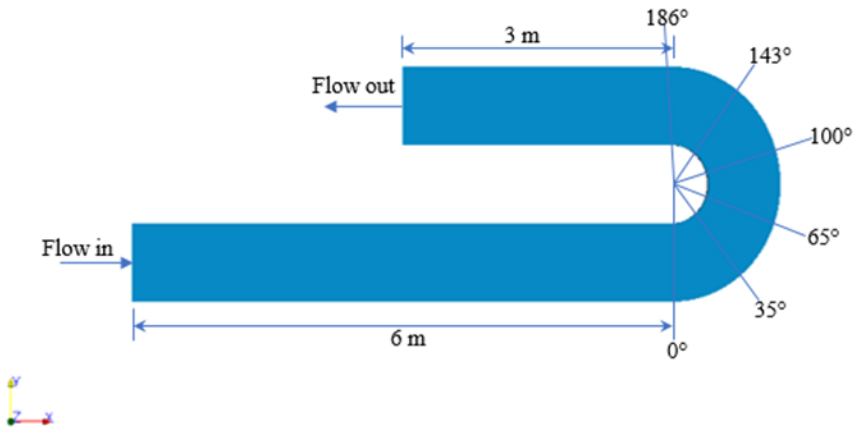

Figure 2.9: Model setup for the closed curved channel (Shaheed et al., 2018)

Two turbulence models were used to perform the simulation of flow in closed river bends: the standard k–ε model and the realizable k–ε model. The distribution of the velocity is shown in the Figure 2.10 below. The velocity increases near the inner bank at the beginning of the bend, and then moves towards the outer bank at the end of the bend.

Figure 2.10: Velocity distribution for closed curved channel (Shaheed et al., 2018)

In order to examine the flow velocity, cross-sections were taken in the bend as shown in Figure 2.11. The comparison between the experimental data and the two models is shown in the figure, where: U is the depth-averaged velocity magnitude; and u_1, u_2, and u_3 are the longitudinal, vertical, and lateral velocity averaged over the depth, respectively. Note that the depth-averaged velocity is represented by the vertical axis and is non-dimensionalized by U_1, which is the downstream mean velocity. The horizontal axis represents the radial distance $(r - r_i)/B$, non-dimensionalized by the channel width, where B is the channel width and r and r_i are the radius of curvature for the

outer and inner banks, respectively. Both models performed well in the flow simulation of the bend. In addition, the comparison in the figure showed that the two models performed well compared to other numerical models that were used by other researchers. However, near the bend exit, there is a slight variation in the two models, particularly at the inner bank, due to the change from a curved to a straight channel, which makes the flow features in this region complex and not easy to capture, showing the weaknesses of the two models in this area (Shaheed et al., 2018).

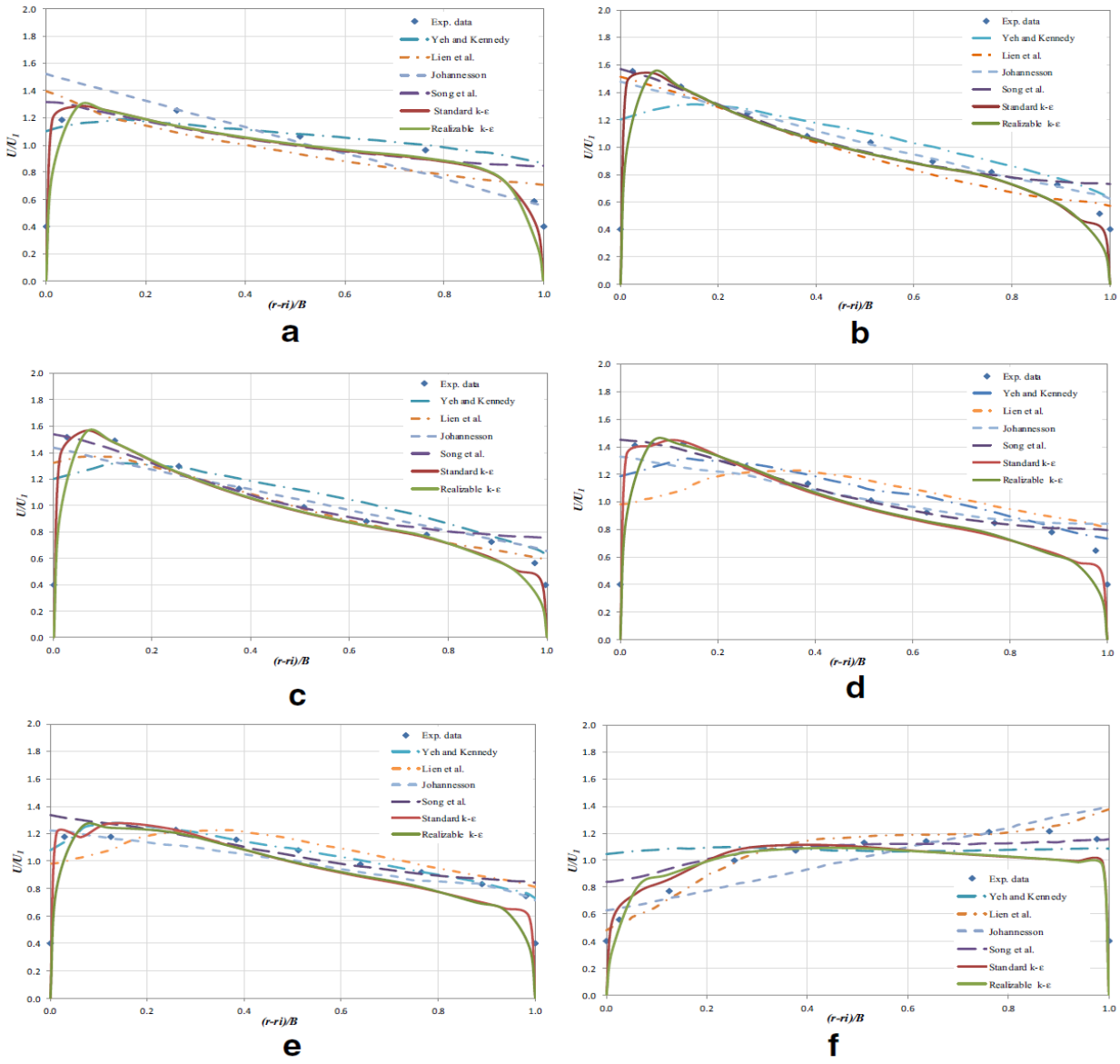

Figure 2.11: A comparison of resultant velocities across dimensionless channel width for the Rozovskii channel. (**a**) at θ = 0°; (**b**) at θ = 35°; (**c**) at θ = 65°; (**d**) at θ = 100°; (**e**) at θ = 143°; and (**f**) at θ = 186° (Shaheed et al., 2018)

Different kinds of RANS turbulence models including standard k-ε, Re-Normalization Group (RNG) k-ε, realizable k-ε, k-ω, and shear stress transport (SST) k-ω were used by Yan et al. (2020) to simulate the flow in a high-curvature 135◦ channel bend with an assessment of side slopes and its effects on the secondary flows. The channel was rectangular, and it included a straight inlet section of 12.19 m followed by a 135◦ bend and then a straight exit section of 2.44 m. The width was 1 m, and the height was 0.9 m with vertical acrylic walls. The performances of different turbulence models were compared against experimental measurements, and the best performing model was used to perform additional computations to assess the impact of different side slopes on the flow distribution. In addition to the velocity profiles, the models were also compared with more details in terms of the streamlines of secondary flow at the section 60◦ from the bend. Two circulation cells appeared in the observations the main, bigger one that was rotating clockwise, and the smaller one that was rotating counterclockwise, which was also called the outer bank cell. The realizable k-ε model was found to be the best among the tested models, especially in capturing some small flow features, such as the outer bank cells. There are other numerical simulation models in river bends that have been used in previous research studies. The effect of secondary flow on depth-averaged equations using a stress diffusion matrix was studied by Lien et al. (1999). They used a 180◦ bend with a rigid bed to examine the flow pattern using a two-dimensional numerical model. Accordingly, the effect of secondary flow on the maximum velocity path along the channel was indicated.

LES and RANS (k-ε model) were used by Booij (2003a) to simulate the flow pattern in a mild 180 bend with a rectangular section and rotating annular flumes. He concluded that the main characteristics of secondary flow and main flow could be produced by RANS computations. However, there were no satisfactory reproductions of the complicated secondary flow fields that could be given by RANS for the flow in rotating annular flumes and river bends. The secondary and main flow were reproduced well by LES for the mildly curved river. The turbulence was reproduced reasonably by LES and there was a low level of deviations in the computed secondary flow pattern of the rotating annular flume from the measured flow pattern. Additionally, the outer bank cell was reproduced well by the LES computations, unlike the RANS computations. LES computations had a small sensitivity towards the exact choice of modeling parameters.

Three types of turbulence models, including standard k-ε, k-ω and RSM, were used to model the flow pattern in a 180° bend by Safarzadeh Gandoshmin and Salehi Neishbouri (2005). They found

that the flow pattern could be predicted reasonably by all three models within the direct channel. However, during the curve, the prediction of RSM was superior. In addition, the k-ω model could predict the rotation and the separation effect of flow more precisely than the standard k-ε model.

The currents and mass transport in curved channels were simulated via a 3D hydrodynamic model of free surface turbulent flows by Jian and McCorquadale (1998). They modified the standard k-ε model and applied it to two typical curved open channel flows: a 270° channel bend with a sloped outer bank and a meandering channel with mass transport. Then, they compared the model results with available data and obtained generally good agreement. According to their simulation, the secondary flows of the single bend were much stronger than that of the meanders. The reason might be related to the opposite spiral movement generated by the alternate bends of the meandering channels. Additionally, there could be a large lateral mass transport in the curved channel because of the secondary flows.

A 3D numerical model was applied by Lu et al. (2004) to simulate the flow pattern in a channel with a 180° bend using the standard k-ε turbulence model. The results of the comparison between the numerical model and experimental data showed acceptable agreement. However, the model was not able to predict the minor secondary rotational cell in the outer wall.

A numerical simulation of turbulent free-surface flow was presented by Bodnar and Prihoda (2006) using the k-ω turbulence model to analyze the non-linearity of the water surface slope at sharp river bends. The predictions of the model for the turbulent quantities and free-surface position were qualitatively correct.

The flow pattern in two types of bends, including a sharp one with a 180° bend and a mild one with a 270° bend, was simulated using a two-dimensional depth-averaged model by Zhou et al. (2009). The simulation was performed with and without the consideration of secondary flow. The results showed a better agreement in the first state of the effect of the secondary flow.

The Detached Eddy Simulation (DES) model was used by Constantinescu et al. (2010) to simulate the flow in a strongly curved channel with a 193° bend. They concluded that the prediction of the secondary flow and velocity components distribution by the model was satisfactory.

A sharply curved open channel bend (width of channel =1.3 m, the radius of curvature =1.7 m) with a flat horizontal bed was used by Blanckaert in 2009 to measure the secondary flow using an acoustic Doppler vertical profiler (ADVP). The main target of this study was to examine the impact of relative curvature (the ratio of the flow depth (H) to the radius of curvature (R)) on secondary

flow. Blanckaert's results indicated that there was a strong increase in the turbulent kinetic energy in the curve.

Van Balen et al. used the RANS and LES models in 2010 to carry out numerical simulations of the sharp curve studied by Blanckaert in 2009. They found that the main secondary flow was underestimated by the RANS model, while the friction loss was overestimated by the same model. According to van Balen et al. (2009), the outer bank cell was not shown by the RANS model, while it was shown by the LES model. As a result, they concluded that secondary flow in curved channels was the result of both centrifugal effects and turbulence anisotropy.

A rectangular channel with two linked curves (channel width = 0.25 m, the radius of curvature = 1.0 m) was used by Stoesser et al. (2010) to compare LES and RANS models with experimental results. They concluded that the generation of an outer bank cell could be predicted by the RANS model, which contrasts with observations by van Balen et al. (2009; 2010). The flow in a 60◦ compound meandering channel with seminatural cross-sections was studied by Jing et al. (2009) experimentally and numerically. The 3D numerical turbulence model that was applied to simulate the flow was the Reynolds stress model (RSM). The water depth impacts on wall shear stresses and secondary flow were studied as well. The calculations of velocity fields, wall shear stresses, and Reynolds stresses were performed for a range of input conditions. The comparison results between the measurements and simulated velocity fields and Reynolds shear stresses were in a reasonably good agreement. This indicated that the complex flow could be successfully predicted by RSM. Additionally, the Reynolds stress model (RSM) was used by Jing et al. (2011) to investigate the structure of turbulent flow in meandering compound open channels with trapezoidal cross-sections. The water depth impacts on secondary flows were studied as well. The results of the simulated and measured data showed that there was a considerable difference between the secondary flows of the overbank flow and that of inbank flow. Additionally, the simulation indicated that the magnitude and direction of the secondary flows were affected significantly by the water depth. The comparison results between the numerical simulation and the experimental data for the calculated velocity fields and Reynolds shear stresses were in good agreement, indicating the capability of this model on simulating the complex turbulent flow in meandering compound open channels.

2.5.2. Secondary Flow and Pollutant Dispersion

One of the effects of secondary flow in river bends is pollutant dispersion. As the inflow enters the curve of the river, there is a redistribution of flow momentum that occurs because of the secondary flow. As a result, there is considerable lateral mixing of pollutants. Thus, the pollutant spreading in curved rivers is much stronger than that in a straight river. Additionally, the distribution of contaminants discharged at the centerline of the river along the cross-section is nonsymmetric in curved rivers. According to Holley and Abraham (1973), the pollutant dispersion at the inner bank is less than at the outer bank. Table 2.2 summarizes the relevant research used in this section and their key findings.

Table 2.2. Summary of studies about pollutant dispersion in curved channels used in Section 2.5.2

Shape of channel	Numerical model	Key findings	Reference
The flume consists of a single meander of two 90° bends in alternating directions	Depth-averaged 2D numerical model	There is an agreement between the simulated and measured results.	(Duan, 2004)
Three different meander situations were used including wide, shallow channels with a smooth bed, and two narrow channels with one having a smooth and the other a rough bed.	Standard k-ε turbulence model	The agreement was fairly good in the case of the smooth bed for the vertical profiles of longitudinal velocity, but it was not so good for the case of the rough bed.	(Demuren and Rodi, 1986)

The experiments of Chang (1971) were used by Duan (2004) to apply the 2D numerical model and evaluate its ability to simulate mass transport in meandering channels. The flume consisted of a single meander of two 90° bends in alternating directions connected by short tangents. The flume width was 2.34 m, the ratio of actual length to the straight length was 1.17, while the sinuosity in the natural meandering channel is usually more than 1.5 (Leopold and Wolman, 1957). The cross-section was rectangular with nominally smooth bed and sidewalls. The convection and diffusion equation were solved to obtain the concentration of transported mass:

$$\frac{\partial(\mathrm{h}\bar{\mathrm{C}})}{\partial \mathrm{t}} + \frac{\partial}{\partial \mathrm{x}}\left(\mathrm{h}\overline{\mathrm{uC}} - \frac{\nu_\mathrm{t}}{\sigma_\mathrm{c}}\frac{\partial \mathrm{h}\bar{\mathrm{C}}}{\partial \mathrm{x}}\right) + \frac{\partial}{\partial \mathrm{y}}\left(\mathrm{h}\overline{\mathrm{vC}} - \frac{\nu_\mathrm{t}}{\sigma_\mathrm{c}}\frac{\partial \mathrm{h}\bar{\mathrm{C}}}{\partial \mathrm{y}}\right) - (\mathrm{D_b} - \mathrm{E_b}) = 0 \qquad (2\text{-}12)$$

where C is the concentration, D_b and E_b = rates of mass deposition and entrainment, respectively; and σ_c = turbulent Schmidt number for mass diffusion, which represents the ratio of eddy viscosity to eddy diffusivity. In order to study the dispersion of a pollutant, a constant concentration of pollutant was introduced at the inner bank, the midpoint of an upstream cross-section, and the outer bank for three separate runs. The velocity vector field and the water surface elevation are shown in Figure 2.12 below for the dye injection at the midpoint of the channel. It can be observed that the higher velocity transfers from the left bank of the first bend towards the right bank of the second bend because of the secondary flow. At the inner bank, the simulated elevation of the water surface is much lower than that at the outer bank.

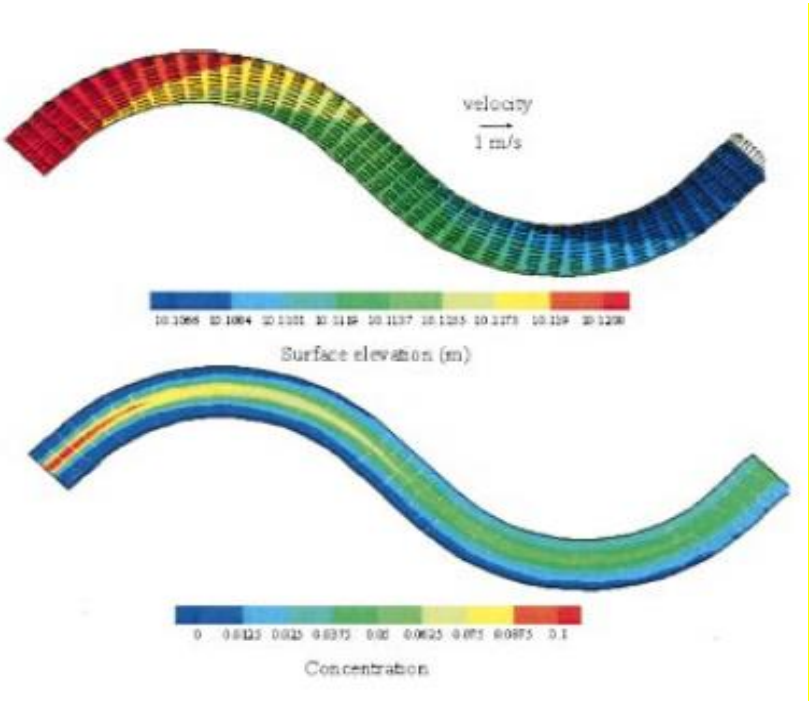

Figure 2.12: Flow and concentration field (Reproduced from Duan (2004) with permission from ASCE)

The comparison between the simulated depth-averaged velocity and concentration distribution and the measured experimental results at the second bend is shown in Figure 2.13. It is clear that there is good agreement between the simulated and measured results. This can give the impression that this model is able to simulate the depth-averaged flow field in meandering channels. However, as the simulation of secondary flow by the depth-averaged model is limited, calibration was performed for the Schmidt number to achieve the results in the simulations (Duan, 2004).

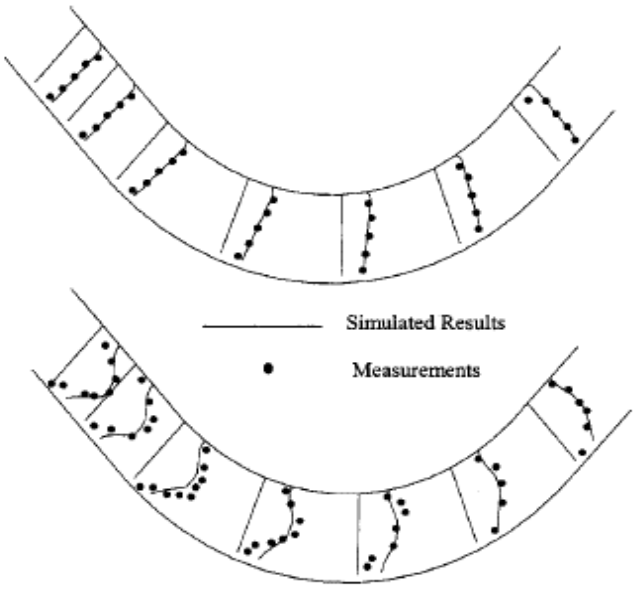

Figure 2.13: Comparison of simulated and measured depth-averaged velocity and concentration field (Reproduced from Duan (2004) with permission from ASCE)

The flow and pollutant dispersion in meandering channels were calculated mathematically and numerically by Demuren and Rodi (1986) taking into account the three-dimensionality of the flow and pollutant concentration fields. The new model was an extension of the Leschziner and Rodi (1979) three-dimensional numerical model. The standard k-ε turbulence model was used to improve the numerical accuracy. Three different meander situations were used to apply the new model. The three cases include a wide, shallow channel (width-to-depth ratio B/h = 20) with a smooth bed, and two fairly narrow channels (B/h = 5) with one having a smooth bed and the other a rough bed. The boundary conditions of the model were used as solid walls (bed and banks) and the surface is treated as a "rigid lid". There was a large secondary motion eddy that appeared in the wide-flume case. The results of the new model for longitudinal and secondary velocity field compared to the measurement were generally good. The pattern of the secondary flow in the smooth narrow flume was more complex with several developing and decaying eddies. The agreement was fairly good in the case of the smooth bed for the vertical profiles of longitudinal velocity, but it was not so good for the case of the rough bed. However, the prediction of the development of the depth-averaged longitudinal profile was fairly good for all cases. The prediction of secondary flow was realistic in all cases as well. Lastly, the bed shear stress, which is the main reason for bed erosion, appeared at the areas close to the depth-averaged velocity distribution. The rate of mixing in general as proceeding the downstream from one bend to another was reproduced well. Particularly, the model

predicted the mixing well, which was much faster in the central discharge case than the inner or the outer bank discharge cases, and this could be due to the diffusivity that is generally larger in the center of the channel compared to near the banks. The agreement between the predicted and measured pollutant concentration was generally very good.

2.5.3. Secondary Flow and Sediment Transport

Another effect of secondary flow in river bends is sediment transport. Table 2.3 summarizes the research studied in this section and their key findings.

Table 2.3: Summary of studies about sediment transport in curved channels used in Section 2.5.3

Shape of channel	Numerical model	Key findings	Reference
A channel in 90° bend	Standard k-ε model and the low-Reynolds number k-ω model	The low-Reynolds k-ω turbulence model is better than the standard k-ε model	(Khosronejad et al., 2007)
A channel in 135° bend	Standard k-ε model and the low-Reynolds number k-ω model	The low-Reynolds k-ω turbulence model is better than the standard k-ε model	(Khosronejad et al., 2007)
A channel in 180° bend	k-ε turbulence model	There is good agreement between the measurements and the predicted results	(Wu et al., 2000)

Khosronejad et al. (2007) used the channels of Matsuura (2004) to apply the standard k-ε model and the low-Reynolds number k-ω model in the simulations of two different river bends as follows: The first channel of Matsuura (2004) consisted of a rectangular open channel with a 90° bend. The length of the channel was 20 m, the bed slope was 0.001, the width was 46 cm, the depth was 25.4 cm, and the radius of the bend was 672 mm. The bend entrance velocity was 0.285 m/s, and the uniform flow depth was 10.2 cm. Matsuura's channel is shown in Figure 2.14 below:

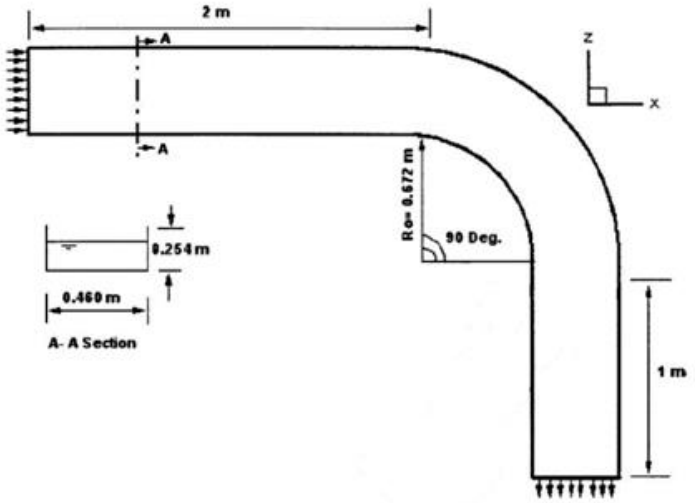

Figure 2.14: Geometric parameters and characteristics of 90° bend channel used in Matsuura 2004 study (Reproduced from Khosronejad et al. (2007) with permission from ASCE)

A significant helical flow was noticed in this area as well. This helical flow caused transverse sediment transport directed towards the inner bank of the bend. It is reported that the transverse sediment transport is the main cause of the degradation occurring near the outer banks and aggradation occurring near the inner banks of alluvial channel bends (Dietrich and Whiting 1989). The comparison between the simulated and measured bed topography showed that the low-Reynolds k-ω model fits the bed changes data better than the standard k-ε model. The mean error was also calculated. The results show that the mean absolute difference (M.A.D.) of the predicted from the observed bed levels was significant at 0.05 level of risk ($\alpha < 0.05$) for the k-ω model (6.6 mm) and the k-ε model (8.2 mm). Additionally, the M.A.D. of the maximum observed scour depth of the k-ω and k-ε models was 11 and 13% and the standard deviations of absolute differences were 4.6 and 5.3 mm, respectively. Furthermore, standard deviations of absolute differences (S.D.A.D.) were 4.6 and 5.3 mm, and the coefficient of determination (r^2) for k-ω model (0.87) was relatively higher than the k-ε model (0.84). All these statistical measurements give an indication that the low-Reynolds k-ω turbulence model is better than the standard k-ε model. Based on this, it could be concluded that the k-ω model can predict the bed-shear stress and friction factor better than the k-ε model. The bank erosion was not considered because the walls were rigid in both physical and numerical models.

The second channel of Matsuura (2004) consisted of a rectangular open channel with a 135° bend. The inflow velocity was set at 0.283 m/s and the flow depth was 10.2 cm. The maximum scour depth observed (12.7 cm), which is higher than the 90° case, was noticed along the outer bank at the bend exit (Figure 2.15). The observations showed strong secondary flow and caused transverse sediment transport and aggradation toward the inner bank of the bend. The 135° bend case was modeled considering the two turbulence models (standard k-ε and the low-Reynolds number k-ω) and the results of the simulation runs were compared to the corresponding observed results.

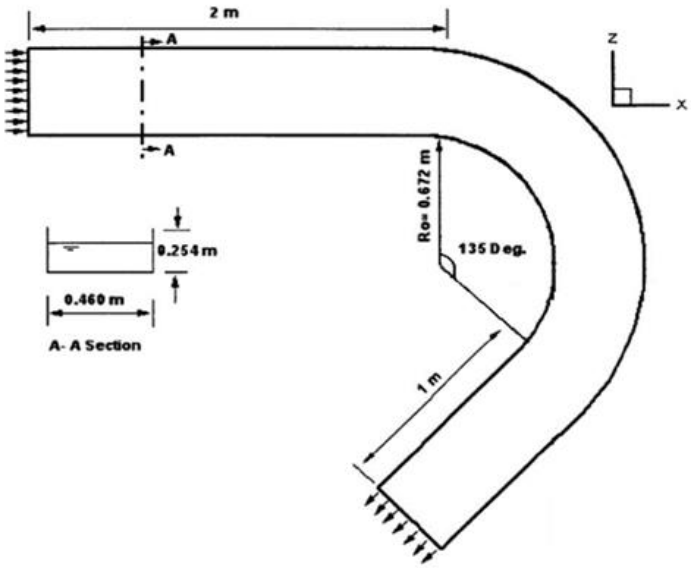

Figure 2.15: Geometric parameters and characteristics of 135° bend channel used in Matsuura 2004 study (Reproduced from Khosronejad et al. (2007) with permission from ASCE)

Similar to the 90° case, statistical analyses were conducted for comparison purposes. The mean absolute difference (M.A.D.) was found to be significant at a 0.05 level of significance ($\alpha < 0.05$) for the k-ω (11.2 mm) model and the k-ε model (13.3 mm). In addition, mean errors of the maximum scour depth for k-ω and k-ε models were 8.8 and 11%, respectively. The standard deviations of absolute differences (S.D.A.D.) and the coefficients of determination (r^2)) for k-ω and k-ε models were 7.4 and 8.7 mm, and 0.91 and 0.88, respectively. Based on the above and compared with the results obtained from the 90° bend case, it could be concluded that the maximum depth of scour for the 135° bend was slightly underpredicted with both of the turbulence models, and the position of the maximum scour depth was not predicted as well as for the 90° bend.

The flow and sediment transport are simulated by Wu et al. (2000) in open channels through the use of a 3D numerical model. The 3D model was based on the general-purpose FAST3D flow solver developed at the University of Karlsruhe. The full Reynolds-averaged Navier–Stokes equations with the k-ε turbulence model were solved to calculate the flow. In order to validate the 3D numerical model, it was applied in a 180° open channel bend that was studied experimentally by Odgaard and Bergs (1988). The channel was 80 m in length and 2.44 m in width and has a 180° bend with 20 m long straight sections before and after the bend. The cross-section of the channel was trapezoidal with vertical side walls. At the beginning of the experiment, the channel was filled with a 30 cm thick layer of sand with an initially flat surface. The median diameter of the sand was d_{50} = 0.3 mm, and the geometric standard deviation was 1.45. The water depth, cross-stream bed profiles, and the streamwise development of the water depth were calculated and compared with the measurements obtained from the experiment. The results showed that there is good agreement between the compared values that can be observed with regard to the bed features. The calculated streamwise depth-averaged velocity was compared with measured velocities in the channel bend. The results showed good agreement with experimental data, taking into consideration the appearance of maximum velocities near the outer bank and the minimum velocities near the inner bank. This mainly could be a consequence of the water depth, which is larger near the outer bank than near the inner bank. The secondary flow motion was predicted well by the model. This could be seen by the appearance of positive angles near the surface that indicate motion to the outer bank and negative angles near the bottom motion toward the inner bank in the profiles of streamwise velocity vector. The model predicted the transverse bed slope and its downstream development well in general. There was good agreement between the measurements and the predictions regarding the bed form and the transverse slope.

Dietrich and Whiting (1989) investigated boundary shear stress, sediment transport, and bed morphology in a segment of a river during high and low flow. The segment was a sand-bedded river meander. They mapped the velocity, boundary shear stress, water surface, bedload, bedform, and suspended load transport fields during the spring snowmelt season for 1976–1979. They found that secondary flow changed the distribution of bed shear stress, which, in turn, affected the sediment transport processes. For example, Dietrich and Whiting (1989) noticed that there was an outward shifting zone of maximum boundary shear stress through the bend due to the secondary flow, and the zone of high bedload transport clearly followed this zone. Jamieson et al. (2010) investigated

the spatial variability of three-dimensional Reynolds stresses in a developing channel bend. Experiments on the mean flow field and turbulence characteristics for flow in a mobile sand bed were conducted. In the experiments, the three components of instantaneous velocities at multiple cross-sections for different tests at different stages of clear water scour conditions were measured using Acoustic Doppler velocimeters. The experimental results showed that the secondary flow clearly altered the Reynolds stresses and, in turn, affects the sediment transport. For example, it was found that the near-bed maximum positive streamwise cross stream Reynolds stress coincides with the leading edge of the outer bank scour hole.

These studies demonstrated that the secondary flow could alter the boundary shear stresses and turbulence shear stresses, which, in turn, affects the sediment transport processes.

2.5.4. Secondary Flow in Bend over Topography

The research studied in this section focused on the secondary flow in bends over topography and they are summarized in Table 2.4.

Table 2.4: Summary of studies about bend over topography used in Section 2.5.4

Shape of Channel	Numerical Model	Key Findings	Reference
A channel in 193° bend	The k-ω Shear Stress Transport (SST) model, or the Spalart–Allmaras (SA) model in low-Reynolds number versions	It could be considered that the accuracy and predictive capacity of the model is satisfactory.	(Zeng et al., 2008)
A channel in 193° bend	LES model	There is a good qualitative agreement between the LES model and the experimental findings	(Van Balen, et al., 2010)

The laboratory flume data of Blanckaert (2003) were used by Zeng et al. (2008) to study the flow in sharp open channel bends. The flume consisted of a 9-m-long straight inflow channel reach followed by a 193° bend with a constant centerline radius of curvature R = 1.7 m and a 5-m-long straight outflow reach. The flume was 22.7 m in length and 1.3 m in width with vertical lateral walls. The bed was covered with quasi-uniform sand having diameters in the range of 1.6–2.2 mm with an average of about d_{50} = 2 mm. Two types of experiments were carried out: the first one with a flat bed and the second one with a mobile bed. The simulation of these two types of flumes was performed via the finite-differences RANS code to predict flow, sediment transport, and bathymetry

in open channel geometries with loose beds. Two turbulence models were used to provide the eddy viscosity: the k-ω Shear Stress Transport (SST) model and the Spalart–Allmaras (SA) model in low-Reynolds number versions. The main characteristics of the complex 3D flow field over a fixed bathymetry were accurately simulated by the RANS model, such as the interaction between the deformation of the streamwise velocities profiles and the strength of the cross-stream circulation cells, the production of turbulent kinetic energy, and others. The errors for the transverse velocity profiles were larger compared to the streamwise profiles. The RANS model also captured the main features of the flow field and the mobile bed. However, the deviations between model predictions and measurements increased. Accordingly, it could be considered that the accuracy and predictive capacity of the model was satisfactory. The major differences between the simulation and the measurement happen in the area close to the outer bank of the flume. The outer bank cell of the circulation measured in the flat bed experiment could not be predicted by the model in the simulation. In addition, a significant difference between the simulation and the measurement is observed for the turbulent kinetic energy in the equilibrium experiment. The turbulence models required in the simulation of both processes according to Blanckaert and De Vriend (2004) are the ones that resolve turbulence anisotropy and the kinetic energy transfer between mean flow and turbulence.

The laboratory flume data of Blanckaert (2010) were used by van Balen et al. (2010) to apply the LES model to the simulation of a curved open-channel flow over an erodible bed. The flume had a movable sand bed and vertical sidewalls. The movable bed exhibited both the small-scale dunes on the bed and the large-scale point bar-pool structure of the bed along the bend. In the numerical model, the inflow section and outflow section are shortened to a length of 3.8 m each to save computational costs (see Figure 2.16).

The boundary conditions are treated as follows: free surface as a horizontal, impermeable rigid lid, solid walls with the wall-function approach, and for the outflow boundary, a convective boundary condition is imposed. When the geometry of the channel changed from straight to curved, the flow pattern along the bend will vary according to the location.

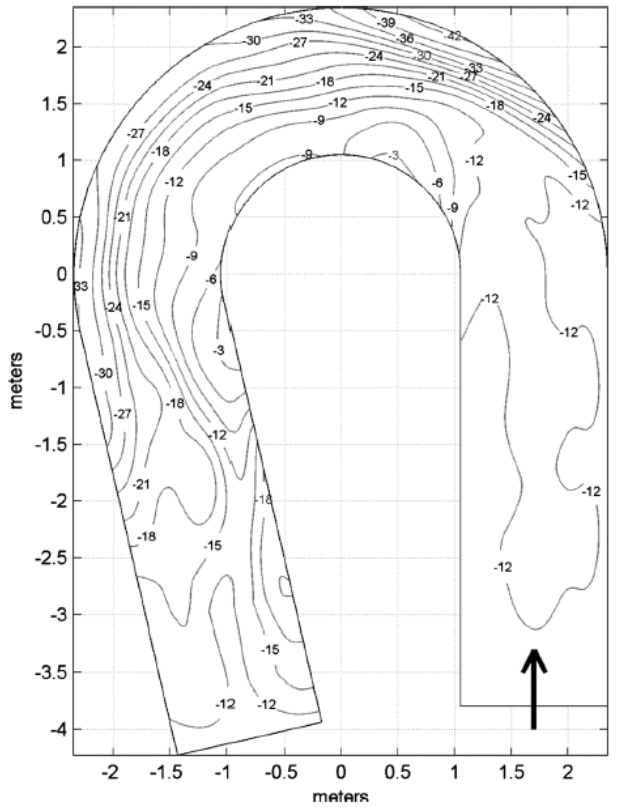

Figure 2.16: Bottom topography of the laboratory flume. The arrow denotes the flow direction (Reproduced from van Balen et al. (2010) with the permission of AIP Publishing).

In such a case, the distribution of the streamwise velocities at the entry of the bend is skewed toward the inner bank due to the presence of the sudden favorable longitudinal pressure gradient. The simulations were run for three separate LES computations, including a different roughness height of the bottom as shown in Table 2.5 below. The results showed that there are small differences between the three simulations regarding the primary flow structure. In addition, the flow structure of the three cases is fully determined by the large-scale bed topography. The flow decelerates in the upstream part of the bend, while the main flow accelerates approximately halfway in the bend and the return flow (backflow) exists near the inner bank. The flow in the downstream part of the bend recovers from the strong curvature-induced effects and the recirculation zone in the upstream part of the bend. Accordingly, there is a good qualitative agreement between the LES model and the experimental findings. However, the impact of the complex bed topography and sharp channel bend made the flow pattern very complex. The existence of the small-scale dune forms could be explained by quantitative differences. LES could not directly account for these small-scale dune forms because of the coarse measurements of the bed topography. There could be a spatial lag in

the streamwise development of the flow due to the existence of dunes on the bed. The differences were marginal between the LES model and the RANS model as carried out by Zeng et al. (2008) for the bigger part of the flow. This may be due to the turbulence-related momentum transport that does not play a role in the complete pattern of the momentum transport, and this is because of the combination of strong curvature and the presence of complex topography. Additionally, in the curvature, the turbulence stresses tend to be strongly isotropic.

Table 2.5: Hydraulic parameters of the three simulation runs. Q is the discharge, Vav the bulk velocity, H the mean water depth, B the width of the channel, Ks the roughness height of the bed, and Re the Reynolds number based on the bulk velocity and the mean water depth (van Balen et al., 2010)

Run	*Q (l/s)*	*Vav (m/s)*	*H (m)*	*B (m)*	*Ks (m)*	*Re*
A	89	0.49	0.141	1.3	0.037	68,000
B	89	0.49	0.141	1.3	0.006–0.037	68,000
C	89	0.49	0.141	1.3	0.006	68,000

2.6. Discussion

Numerical models are considered one of the important tools for predicting flow in a curved channel, allowing for various environmental studies, such as sediment transport and pollutant dispersion. Different kinds of models such as standard k-ε, k-ε (RNG), k-ω, k-ε (Realizable), non-linear k-ε, LES and others were used previously by researchers for simulating the flow in different kinds of curved channels in order to study the secondary flow and its effects on these channels. It is not easy to determine a model that is best for all types of curved channels because each model has to specifically be the best in some cases of the curved channel, while it could not be able to capture the flow features accurately in other cases. Additionally, the model could be able to capture some characteristics of curved channels accurately, while its performance could be less reasonable for other features such as secondary cells and outer cells. However, LES models have been generally reported to be more accurate than most of the other tested models.

In river bends, some variables should be taken into consideration such as the radius and skewness of curvature, the curve's length, and the asymmetry of the channel cross section. These variables might have a significant impact on the secondary flow, which, in turn, could affect the flow characteristics of one side, and other fluvial processes, of the river (mixing, transport of sediment, bank erosion, and meandering) as compared to the other side (Church et al., 2012).

Uniform channel sections have been adopted in some studies to isolate the impact of the channel bend on the dynamics of the flow, therefore decreasing the number of problem dimensions (Booij, 2003a; Blanckaert, 2009; van Balen et al., 2009; van Balen, et al., 2010). These studies shed light specifically on the formation of a second counterrotating secondary flow cell due to its significance in determining shear stress and the outside wall erosion on the curved channel.

The choice of turbulence model depends on the type of secondary circulation being sought by numerical simulations. Generally, two types of secondary flow circulation can be observed in curved channels (Nezu and Nakagawa, 1993). The first type occurs due to the generation of centrifugal forces and pressure gradients. Reproduction of this type of secondary circulation in the numerical models is usually more feasible using both RANS and LES methods. The second type of secondary circulation occurs at the outer bank of the curve. This type is usually weaker than the first one and circulates in the opposite direction (Almeida and Ota, 2020). This type is formed by the non-homogeneity and anisotropy of Reynolds stresses (Nezu and Nakagawa, 1993; Blanckaert and De Vriend, 2004). According to Demuren and Rodi (1984) and van Balen et al. (2009), this type is more difficult to reproduce correctly by isotropic turbulent models. Moreover, Booij and Tukker (1996) mentioned that there is no justification to use equal eddy viscosities for the different momentum transport terms in a curved channel.

Another important concept to be considered is the interaction of mean flow and turbulent fluctuations and energy transfer. The turbulence-induced near-bank circulation cells are usually hard to be represented by the linear turbulence closure models, despite the certain anisotropy of the cross-stream turbulence that they may well produce. On the one hand, the kinetic energy could be transferred from mean flow to turbulence and the mean flow vorticity is dissipated by the turbulent stresses. On the other hand, there is a transfer of the kinetic energy from turbulence to the mean flow as the experimental results indicated. However, comparing with the total production of turbulent kinetic energy, the amount of resituated kinetic energy is considered small. This could be mainly attributed to the boundary friction, which plays an important role in the outer bank cell dynamics. Therefore, in order to reproduce the outer bank cell accurately, turbulence closures that contain the ability to transfer kinetic energy between the turbulence and the average flow in either direction are required (Blanckaert and De Vriend, 2004). For example, some dynamic LES models can reproduce this two-way transfer. Indeed, LES models aim at capturing the scales that are large and contain energy in turbulent flow and modeling the interaction between the small and large

scales. Most commonly used models assume that the essential function of the unresolved scales is to remove energy from the large scales. Then, the energy is dissipated through the action of viscous forces. While the energy on average is transmitted from large scales to the small ones, the inverse transfer is also recognized from small to large scales which could be quite important, and the employed LES model should be able to represent this property in order to accurately simulate near-bank circulation cells (Iliescu and Fischer, 2004).

2.7. Future Research Needs

Although studying the secondary flow mechanisms in river bends and their relationship with other river processes has developed significantly, there are still some matters in this area that should be focused on and understood. Some aspects of secondary flow and the interrelation of flow characteristics and other fluvial processes of the river are discussed below:

The relation between the secondary current and turbulence is one of the important aspects that should be better understood, especially how they actually depend on each other. Despite the significant advances in studying flows in meandering channels, demonstrated by recent publications, knowledge on the effects of mean flow three-dimensionality and secondary currents on turbulence in more complex flows is less complete. There are different facets of turbulence that should be further studied, and they can be studied by using several conceptual frameworks, such as the Reynolds-averaging framework, the coherent structures concept, and the eddy cascade concept.

The influence of secondary flows on hydraulic resistance is another important matter that should be taken into consideration. Generally, the transverse distributions of mean velocities are modified by the secondary flows. The fluid shear stresses, and bed shear stress are modified as well. The bulk friction factor increases according to these modifications as often assumed, compared to the same situation when the secondary flows are absent. Sometimes, the bulk friction factor is not affected by secondary currents, while the boundary shear stress and near-bank velocities change significantly (Kean et al., 2009).

As it is known from previous studies, channel deformation, bank stability, and sediment transport are affected significantly by secondary flows, and the mechanisms and regular patterns require further investigation. In addition, suspended sediments are involved as a key factor of secondary current generation (Vanoni, 1946). The sediment transport affected by secondary flows in river bends and the bend curvature has important impacts on the sediment dynamics. The hydrodynamic features of rivers including secondary currents are highly influenced by river bends, and

accordingly, cause a higher erosion power and enhanced sediment transport rates leading to increased channel migration rates (Church et al., 2012).

Vertical, transverse, and longitudinal mixing are also highly affected by secondary flows (Rutherford, 1994), and the effects should be investigated further. The mixing rate may be enhanced by secondary flows or dampened in all directions or selectively according to the specific flow configuration. For the case of curved channels, the longitudinal dispersion increases in the bend, which, in turn, reflects an increase in the turbulence intensity. On the other hand, the dispersion decreases in the curvature by enhancing transverse mixing. Accordingly, there is a highly efficient longitudinal dispersion at the beginning of the bend, and then it reduces greatly after the bend apex (Boxall et al., 2003; Marion and Zaramella, 2006; Rowinski. et al., 2008).

Some other matters should be considered and focused on in future research studies with respect to flow in river bends. For example, the flow characteristics at more positions should be studied in order to closely examine the redistribution of the main flow and the evolution of the secondary flow. The velocity at the bottom and near the side walls should be studied carefully due to its significant impact on sediment transport. In numerical models, boundary conditions, roughness, and turbulence should receive more attention in river bends in order to gain more accurate results.

The outer bank cell plays an important role in the erosion of the outer bank and the mixing abilities in this region and needs to be well predicted. Thus, it is important to develop new techniques or models to better predict the outer bank cell. Although many numerical models have been used to study the flow in river bends, the complexity of flow structure in this area, in addition to difficulty in prediction and understanding, indicate the need for further studies of numerical modeling, especially those that can accurately simulate the main secondary cell and the outer bank cell. A wider variety of numerical models such as LES, Detached Eddy Simulation (DES), Delayed Detached Eddy Simulation (DDES), and anisotropic RANS models is needed to be further assessed in simulations of the flow in river bends.

2.8. Concluding Remarks

Flow in river bends is obviously three-dimensional in nature, and different turbulence models have been used in the literature to simulate the flow at these areas. This study provides a comprehensive review on secondary flows in river bends, which is useful for a better understanding of the flow features in nature. The following conclusions can be drawn from the outputs of the simulations.

Theoretically, the results provided by a 3D model are more likely to outperform a depth-averaged (2D) model. However, 2D models might be more preferable due to their computational cost-effectiveness. A reasonable approximation was obtained from 2D models used in the study of mildly and sharply curved bends. In order to obtain more accurate results, a large number of measurements should be made available for calibration and verification.

The velocity distribution is significantly affected by the radius of the curvature. Higher velocity at the strongly curved bends occurs near the inner bank at the beginning of the bend, then it moves gradually towards the outer bank. The maximum velocity of the secondary velocities occurs below the free surface. The secondary velocities decrease as the radius of curvature increases. In addition, the higher velocity is displaced from the entrance towards the central part of the bend. The longitudinal velocities in strongly curved bends give a rough approximation of reality; moving the higher velocity from the inner bank of the bend towards the outer bank is predicted well. However, in reality, this occurs over a shorter distance. The longitudinal velocities in smoothly curved bends were predicted well in the central region and near the outer bank.

In the strongly curved bend, turbulence plays a significant role in the flow. The boundary conditions also play an important role in the distributions of the velocity in the cross-section. Choosing the correct and appropriate boundary conditions may lead to a more accurate simulation and better results.

Based on all studies reviewed in this paper, it can be seen that most of the RANS models and LES models performed well in simulating the main secondary cell in bends with some differences between them in accuracy. The differences could be attributed to some factors such as the geometry of the channel, curvature, roughness, etc., on the one hand, and the factors that were studied in the curved channel by these models such as type of the secondary cells, sediment transport, pollutant dispersion, etc., on the other hand. However, LES and related models could be recommended to use in order to better capture secondary flow structure, particularly the outer bank cell.

Chapter 3. Chapter 3. Review and Comparison of Numerical Simulations of Secondary Flow in River Confluences

Abstract

River confluences are a common feature in natural water resources. The flow characteristics in confluences are complicated, especially at junction areas between tributaries and the main river. One of the typical characteristics of confluences is secondary flow, which plays an important role in mixing, velocity, sediment transport, and pollutant dispersion. In addition to the experimental and field studies that have been conducted in this area, the development of computational fluid dynamics has allowed researchers in this field to use different numerical models to simulate turbulence properties in rivers, especially secondary flows. Nowadays, the hydrodynamics of flows in confluences are widely simulated by using three-dimensional models in order to fully capture the flow structures, as the flow characteristics are considered to be turbulent and three-dimensional at river junctions. Several numerical models have been recommended for this purpose, and various turbulence models have been used to simulate the flows at confluences. To assess the accuracy of turbulence models, flows have been predicted by applying different turbulence models in the numerical model and the results have been compared with other data, such as field, laboratory, and experimental data. The purpose behind these investigations was to find the suitable model for each case of turbulent flow and for different types of confluences. In this study, the performances of turbulence models for confluences are reviewed for different numerical simulation strategies.

Keywords: river confluences; secondary flow; numerical model; flow field

---

[3] This chapter has been published as Rawaa Shaheed, Xiaohui Yan, and Abdolmajid Mohammadian (2021) Review and Comparison of Numerical Simulations of Secondary Flow in River Confluences. Water journal, 13, 1917. https://doi.org/10.3390/w13141917.

3.1. Introduction

Confluent channels are a common type of channel in river systems. They usually occur due to the confluence of two or more streams to form one single stream. This phenomenon is considered extremely complicated because when two rivers with different hydraulic conditions join, they will form a single river with new hydraulic conditions. There are six different zones in river confluences according to the generalized model proposed by Best (1987): a stagnation zone, deflection zone, separation zone, maximum velocity zone, flow recovery zone, and shear plane (Figure 3.1). The shear plane basically occurs as the branch river enters the main river because of the differences in their velocity fields, and this is the main source of turbulence generation. The stagnation zone is the start of the shear plane, and the separation zone is the area immediately after the junction close to the inner bank of the main river, and it is considered as a source of turbulence. The velocity magnitude in the separation zone is usually small. The maximum velocity occurs in the contraction zone or acceleration zone, which is in the area close to the outer bank of the main river directly after the junction (Yang et al., 2013).

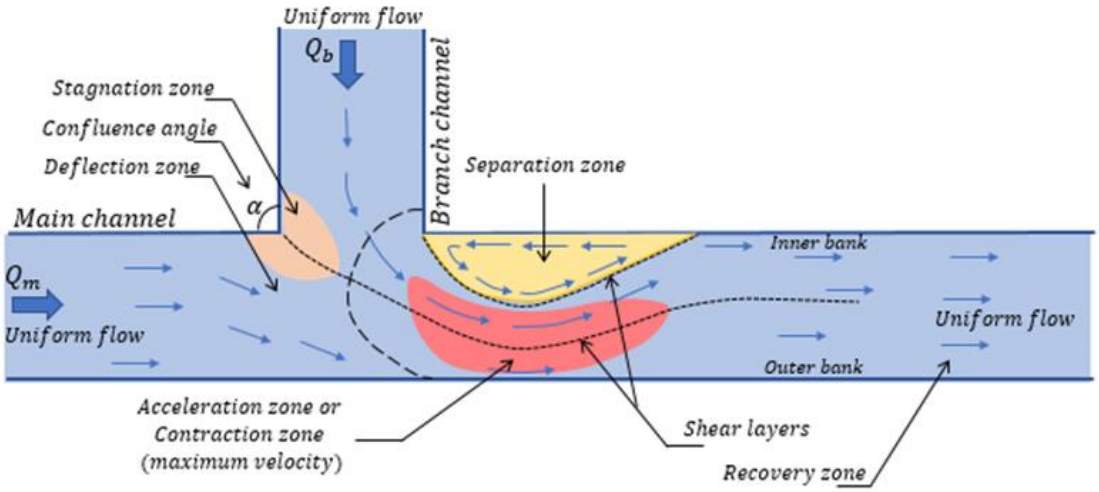

Figure 3.1: Flow characteristics in channel confluences (based on Shakibaeinia et al., 2010, from Best, 1987)

Several features in the river could be affected after the junction, such as the water surface and bed level, while other phenomena could be observed, like sediment transport, pollutant dispersion, erosion, deposition, river migration, and river meander formation (Weerakoon, 1990). The features observed in river confluences are also significantly affected by secondary flows. Secondary flows

are one of the significant flow characteristics in river confluences. These are caused by the change in flow direction of the branch river as it enters the main river. The centrifugal force causes a surface radial flow opposite to the deflection as well as an inward bottom current. Accordingly, two types of secondary flow are produced downstream in the main river: one of them is from the main river, and the second is from the branch river. They rotate against each other and gradually fade downstream because of the fluid viscosity (Song et al., 2012).

Understanding river confluences is not an easy matter because it depends on variables like the type of confluence (symmetrical, i.e., Y-shape; asymmetrical), the confluence angle, river width and depth, bed slope, discharge rate, direction of the flow, bed roughness, and Froude number (Sivakumar et al., 2004). Some researchers have studied the effects of these variables such as the flow rate ratio and confluence angle between the main and branch channel (Best and Reid, 1984) in order to examine the impact of these variables on the flow structure and bed deformation in the junction. The differences in flow structures between symmetrical and asymmetrical confluences were studied by Bradbrook et al. (2000a), Bradbrook et al. (2000b), and Bryan and Kuhn (2002) through the use of numerical simulations and flume tests. In addition, the spatial patterns of water surface topography in confluent rivers were studied by Biron et al. (2002).

Recently, numerical models have been used to study the features of flows in river confluences, and the complexity of these features has made it preferable to use three-dimensional numerical models. The flow in a right-angle confluent channel was studied by Huang et al. (2002) through three-dimensional simulation, and the results were compared with experimental data to verify the model used. As a result, the flow structure was then investigated with different confluence angles based on the model. A three-dimensional simulation was carried out by Biron et al. (2004) to study the flow in a confluent channel with a discordant bed, and the results indicated that there was a good agreement with experimental data. In addition, Shakibaeinia et al. (2010) used a three-dimensional model to investigate the flow properties in the separation zone of a secondary flow in a confluence area with different junction angles. The model's predictions were compared with those of the two-dimensional model by Lane et al. (1999) through the use of high-quality field data, and the results indicated that the predictive ability of the three-dimensional model was higher, especially if the impacts of secondary flow on the flow structure were not captured by a two-dimensional model. However, a rigid lid assumption was usually used for the free water surface in simulations with the three-dimensional model, or it could be captured by multi-phase modes. Accordingly, the velocity

distribution could not be simulated accurately because of inaccurate pinpointing of the free surface position.

The flow direction changes as the flow of a tributary enters the main river. This change causes a surface radial flow to be induced by centrifugal force that is opposite to the deflection and bottom inward current. In contrast, the secondary current of the main channel flow rotates in the opposite direction to that of the secondary flow in the branch channel, as illustrated in Figure 3.2. Due to the joining of the branch and main channel flows in this case, a shearing action on the main flow is set up by the tributary channel, and then two surface flows result. The influences of the comparative magnitudes of the consolidated flows and the profile of the non-uniform vertical velocity are the reason behind the skewing of the shear plane. The new merged flow has three-dimensional features induced by the non-uniform vertical velocity profile. Subsequently, a clockwise rotating secondary vortex can be found downstream of the main channel close to the inner bank (B. Barkdoll, 2003). At the outer bank of the main channel downstream, another secondary vortex appears and rotates against the secondary flow of the branch channel. Lastly, the downstream secondary currents of the two channels gradually fade, and this takes place mainly because of the fluid viscosity (Song et al., 2012).

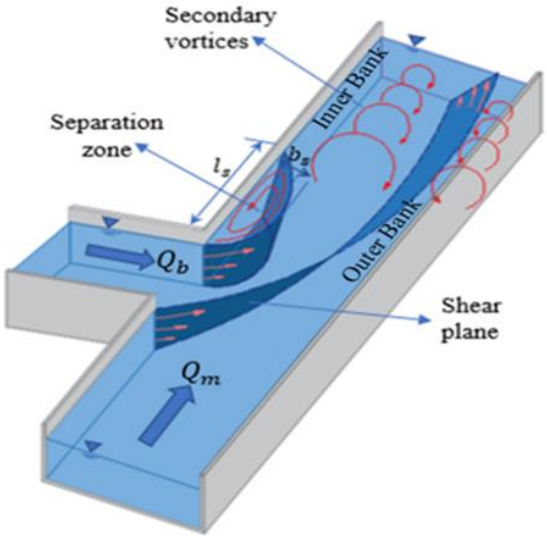

Figure 3.2: The structure of secondary flows in a confluent channel (based on Weber et al., 2001, from Shaheed et al., 2018)

There are some features that characterize the flows in confluent channels according to previous studies, which can be summarized as follows (Weerakoon, 1990): one of these features is two

oppositely circulating secondary flow cells. The secondary flow of the branch channel that occurs near the internal bank of the main channel could be more intense than the ones of the main channel near the external bank of the main channel (see Figure 3.2) because of the higher curvature experienced by the branch channel flow. At the corner of the junction's inner bank, super-elevation of the free surface appears because of the balancing centrifugal forces connected with the cells of the secondary flow. A recirculation zone appears near the inner bank of the main channel directly after the junction due to the separation of the accelerated branch channel flow from the wall, forming a steep pressure drop. Then, a strong counterflow occurs, forming a recirculation zone. Away from the water surface, the recirculation zone size becomes smaller. This could be because of the entrainment by the secondary flow and is distinguished in the deeper water confluences. Transfer of momentum to the recirculation region is shown by vortices which ascend with the secondary flow. The mixing resulting from the gradient of lateral velocity in the shear layer is related to the vortices at the interface, especially the vortices that arise at the corner of the inner bank. However, this is not strong compared to the scattering produced by the secondary flow.

In the light of previous research, these mentioned features might increase with increases in the confluence angle and discharge ratio.

The aim of this study is to review some previous studies that used numerical models to simulate the secondary flow in river confluences, and to evaluate each model from the researcher's point of view. Validating and evaluating models against well-controlled experimental results is the prerequisite for applying the models to practical applications. Therefore, most of the numerical studies reviewed in this paper were tested against experimental works.

This paper is organized as follows. Section 2 deals with mathematical description of the main flow and secondary circulation, while Section 3 covers boundary conditions. Sections 2 and 3 picked up the knowledge points that are relevant to river confluence flows modeling, and neglected the other knowledge that are irrelevant, to provide a quick and efficient understanding of the problem reviewed in this paper. Section 4 reviews some numerical studies on river confluences, including different kinds of confluences in different situations and some effects of secondary flows in these rivers. Section 5 presents a discussion, and Section 6 suggests future research needs. Finally, the conclusions complete the paper.

3.2. Mathematical Description of the Main Flow and Secondary Circulation

There are many different equation systems that can describe three-dimensional fluid flows. For example, an elliptic form of the Reynolds-averaged Navier–Stokes equations for steady flows, which in Cartesian coordinates, are written as follows (Bradbrook et al., 1998):

Continuity equation:

$$\frac{\partial u}{\partial x}+\frac{\partial v}{\partial y}+\frac{\partial w}{\partial z}=0 \tag{3-1}$$

Momentum equations:

$$\text{x-direction } \mathrm{u}\frac{\partial \mathrm{u}}{\partial \mathrm{x}}+\mathrm{v}\frac{\partial \mathrm{u}}{\partial \mathrm{y}}+\mathrm{w}\frac{\partial \mathrm{u}}{\partial \mathrm{z}}=-\frac{1}{\rho}\frac{\partial \mathrm{p}}{\partial \mathrm{x}}+\frac{1}{\rho}\left(\frac{\partial \tau_{\mathrm{xx}}}{\partial \mathrm{x}}+\frac{\partial \tau_{\mathrm{xy}}}{\partial \mathrm{y}}+\frac{\partial \tau_{\mathrm{xz}}}{\partial \mathrm{z}}\right) \tag{3-2}$$

$$\text{y-direction } \mathrm{u}\frac{\partial \mathrm{v}}{\partial \mathrm{x}}+\mathrm{v}\frac{\partial \mathrm{v}}{\partial \mathrm{y}}+\mathrm{w}\frac{\partial \mathrm{v}}{\partial \mathrm{z}}=-\frac{1}{\rho}\frac{\partial \mathrm{p}}{\partial \mathrm{y}}+\frac{1}{\rho}\left(\frac{\partial \tau_{\mathrm{xy}}}{\partial \mathrm{x}}+\frac{\partial \tau_{\mathrm{yy}}}{\partial \mathrm{y}}+\frac{\partial \tau_{\mathrm{yz}}}{\partial \mathrm{z}}\right) \tag{3-3}$$

$$\text{z-direction } \mathrm{u}\frac{\partial \mathrm{w}}{\partial \mathrm{x}}+\mathrm{v}\frac{\partial \mathrm{w}}{\partial \mathrm{y}}+\mathrm{w}\frac{\partial \mathrm{w}}{\partial \mathrm{z}}=-\frac{1}{\rho}\frac{\partial \mathrm{p}}{\partial \mathrm{z}}+\frac{1}{\rho}\left(\frac{\partial \tau_{\mathrm{xz}}}{\partial \mathrm{x}}+\frac{\partial \tau_{yz}}{\partial \mathrm{y}}+\frac{\partial \tau_{zz}}{\partial \mathrm{z}}\right) \tag{3-4}$$

where u, v, and w are the time-averaged Cartesian velocity components in the x, y, and z directions, respectively, ρ is the density, and p is the pressure.

$$\tau_{\mathrm{ij}}=\nu\left(\frac{\partial u_j}{\partial x_i}+\frac{\partial u_i}{\partial x_j}\right)-\overline{u_i' u_j'} \tag{3-5}$$

where ν is the kinematic viscosity and $\overline{u_i' u_j'}$ are the time-averaged turbulent Reynolds shear stresses (Lane, 1998), where i and j are standard tensor notations indicating two out of the three orthogonal coordinate directions.

3.3. Boundary Conditions

The boundary conditions that should be considered for the numerical models include walls, free surface, inlet, and outlet, and detailed explanations of each one is provided below.

3.3.1. Wall Function Boundaries

Parameters for the turbulence and the velocity are needed in the cell adjacent to the wall because there is usually not enough cell spacing close to the solid boundaries to resolve the laminar sublayer. Usually, the ‘universal’ law of the wall, which is based on a shear velocity, is used. The assumptions

of this law basically depend on the existence of a local equilibrium of turbulence which does not hold under conditions of flow separation. Thus, the non-equilibrium version of the law of the wall (Launder and Spalding, 1974) may be used, which takes the square root of the turbulent kinetic energy, rather than the shear velocity, as the characteristic velocity scale (Bradbrook et al., 1998). The 'universal' law of the wall is:

$$\frac{U_r}{U_\tau} = \frac{ln\,(EY^+)}{\kappa} \tag{3-6}$$

with $U_\tau = \sqrt{\tau/\rho}$ and $Y^+ = \frac{U_\tau Y}{\mu}$, where U_r is the velocity parallel to the wall, U_τ is the shear velocity, τ is the bed shear stress, E is the roughness parameter, Y^+ is the nondimensional wall distance, Y is the normal distance to the wall, μ is the fluid kinematic viscosity, and κ is the von Karman constant (0.4). Assuming a local equilibrium of turbulence, the shear velocity can be related to the local kinetic energy by using (Launder and Spalding, 1974):

$$k = \frac{U_\tau^2}{\sqrt{c'_\mu}} \tag{3-7}$$

The boundary condition for ε is given by:

$$\varepsilon = (c'_\mu)^{3/4}\frac{k^{3/2}}{\kappa Y} \tag{3-8}$$

The assumption of local equilibrium (Equation (7)) does not hold under conditions of separation, so instead of using U_τ as the characteristic velocity scale, $\sqrt{k}$ is used in the non-equilibrium wall function as below (Launder and Spalding, 1974):

$$\frac{U_r.\sqrt{k}}{U_\tau^2} = \frac{ln\,(0.25c'_\mu E\sqrt{k}Y)}{0.25c'_\mu\kappa} \tag{3-9}$$

where k is taken from the transport equation (Equation (10)) below (Launder and Spalding, 1974) with the diffusion of energy to the wall set to 0.

$$u_i\frac{\partial k}{\partial x_i} = \frac{\partial}{\partial x_i}\left(\frac{\nu_t}{\sigma_k}\frac{\partial k}{\partial x_i}\right) - \nu_t\left(\frac{\partial u_i}{\partial x_j}+\frac{\partial u_j}{\partial x_i}\right)\frac{\partial u_i}{\partial x_j} - \varepsilon \tag{3-10}$$

convection owing to transport by mean flow	=	diffusion into mean flow	−	production (=P)	−	viscous dissipation rate

The shear velocity production term is:

$$P = \frac{U_\tau^2 U_r}{2Y} \tag{3-11}$$

and the boundary condition for ε is:

$$\varepsilon = \frac{(c'_\mu)^{3/4} k^{3/2} ln\,(0.25 c'_\mu E\sqrt{k}Y/\mu)}{2kY} \tag{3-12}$$

However, under local equilibrium conditions, Equation (12) reduces to Equation (8), and $P/\varepsilon = 1$ (Bradbrook et al., 1998). It is to be noted that the above expression for P is commonly used for eddy viscosity models.

3.3.2. Free Surface

The free surface in the model needs to be simulated due to surface depression and elevation, which are considered as features of confluence flow dynamics (Weerakoon and Tamai, 1989; Rhoads, 1996). The assumption of a 'rigid lid' has been used widely in previous works, which considered the surface as a plane because of the difficulty of determining the exact contours of the free surface elevation. As for the symmetry plane, all the normal derivatives at the surface are set to zero. Variation in water depth, which could occur if the surface is not fixed, is represented by the pressure on the surface, and it is not set to zero. Therefore, super-elevation is represented by a pressure of more than zero, while a pressure of less than zero represents surface depression. This means that the pressure gradient term in the momentum equations considers the variance in the position of the water surface, while it is not considered in the mass continuity equation, which could lead to maximum velocity predictions at an area of super-elevation (Weerakoon and Tamai, 1989), and the opposite at an area of surface depression. In confluent channels, streamline curvature plays a significant role.

Another approach is based on free-surface capturing (e.g., the volume of fluid method), in which the free surface location is simulated. Typically, free-surface capturing methods are more accurate than rigid lid methods.

3.3.3. Inlet

The distribution of velocity should be determined at the furthest upstream cross-section. It could be

possible to define a uniform velocity, but this requires a large number of cells before the junction to guarantee that the flow is completely developed at the location of intersection with respect to the friction impact from the bed and walls. The velocity distribution for the upstream cross-sections can be calculated by using a separate model in order to avoid the additional computations that could be required. For each tributary, the cross-section dimensions and the rate of the mass flow are needed, and for each cross-section, the fully developed flow boundary condition needs to be calculated. The turbulence parameters k and ε should be also provided at the upstream boundary for each tributary channel (Bradbrook et al., 1998).

3.3.4. Outlet

At the outlet cross-section downstream, the boundary condition is also required, for which the pressure must be determined. In addition, negative velocities can occur in this cross-section if the regions of negative pressure extend downstream. This is usually considered undesirable and has been used to indicate that the solution field should be extended even further. Further, at the end of the solution field, it is considered suitable to have small secondary currents (Bradbrook et al., 1998).

3.4. Numerical Research of River Confluence Flows

The hydrodynamic characteristics of river confluences are different according to type of the confluence (Liu et al., 2019). The type of confluence (symmetrical or asymmetrical), confluence ratio, confluence angle, discharge ratio, bed level (accordant or discordant) could have an important role in turbulence and secondary circulation of the confluence. Accordingly, the morphology of the confluent areas is affected as well (Bilal et al., 2020). Given the importance of these factors and its effects on confluences, this section is divided into three subsections to shed light on each case and indicate its importance and impact on river confluences through the previous studies that have been conducted. There is a lack of detailed review of numerical simulations of secondary flow in confluences, and thus these sections are believed necessary for the community of hydraulic engineering.

3.4.1. Secondary Flow in a 90° Confluent Channel with Bed Concordance

In this section, the numerical modeling of secondary flows in river confluences from several previous studies is discussed. Secondary flows in a 90° confluent channel were considered in these studies and the different turbulence models were taken into account, and then the numerical models

were assessed accordingly. In addition, the studies are divided according to the numerical models that used.

3.4.1.1. RANS Models

The numerical research studies that used RANS models to simulate the flow in river confluences are summarized in Table 3.1.

Table 3.1: Summary of selected studies about secondary flow in confluent channels used in Section 3.4.1.1

Shape of Channel	Numerical Model	Key Findings	Reference
Asymmetrical, ⊥ shaped	k-ω model	The strength of the secondary flow was underpredicted	(Huang et al., 2002)
Asymmetrical, ⊥ shaped	The CFD package, PHOENICS (version 3.5), the turbulence model was not specified in this paper	There was a good agreement at the upstream end of the junction, and the discrepancy increased at other downstream locations	(Sivakumar et al., 2004)
Asymmetrical, ⊥ shaped	3D k-ω model	The results of the numerical model agreed well with the experimental data	(Zhang et al., 2009)
Asymmetrical, ⊥ shaped	RNG form of k-ε model	The secondary flows appeared directly after the junction in approximately three counter-rotating helical cells	(Shakibaeinia et al., 2010)
Asymmetrical, ⊥ shaped	A hybrid RANS-LES model was developed	The new modeling approach is more accurate than the RANS approach in addition to its ability of saving computational effort comparing to the LES approach	(Zeng and Li, 2010)
Asymmetrical, ⊥ shaped	Standard k-ε, RNG k-ε, and RSM turbulence models	At the section immediately after the junction, the secondary flow predicted by the numerical models was smaller than that of the experiment	(Yang et al., 2011)
Asymmetrical, ⊥ shaped	RNG form of k-ε model	The results showed good agreement between the simulation and the measured data	(Mignot et al., 2012)
Asymmetrical, ⊥ shaped	Standard k-ε, realizable k-ε, and k-ω	The preferable model for the confluence flow simulation was k-ω	(Yang et al., 2013)
Asymmetrical, ⊥ shaped	Reynolds Stress Modeling (RSM)	Flow pattern could be improved significantly by employing some geometrical adjustments	(Mohammadiun et al., 2015)
Asymmetrical, ⊥ shaped	Standard k–ε model and the realizable k–ε model	The realizable k–ε model is better	(Shaheed et al., 2018)
Asymmetrical, ⊥ shaped	Reynolds averaged Navier–Stokes equations	The contaminants mixing basically happens in the mixing layer at the interface of two confluent flows	(Tang et al., 2018)

Shape of Channel	Numerical Model	Key Findings	Reference
	and Reynolds stress turbulence model (RANS and RSM)		
Asymmetrical, ⊥ shaped	A modified 1D nonlinear dynamic model and fully 3D non-hydrostatic, Reynolds-averaged Navier–Stokes equations (RANS) model	The strategies of 1D and 3D modeling could be applied to other flow diversion problems like river meander	(Luo et al., 2018)

The experimental data from Shumate (1998), which included a 90° open-channel junction was used by Huang et al. (2002) to simulate the flow in an open confluent channel by developing and validating a three-dimensional numerical method. Reynolds-averaged Navier–Stokes (RANS) equations with incompressible and steady-state assumptions were used, and the $k-\omega$ model by Wilcox (1993) was selected. The model was first applied and evaluated on Shumate's (1998) experimental data with two distinctive flow discharges, and then it was used to examine the impact of different junction angles on the flow features. The boundary conditions for the normal gradients at the free surface were set to zero. The flow velocities and the turbulence quantities were specified at the inlet's boundaries of the two channels, and the standard wall-function approach was used at the solid walls. The free surface elevation was specified at the outlet boundary condition, and the piezometric pressure P was fixed. Generally, the results showed that the flow features in junctions could be reproduced by the 3D model, and agreement be-tween the predicted and experimental data was adequate. In particular, the authors concluded that the separation zone was located along the left bank of the main channel directly after the junction, and that it was smaller near the bed of the channel than near the water surface. The size of the separation zone increased with increases in the junction angle. There was a depression in the surface elevation of the separation zone, and this de-pression increased with increased junction angles. In addition, the strength of the secondary flow increased with increases in the junction angle. The strength of the secondary flow was underpredicted by the employed isotropic turbulence model, partially because the isotropic eddy viscosity model cannot correctly evaluate the mechanical generation term in the transport equation for turbulent kinetic energy. This weakness also led to poor pre-dictions for separation zones. Therefore, turbulence models with higher orders could be needed to improve the prediction (Huang et al., 2002).

The data from the laboratory experiment by Weber et al. (2001), which included a 90° open channel confluent flume, were used by Sivakumar et al. (2004) to simulate the flow using numerical models. The 3D numerical simulation was carried out by using the CFD package, PHOENICS version 3.5 (CHAM, Inc., London). In addition, the height of liquid (HOL) technique, which is a built-in algorithm to track the free surface in PHOENICS, was used in this study. The input data, including for velocities and water depths, were calculated and applied at the inputs of the main and branch channels. The boundary condition of the solid walls was applied as no-slip boundary condition. The vertical planes above the water were applied as a zero-gauge pressure boundary condition at the inlet of the two channels as well as at the outlet. The simulation showed that the recirculation zone was bigger at the area close to the free surface and smaller close to the bed. The results showed that at the upstream end of the junction, there was a good agreement between the simulated and experimental data; however, the discrepancies increased between the two mentioned datasets at locations downstream. The reason for the discrepancies could be partially due to the coarse mesh used (Sivakumar et al., 2004).

The impact of discharge ratio on the separation zone shape, the cross-sectional angle of mean flow, and the contraction coefficient were investigated by Zhang et al. (2009). A 3D k-ω model that solve the Reynolds averaged Navier–Stokes equations was applied, and the experimental data of Weber et al. (2001) that include a 90° equal-width open-channel junction flow was used to validate the model. The results of the numerical model agreed well with the experimental data. The free surface elevation and the secondary flow were reproduced faithfully. The impact of discharge ratio on the flow characteristics was investigated as well, and the results indicated that the increasing in the discharge ratio causes a decreasing in the size of the separation zone, while the flow deflection at the upstream corner of the branch channel entrance increases with the discharge ratio. Accordingly, the model could be convenient to obtain various flow parameters in such type of channels.

The experimental data obtained by Shumate and Weber (1998) that included a 90° confluent channel was used by Shakibaeinia et al. (2010) to analyze the flow in a confluence with different confluence angles, discharge and width ratios, and downstream Froude numbers. SSIIM2.0 (NTNU, Inc., Norway), which is a three-dimensional model, was used along with the RNG form of the k-ε model. Then, the various parameters' impacts on the flow structure were investigated. In addition to the experimental data from Shumate and Weber (1998), the study included another three confluence angles, 15°,45°, and 105°; three discharge ratios, 0.25, 0.50, and 0.75; two width ratios,

1.00, and 0.66; and three downstream Froude numbers, 0.26, 0.34, and 0.43. Based on these parameters, 26 various numerical simulations were conducted. The secondary flows appeared directly after the junction in approximately three counter-rotating helical cells. The first helical cells occurred due to the separation zone, and this type of cell might fade away in natural rivers because of sediment deposition at this area. The second helical cells occurred due to the deflection of the tributary flow towards the direction of the main channel. These cells are considered the strongest ones in the confluence and decreases gradually downstream of the main channel. The third helical cells occurred at the main channel due to the interaction between the second cells and the main channel's flow and rotated against the second cells (Figure 3.3).

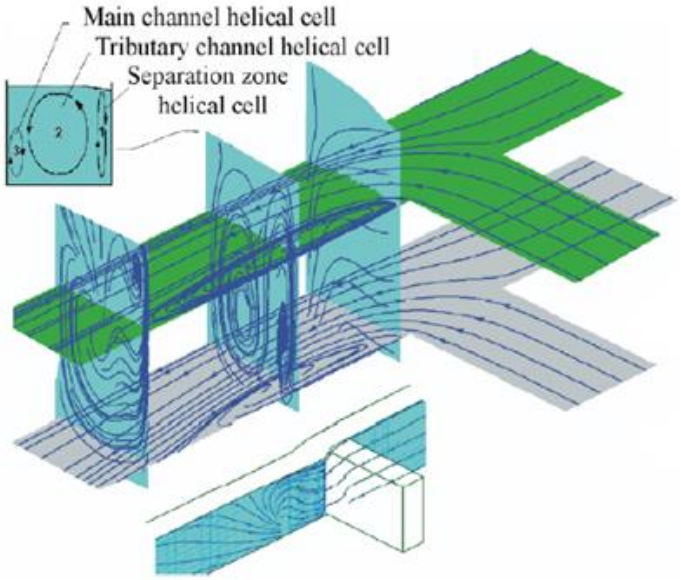

Figure 3.3: Streamlines in an equal width 90° confluence for Q_r = 0.50 in different sections (Shakibaeinia et al., 2010)

The study showed that the secondary flows were affected by changes in the confluence angles. For example, with a high confluence angle, all the helical cells can be distinct, while with low confluence angles, the second helical cells fade away and the third cells are eliminated (Figure 3.4). The separation zone (see Figure 3.1) occurred immediately after the junction near the inner bank of the main channel due to the change in the direction of the tributary flow. This zone was also affected by the confluence angles, discharge ratios, width ratios, and Froude numbers. For example, the dimensions of the separation zone decreased as the discharge ratio increased. Increased confluence angles up to 90° caused an increase in the separation zone dimensions; however, for angles greater than 90°, the situation was different because the flow of the tributary into the main channel would

be in the opposite direction and so the flow mixing occurs over a shorter distance, which leads to a shorter length of the separation zone. In addition, the dimensions of the separation zone for angles less than 45 degrees may be reduced or not occur at all, as with the angle of 15°. The width ratio, i.e., the width of the tributary divided by the width of the main channel, is equal to 1.00 when the widths of the two channels are equal and are less than one when the width of the tributary is less than that of the main channel. The separation zone dimensions increased as the width ratio decreased from 1.00 to 0.66, and the maximum velocity occurred at the contraction zone (see Figure 1) near the outer bank of the main channel. In addition, the maximum velocity was impacted by the flow parameters. For example, as the discharge ratio increased, the maximum velocity decreased. However, the non-dimensional maximum velocity was not overly sensitive to the discharge ratio for smaller confluence angles. The velocity increased with increases in the confluence angle, while in a channel with small angles, the flow contraction was not significant. Further, as the width ratio decreased, the maximum velocity increased, and the maximum velocity increased as the Froude number increased. Increases in the confluence angles caused increases and decreases in the maximum and minimum water surface elevation respectively, and water surface variations were impacted considerably by the width ratio only at low discharge ratios. Increased Froude numbers caused an increase in the maximum water surface elevation and a decrease in the minimum elevation.

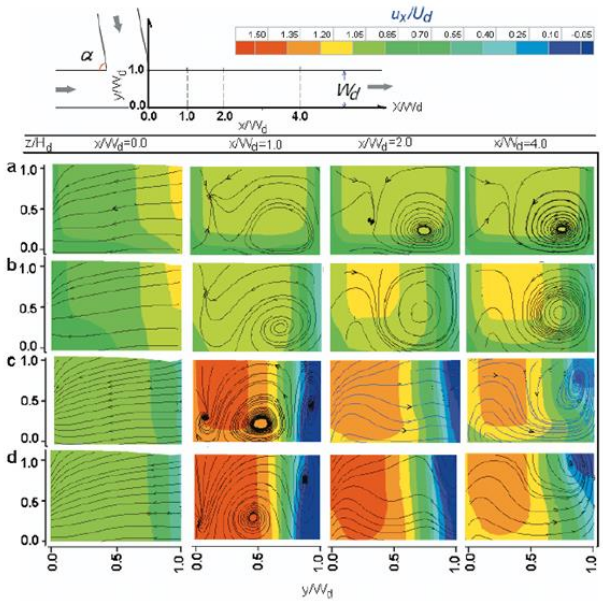

Figure 3.4: Main channel cross section showing calculated flow pattern and secondary currents in confluences for Q_r = 0.50, W_r = 100, and four different confluence angles. (a) α = 15°, (b) α = 45°, (c) α = 90°, (d) α = 105° (Shakibaeinia et al., 2010)

In order to simulate the flow in an open channel T-junction, a hybrid RANS-LES (Reynolds Averaged Navier–Stokes equation—Large Eddy Simulation) model was developed by Zeng and Li (2010). The computational results were compared with the experimental data and showed that the new modeling approach is more accurate than the RANS approach in addition to its ability of saving computational effort comparing to the LES approach.

An experiment and 3D numerical simulation were used by Yang et al. (2011) to examine the flow in an asymmetrical 90-degree confluent channel. They utilized the standard k-ε, RNG k-ε, and RSM turbulence models to simulate the secondary flows and separation zones, and then the results of the numerical models' predictions and the experimental data were compared and evaluated. In order to conduct the simulation, FLUENT 6.3 (ANSYS, Inc., Canonsburg, PA, USA) was used. The boundary conditions were applied as follows: the intake of the main channel and the output from the branch channel were set as the velocity inlet, and the pressure outlet and symmetry were used to set the outlet and top of the channel, respectively. The results showed that at the section immediately after the junction, the secondary flow predicted by the numerical models was smaller than that of the experiment. In addition, the predicted scales of the separation zone were smaller than that of the experiment. At the section where the separation zone started to disappear, the results were almost the same, including smaller predicted secondary flows and separation zones than from the experiment. However, there was a big similarity between the RNG k-ε model and the experiment results in the shape of the simulated zone. Then, at the section where the separation zone had completely disappeared, the results obtained by the standard k-ε model and RNG k-ε model each included a fully developed vortex, which was the same as from the experiment, while the secondary flow obtained from the RSM model included several vortexes, which was different from the results of the standard k-ε and RNG k-ε models. The differences between the simulated results and the experimental data could be due to some reasons described below. The flows in the turbulence models were assumed as being fully developed turbulence flows, while in the experiment, the flow may have transitioned from laminar to turbulence flow. In addition, there was a rapid change in the surface elevation at the junction area, which was not easy to simulate accurately, and so there may have been some errors in the flow field (Yang et al., 2011).

The flow pattern in a 90° junction was measured experimentally and simulated numerically by Mignot et al. (2012) to analyze the effect of the junction on the velocity distribution, and to evaluate the typical error derived from calculating the flow rate near the junction. The commercial Ansys—

CFX CFD (ANSYS, Inc., Canonsburg, PA, USA) software package was used in the simulation to carry out the 3D numerical modelling. The results showed good agreement between the simulation and the measured data.

The experimental data from Weber et al. (2001) was used by Yang et al. (2013) to simulate and study the flow features in a right-angle confluence flume using three types of surface treating methods: rigid lid, VOF, and dynamic mesh techniques. Three turbulence models were chosen to conduct the simulations: the standard k-ε, realizable k-ε, and k-ω. All of the models were two-equation turbulence models. ANSYS FLUENT (ANSYS, Inc., Canonsburg, PA, USA) was used to conduct the simulations. Five simulation runs were carried out, as shown in Table 3.2.

Table 3.2: Flow conditions in the experiment and five simulation runs (Yang et al., 2013)

Flow conditions in the experiment						
Runs	$Q_b\ (m^3/\text{s})$	$Q_m\ (m^3/\text{s})$	$Q_d\ (m^3/\text{s})$	$q_b\ (m^2/\text{s})$	$q_d\ (m^2/\text{s})$	$R_q\ (q_b/q_d)$
1	0.127	0.042	0.169	0.139	0.185	0.750
Runs for three-dimensional simulation of confluence flow						
Runs	Cases	Turbulence model	Surface treating	Meshes adopted		Computing time (hours)
1	$R_q = 0.75$	Standard k-ε	Dynamic meshes	165,456		118
2		Realizable k-ε	Dynamic meshes	165,456		124
3		k-ω	Dynamic meshes	165,456		130
4		k-ω	Rigid lid	165,456		50
5		k-ω	VOF	232,200		245

The mass flow inlet was used to set the intakes of the two channels' boundary conditions, and the pressure outlet was used for the outlet of the channel. The symmetric plane boundary condition was used to set the free surface of the channel, and self-proposed surface tracking codes were used to update the position. The free surface was set as the pressure inlet when the VOF method was used. The three turbulence models were used to simulate the free shear flow, separated flow, and secondary flow that occur at the same time in confluences. Accordingly, the performances of the models were verified and evaluated. There was a triangular projection in the horizontal plane of the mesh, and a rectangular projection in the vertical plane. The results of the simulations showed that in the case of the dynamic mesh techniques, there was a satisfactory agreement between the predicted and observed water levels. However, in the case of the VOF method, the results were

much poorer. This means that the simulation per-formed well when the proposed surface tracking codes were used. For the longitudinal velocity and regarding the scale of the separation zone, the results observed from the realizable k-ε method were the best in comparison with the experimental data, while for the magnitude of the velocity, the k-ω model was the best. For the circulation cells, all the models performed correctly except for the model with the rigid lid surface. The preferable model for the confluence flow simulation was concluded to be the k-ω model (Yang et al., 2013).

The impacts of open channel geometry on flow pattern in a 90° junction were studied by Mohammadiun et al. (2015). The FLUENT software (ANSYS, Inc., Canonsburg, PA, USA) and Reynolds stress modeling (RSM) turbulent model were used in simulation, and the experimental data of Weber et al. (2001) was used for validation. They concluded that the arc at the downward corner of the confluence might cause sedimentation due to the full elimination of the separation zone, and reduction in erosion potential due to its significant impact on reducing the maximum flow velocity. The formation of a stagnation area could be prevented through the adjustment of the sharp-angle upstream corner of the confluence. In addition, the flow pattern could be improved significantly by employing some geometrical adjustments that eliminate the recirculation zone and reduce the flow maximum velocity after the confluence. Accordingly, sedimentation and erosion potential are reduced, and the stagnation zone is contracted as well.

The experimental data from Shumate (1998) were also used by Shaheed et al. (2018) to simulate the flow in a 90° closed-channel junction. A 3D OpenFOAM numerical model was employed, and two turbulence models, including the standard k–ε and realizable k–ε were applied to simulate the effect of secondary currents on water velocity in channel confluences. The boundary conditions included the flow discharge with initial velocities at the inlets of the two channels, a zero gradient at the outlet of the channel, the pressure and turbulent viscosity defined as zero gradients for the inlet and outlet, the standard wall function for the walls, and a symmetry plane for the channel surface. The maximum velocity moved from the branch channel towards the outer bank of the main channel as the branch channel's flow entered the main channel. The velocity curve after the junction was studied by taking some cross-sections of the main channel directly after the junction (Figure 3.5). A comparison between the numerical models and the experimental data was conducted, and the two models achieved a good agreement (Figure 3.6) where U is the depth-averaged velocity magnitude, U1 is the downstream mean velocity, and the coordinate system was non-dimensionalized with the channel width by $x^* = x/B$ and $z^* = z/B$. However, there were some

differences in the cross-sections directly after the junction that could be due to the sudden change in flow direction, which led to difficulty in identifying the flow features in this region. This is in addition to the generation of the separation zone at the inner bank of the main channel immediately after the junction, which led to complexity of the flow features in this area. In terms of preference, the realizable *k–ε* model was found to be better in this case (Shaheed et al., 2018).

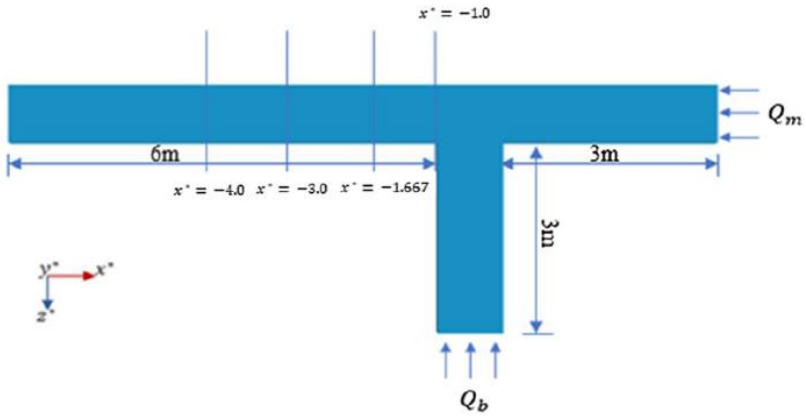

Figure 3.5: Model setup for the confluent channel (Shaheed et al., 2018)

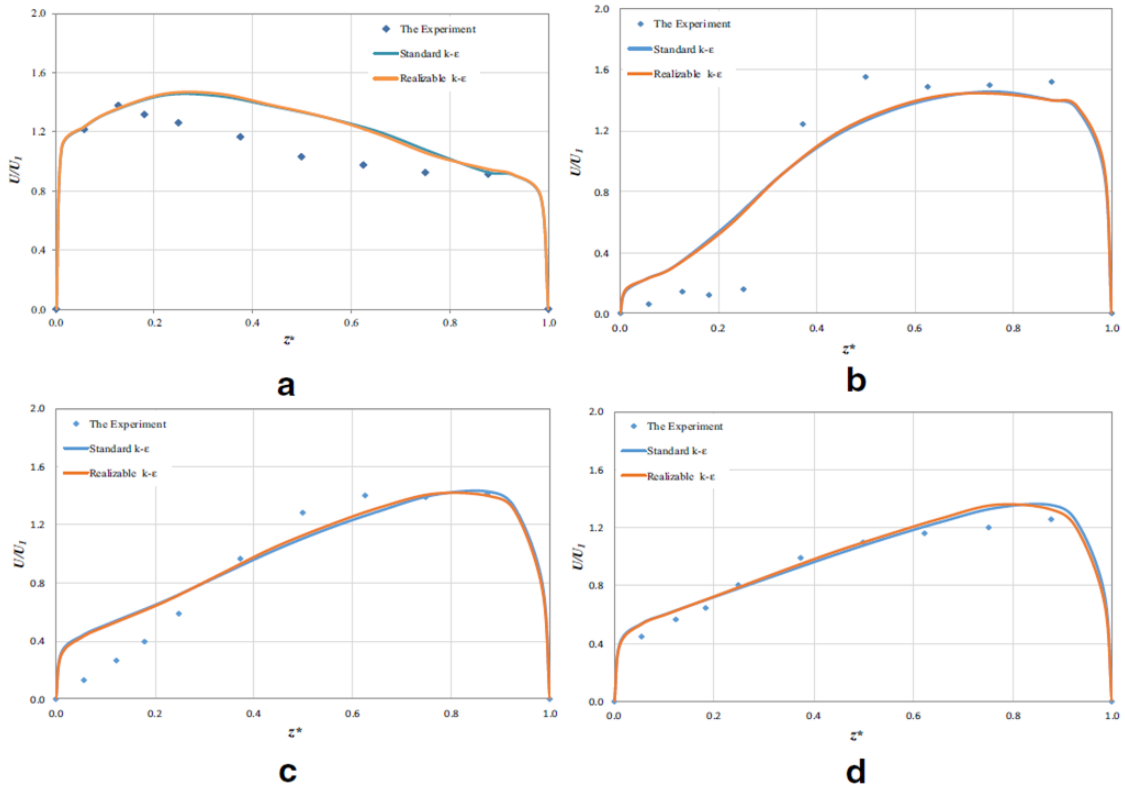

Figure 3.6: Resultant velocities across dimensionless transverse distance for confluent channel: (a) at x* = −1.0; (b) at x* = −1.667; and (c) at x* = −3.0, (d) at x* = −4.0 (Shaheed et al., 2018)

The flow patterns and contaminant transport at a 90-degree channel confluence were analyzed by Tang et al. (2018) Various bed morphologies and discharge ratios were used in this study, and a 3D numerical model (ANSYS FLUENT 14.0) (ANSYS, Inc., Canonsburg, PA, USA) based on Reynolds averaged Navier–Stokes equations and Reynolds stress turbulence model was used as well. They concluded that the contaminants mixing basically happens in the mixing layer at the interface of two confluent flows. The formation of this mixing layer is influenced by the helical cell distribution and development. Mixing is enhanced with an increase in the discharge ratio accompanied by movement towards the outer bank and deformation of the mixing layer. In addition, mixing is affected by bed morphology through the shear layer formation, and contaminant transport could be affected by the confluence angle as well.

The experimental data of Weber et al. (2001) that includes a sharp-edged 90°smooth confluent channel was used by Luo et al. (2018) to conduct the comparative 1D and 3D numerical investigation of open channel flows and energy losses. They indicated that the strategies of 1D and 3D modeling could be applied to other flow diversion problems like river meander. They also pointed out that although 1D modeling is considered economic and often sufficient for real-time monitoring, the use of 3D modeling could bring the hydrodynamic understanding provided by the 3D CFD model into the efficiency of the 1D model, improving the accuracy of unsteady flow simulations while optimizing computational cost.

The hydrodynamics and passive scalar dispersion were measured by Pouchoulin et al. (2018) on flat and degraded beds at a 90-degree channel confluence. The direction of rotation of secondary flows has been discussed in comparison with other studies in terms of calculations and measurements, and even for slightly different geometries.

3.4.1.2. LES Models

The numerical research studies that used LES models to simulate the flow in river confluences are summarized in Table 3.3.

Table 3.3: Summary of selected studies about secondary flow in confluent channels used in Section 3.4.1.2

Shape of Channel	Numerical Model	Key Findings	Reference
Asymmetrical, ⊥ shaped	LES	A reasonable agreement with experimental data and analytical solutions was achieved.	(Liu et al., 2009)
Asymmetrical, ⊥ shaped	LES	New features of the flow patterns were induced due to the flow of the tributary.	(Schindfessel et al., 2015)
Asymmetrical, ⊥ shaped	LES	There was a significant difference in the separation zone dimensions for non-rectangular shapes.	(Schindfessel et al., 2017)
Asymmetrical, ⊥ shaped	LES	Oversimplification of free surface numerical processing leads to lower accuracy of secondary flow and turbulent kinetic energy predictions.	(Ramos et al., 2019)

The flow in a confluent channel was studied numerically and experimentally by Liu et al. (2009). The flow was simulated numerically by developing a two-dimensional multi-block lattice Boltzmann model in which the Large Eddy Simulation model is coupled with shallow water equations for turbulence modeling. The model was validated by comparing the numerical results with the experimental data for a 90° junction flow, and then it was used to investigate the impact of junction angle on flow characteristics. A reasonable agreement with experimental data and analytical solutions was achieved by the model and it proved its capability in producing depth-averaged hydrodynamic characteristics of the junction flow with a wide range of junction angles.

The flow features in a confluent channel when the tributary becomes increasingly dominant were studied by Schindfessel et al. (2015). The flow patterns were investigated in a 90° confluence with a fixed concordant bed by using large-eddy simulations and three different discharge ratios. They found that the flow of the sufficiently dominant tributary affects the opposite bank and induces new features of the flow patterns such as a recirculating eddy in the upstream channel of the confluence which leads to significant changes in the incoming velocity distribution, a stronger helicoidal cells in the downstream of the channel. The flow recovery and mixing layer were also influenced by this change in the flow patterns, and a stronger upwelling flow are discerned.

The influence of different cross-sectional shapes on the separation zone in a 90° open channel confluence was studied by Schindfessel et al. (2017). Four different cross-sectional shapes were studied by using large-eddy simulation (LES) model. According to the results, there was a

significant difference in the separation zone dimensions for non-rectangular shapes, and this is because of the lateral currents that may reduce the local momentum deficit.

Large eddy simulation (LES) was applied by Ramos et al. (2019) on four open-channel confluence flows through the using of a frictionless rigid-lid to treat the free-surface. The simulation was carried out on a flat rigid-lid for three of the confluences with different elevations while the fourth simulation was conducted on a curved rigid-lid which is closer to the true free surface flow, and the experimental data of Weber et al. (2001) were used. The aim of this study was to show the differences that these two approaches produce in terms of mean flow, secondary flow, and turbulence. It was found that oversimplification of free surface numerical processing leads to lower accuracy of secondary flow and turbulent kinetic energy predictions.

3.4.1.3. ANN Models

The numerical research studies that used artificial neural network (ANN) models to simulate the flow in river confluences are discussed below.

The capacity of artificial neural network (ANN) models (which were constructed by using data derived from computational-fluid-dynamics models) was investigated by Sun et al. (2014) for modeling the velocity distributions of flows in a combined open channel. The ability of ANN models in predicting the velocities of flow was acceptable with NS indices (Nash–Sutcliffe efficiency index (Nash & Sutcliffe, 1970)) higher than 0.8.

The artificial neural network (ANN) and three-dimensional modelling were used by Zaji and Bonakdari (2015) to investigate the velocity in a 90° open channel junction. The ANN model was optimized by introducing a modified genetic algorithm (GA) and used to predict the flow velocity, and the ANSYS-CFX software (ANSYS, Inc., Canonsburg, PA, USA) was used for the three-dimensional simulation of free surface flow. The results of ANN and CFX models were compared with laboratory data, and it indicated that the performing of ANN was better than CFX in modelling velocity, and it was able to predict accurate in various areas and flowrates.

3.4.2. Secondary Flow in Differently Angled Confluent Channels with Bed Concordance

3.4.2.1. RANS Models

The numerical modeling of river confluences and secondary flows with different confluence angles are discussed in this section and is summarized in Table 3.4.

Table 3.4: Summary of selected studies about secondary flow in confluent channels used in Section 3.4.2.1

Shape of Channel	Numerical Model	Key Findings	Reference
Asymmetrical, 60° angle	Standard k–ε turbulence model	The comparison between the numerical and experimental results was good	(Weerakoon and Tamai, 1989)
Asymmetrical, 60° angle	Standard k–ε turbulence model	Experimental comparison good, but size of lateral separation zone underpredicted	(Weerakoon et al., 1991)
Different styles of channels	Turbulence model based on a renormalized group (RNG)	As asymmetry increases, the structure of back-to-back helical cells thought to be less representative of the flow field	(Bradbrook et al., 2000a)
Asymmetrical, 60° angle	Turbulence model based on a renormalized group (RNG)	As asymmetry increases, the structure of back-to-back helical cells thought to be less representative of the flow field	(Bradbrook et al., 2000a)
Asymmetrical, 30° angle	RNG k-ε model	The mixing was faster at higher junction angles, especially for concordant beds	(Biron et al., 2004)
Asymmetrical, 70° angle	k-ε, RNG k-ε, k-ω, SST k-ω, EARSM	The numerical results indicated the importance of simulating the secondary flows due to their great impact on the separation zone and velocity contour lines	(Brito et al., 2014)
Ten different confluences from 45° to 90°	k-ε turbulence closure model	The increase in the confluence angle caused a wider and longer retardation zone at the corner of upstream junction and the separation zone	(Penna et al., 2018)

A three-dimensional mathematical model with the k-ε turbulence model was used by Weerakoon and Tamai, (1989) to predict the steady state confluence flow in a 60° angle confluent channel without a recirculation zone, and levee performance was demonstrated as well in this study. This levee facilitated the two streams' mixing flows gradually, thus reducing the secondary flow and super-elevation in the mainstream. The boundary conditions were specified as follows: fully developed flow conditions for the inflow of the two channels, a zero-gradient imposed for all variables of the outflow except pressure, and the wall function was used to treat the side walls and the bottom of the channel. The TDMA (tridiagonal matrix algorithm) solver was employed in this study. There was a good agreement between the computed and the experimental results. Strong mixing was prevented by the levee, and there was a considerable reduction in the super-elevation at the junction area. The strong secondary flow was reduced as well in the mainstream by the levee. In addition, the recirculation zone was eliminated, and accordingly the effective channel width was increased (Weerakoon and Tamai, 1989).

Weerakoon et al. (1991) investigated the flow structure in a 60° angle confluent channel experimentally and computationally. The k–ε turbulence model was employed based on the finite volume approach. The same boundary conditions as in Weerakoon and Tamai (1989) were employed as well as the TDMA solver, except for the pressure correction, where the MSI (modified strongly implicit) solver by Schneider and Zedan (1981) was applied. There was a reasonable agreement between the predictions and the experimental results. The flow features that were reported in the study were as follows: two secondary flows appeared at the confluence rotating against each other because of the streamline curvature, and secondary flow caused higher velocities to appear near the bed of the channel. Accordingly, this study demonstrated the capability of fully three-dimensional numerical models to effectively reproduce the patterns of secondary rotation associated with planform curvature (Weerakoon et al., 1991).

The Kaskaskia River and Copper Slough (Figure 3.7) as a field confluence as well as a rectangular laboratory confluent channel were used by Bradbrook et al. (2000a) to study the structure of flow at this type of channel.

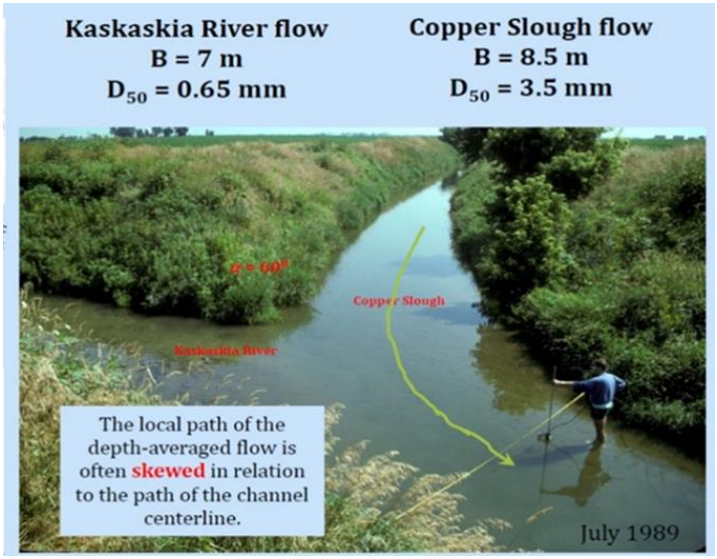

Figure 3.7: Kaskaskia River - Copper Slough confluence (Gökçen, 2015)

A three-dimensional numerical model with a fully elliptic solution, free surface treatment, and a turbulence model based on a renormalized group (RNG) was used in this study, and the free surface boundary condition was adopted for the water surface. First, different styles of laboratory channels (Figure 8) were used to apply the model, and then the model was applied at the Kaskaskia River

and Copper Slough, which is an asymmetrical confluent channel in a 60° angle and includes a scour hole. The results of the numerical model's prediction of the laboratory channels (Figure 3.8) showed that there was a circulation of two secondary flows rotating against each other in the case of symmetrical confluence, while in the case of asymmetrical confluence there was only one single cell on the side of the curved tributary. The pressure at the center of the main channel in the symmetrical confluence increased due to the convergence of the two flows and decreased at the banks due to the flow separation. Although the flow at the bed was slower than that at the surface, it was affected more quickly by the pressure gradient causing a convergent flow near the channel surface and a divergent flow near the channel bed associated with twin cells. In the asymmetrical confluence, as there was only one curvature at the side of inclined tributary, there was no divergent bed flow because the pressure gradient along the channel width was in the same direction, and this resulted in the formation of only a single cell. The deflection of the flow in the straight channel of the asymmetrical confluence was affected by the width ratio, and the flow deflection increased as the width ratio decreased, causing a flow curvature in the opposite direction to that formed by the inclined tributary.

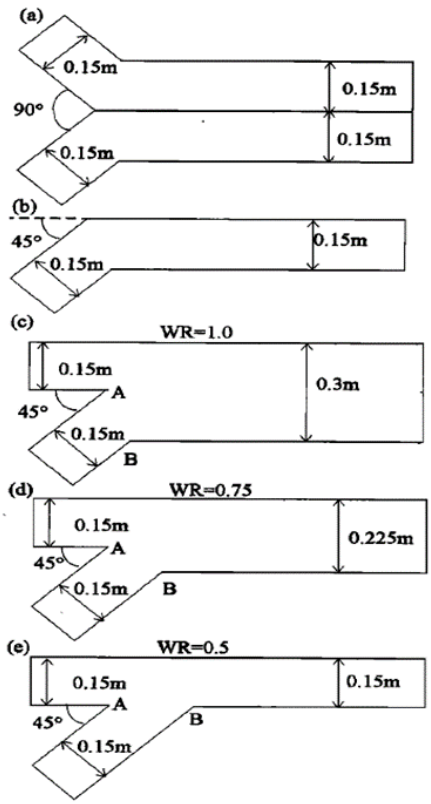

Figure 3.8: Geometry of the five laboratory simulations:
(a) symmetrical confluence
(b) single-meander bend
(c) asymmetrical confluence with width ratio (WR) of combined upstream width of tributaries to width of post-confluence channel of 1.0
(d) asymmetrical confluence with WR = 0.75
(e) asymmetrical confluence with WR = 0.5, where "A" indicates the upstream junction corner and "B" indicates the downstream junction corner (Bradbrook et al., 2000a)

For the Kaskaskia River and Copper Slough, the flow patterns that were predicted by the numerical model were qualitatively similar to the measured data; however, the quantitative terms of the predictions included some differences. The patterns of the secondary flow along the confluence were more asymmetrical, and the weak pattern of counterrotation downstream of the confluence was replaced thereafter by a single clockwise rotation. As the tributary flow entered the main channel, the tributary streamlines curved strongly in the anticlockwise direction. The flow of the main channel was deflected by the tributary flow, and the streamlines of the main channel curved in the clockwise direction. Then, the deflection caused an inflection in the direction of curvature, and both of the channels' streamlines curved in the same direction. Accordingly, an adjustment between the pressure gradients and the redistribution of mass and momentum that resulted from the streamline curvature had a significant impact on the flow structures formed. The numerical modeling of the field and laboratory confluence found that as the asymmetry increased, the structure of the back-to-back helical cells was thought to be less representative of the flow field (Bradbrook et al., 2000a).

A three-dimensional numerical model PHOENICS, version 3.4 (CHAM, Inc., London) (more details can be found in Bradbrook et al., 1998, 2001) was used by Biron et al. (2004) to study the flows in channel confluences. Two types of confluence were used: a laboratory confluence (Bradbrook et al., 2001) and a field confluence (Lane et al., 1999). The three-dimensional form of Reynolds-averaged Navier–Stokes equations for a steady-state flow was solved by the model. The RNG k–ε turbulence model was applied because it was considered to be better for cases of flow separation (Yakhot et al., 1992; Bradbrook et al., 2000b). For the cells close to the bed, the nonequilibrium log-law wall function was used (see Bradbrook et al., 1998). There was a lateral tilt at the water surface of the asymmetrical river junction which was comparable to that in a meander (Bradbrook et al., 2000a; Weber et al., 2001; Biron et al., 2002). In this case, PHOENICS was used to examine mixing in a laboratory confluence with a concordant bed. The laboratory experiment from Biron et al. (1996a, b) was used, and it included a junction angle of 30°, as shown in Figure 3.9. The 3D secondary flow significantly affected the transverse mixing in the channel confluences (Boxall et al., 2003). The mixing interface occurred at the middle of the channel and was vertical immediately downstream of the branch channel's entrance. The mixing interface expansion was comparatively low as the flow moved downstream. Standard deviation was used to estimate the mixing rate. The value of standard deviation was decreased by 10% within a distance five times

that the channel width for concordant beds. The main channel velocity in those simulations was lower than that of the tributary. The impact of the flow rate ratio on the mixing rate was tested by using two other simulations, the first one with more flow rate ratio and the second one with less. The results showed that there was no significant impact on the general trend described above due to major changes of the flow rate. In order to investigate the impact of junction angle on mixing rate, two different angles were used, a 60° angle and a 90° angle, and it was shown that the mixing was faster at higher junction angles, especially for concordant beds. The simulations of the extended channel showed that as the downstream distances increased, the mixing got slower; however, the mixing process in the discordant bed case was much faster (Biron et al., 2004).

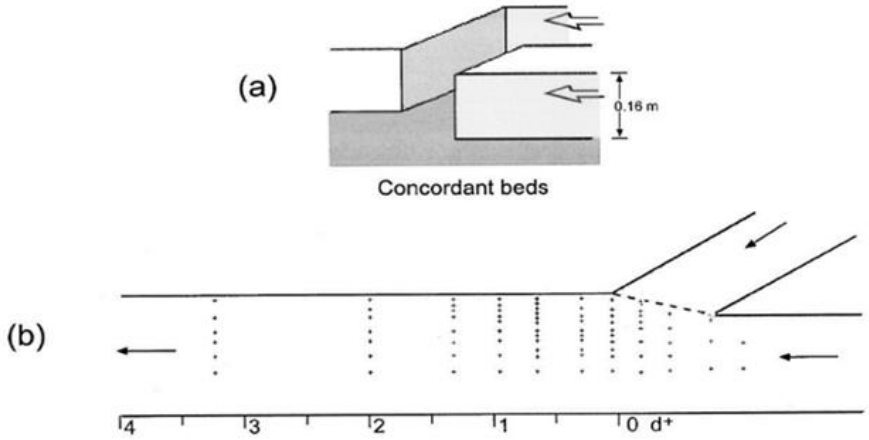

Figure 3.9: Laboratory experiment by Biron et al. (1996a, b) : (a) oblique view of junction; (b) planview showing measuring points (Biron et al., 2004)

The flow in a 70° open-channel confluence was studied experimentally and numerically by Brito et al. (2014) through the use of a 3D numerical simulation. The simulation was performed by using Reynolds-averaged Navier–Stokes (RANS) equations and five turbulence closure models (k-ε, RNG k-ε, k-ω, SST k-ω, and EARSM). The interaction of the air and water at the free surface was simulated by the volume of fluid (VOF) method. In the boundary conditions of the turbulence models, wall functions were used near the bed of the channel. The side walls were set as a non-slip boundary condition. The experimental information included that the velocity field and flow depth were used to describe the inlet of the main and tributary channel. The outlet was set as hydrostatic pressure with zero velocity derivatives. The top of the channel was prescribed as air with an open channel condition. The four turbulence models (k-ε, RNG k-ε, k-ω, and SST k-ω) showed high

discrepancies between the experiments and the simulations, while the EARSM model showed a good agreement between the simulation predictions and the measured data for the separation zone (Figure 3.10). However, for the zone of maximum velocity, the time-averaged streamwise velocity was underestimated by the EARSM model, and this could be due to free surface deformations, which were not easy to reproduce by the simulations. The numerical results indicated the importance of simulating the secondary flows due to their great impact on the separation zone and velocity contour lines, and as these areas are characterized by high turbulence intensities and shear stresses (Brito et al., 2014).

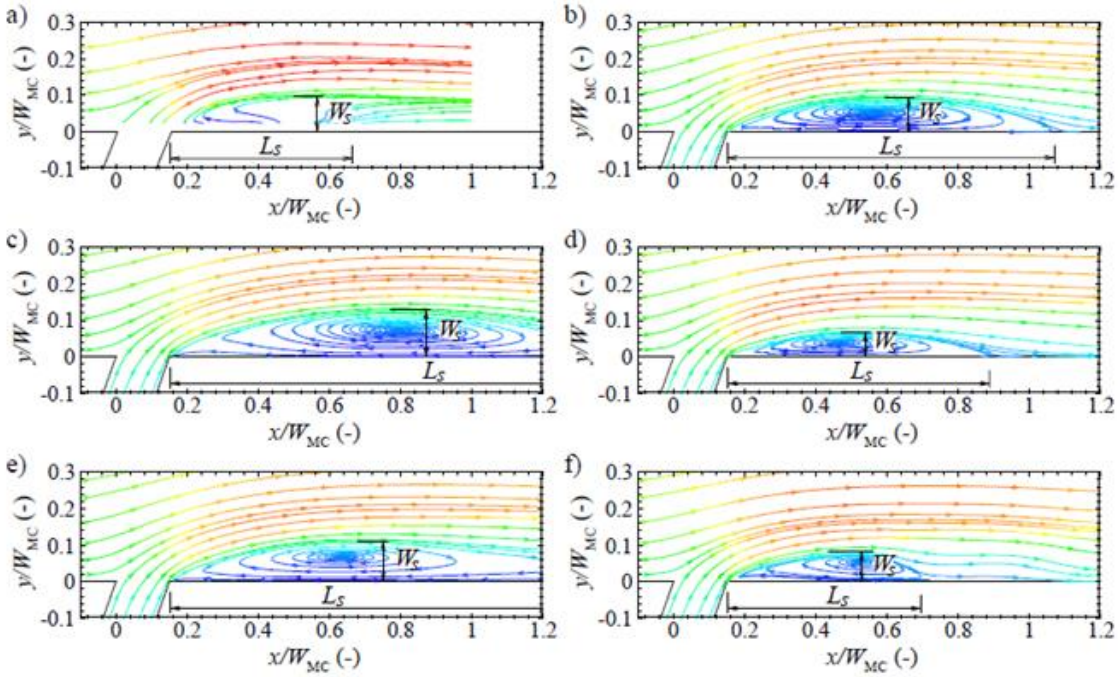

Figure 3.10: Geometry of separation zone: (a) experimental; (b) k-ε; (c) RNG k-ε; (d) k-ω; (e) SST k-ω; (f) EARSM. (Brito et al., 2014)

The impacts of confluence angle on the flow structure were studied by Penna et al. (2018) through the simulation of ten different confluences from 45° to 90°. The 3D Reynolds averaged Navier–Stokes (RANS) equations were solved using a numerical code with a k-ε turbulence closure model. The results indicated that the increase in the confluence angle caused a wider and longer retardation zone at the corner of upstream junction and the separation zone. The deflection of flow increases as well at the entrance of the tributary to the main channel due to the increase in the angle of confluence. However, the higher streamwise velocity does not necessarily increase with the confluence angle.

3.4.2.2. DES Models

The impacts of density differences between incoming flows were investigated by Horna-Munoz et al. (2020) at a small-size, concordant bed natural river confluence. A detached eddy simulation (DES) model was used to perform the simulation. The predicted flow patterns for both the weak (Froude number Fr = 4.9) and strong (Fr = 1.6) density impacts cases showed that secondary flow improves as the distance from the confluence peak increases.

3.4.3. Secondary Flow in Confluent Channel with Bed Discordance

Several types of junctions including concordant and discordant forms were discussed by Kennedy (1984) who provided the first substantial review of confluence morphology. The bed elevations of the tributary and the main river at the concordant confluence are approximately the same, or the two rivers are connected by relatively mild bed slopes. The tributary bed level at the discordant confluence is perched above the bed of the main river, and the two rivers are connected by a relatively steep slope (Sukhodolov et al., 2017). Bed discordance plays an important role in enhancing the turbulence and secondary flows that affect the morphology of confluent regions. Bed discordance in different types of confluent channels is discussed in this section which divided according to the type of the used models.

3.4.3.1. RANS Models

The RANS numerical models of river confluences with bed discordance and secondary flows are summarized in Table 3.5.

Table 3.5: Summary of selected studies used in Section 3.4.3.1 about secondary flow in confluent channels

Shape of Channel	Numerical Model	Key Findings	Reference
Asymmetrical, 30° angle	RNG k-ε model	The efficiency of secondary flows in the bend was less for mixing at the low flow than for the high flow.	(Biron et al., 2004)
Asymmetrical, 60° angle	RNG k-ε model	The efficiency of secondary flows in the bend was less for mixing at the low flow than for the high flow.	(Biron et al., 2004)
Symmetrical, ⅄ shaped	Linear Renormalization Group (RNG) k-ε turbulence model	The results appeared to be an accurate prediction by the numerical model.	(Wang & Yan, 2007)
Asymmetrical, ⊥ shaped	Standard k–ε turbulence model	The perpendicular velocities were enhanced by the tributary bed steps along the side wall of the intersection and by the main channel bed steps along the opposite wall.	(Dordevica and Stojnic, 2016)

As mentioned before, Biron et al. (2004) studied the flow in channel confluences in two cases, a laboratory confluence (Bradbrook et al., 2001) and a field confluence (Lane et al., 1999). In this case, PHOENICS (CHAM, Inc., London) was used to examine mixing in the same laboratory confluence as in Figure 3.7 but with discordant beds (Figure 3.11), and in a natural discordant stream confluence (Figure 3.12). For the laboratory confluence with discordant beds, the mixing was impacted by the bed discordance, while the mixing was significantly enhanced by the distortion of the mixing layer towards the shallower tributary. The expansion of the mixing interface for discordant beds was more rapid than for the concordant beds. The value of standard deviation decreased by 30% within a distance five times the channel width for discordant beds, while for the natural discordant stream confluence, i.e., the confluence of the Bayonne and Berthier Rivers, there was a 60° junction angle and bed discordance between the two tributaries (Figure 3.12). The simulation was conducted for two contrasting flow conditions: low flow and high flow. For the low flow condition, comparison between the numerical simulation and the field data showed a good agreement regarding the downstream and lateral velocities. For both the low flow condition and high flow condition, the decreases in the patterns of standard deviation for the natural site and the laboratory were similar; however, the impact of bed discordance on the low flow was much more significant than that on the high flow. The mixing efficiency of secondary flows in the bend was less for the low flow than for the high flow, as the values of the standard deviation for the high flow were considerably smaller (Biron et al., 2004).

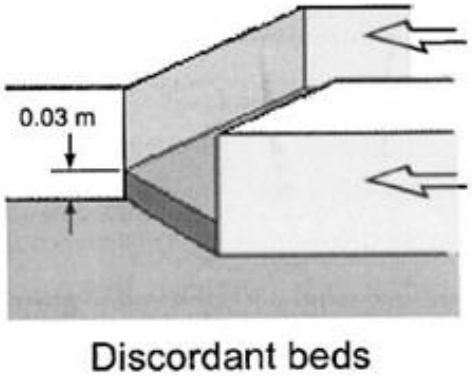

Figure 3.11: Laboratory experiment by Biron et al. (1996a, b) (Biron et al., 2004)

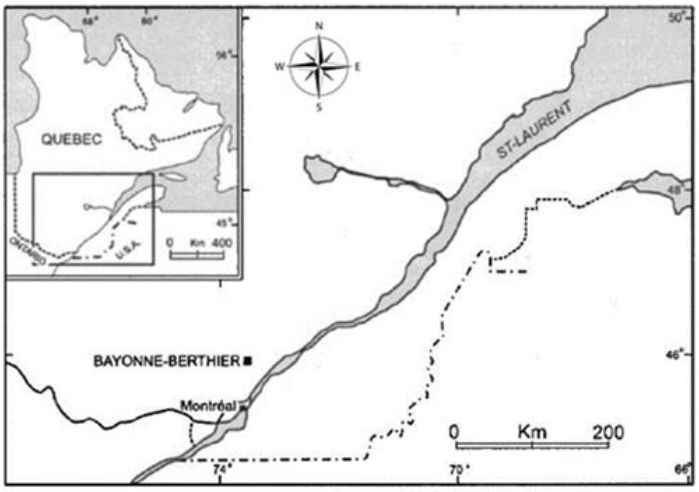

Figure 3.12: Location of confluence of Bayonne and Berthier rivers, Québec, Canada (Biron et al., 2004)

The symmetrical "Y" shaped open-channel confluence in Figure 3.13 was used by Wang and Yan (2007) to study the impacts of bed discordance on the flow patterns. A 3D numerical simulation was used to study the flow in this type of channel. The junction angle was 90° and the discordant bed height was 0.05 m. The standard time-averaged Navier–Stokes equations were used in the linear renormalization group (RNG) k-ε turbulence model. The boundary conditions of the inlet and outlet are shown in Figure 3.14 below.

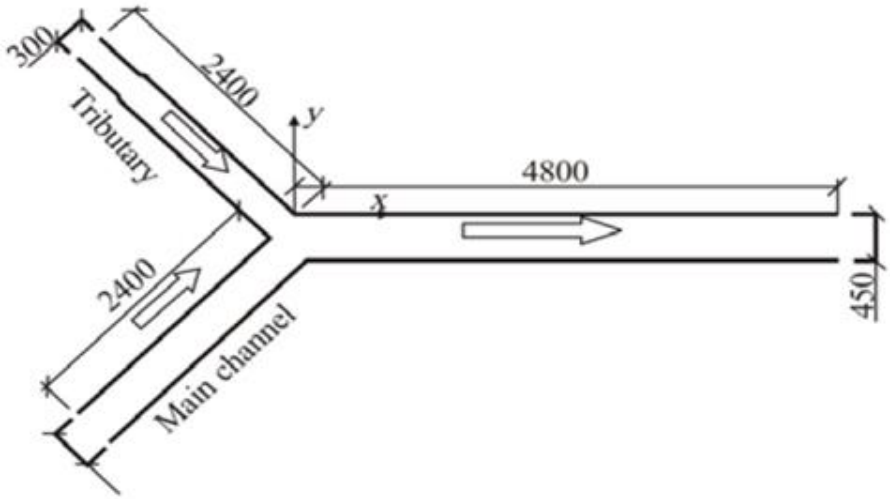

Figure 3.13: Y-shaped open junction (Wang & Yan, 2007)

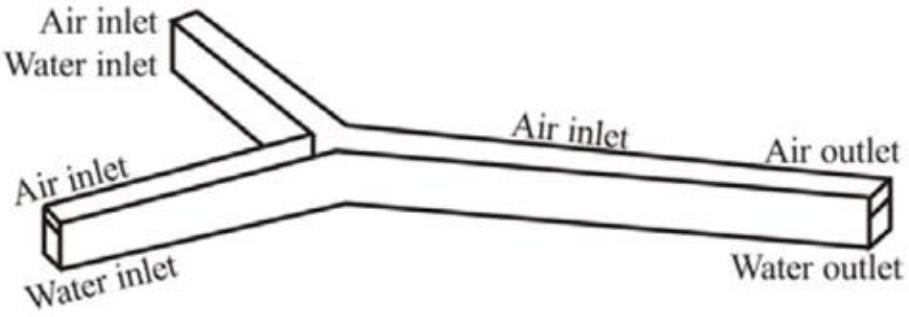

Figure 3.14: Inlet and outflow boundary conditions (Wang & Yan, 2007)

Some zones in the channel, e.g., the separation zone, maximum velocity zone, flow deflection zone and mixing layer, were focused on to examine the impacts of bed discordance. In the case of asymmetrical confluences, the separation zone usually lies on the tributary side. This is mainly because of the linear planform of the main channel. In the Y-shaped confluences, the separation zone could appear at the side of the main channel, or in the case of bed concordance, it could be observed both on the tributary and main channel sides. The main difference between the asymmetrical confluences and the Y-shaped junction is the planform of the curvature in the junction. In the Y-shaped junction, the separation zone pattern is affected by the planform curvature of the confluent channel and is also affected significantly by the discharge ratio. The separation zone in the symmetrical confluent channel with discordant beds disappears near the bed on the tributary side, and this is similar to the asymmetrical channels (Biron et al., 1996a). Two reasons behind this are explained in the following. The first reason is that the fluid momentum is low in the area near the bed, and the second one is that the secondary flow intensity is enhanced significantly by bed discordance downstream of the junction area. The lateral mixing of flow increased in the case of a confluent channel with bed discordance, and the separation zone increased accordingly close to the surface of the tributary side. The maximum velocity of the discordant bed confluence appeared near the surface of the channel towards the main channel bank, which was similar to the case of concordant bed confluence. Thereafter, a decrease in the separation zone near the water surface occurred at the main channel's side. For the discordant bed confluence, there was a transfer of the near-bed flow in the shallower tributary towards the low-pressure area formed on the tributary side after the junction. At the water surface on the tributary side in the case of discordant bed confluence, there was a zone of maximum turbulent kinetic energy, which was one of the features

of the mixing layer, and this did not appear in the case of a concordant bed confluence. The reason behind this was considered to be the height of the bed discordance, which caused an increase in the secondary flow intensity, and the presence of a separation zone close to the water surface on the tributary side. This implied that the mixing layer was deformed due to the height of the bed discordance. The numerical model was compared with the data measured for the downstream, cross-stream, and vertical velocity (u, v, and w respectively), and the results appeared to be an accurate prediction by the numerical model (Wang & Yan, 2007).

Shumate's laboratory confluence channel was used by Dordevica and Stojnic (2016) to examine the flow through the use of the SSIIM2 (NTNU, Inc., Norway) 3D finite-volume based numerical model. The confluence consisted of a junction of two straight channels at a 90-degree angle (Figure 3.15). The Reynolds-averaged Navier–Stokes equations were solved by this model on unstructured space grids. In addition, various types of two-equation turbulence models are offered by SSIIM2 to solve such problems.

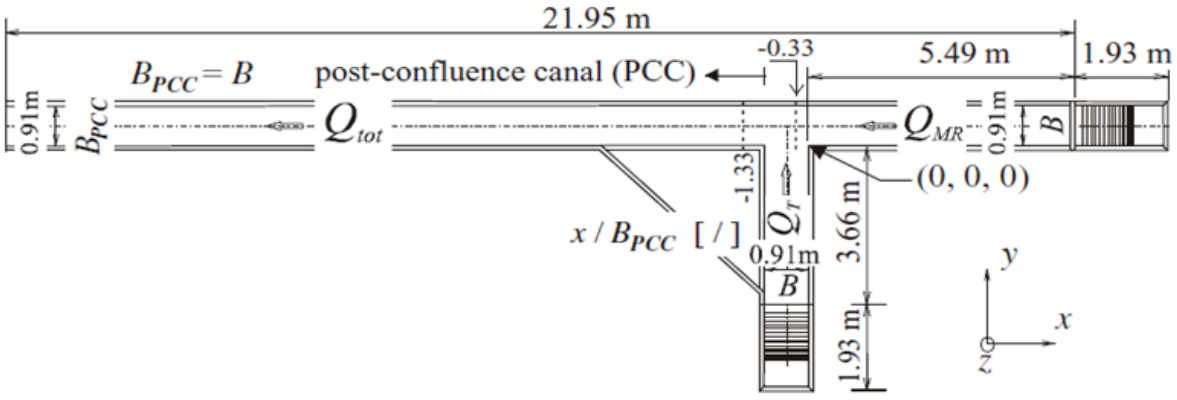

Figure 3.15: Plan view of Shumate's laboratory channel (Shumate, 1998) from (Dordevica & Stojnic, 2016)

In order to study the bed elevation discordance in both types of converging channel, nine combinations of the following bed-elevation discordance-ratio values were used: $\Delta zT/hd$ = {0.10, 0.25, 0.50}, and $\Delta zMR/hd$ = {0.10, 0.25, 0.50}, where ΔzT is the difference in bed elevation between the tributary and post-confluence channels, as shown in Figure 3.16a, ΔzMR is the difference between stretches of the main river upstream and downstream of the upstream junction corner, as shown in Figure 3.16b, and hd is the flow depth in the main river at the confluence. There were two parts in the main channel, the upstream (shallower) and downstream (deeper), as shown

in Figure 3.16c. The results are summarized in the following. In the case when the branch channel was shallower than the main channel, there was a redirection of part of the branch channel flow towards the face of the bed step in the layers under the step crest. As the difference in the bed step heights increased, the amount of redirected flow increased. In addition, at the lower part of the water column, the deflection of the perpendicular flow was reduced by the bed step. The existence of bed steps in the main channel caused an enhancement in the 3D flow of the junction and the post-confluence channel, while its existence in the tributary caused a delay in the evolution of the recirculation zone in the post-confluence channel and affected its shape as well. The perpendicular velocities were enhanced by the tributary bed steps along the side wall of the intersection and enhanced by the main channel bed steps along the opposite wall. Consequently, both sides of the river were at risk of erosion in this type of channel.

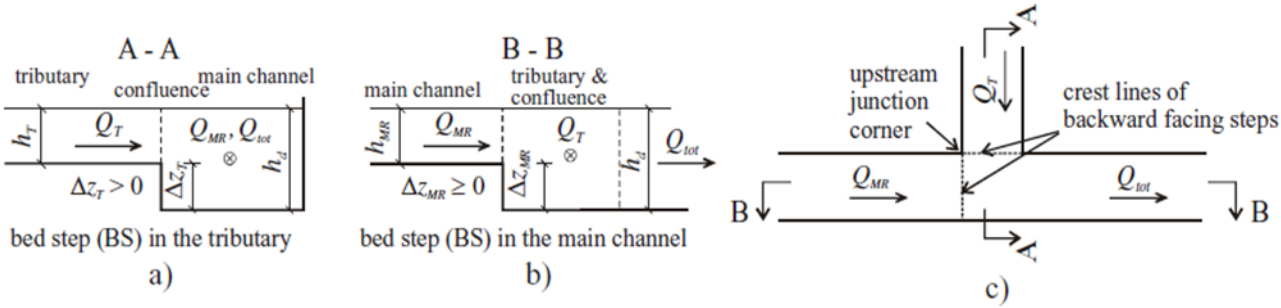

Figure 3.16: Bed elevation discordance in a) tributary; b) main channel; c) locations of backward facing steps in tributary and main channels (Dordevica and Stojnic, 2016)

3.4.3.2. LES Models

The LES models of river confluences with bed discordance and secondary flows are summarized in Table 3.6.

Table 3.6: Summary of selected studies used in Section 3.4.3.2 about secondary flow in confluent channels

Shape of Channel	Numerical Model	Key Findings	Reference
Asymmetrical, parallel channels	LES	The numerical simulation agreed well with the laboratory experiments.	(Bradbrook et al., 2000b)
Asymmetrical, 65° angle	LES	The mixing data and the detailed flow provided by the model were helpful in understanding the production and evolution of large-scale turbulence features in confluence channels.	(Bradbrook et al., 2000b)

Large Eddy Simulation was used by Bradbrook et al. (2000b) to simulate the flow and investigate the formation of flow features in river confluences. The model was applied on a parallel laboratory confluence channel with unequal depths as well as a natural river confluence with bed discordance. The two parallel tributaries in the laboratory confluence channels were divided by a splitter plate, and they joined together at the end of this splitter plate to form the post-confluence channel. The depths of the two tributaries were different, where the depth of one tributary was half of the other, and the post-confluence channel was the same depth as the deepest tributary (0.1 m). However, the width of the post-confluence channel was equal to the combined widths of the two tributaries and the splitter plate. For the boundary conditions, the standard law-of-the-wall was used at the banks and beds of the channels. The model predicted a rise in the fluid free surface from the deep channel along the shallow one, and there was a recirculation area below the step and a strong lateral pressure gradient towards this area. The simulation showed that there was instability that was inherent in the flow dynamics of this type of confluence channel. The numerical simulation agreed well with the experimental observations, which implied that the simulation was capable of capturing some of the key flow periodicities. For the natural river confluence with bed discordance, the confluence of the Bayonne and Berthier Rivers in Québec, Canada was adopted (Figure 3.17). The mixing data and the detailed flow provided by the model were helpful in understanding the production and evolution of large-scale turbulence features in confluence channels (Bradbrook et al., 2000b).

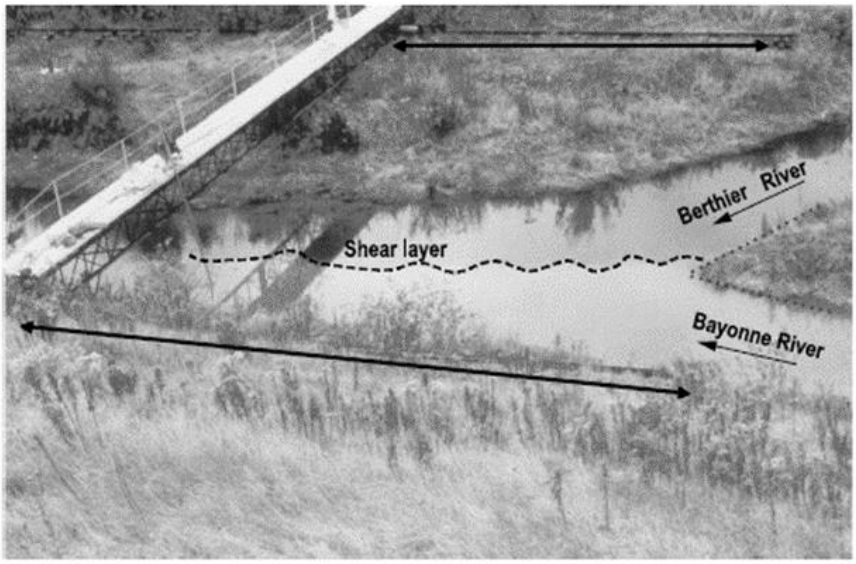

Figure 3.17: View of the junction of the Bayonne and Berthier Rivers (Boyer et al., 2006)

3.4.3.3. DES Models

A confluence in a medium-size stream and a highly discordant bed was used by Cheng and Constantinescu (2020) to investigate the impacts of stratification which induced by the differences in density between two incoming flows. Detached eddy simulation (DES) model was used in this study. The study found that flow hydrodynamics and thermal mixing is affected significantly by the stratification impacts. A two-layer structure of flow is induced in the confluence upstream due to the differences in density of the two incoming flows: one of them near the bed and the other near the free surface. These two layers mix much faster compared to the case when the two streams have the same density.

3.5. Discussion

Although the flows in river confluences are complicated, three-dimensional numerical modeling is considered a powerful tool for predicting the flow field and mixing rates. Several comparisons have been conducted between numerical simulations and field or laboratory flow velocity data to determine the adequacy of these 3D models for predicting complex flow fields (Bradbrook et al., 1998, 2001; Bradbrook et al., 2000a; Bradbrook et al., 2000b; Lane et al., 1999; Huang et al., 2002). In addition, the water surface was also well predicted, whether compared with field data (Biron et al., 2002) or laboratory data (Huang et al., 2002).

In river confluences, and as the tributary moves towards the main channel in curved streamlines, a local imbalance occurs between the centrifugal force and the transverse pressure gradient generated by the super-elevation of the water surface where the tributary and the main channel meet. This results in transverse water slopes moving towards the outer bank of the main channel and away from the tributary (Bradbrook et al., 2000a). Accordingly, secondary flows are generated. The two counterrotating helical cells of secondary flows appeared in both the symmetric and asymmetric planforms of river confluences (Rhoads and Kenworthy, 1995,1998; Rhoads, 1996).

The main difference between the symmetric and asymmetric channels is the merging degree of the angle between the tributary and the main channel. In the case of a symmetric channel, two tributaries join to form a new channel or the main channel in one downstream flow direction, while in the case of an asymmetric channel, one tributary enters directly to the main channel. The planform of the confluent channel plays an important role in the secondary flow's strength; according to Mosley (1976), the turbulence was enhanced with large confluence angle degrees. Bradbrook et al. (2001) found from their numerical modeling results that the secondary flow circulation in a 30-degree confluence angle was much stronger than in a 0-degree confluence angle. The hydrodynamic and morphodynamic characteristics of river confluences are affected significantly by the symmetric or asymmetric planforms (Riley et al., 2015). Referring to the suggestion by Parsons et al. (2008), the middle bar of the channel is developed in the case of a symmetric confluence, while in the case of an asymmetric confluence, erosion happens on the bank opposite the tributary and deposition happens at the downstream corner of the tributary (Mosley, 1976).

There are some other factors that could be considered in the evaluation of symmetric or asymmetric junctions, like the velocity ratio, discharge ratio, momentum ratio, and others. The meaning of "ratio" here refers to a particular value of the tributary divided by the relevant value of the main channel (Bilal et al., 2020). The impact of velocity ratio on the flow field depends considerably on the planform of the confluence. It could be large for a degree of confluence greater than 30 (Bradbrook et al., 2001), and it could be small in parallel confluences (Bradbrook et al., 1998). The location of secondary flows and their strength depend largely on the discharge ratio (Bradbrook et al., 1998). The mixing layer position (Rhoads and Kenworthy, 1995), higher turbulence, and shear stress (Constantinescu et al., 2012) depend on this ratio as well. The migration of flow structures in confluent rivers could be promoted by the discharge ratio (Bilal et al., 2020). The momentum ratio should also be considered during the evaluation of the formation, duration, and strength of

secondary flows (Constantinescu et al., 2001). The mixing interface is pushed by the high momentum ratio towards the right bank (Rhoads and Kenworthy, 1995), especially when the flow is low. At the same time, the mixing interface moves nearer the center with a low momentum ratio. The flow field of a river confluence is also significantly affected by bed discordance. There is a big variance between concordant and discordant confluences, where the deformation of the shear layer is more important than the presence of helical cells (Bilal et al., 2020). In addition to the flow regime, the sediment motion and morphology of the confluence are also impacted by the bed discordance, and it should be taken into consideration that the impact of bed discordance differs with the various stages of the river (De Serres et al., 1999).

Most of the existing studies on the numerical modeling of secondary flow in river confluences that considered turbulence models, advection schemes, and water surface capturing schemes were compared to experimental-scale studies. Experimental-scale studies were adopted instead of prototype cases because studies with well controlled conditions can better reveal the underlying mechanisms and provide basis for modeling prototype cases. Turbulence models, advection schemes, and water surface capturing schemes are typically less concerned in the current practice of river modeling compared to other factors, such as boundary conditions, physical processes, and roughness field. However, it is important to investigate these techniques to further improve the practice of modeling river flows. To accurately simulate river confluence flows, three factors should be considered with cautions: (1) the turbulence models, (2) the discretization schemes, and (3) the water surface predictions techniques. As for turbulence modeling, the present paper reviewed the most widely used turbulence modeling techniques, such as RANS and LES. Generally, advanced techniques, such as LES, can provide better predictions; however, RANS models are typically more efficient and can provide a better balance between accuracy and efficiency. Therefore, the optimal selection of turbulence models depends on the requirements of the specific applications. As for the discretization schemes, few studies have been conducted to investigate the influence of discretization schemes on river confluence flows, partially because the influence is theoretically minor compared to other factors if the grid resolution is sufficiently high and the computational time step is sufficiently small. Theoretically, higher-order schemes perform better in terms of accuracy than lower-order schemes, and best balance could be figured out via a trial-and-error manner. The present paper also reviewed water surface prediction techniques. Overall, the VOF method is currently the most popular techniques, but some other surface-tracking or surface-

capturing may also be preferable for some applications; for example, the rigid lid approach is acceptable if the super-elevation can be neglected.

Generally, for applications that requires very high level of accuracy, some advanced turbulence modeling techniques, such as LES and DNS, should be employed, but for most applications, RANS models should be sufficiently satisfactory. Similarly, advanced numerical schemes (such as the skew-linear discretization approach) should be used if the desired accuracy is high. However, for most applications, where the modeling efficiency is also very important, some simpler numerical schemes (such as the linear upwind discretization approach) should be selected. There is still some room to improve the turbulence models and numerical schemes. For example, some anisotropic information could be added into the isotropic turbulence models to improve its performance without substantially increasing the computational costs.

3.6. Future Research Needs

There is a lot of variation between symmetric and asymmetric confluences, and each of them needs further study and assessment of the flow dynamics in the future, including numerical modeling or laboratory experiments that include different discharge ratios, mobile beds, and different discordant bed heights (Wang and Yan, 2007).

The flow patterns in river confluences also need more analysis, taking in consideration the turbulent kinetic energy, bed shear stress, and free surface deformation (Brito et al., 2014).

Turbulence modeling is one of the greatest uncertainty factors in numerical modeling, and thus it has been discussed in detail in this paper. The RANS models had some weaknesses in predicting the strength of the secondary flow. Future studies should be conducted to improve the practice of turbulence modeling using RANS models. For example, some equations can be modified to implicitly consider some anisotropy information (Yan et al., 2020). Some other turbulence modeling techniques, such as LES and DNS (direct numerical simulations), which are more advanced, can further improve the modeling accuracy. Nowadays, due to the heavy computational costs, it is less practical to apply these turbulence modeling techniques to modeling secondary flow in river confluences. However, it is still meaningful to assess the applicability of these techniques since they may become feasible in the future because of the advances in computing techniques. To better assess the superiority of different turbulence models, it is necessary to compare the turbulence quantities such as Reynolds stresses together with mean flows at representative locations. However,

these comparisons are still lack in the current literature, and thus further investigations and detailed comparisons are needed for future studies.

The accuracy of discretization of advection terms has a significant impact on the results, and thus it should be used with caution. For example, it is better to adopt a high-resolution scheme for flows at high Reynolds numbers. However, very few previous studies considered this, which may have introduced a significant discretization error in the numerical results. Therefore, it is better for future studies to present the studies of discretization error and grid sensitivity.

In order to better understand the morphodynamics of river confluences, more consideration is required to the changes on the total discharge, river-runoff, and the flows in river confluences with bed discordance, since these factors have a major influence on the morphological dynamics of a river (Bilal et al., 2020).

Sediment transport plays an important role in the morphodynamics of river confluences due to the sediment influxes that come from the tributary into the main river. In addition to the morphology of a confluence, the main river may undergo many changes in its properties as a result of sediment transport, such as rerouting or changes in the slope of the main river (Ferguson and Hoey, 2008). According to some studies, turbulence also has an influential role in the transport of sediment (De Serres et al., 1999; Biron et al., 1996b). The theories and assumptions for the flow field, bed shear stress, etc., in addition to examining the dynamics of sediment transport, could help in the understanding of sediment mechanics (Biron et al., 1993). Although studies have been done in this field, more numerical modeling could also be used to predict the sediment transport in confluences, which may help in better understanding of the mechanisms in this process. Different modeling can be used for various types of confluences.

The implementation of this type of studies (sediment transport, changes of total discharge) in numerical flow simulations should be considered, or at least of the implementation challenges should be included.

Although studies have been done at this field such as (Tang et al., 2018), contaminant transport and pollutant dispersion should be taken into further consideration during the investigation of river confluences through numerical modeling. Some experimental and field studies have found that the pollutants most likely concentrate close to the intersection of the two rivers and are thereafter compressed and diffused in the main river (Liu et al., 2019). Various types of numerical modeling could help in predicting pollutant dispersion and how to treat it. The investigations of secondary

flows in confluences are the basis of investigating the mixing in confluences, but the mixing processes include contaminant transport and dispersion, which is out of the scope of this review, and thus the mixing in confluences could be reviewed in future studies.

3.7. Conclusions

Generally, it appears that 3D CFD models are both beneficial and affordable in getting specific information about flow fields and are especially helpful in perceiving and understanding changes in the flow features that are caused by changes in significant flow parameters (Huang et al., 2002). The concentration ranges that may happen at various points of the flow in river confluences could be predicted reasonably by large eddy simulations (Bradbrook et al., 2000b).

The size of the separation zone increases with increases in the junction angle. As well, there was a depression in the surface elevation of the separation zone, and this depression increased with increases in of the junction angle. In addition, the strength of the secondary flow increased with increases in of the junction angle (Huang et al., 2002).

Mixing processes near the junction are considerably enhanced by bed discordance. Although the flow was impacted by the bed discordance, this impact in a low flow was more important than in a high flow (Biron et al., 2004).

The accuracy of simulation results is affected significantly by the surface treatment method, even for the same turbulence model. If the free surface is treated as an assumed surface by the rigid lid method, it generates a large error when there is a big difference in the actual free surface. The accuracy of the VOF method is better than that of the rigid lid method, as it captures the free surface by a multi-phase method. However, the accuracy of the VOF method is still poor in the case of shallow water flows (Yang et al., 2013).

There is a difference between the flow fields in symmetrical confluences (Y-shaped) and asymmetrical confluences. Bed discordance has great impacts on asymmetrical confluences, which include: the appearance of a separation zone near the water surface on the tributary side and its disappearance near the bed; a decrease in the separation zone near the water surface of the main channel side; and higher velocity near the water surface and towards the main channel side. The mixing layer is distorted by the bed discordance, and the secondary current intensity is increased on the tributary side (Wang and Yan, 2007).

The discharge ratio, bed discordance, and angle of confluence have a big impact on control of the secondary flows and separation zone, and accordingly, many tests have been conducted to study these factors (Yang et al., 2011).

The angle of confluence, Froude number, and discharge and width ratios could have a great impact on the river confluence features, such as increases in in the confluence angle and Froude number with a decrease in discharge, and width ratios causing stronger helical cells, larger separation zones, and narrower contraction zones with higher velocity (Shakibaeinia et al., 2010).

The flow of water in different directions in river confluences, or in other words, variances in the direction of the flow and instabilities in the mixing layer, might be the main reason for the load transport, sediment reworking, and accordingly erosion and deposition at confluences (Bradbrook et al., 2000b).

Increased angles of confluence and discharge and velocity ratios, and the appearance of bed discordance play an important role in enhancing turbulence and secondary flows, which in turn impact the morphology of confluent regions (Bilal et al., 2020).

Chapter 4. A comparison of standard k–ε and realizable k–ε turbulence models in curved and confluent channels

Abstract

Bends and confluences are often observed in rivers, and one of the phenomena that characterize flows in open channel bends and confluences is secondary current. Instead of moving somewhat parallel to the channel axis, the movement of the fluid particles in curved and confluent channels take a spiral path. In this paper, a 3D OpenFOAM numerical model is employed to simulate the effect of secondary currents on water velocity in channel bends and confluences. The behavior of these currents is simulated by using the finite volume method (FVM). The experimental data of a sharply curved channel and a confluent channel were used to compare the numerical results and to evaluate the validity of the model. To assess the performance of different models in predicting the behavior of these secondary flows, two turbulence models (i.e., standard k–ε and realizable k–ε) were applied in the current study, and the accuracy of the standard and realizable k–ε turbulence models was evaluated and discussed. The results of this study showed the better performance of the standard k–ε model in curved channels and the realizable k–ε model in confluent channels.

Keywords: Secondary flow · Rigid-lid model · Standard k–ε · Realizable k–ε · OpenFOAM

---

[4] This chapter has been published as Rawaa Shaheed, Abdolmajid Mohammadian, and Hossein Kheirkhah Gildeh (2018) A comparison of standard k–ε and realizable k–ε turbulence models in curved and confluent channels. Environmental Fluid Mechanics, 19:543-568. https://doi.org/10.1007/s10652-018-9637-1.

4.1. Introduction

Rivers are one of the most significant water resources in our natural environment and play a main role in providing drinking water to living organisms. Most rivers are subject to change, and they evolve over time due to erosion and migration factors. According to these ever-changing conditions, they tend to also change their morphology to keep in equilibrium, and bends and confluences are phenomena that result from this kind of change (Cameron and Bauer, 2014). The complexity of the flow at these regions of rivers can be due to several factors, such as turbulence and 3D nature of the flows, bed topography and depth variations, which are generally a result of erosion, sediment transport, and sedimentation processes. The flow is affected by centrifugal force once it enters the bend, as explained in the following, and due to variations in velocity, this force can be variable based on the radius of the bend and the depth direction. Centrifugal force is one of the factors responsible for secondary current, which is one of the most dominant features of the flow in curved open channels (Blankaert and De Vriend, 2004). According to Thorne et al. (1985), secondary currents are defined as "currents that occur in a plane normal to the axis of primary flow". The imbalance between the force caused by the transverse water surface gradient and the centrifugal force over the depth leads to the secondary flow, as shown in Figure 4.1 (Lien et al., 1999). In light of Rozovskii's (1961) and De Vriend's (1980) measurements, the secondary flow moves in a helical path towards the outer wall near the water surface and toward the inner wall near the bed.

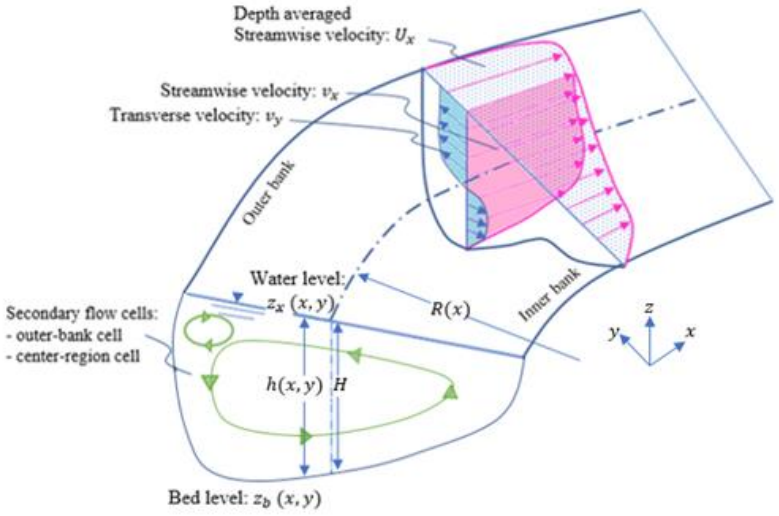

Figure 4.1: Sketch of flow in channel bend (based on (Blanckaert (2011))

There are two types of secondary current. The first type is curvature-induced, which occurs in laminar and turbulent flows (Talebpour and Liu, 2018), and the second type is generated by turbulence and according to some researchers occurs, e.g., in straight and non-circular channels (Bradshaw, 1987; Colombini, 1993; Einstein and Li, 1958). The focus of this paper is on the first type of secondary current, which occurs in river bends and confluences. Numerical methods, as compared with analytical and experimental approaches, can be considered more applicable. The reasons for this include various physical interactions, the impossibility of considering all conditions in experimental methods, the high costs of experimental equipment, and the limitations of measurement techniques (Tajnesaie et al., 2018).

Several numerical studies have been performed regarding bend context. The standard k-ε turbulence model was by Leschziner and Rodi (1979) to analyze the flow in a strongly curved channel with a turbulent condition and three-dimensional state. They found that the model was successful in predicting that the maximum velocity moves towards the outer bank near the bend exit. An experimental and numerical analysis was carried out for meandering rivers by Shams et al. (2002), who studied a river model followed by analyzing a scaled physical model of a meandering river. Then, they used the Reynolds stress transport model of the Fluent code in the simulations to evaluate the mean-flow properties, turbulence intensities, and sedimentation patterns for both the laboratory model and the actual river. Their findings indicated that there was a similarity in the mean-flow quantities; however, there was a difference between the turbulence parameters obtained from measurements of the physical river and the numerical results. In another study by Blanckaert and Graf, (2004), a laboratory bend flume was used to study the velocity distribution, boundary shear stress and bed topography in bends. They showed through their study that the analysis of experimental data could be complemented and confirmed by the analysis of numerical modelling results. They coupled the proposed model to depth-integrated flow simulation tools to obtain a quasi-three-dimensional flow model which provides an engineering tool for numerical investigations of river problems. The flow pattern in a curve of 90 degrees was studied by Naji et al. (2010) both experimentally and numerically, and they used the numerical model SSIIM-1.1 in their study. Turbulence was simulated by using the k–ε model. According to their conclusion, the SSIIM-1.1 model is able to simulate accurately the flow pattern in a 90° bend. Both Reynolds–Averaged Navier–Stokes equations (RANS) and Large Eddy Simulation (LES) were used by Stoesser et al. (2010) to compute the turbulent flow in curved channels, and both models agreed

well with respect to wall shear stress calculation. The accuracy of 2D and 3D numerical models for secondary currents was studied by Riesterer et al. (2016) in a curved laboratory channel section by using the open-source Telemac–Sisyphe program package, and they found that the secondary flow observed in the laboratory was described better by the 3D model. In summary, although various studies have been performed for the numerical simulation of bends, there is still a need to examine the performance of efficient and accurate turbulence models such as the realizable k-ε model for flows in bends, because complicated models are still impractical for engineering design applications.

The other prevalent case observed in many rivers is confluence. Confluence in rivers results from the junction of two separate river flows. A complex hydro- and morphodynamic environment is produced in the region of convergence. The main river receives the water flow and sediment that comes from the tributary and must assimilate it. Several items are affected by this assimilation, such as fluid motion, sediment transport, and channel morphology, which occur at river confluences (Riley, 2013). When the flow of the branch channel enters the main channel, the direction of the flow changes immediately, causing a surface radial flow to be induced by the centrifugal force, and opposite to the deflection and a bottom inward current. A schematic view of the flow in this case is shown in Figure 4.2.

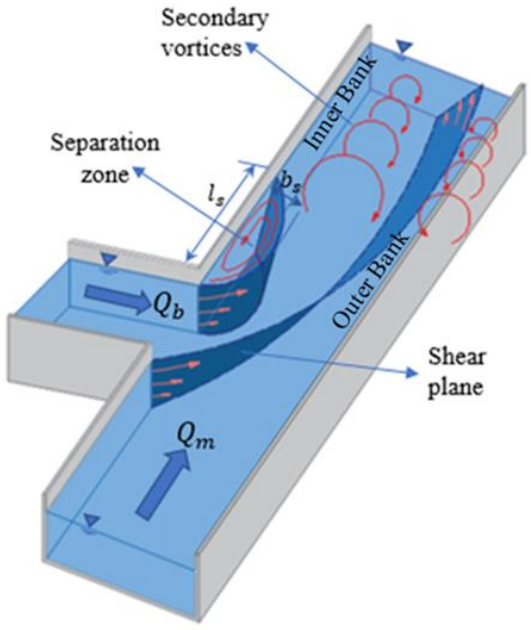

Figure 4.2: The structure of secondary flow in confluent channel (based on Weber et al. with permission from ASCE)

Due to the complex hydrodynamic that occurs in river junctions (as shown in Figure 2), analysis of flows in this region is considered to be a difficult task. One of the features that affects the flow pattern in river confluences is the separation zone generated by the pressure gradient forces as the flow of the tributary enters the main river. The structure of the flow and mixing patterns in river confluences has also been studied extensively. Natural confluences were adopted to conduct some of these studies, such as in Rhoads and Kenworthy (1995) and De Serres et al. (1999). Other studies have been carried out in either a laboratory fixed bed confluence, such as Weber et al. (201), or in a laboratory mobile-bed confluence like the experiment conducted by Ribeiro et al. (2012). Numerical studies have also been conducted on confluent channels, including studies by Lane et al. (1999) and Bradbrook et al. (2000; 2001). There is a resemblance in the flow structure between river confluences and river bends, according to Rhoads and Kenworthy (1995). This resemblance is mainly due to the presence of helical cells downstream of the confluence, which are produced by the curvature in the flow deviation area. Confluences can be asymmetrical (as in the case studied in this paper) or symmetrical (Y-shaped) according to the planform geometry. Asymmetrical cases occur when tributaries join the main channel laterally (Ludeña, 2015), while symmetrical ones occur when two channels join and form a new channel downstream (Mosley, 1976). The helical cells of asymmetrical confluences are more developed (Rhoads and Kenworthy, 1995; Rhoads and Sukhodolov, 2001) than those of symmetrical confluences (Rhoads and Sukhodolov, 2001). The reason is that the curvature of the tributary inflow is greater in asymmetrical confluences than in symmetrical ones. The numerical simulation of river confluences has been examined by using 2D and 3D approaches in different studies (Ludeña, 2015). A three-dimensional model based upon the full three-dimensional form of the Navier–Stokes equations as well as two-dimensional equations for the depth-averaged form of Navier–Stokes equations was studied by Lane et al. (1999) and a comparison was made between these models' predictions and high-quality field data. Given the good agreement obtained from comparisons between the numerical results and field measurements, they recommended the use of 3D models in the simulation of confluence hydrodynamics principally if the 2D numerical model does not incorporate any arrangements for the influence of the secondary current on the flow structure. A 3D numerical model was developed by Huang et al. (2002) through a k–ω turbulence closure to investigate the flow at open-channel junctions, and the influence of junction angle on the elevation of the water surface and the strength of secondary currents was investigated as well.

Despite all the experimental and mathematical studies that have been carried out to study the flow characteristics in curved open channels and confluences, understanding the dynamics of meanders is still incomplete, particularly regarding how variations in channel characteristics control the flow dynamics. The numerical simulation of secondary currents is usually done based on the Reynolds-averaged Navier–Stokes (RANS) models due to their computational efficiency (Tajnesaie et al., 2018). Indeed, because direct numerical simulation (DNS) methods are extremely computationally expensive, it is almost impossible to use them for simulations of a secondary current cell (Talebpour, 2016). Furthermore, despite the accuracy of the Large Eddy Simulation (LES) for turbulent secondary currents, LES methods are still less practical for engineering applications. Compared to LES, Reynolds–averaged Navier–Stokes (RANS) models are considered more affordable and practical for engineering design applications and requires less computational resources (Tajnesaie et al., 2018). The 3D OpenFOAM numerical model is used in this paper to simulate the horizontal distribution of flows in curved and confluent channels and to understand the dynamics of flows in these channels. The objective of this paper is to understand to what extent selected turbulence models can model the flow field in channel bends and confluent channels. In light of this, two widely used efficient turbulence models (standard k–ε and realizable k–ε) were chosen to assess their performance in such simulations. This paper is organized as follows. Section 2 describes the numerical model, where governing equations and turbulence models are explained. Section 3 deals with numerical model verification, where the cases of channel bends and confluent channels are numerically simulated and compared with available data. Discussion of the two models used in the study and future works is provided in Section 4. Some concluding remarks complete the study in Section 5.

4.2. Numerical Model

Flows in rivers have been widely studied by using numerical modeling, which has become one of the most beneficial tools in river engineering in the past few decades. To simulate river flows in this study, the OpenFOAM model was used. OpenFOAM (OPEN Field Operation And Manipulation) is an open-source computational fluid dynamics model written in C++ which has been used in hydraulic engineering problems more frequently in past years (Gildeh et al., 2014, 2015). OpenFOAM has the feature of being open source for changes and developments, and new ideas can be contributed by users to help in extending the software features. It makes possible the modeling of flow fields using various numerical schemes and turbulence models. The model also

has the capability of parallel processing. Two types of application are available with this model: solvers that designed to solve a specific fluid mechanics problem, and utilities which are used to perform data manipulation (Lambert, 2012). OpenFOAM uses the finite volume method and includes various numerical schemes that are implemented for both time and space integration. For further information about how to use and program OpenFOAM, see (OpenFOAM, 2015). The solver used in this study is pisoFoam, which is mostly used for incompressible and turbulent flows in closed channel cases (also referred to as the Rigid-lid Model, or RLM).

4.2.1. Governing Equations

In this study, the Navier–Stokes and continuity equations have been used in the x, y and z directions to describe the flow, as described below.

Momentum in the x-direction:

$$\frac{\partial}{\partial t}(\rho u)+\frac{\partial}{\partial x}(\rho uu)+\frac{\partial}{\partial y}(\rho vu)+\frac{\partial}{\partial z}(\rho wu)=-\frac{\partial P}{\partial x}+\mu\left(\frac{\partial^2 u}{\partial x^2}+\frac{\partial^2 u}{\partial y^2}+\frac{\partial^2 u}{\partial z^2}\right) \tag{4-1}$$

Momentum in the y-direction:

$$\begin{aligned}\frac{\partial}{\partial t}(\rho v)+\frac{\partial}{\partial x}(\rho uv)+\frac{\partial}{\partial y}(\rho vv)+\frac{\partial}{\partial z}(\rho wv)\\ =-\frac{\partial P}{\partial y}+(v+\ v_t)\left(\frac{\partial^2 v}{\partial x^2}+\frac{\partial^2 v}{\partial y^2}+\frac{\partial^2 v}{\partial z^2}\right)\end{aligned} \tag{4-2}$$

Momentum in the z-direction:

$$\begin{aligned}\frac{\partial}{\partial t}(\rho w)+\frac{\partial}{\partial x}(\rho uw)+\frac{\partial}{\partial y}(\rho vw)+\frac{\partial}{\partial z}(\rho ww)\\ =-\frac{\partial P}{\partial z}+(v+\ v_t)\left(\frac{\partial^2 w}{\partial x^2}+\frac{\partial^2 w}{\partial y^2}+\frac{\partial^2 w}{\partial z^2}\right)\end{aligned} \tag{4-3}$$

Continuity:

$$\frac{\partial}{\partial x}(\rho u)+\frac{\partial}{\partial y}(\rho v)+\frac{\partial}{\partial z}(\rho w)=0 \tag{4-4}$$

where the y-axis of the Cartesian coordinate system is aligned in the vertical direction; $u, v,$ and w are the velocity components in the x, y, and z directions respectively; ρ is the mass density; μ is the viscosity; v_t is the turbulent kinematic viscosity; t is the time; and P is the pressure (Cable, 2009).

4.2.2. Turbulence Models

The simulation of turbulent flows is considered a complicated task because of the features that characterize this type of flow, such as three-dimensionality, unsteadiness, and the inclusion of many scales (Tajnesaie et al., 2018). Therefore, it is a delicate task to choose the most appropriate turbulence model, and the selection process will depend on factors like the physics encompassed in the flow, the level of accuracy desired, and the computational resources available (Gildeh, 2013).
In this study, the simulation of flows in river bends and confluences has been performed by using two widely used turbulence models: the standard k–ε model and the realizable k–ε model. These two RANS models have been selected due to their competitional efficiency and their wide usage compared to other RANS models such as LRR (Launder et al., 1975) or LES models.
The two models are described in the following.

- Standard k–ε model

The turbulence model that is most commonly used in CFD is the standard k–ε model. This model is based on the eddy viscosity concept. Two partial differential equations (transport equations) are solved in this type of turbulence model: the turbulent kinetic energy k and the turbulence eddy dissipation ε (i.e., the rate at which the turbulent kinetic energy dissipates) (Olsen, 2000). The incapability of capturing the subtler relationships between the turbulent energy production and the turbulent stresses caused by anisotropy of the normal stresses is one of the problems of some two-equation turbulence models such as the k–ε model. In addition, the performance of the k–ε model is considered poor in some significant cases, like: (1) some unconfined flows; (2) flows with large extra strains (e.g., curved boundary layers, swirling flows); (3) rotating flows; and (4) flows driven by anisotropy of normal Reynolds stresses (Versteeg and Malalasekera, 1995).
In this model, the following equations are used to obtain the turbulent kinetic energy and its rate of dissipation (Gildeh, 2013):

$$\frac{\partial k}{\partial t} + \frac{\partial k u_i}{\partial x_i} = \frac{\partial}{\partial x_i}\left(D k_{eff} \frac{\partial k}{\partial x_i}\right) + G_k - \varepsilon \tag{4-5}$$

$$\frac{\partial \varepsilon}{\partial t} + \frac{\partial \varepsilon u_i}{\partial x_i} = \frac{\partial}{\partial x_i}\left(D \varepsilon_{eff} \frac{\partial \varepsilon}{\partial x_i}\right) + C_{1\varepsilon} \frac{\varepsilon}{k} G_k - \mathrm{C}_{2\varepsilon} \frac{\varepsilon^2}{k} \tag{4-6}$$

where G_k is the generation of turbulent kinetic energy due to mean velocity gradients, and Dk_{eff} and $D\varepsilon_{eff}$ are the effective diffusivity for k and ε, respectively, which are calculated as shown below:

$$Dk_{eff} = \nu + \nu_t \tag{4-7}$$

$$D\varepsilon_{eff} = \nu + \frac{\nu_t}{\sigma_\varepsilon} \tag{4-8}$$

The equation for the turbulent kinematic viscosity at each point is:

$$\nu_t = C_\mu \frac{k^2}{\varepsilon} \tag{4-9}$$

where σ_ε is the turbulent Prandtl number for ε and is assumed as equal to 1.3. Furthermore, the constants $C_{1\varepsilon}$, $C_{2\varepsilon}$ and C_μ have the following values:

- $C_{1\varepsilon} = 1.44,\ C_{2\varepsilon} = 1.92,\ C_\mu = 0.09$

G_k is the production of turbulent kinetic energy, which is common in most turbulence models, and is given by:

$$G_k = 2\nu_t {S_{ij}}^2 \tag{4-10}$$

where the strain-rate tensor S_{ij} is written as:

$$S_{ij} = 0.5\left(\frac{\partial u_j}{\partial x_i} + \frac{\partial u_i}{\partial x_j}\right) \tag{4-11}$$

- Realizable k–ε model

In the realizable k–ε model, the turbulent viscosity is calculated by using an improved method. The exact transport equation of the fluctuating component vorticity is used to derive the dissipation rate equation. The realizable k–ε model is considered more accurate compared to the k–ε model in predicting the distribution of the dissipation rate of flat and round jets. Also, better prediction is provided by the realizable k–ε model for the boundary layer characteristics in a large pressure gradient, separated and recirculating flows (Bulat and Bulat, 2013).

- The transport equations in this model are written as:

$$\frac{\partial k}{\partial t} + \frac{\partial k u_i}{\partial x_i} = \frac{\partial}{\partial x_i}\left(Dk_{eff}\frac{\partial k}{\partial x_i}\right) + G_k - \varepsilon \tag{4-12}$$

$$\frac{\partial \varepsilon}{\partial t} + \frac{\partial \varepsilon u_i}{\partial x_i} = \frac{\partial}{\partial x_i}\left(D\varepsilon_{eff}\frac{\partial \varepsilon}{\partial x_i}\right) + \sqrt{2}C_{1\varepsilon}S_{ij}\varepsilon - C_{2\varepsilon}\frac{\varepsilon^2}{k+\sqrt{v\varepsilon}} \quad (4\text{-}13)$$

- with the turbulent viscosity determined by:

$$v_t = C_\mu \frac{k^2}{\varepsilon} \quad (4\text{-}14)$$

- where C_μ is computed by:

$$C_\mu = \frac{1}{A_0 + A_s\frac{kU^*}{\varepsilon}} \quad (4\text{-}15)$$

$$U^* = \sqrt{S_{ij}S_{ij} + \tilde{\Omega}_{ij}\tilde{\Omega}_{ij}} \quad (4\text{-}16)$$

$$\tilde{\Omega}_{ij} = \bar{\Omega}_{ij} - \varepsilon_{ijk}\omega_k - 2\varepsilon_{ijk}\omega_k \quad (4\text{-}17)$$

- where $\bar{\Omega}_{ij}$ is the mean rate of rotation tensor and ω_k is the angular velocity.
- The constants A_0 and A_s are determined as below:

A_0=4, $\quad A_s = \sqrt{6}cos\varphi \quad (4\text{-}18)$

$$\varphi = \frac{1}{3}Arc\cos\left(\min\left(\max\left(\sqrt{6}W, -1\right), 1\right)\right) \quad (4\text{-}19)$$

$$W = \frac{S_{ij}S_{jk}S_{ki}}{\tilde{S}^2} \quad (4\text{-}20)$$

- $C_{1\varepsilon}$ is defined as:

$$C_{1\varepsilon} = \max\left(\frac{\eta}{5+\eta}, 0.43\right) \quad (4\text{-}21)$$

- $\eta = S\frac{k}{\varepsilon}$ (4-22)
- The constants C_2, σ_k and σ_ε were specified by Shih (1995) and are defined as below:
- $C_2 = 1.9,\ \sigma_k = 1.0,$ and $\sigma_\varepsilon = 1.2$

In this model, a new turbulent viscosity equation (14-15) and the transport of the mean-squared vorticity fluctuation equation were used to derive the dissipation rate transport equation (Gildeh, 2013).

4.3. Numerical Model Verification

4.3.1. Curved Channel

For the case of a curved channel, the channel studied by Rozovskii (1961) has been adopted because it is a well-documented experiment with reliable data. A schematic view of this channel is shown in Figure 4.3. It consists of a straight approach channel with a length of 6 m followed by a 180° bend with a mean radius of 0.8 m and an outlet section of 3 m. The channel cross-section is a 0.8 m-wide rectangle.

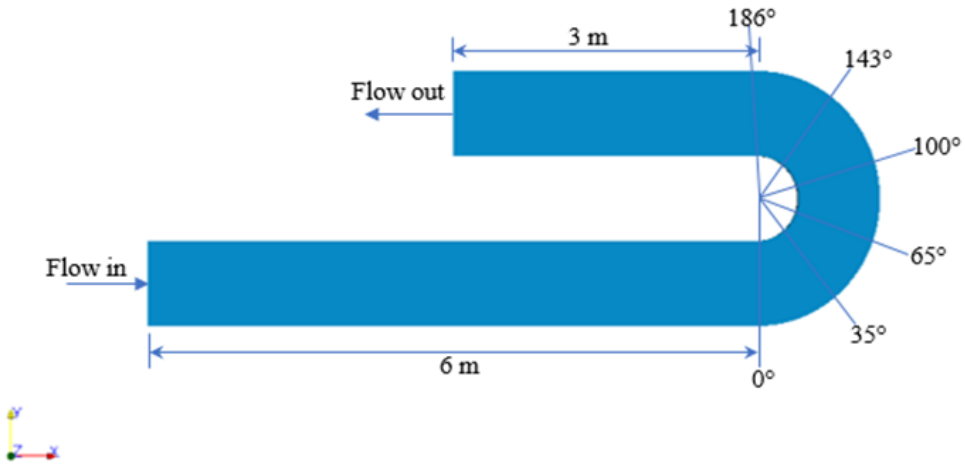

Figure 4.3: Model setup for the curved channel

Table 4.1 shows the characteristics of the channel and some hydraulic data obtained from Rozovskii's experiment that has been adopted in the current study.

Table 4.1: The dimensions of the curved channel and flow conditions

Variable	Symbol	Value
Upstream discharge	Q	0.0123 m^3/s
Downstream water depth	h	0.058 m
Channel width	B	0.8 m
Bend angle	θ	180º
Internal radius of curvature	r_i	0.4 m
Mean radius of curvature	r_c	0.8 m
Mean radius to width ratio	r_c/B	1.0
Chézy factor	C	60
Mean velocity downstream	U_∞	0.265 m/s
Tailwater Froude number	Fr_d	0.35

4.3.1.1. Boundary Conditions

Figure 4.4a shows the boundaries that have been applied in the model for the curved channel. It includes four different boundaries: the inlet of the channel, the outlet of the channel, the walls (including side walls and bottom), and the surface of the channel (symmetry). Figure 4.4b shows the mesh used in the simulation which was refined to better resolve the velocity, particularly near the two banks and the bottom of the channel.

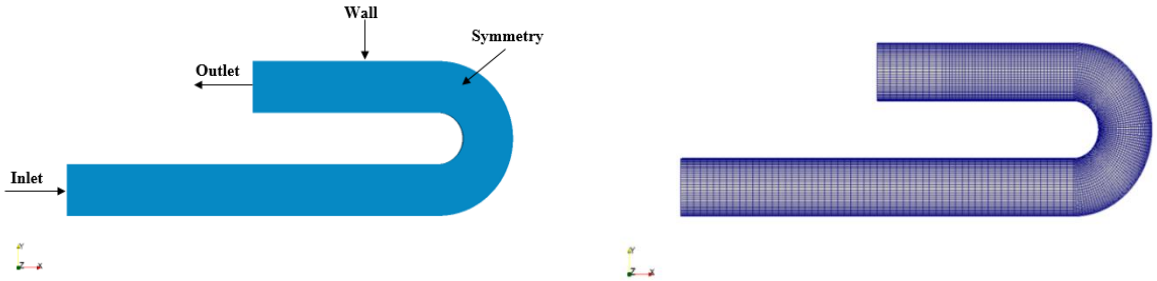

Figure 4.4: (a) Boundary conditions; (b) the refined mesh

The flow is discharged with an initial velocity of U_0. The boundary conditions are chosen as: $u_x = U_0$; $u_y = u_z = 0$; $k = 0.06u^2$; and $\varepsilon = 0.06\, u^3/D$, where D is the average water depth. The boundary conditions of the outlet are defined as zero gradient for $u_x, u_y, u_z, k,$ and ε. The boundary conditions of the pressure and turbulent viscosity are defined as zero gradient for the inlet and outlet. The standard wall function is used for the boundary conditions of the wall in k, ε, and v_t. Finally, the boundary conditions of the channel surface are defined as a symmetry plane. The Courant number was kept below 0.9 in all cases.

4.3.1.2. Results and Discussion for the Curved Channel

4.3.1.2.1. The Secondary Currents' Velocity Profiles

A comparison between the experimental and the numerical profiles of transverse velocity and the experimental results provided by Rozovskii (1961) and Guymer (1998) is shown in Figure 4.5, where ζ is the dimensionless elevation (y/h) and where h is the water depth ($h = 0.058m$) which ranges from $(0 - 1)$, u_2 is the transverse velocity, and U_1 is the mean velocity. Considering the results shown in Figure 5, there is a good agreement between the De Vriend (1977) data and observed data over the depth, while the transverse velocity is overestimated by other numerical profiles. Both the k-ε and realizable k-ε models showed a good agreement with the experiment.

Both of these models predict the transversal velocities in the lower half of the channel cross-section better than upper half, which could be attributed to the effect of wall function and roughness on the flow velocity and suggests that it was chosen properly for both models.

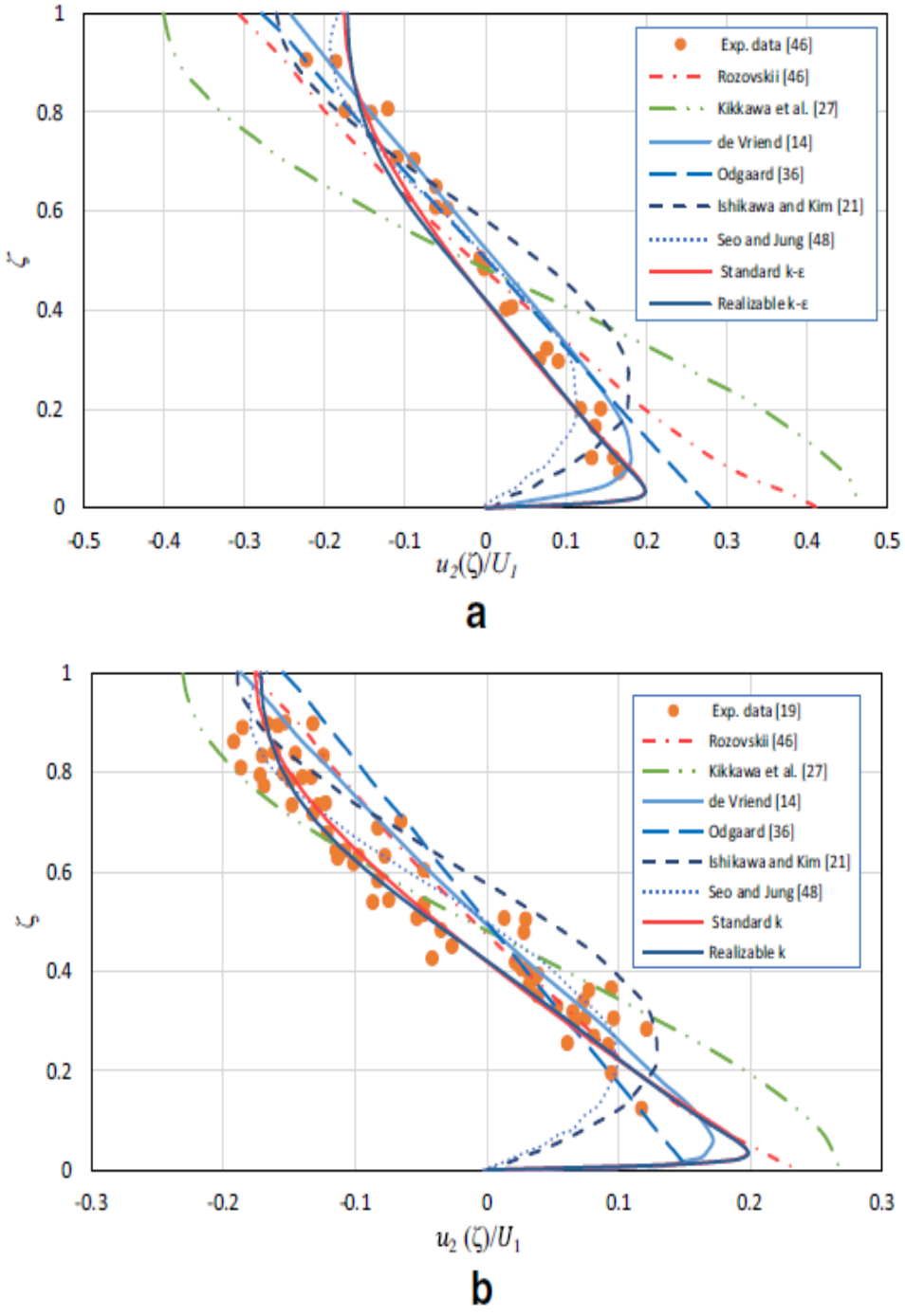

Figure 4.5: Vertical distribution of transverse velocity: a Rozovskii channel and b Guymer channel

To quantify this agreement, root mean square error (RMSE) and the coefficient of determination (R^2) have been used, as shown in Table 4.2.

Despite the similarity between the results for the two models, the RMSE and R^2 values showed a slight difference between them. Although both models have relatively small RMSE and large R^2 values, the values of the standard k-ε model are better than those of the realizable k-ε, implying that it performs better. To indicate the difference in RMSE between the two models more clearly, Table 4.3 shows the relative error compared to mean flow, which confirms a marginal difference between the two models.

Table 4.2: Sectional RMSE and R^2 values of transverse velocity in Figure 4.5

	RMSE		R^2	
The models	Rozovskii experiment	Guymer experiment	Rozovskii experiment	Guymer experiment
Standard k-ε model	0.0571	0.0680	0.9517	0.9173
Realizable k-ε model	0.0642	0.0737	0.9776	0.9024

Table 4.3: The relative error compared to mean flow

	The relative RMSE error	
	Standard k-ε model	Realizable k-ε model
Rozovskii experiment	21.54%	24.22%
Guymer experiment	25.66%	27.81%

4.3.1.2.2. Velocity Patterns

The velocity pattern of the curved channel surface is shown in Figure 4.6, after the flow in the channel reaches the steady state. At the beginning of the bend, the maximum velocity moves towards the inner bank of the channel, and then changes direction towards the outer bank near the bend exit.

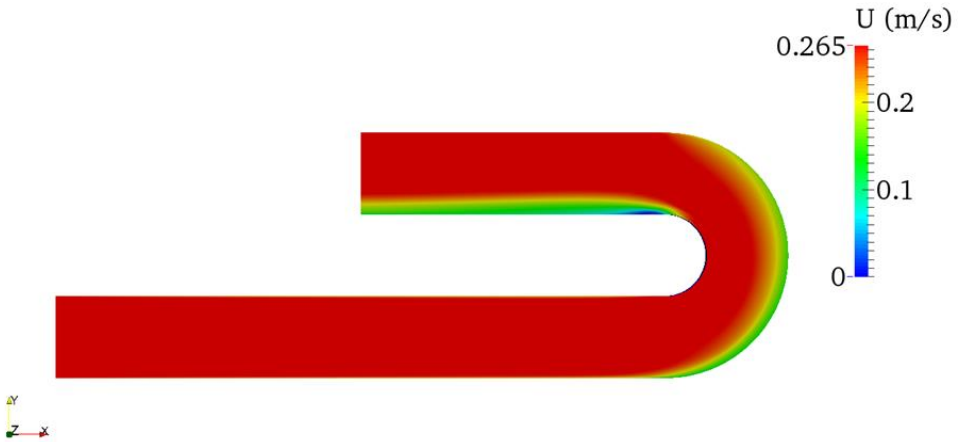

Figure 4.6: Velocity distribution after reaching the steady state

4.3.1.2.3. Flow Velocity Properties

The depth-averaged velocity across the width of the channel is illustrated in Figure 4.7, where: U is the depth-averaged velocity magnitude; and u_1, u_2, and u_3 are the longitudinal, vertical, and lateral velocity averaged over the depth, respectively. Note that the depth-averaged velocity is represented by the vertical axis and is non-dimensionalized by U_1, which is the downstream mean velocity. The horizontal axis represents the radial distance $(r - r_i)/B$, non-dimensionalized by the channel width, where B is the channel width and r and r_i are the radius of curvature for the outer and inner banks, respectively. The cross-sections that have been taken in the bend of the channel to examine the velocity of the flow in this area showed that the two models demonstrated approximately the same results. There is an increase in the velocity near the interior bank of the channel and a decrease near the outer bank at cross-sections 0˚, 35˚, 65˚, 100˚, and 143˚ (see Figure 4.3) of the bend. The velocity of the flow starts to decrease at the inner bank near the end of the bend at cross-section 186˚ and increases towards the outer bank of the channel in the same area. Both models showed a good agreement with other numerical models and the experimental data with some slight variations, particularly near the two banks of the channel. Furthermore, the behavior of the velocity distribution also agrees with the study by De Vriend and Geldof (1983), who studied the flow velocity in river bends in a field investigation on the Dommel River (in the Netherlands) and also performed a numerical simulation of the flow. The river section was in the form of two consecutive curves, both of 90 degrees and in the same direction, with a short straight connection between them. The maximum velocity according to the results occurred at the beginning of the bend near the inner

bank of the river, while at the end of the bend it tended to be oriented toward the outer bank of the river, which is in agreement with the results of the present study.

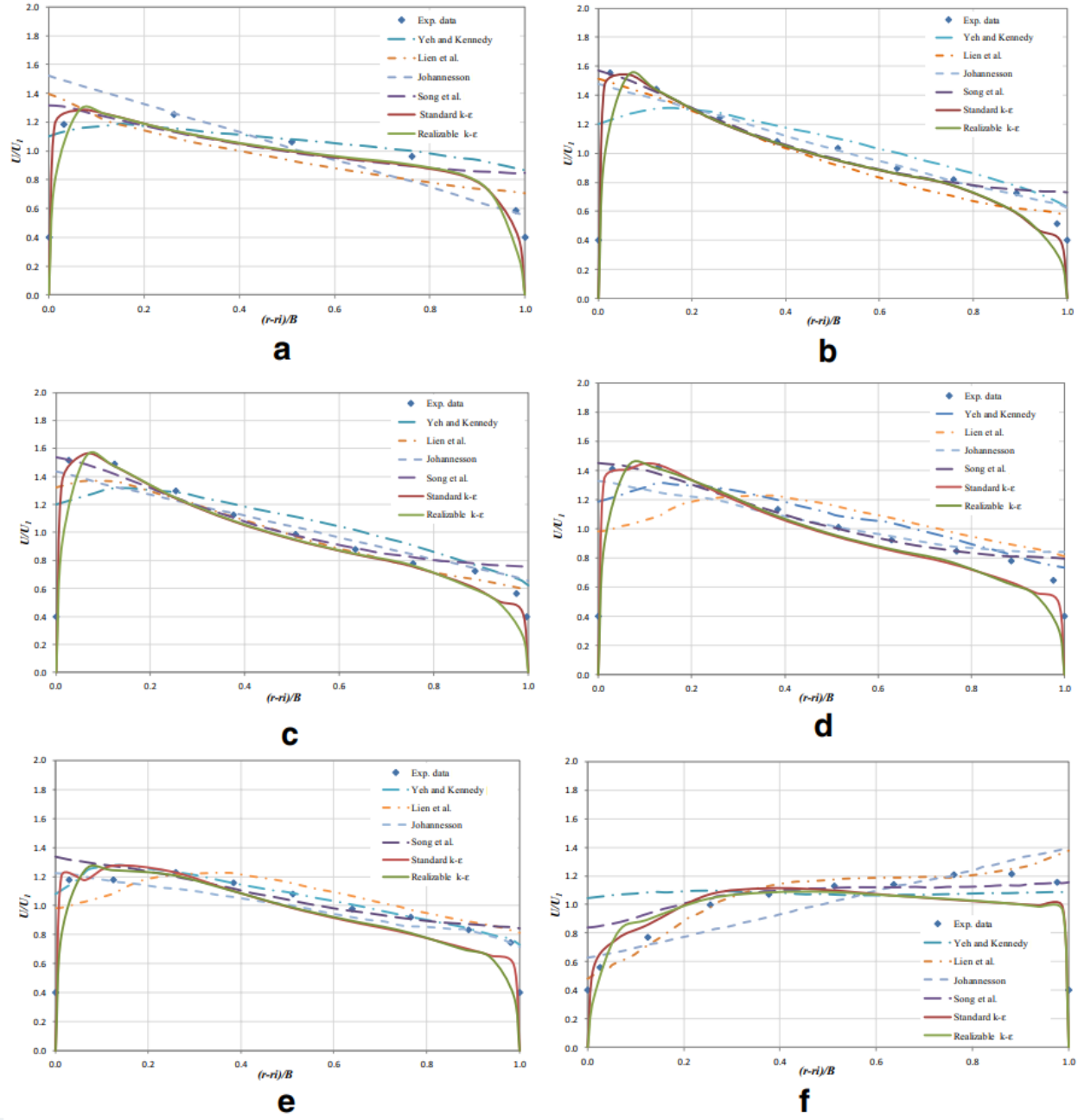

Figure 4.7: A comparison of resultant velocities across dimensionless channel width for the Rozovskii channel: a at θ=0°; b at θ=35°; c at θ=65°; d at θ=100°; e at θ=143°; and f at θ=186°

Moreover, the agreement between the two models and the experiment has been quantified by the RMSE and compared with other numerical models. Table 4.4 below shows the sectional RMSE of the resultant velocity for each model. At cross-section 0°, at the beginning of the bend, the

distributions of the resultant velocity along the transverse direction were different for each model, while there was no significant difference in the values for the RMSE. The standard k–ε model gave relatively lower values for the RMSE at the first three cross-sections. At the last cross-section, close to the bend exit, both models overestimated the velocity, especially near the two banks. The mean RMSE of the standard k–ε model had the lowest value. Also, the relative error compared to mean flow is shown in Table 4.5, and according to the results, the realizable k–ε model seems less accurate than the standard k–ε.

Table 4.4: Sectional RMSE of resultant velocities in Figure 4.7

θ (°)	Models					
	Yeh and Kennedy	Lien et al.	Johannesson	Song et al.	Standard k-ε model	Realizable k-ε model
0	0.1515	0.1462	0.1663	0.1555	0.0972	0.1706
35	0.1790	0.1163	0.0782	0.1026	0.0757	0.1741
65	0.1771	0.1063	0.1070	0.0963	0.0733	0.1668
100	0.1287	0.1020	0.1339	0.0731	0.0855	0.1635
143	0.0476	0.1255	0.0866	0.0887	0.0975	0.1574
186	0.2838	0.0978	0.1682	0.1514	0.1183	0.1262
Mean RMSE	0.1613	0.1157	0.1234	0.1112	0.0912	0.1597

Table 4.5: The relative error compared to mean flow

θ (°)	The relative error	
	Standard k-ε model	Realizable k-ε model
0	36.67%	64.37%
35	28.56%	65.69%
65	27.66%	62.94%
100	32.26%	61.69%
143	36.79%	59.39%
186	44.64%	47.62%
Mean RMSE	34.41%	60.26%

The values of R^2 are shown in Table 4.6; the standard k-ε model values are larger than those of the realizable k-ε model in all sections, which means that it performs better. However, both models have a small value for R^2 in the last section. It is noteworthy that in all cross-sections presented above, both models' predictions were better for the inner curve, which suggests that linear eddy viscosity turbulence models are mostly capable for the smaller extent of curved flows, especially close to the center of curvature in natural streams. As the water level changes toward the outer bank

(i.e., farther from the center of curvature), the flow momentum decreases, and the numerical model results deviate from the experimental data. It is expected that models considering the shear stresses in all directions will perform better for the outer bank.

Table 4.6: R2 values of resultant velocities in Figure 4.7

θ (°)	R^2 values	
	Standard k-ε model	Realizable k-ε model
0	0.9668	0.9272
35	0.9895	0.8383
65	0.9892	0.8575
100	0.9948	0.8677
143	0.9637	0.884
186	0.7494	0.7406

4.3.1.2.4. Turbulence Characteristics

As the maximum velocity moves towards the inner bank at the middle of the bend, circulation occurs at this area, as shown in Figure 4.8. The contours of the turbulent kinetic energy and eddy viscosity are shown in Figure 4.9 and Figure 4.10 respectively in the three cross-sections taken from the standard k-ε model, i.e., at the beginning of the curve, at the middle, and near the bend exit. Note that the aspect ratio has been changed to obtain a clearer picture. As seen in Figure 4.9, the maximum $k/\bar{u}^2$ ranges from 0.017 to 0.036 for the three cross-sections presented, which agrees with the values reported in (Pilechi et al., 2011; Shao and Law, 2009). The maximum kinematic energy extends toward the area with a higher shear stress rate, and similar to the velocity vector map, the maximum values were observed at the inner bank at the middle cross-section. The difference between the contours at the entrance and exit of the bend is noteworthy, as the maximum kinematic energies are slightly different at the two banks. At the bend entrance, higher kinematic energy tends to happen near the outer bank, while it is almost the reverse at the bend exit. The eddy viscosity contours in Figure 4.10 identify the areas of high viscosity, which tend to happen at the top area of the cross-sections. The maximum value of the eddy viscosity is two orders of magnitude larger than the water kinematic viscosity of 1.1×10^{-6} m^2/s, which is in agreement with the widely known range of eddy viscosity to kinematic viscosity.

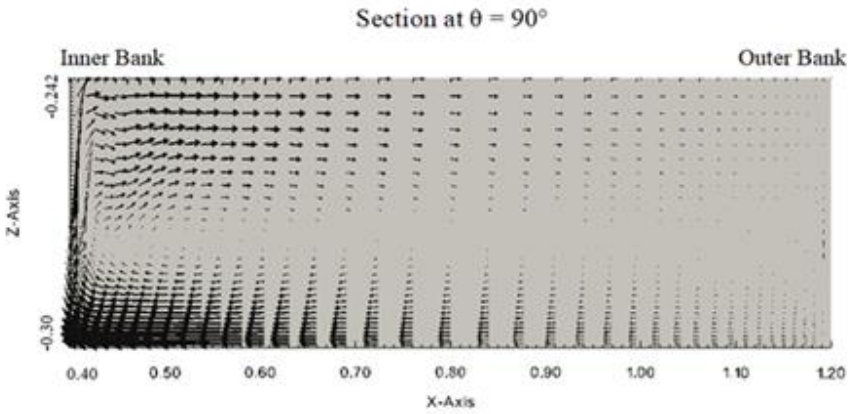

Figure 4.8: The velocity vectors at θ=90°

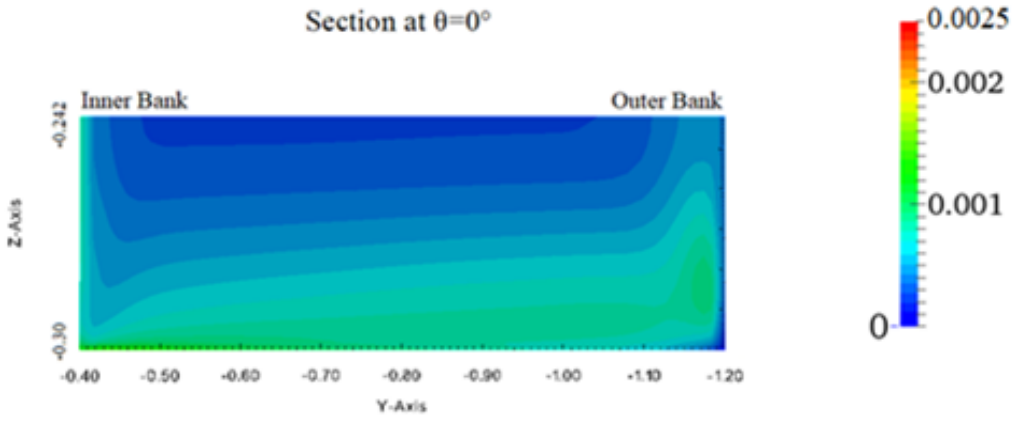

a

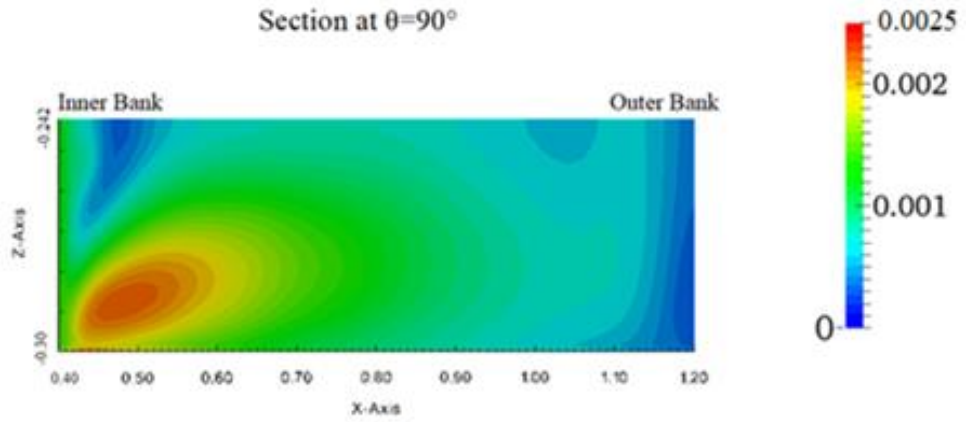

b

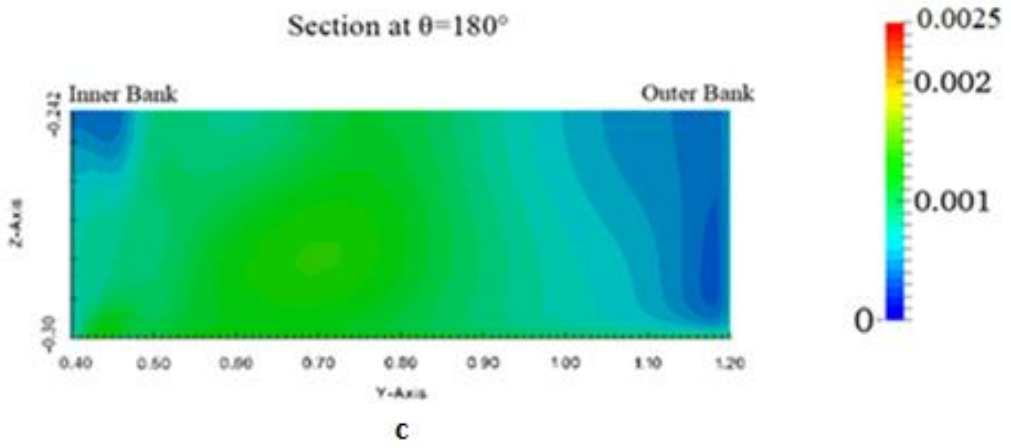

c

Figure 4.9: Turbulent kinetic energy (k) contours: a at θ=0°; b at θ=90°; c at θ=180°

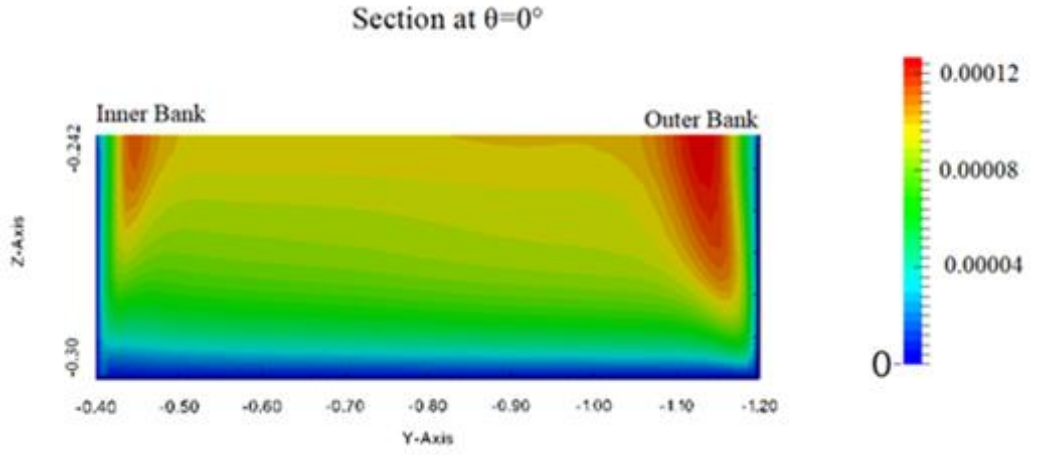

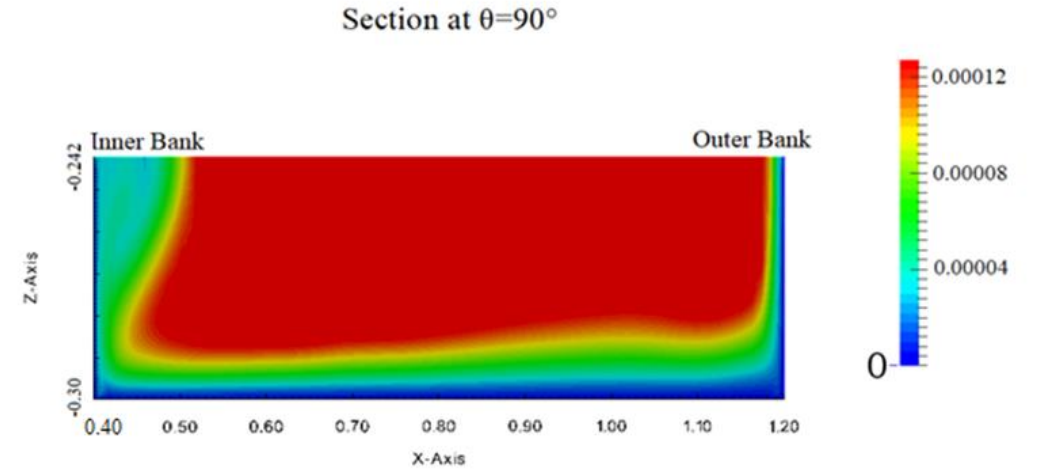

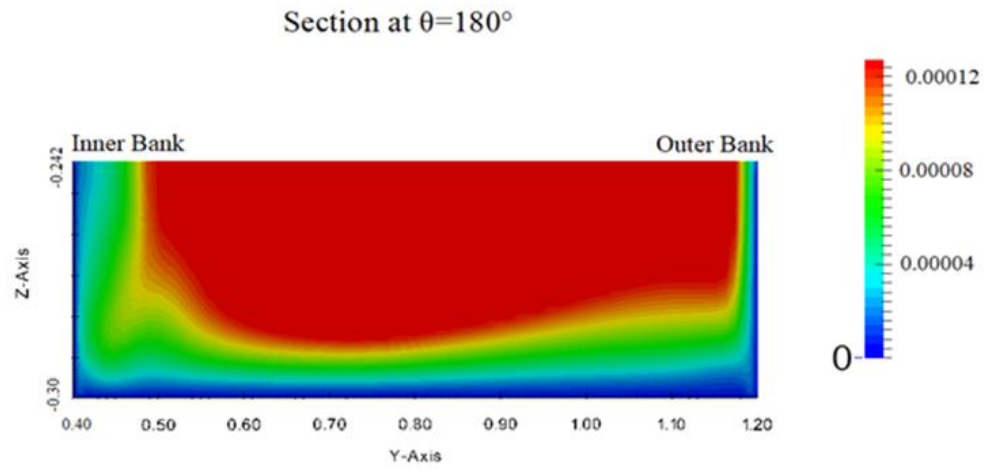

Figure 4.10: Eddy viscosity (m2 /s) contours: a at θ=0°; b at θ=90°; c at θ=180°

4.3.2. Confluent Channel

In the case of the confluent channel, the experiment by Shumate (1998) that includes a confluent open channel was considered. It consists of a branch channel of about 3 m in length denoted by subscript (b) which is connected to a main channel with a length of about 10 m denoted by subscript (m) at a 90° angle, as shown in Figure 4.11.

The information for the channel and flow parameters is shown in Table 4.7.

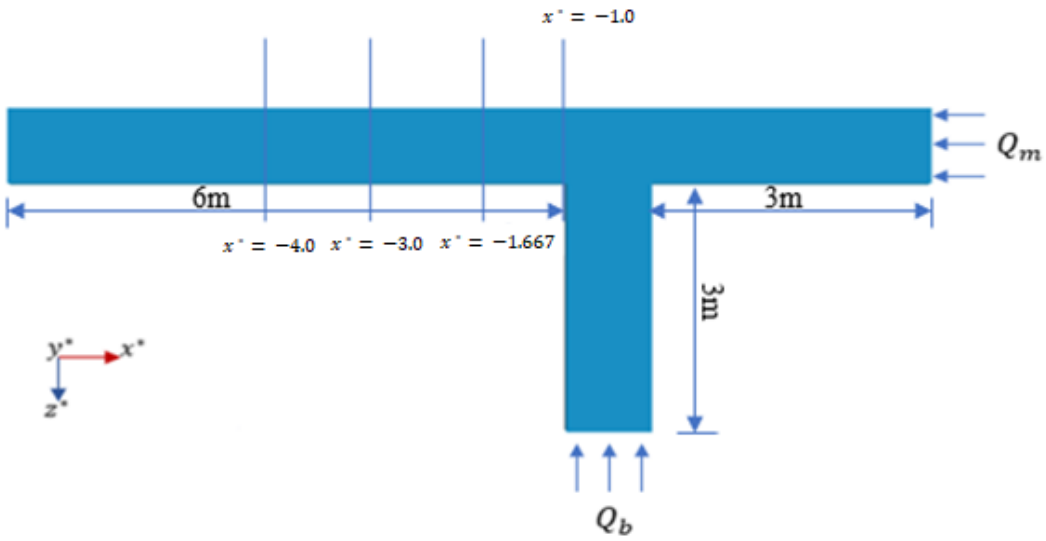

Figure 4.11: Model setup for the confluent channel

Table 4.7: Dimensions of the confluent channel and flow conditions

Variable	Symbol	Value
Main channel discharge	Q_m	0.043 m^3/s
Branch channel discharge	Q_b	0.127 m^3/s
Downstream water depth	h	0.296 m
Channel width	B	0.914 m
Chézy factor	C	60
Mean velocity at downstream	U_∞	0.628 m/s
Tailwater Froude number	Fr_d	0.37

4.3.2.1. Boundary Conditions

The boundary conditions of the confluent channel are shown in Figure 4.12a. They are the same as those of the curved channel mentioned before because of the identical nature of the boundaries. The mesh is shown in Figure 4.12b, and it was also refined to better resolve the velocity, particularly near the two banks.

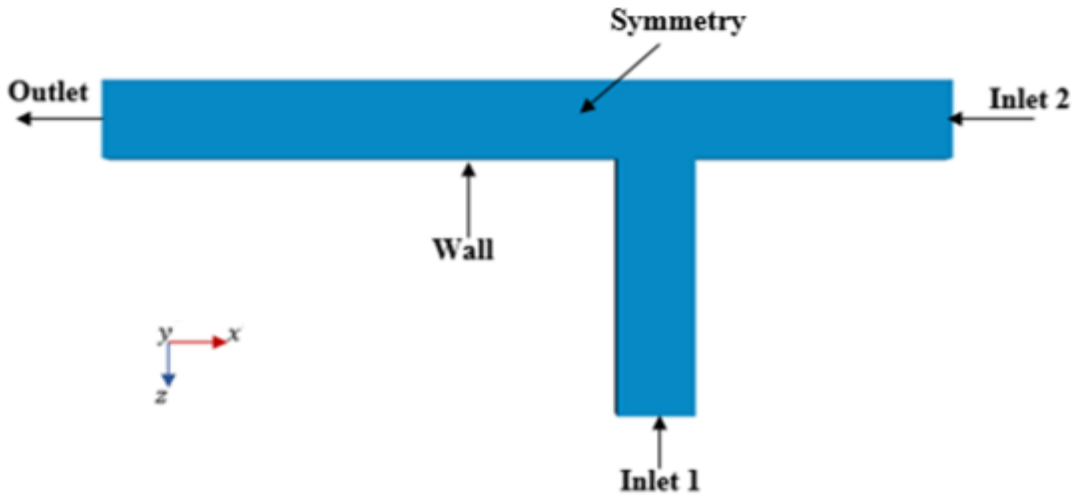

(a)

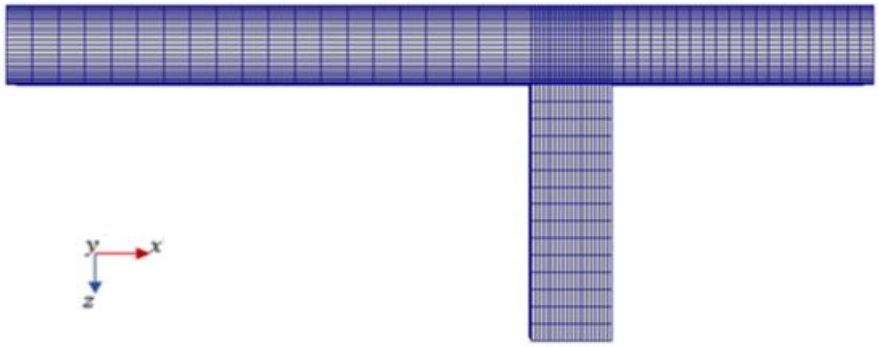

(b)

Figure 4.12: a. Boundary conditions; b. the refined mesh

4.3.2.2. Results And Discussion for The Confluent Channel

4.3.2.2.1. Velocity Patterns

Figure 4.13 below shows the velocity pattern of the confluent channel surface after reaching the steady state. The maximum velocity moves from the branch channel towards the outer bank of the main channel.

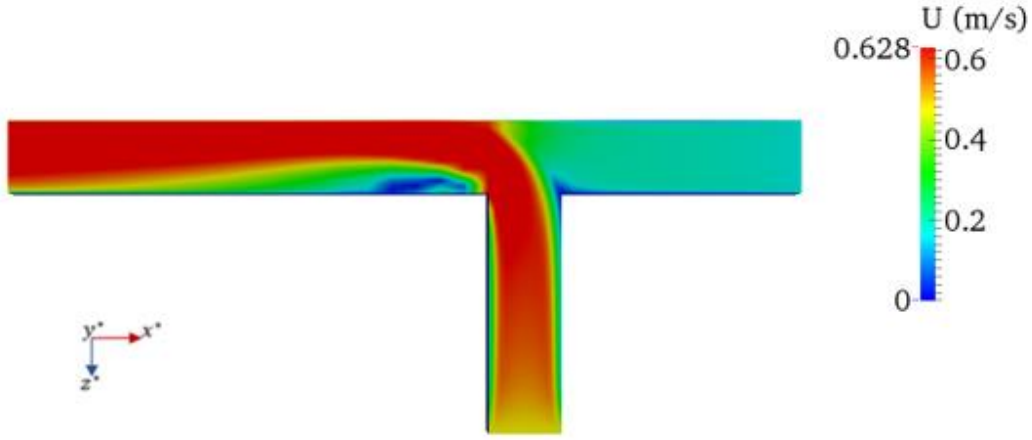

Figure 4.13: Maximum velocity distribution after the steady state

4.3.2.2.2. Flow Velocity Properties

Figure 4.14 shows the depth-averaged velocity across the width of the channel, where: U is the depth-averaged velocity magnitude which is non-dimensionalized by U_1 (the downstream mean velocity); $x^* = x/B$, with the x-coordinate non-dimensionalized by the channel width; $z^* = z/B$, with the z-coordinate non-dimensionalized by the channel width; and B is the channel width.

According to the obtained results, the distribution of the flow velocity for the two numerical models is almost the same. As the secondary flow enters the main channel, the higher velocity moves from the branch channel to the outer bank of the main channel. Cross-sections are taken at the main channel immediately after the convergence in order to study the velocity curve in this area (see Figure 4.11). The velocity curves of the two numerical models were compared with those of the experiment, and both models achieved a good agreement in light of this comparison. However, while the velocity distribution for the first two cross-sections is predicted fairly well by the numerical models, the complexity of the flow features in this region prevented their precise conformity with those of the experiment. According to Thanh et al. (2010), the reason behind the complexity of the flow features in this area is the separation zone (or recirculation zone) that is generated at the downstream of the confluence near the internal bank of the main channel as the tributary enters the main channel, which is shown in Figure 4.14.

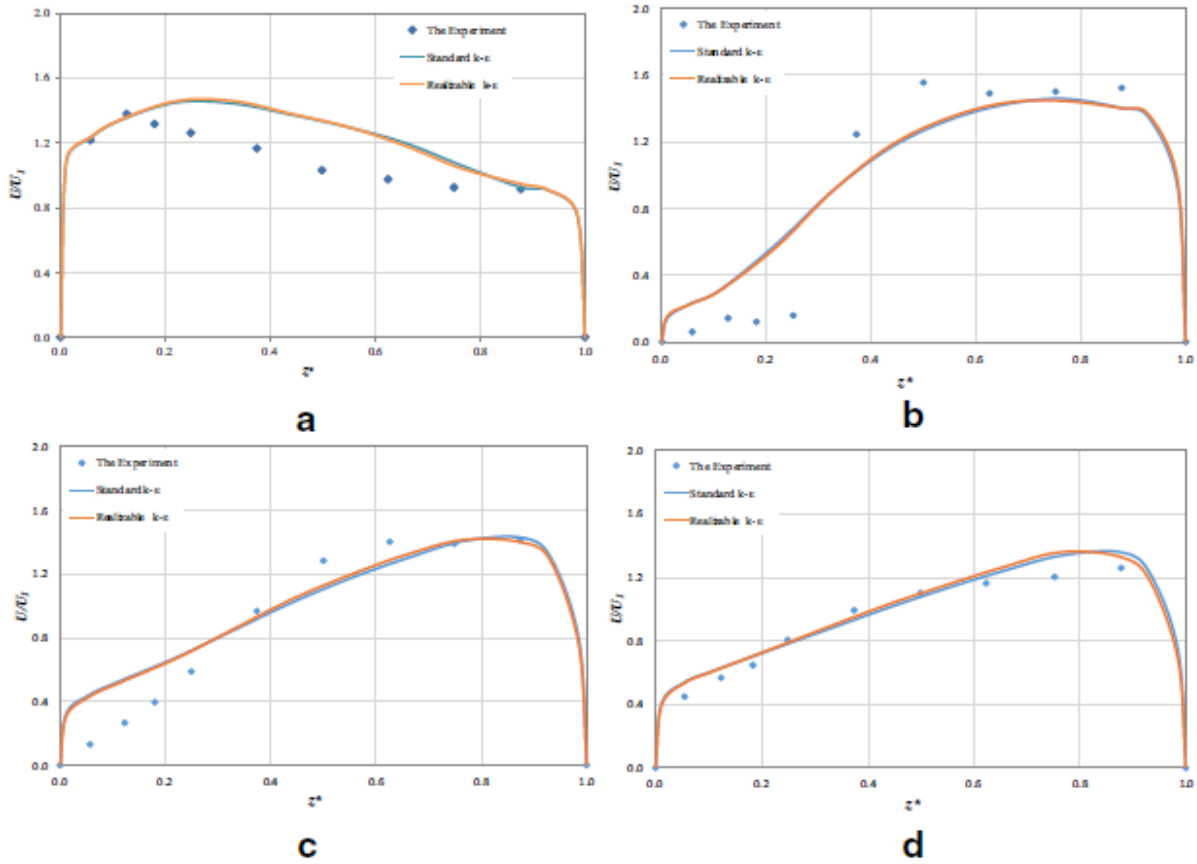

Figure 4.14: Resultant velocities across dimensionless transverse distance for confluent channel: a at x*=−1.0; b at x*=−1.667; and c at x*=−3.0, d at x*=−4.0

According to the RMSE values of the two models shown in Table 4.8 below, the realizable k-ε model was generally more accurate than the standard k-ε model. This suggests that realizable k-ε model is more capable in predicting flow velocities in complex flow geometries such as confluent channels where the shear stresses intersect with each other from the branch and main streams. However, the difference between the two models is slim. The relative error compared to the mean flow is shown in Table 4.9, which shows almost the same amount of relative error for the two models.

Table 4.8: Sectional RMSEs of the resultant velocities in Figure 4.14

Cross-sections	Models	
	Standard k-ε model	Realizable k-ε model
-1.0	0.1775	0.1798
-1.667	0.2688	0.2610
-3.0	0.1795	0.1700
-4.0	0.0708	0.0687
Mean RMSE	0.1741	0.1698

Table 4.9: The relative error compared to mean flow

Cross-sections	The relative error	
	Standard k-ε model (%)	Realizable k-ε model (%)
-1.0	28.26	28.63
-1.667	42.80	41.56
-3.0	28.58	27.07
-4.0	11.27	10.93
Mean RMSE	27.72	27.03

The R^2 values given in Table 4.10 below show almost the same results as those of the RMSE in terms of accuracy of the models. Both models gave small values for R^2 at the first section immediately after the junction where the direction of the flow changes from straight to curved and a strong flow recirculation zone is observed, which means that the two models have a weakness in this zone (due to the complexity of the flow and the separation zone in this region), while for the other sections, the two models predicted the velocity very well. Based on the R^2 values shown in Table 4.10, the realizable k-ε model performs better.

Table 4.10: R^2 values of the resultant velocities in Figure 4.14

Cross-sections	R^2	
	Standard k-ε model	Realizable k-ε model
-1.0	0.5872	0.6081
-1.667	0.9231	0.9301
-3.0	0.9583	0.9707
-4.0	0.9578	0.9647

4.3.2.2.3. Turbulence Characteristics

Figure 4.15 below shows the velocity vectors of the realizable k-ε model at two cross-sections of the main channel after the junction. As can be seen from the figure, the circulation spreads over the width of the channel, leaning toward the outer side where the maximum velocity occurs, and almost the same form can be seen in the second section, with more spread of the circular motion. The contours of the turbulent kinetic energy and eddy viscosity are shown in Figure 4.16 and Figure 4.17, respectively for the three cross-sections of the main channel taken from the realizable k-ε model. The maximum $k/\bar{u}^2$ in Figure 4.16 ranges from 0.025 to 0.058 for the three cross-sections, which is consistent with the typical range of turbulent kinetic energy. The maximum kinematic energy extends toward the inner bank of the channel at the beginning of the junction with a slight appearance near the bottom of the channel and is then concentrated in the bottom of the channel with slight rotational movements near the zone of the secondary flows. The areas of high viscosity are identified by the eddy viscosity contours that are shown in Figure 4.17. The maximum amount of eddy viscosity, with a value of about 0.003, appears near the outer bank in the first section, and then moves towards the inner bank close to the top of the channel in a circulation motion.

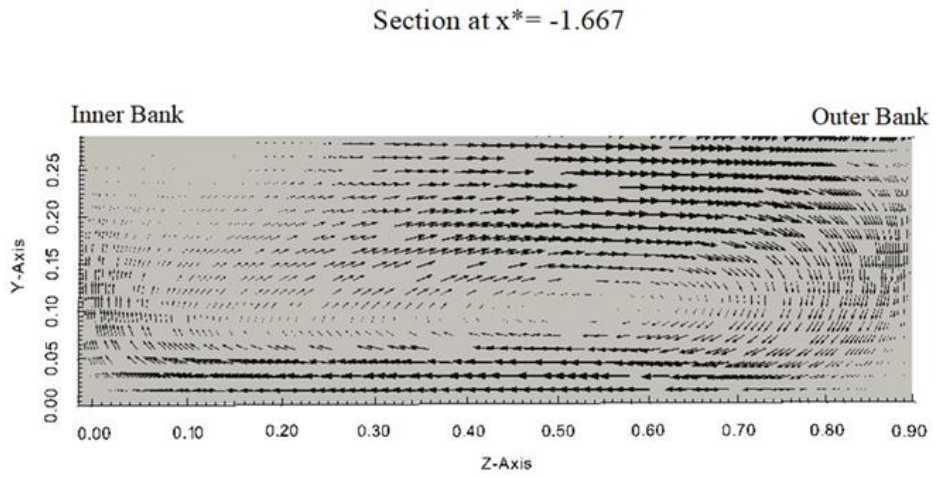

a

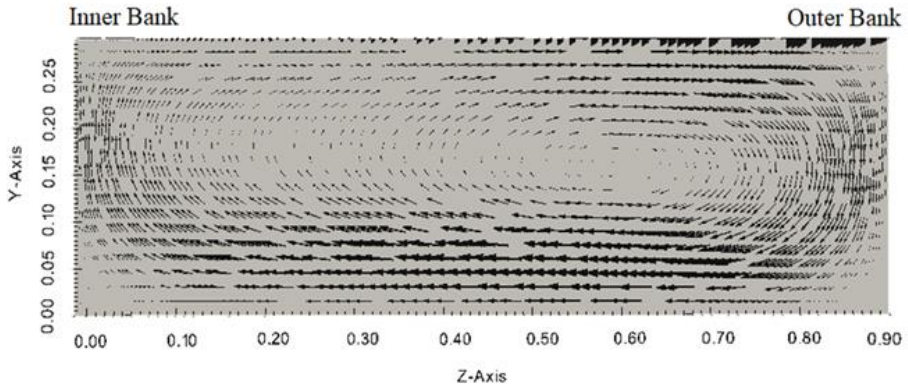

(b)

Figure 4.15: Velocity vectors: a at x*=−1.667; and b at x*=−3.0

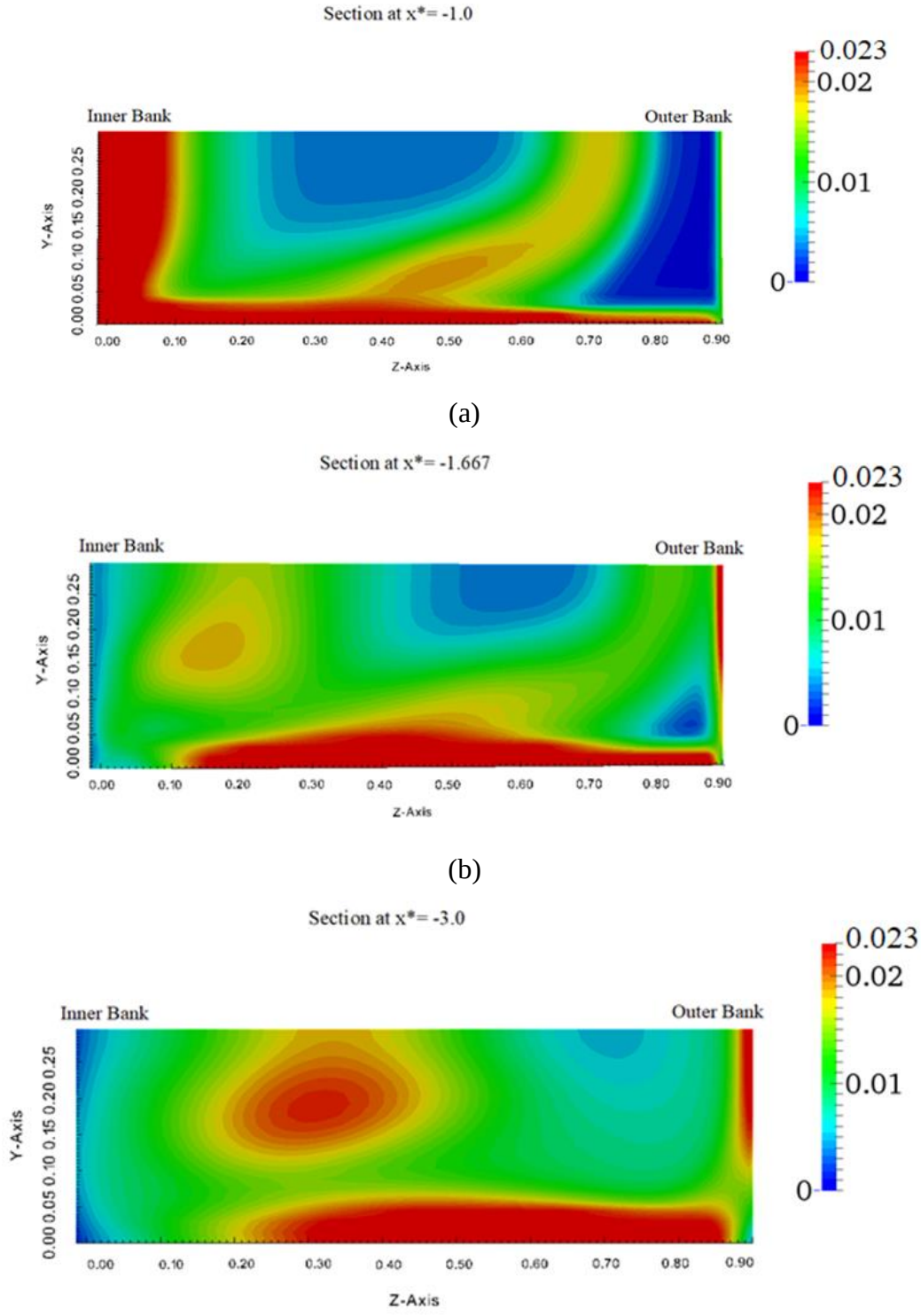

Figure 4.16: Turbulent kinetic energy (k) contours: a at x*=−1.0; b at x*=−1.667; and c at x*=−3.0

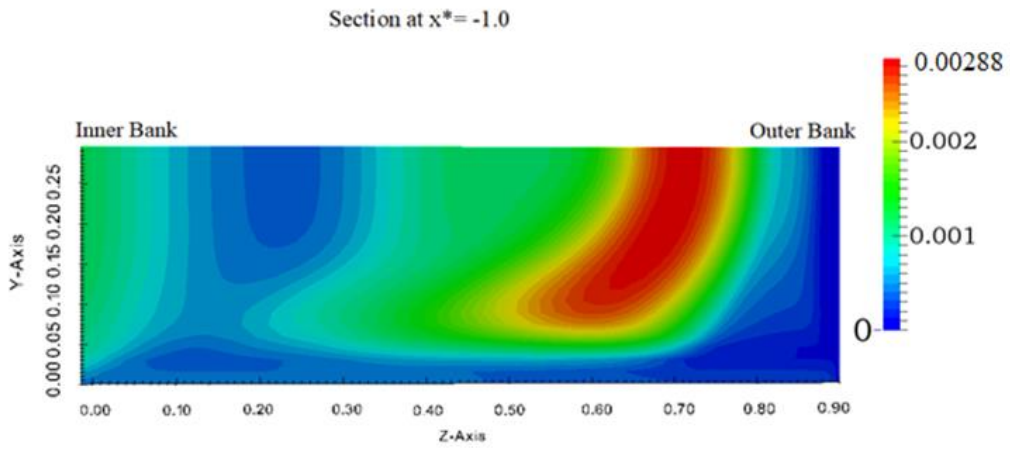

(a)

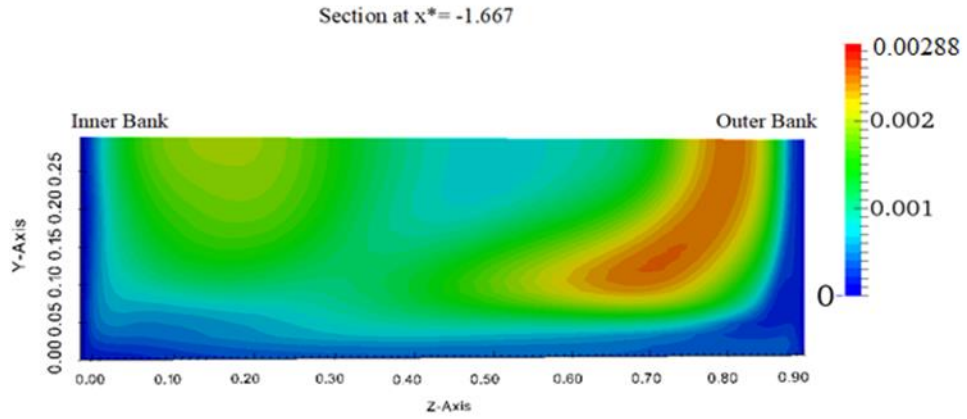

(b)

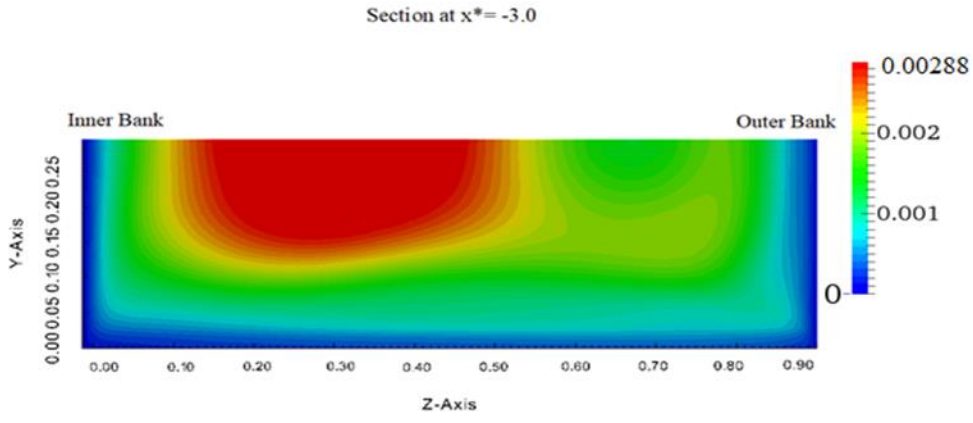

(c)

Figure 4.17: Eddy viscosity (m2 /s) contours: a at x*=−1.0; b at x*=−1.667; and c at x*=−3.0

4.4. Discussion and Remarks

Studies of the flow structures in river bends and confluences have found that vertically sheared and curved flows form secondary currents in the vertical plane normal to the flow direction. The dissipation properties and shear layer behavior of the secondary flow immediately within and downstream of a curve or confluence should be properly captured using the numerical model in order to resolve the secondary current characteristics. Secondary flows observed in river bends and confluences are not often identical due to differences in turbulent flow structures (Song et al., 2012). Turbulent flows in confluent channels are often different than in bend channels due to the perpendicular shear stresses where two streams meet, as well as other differences in flow characteristics. The recirculation zones in river bends and confluences are expected to be different, and thus the performance of turbulence models in capturing secondary flows might be different for each condition. It is therefore vital to understand the differences between the two turbulence models used in this study.

The main difference between the standard k-ε and realizable k-ε models is mainly due to their calculations of eddy viscosity. In the standard k-ε model, the eddy viscosity is based on a constant Cμ (dynamic viscosity coefficient), while in the realizable k-ε model, a non-constant value for Cμ is considered. In reality, all scales of motion affect turbulent diffusion, especially in secondary currents where cross-circulation is created by the interaction of multiple forces, e.g., centrifugal acceleration, transverse water surface slope, and bed shear stress (Chang, 1988; Termini and Piraino, 2011). Although both models are linear eddy viscosity models (LEVMs), the realizable k-ε model is slightly better in the more complex case, i.e., river confluences, in capturing the stress anisotropy that is partially responsible for secondary motions (Gildeh, et al., 2014). Moreover, the effects of the center region cell in river confluences could be better modeled if one takes account of the deformation of the downstream velocity and the center region cell (i.e., incorporating the feedback between the downstream velocity and the secondary circulation).

The standard k-ε model is traditionally used in open channel hydraulics with meanders, successfully (Ramón et al., 2015). Flow geometry is also another important factor in turbulence model performance. Generally, the standard k-ε model works better for simpler geometry (Farhadia et al., 2017). This model performed slightly better in predicting the transversal velocities, with RMSE values of 0.0571 and 0.0680 for the Rozovskii (1961) and Guymer (1998) experiments, respectively, compared to values of 0.0642 and 0.0737 of the realizable k-ε model. The difference

is more obvious for the upper half of the channel cross-section. In terms of velocity distribution along the channel width, the maximum velocity occurs near the inner bank at the beginning of the bend and tends towards the outer bank near the bend exit, which agrees with other researchers who studied the velocity distribution in river bends such as De Vriend and Geldof, (1983). Both models followed the same pattern (i.e., better agreement with experimental data for the inner bank rather than the outer bank), with the standard k-ε model performing slightly better than the realizable k-ε. RMSE values of 0.0855 and 0.1635 were calculated for the standard k-ε and realizable k-ε models for velocity distribution along the channel width, respectively, and the mean RMSE was 0.0912 for the standard k-ε model and 0.1597 for the realizable k-ε.

On the other hand, the realizable k-ε model (also a LEVM) showed slightly greater success in terms of resolving secondary flows in a confluence. Confluent channels are generally more complex due to the interaction of two streams and their perpendicular shear stresses, which could contribute to a better performance of the realizable k-ε model for these channels. In terms of velocity distribution along the channel width, the realizable k-ε model performed slightly better in the confluent channel, with an RMSE value of 0.1700, compared to the 0.1795 value given by the standard k-ε model for the cross-section at x*=-3.0. The mean RMSE was 0.1741 for the standard k-ε model and 0.1698 for the realizable k-ε.

Although this type of model allows significant advances in understanding the dynamics of meanders and confluences, they are not the best models to match experimental and field measurements (Blanckaert and De Vriend, 2010; Seminara, 2006) and should be used with caution. Similar to previous studies [e.g., (Song et al., 2012)], overestimation of velocity at the inner bank and overestimation of velocity at the outer bank could be due to ignoring the proper feedback mechanism between the downstream velocity and the secondary circulation. It is expected that non-linear eddy viscosity models (NLEVMs) and Reynolds stress models (RSMs) would improve secondary current prediction, especially near inner and outer banks (Launder & Rodi, 1981).

To improve the correlation between the existing models and the field data, turbulence models showing the best matches should be looked at closer and improved upon. In addition, different wall function and Large Eddy Simulations (LESs) with higher resolution could be used to obtain results with higher levels of accuracy. The authors are currently working on the implementation of Non-linear Eddy Viscosity Models (NLEVMs) and Reynolds Stress Models (RSMs) in modelling secondary currents in river bends and confluences.

4.5. Conclusion

Given the frequency of bends and intersections in rivers, the study of flow characteristics in these areas is considered an important task. However, the complexity of flow features in these areas makes it difficult for them to be accurately captured and determined. Secondary flows are a flow characteristic in curved and confluent rivers, and so to study these phenomena, a finite volume method (FVM) 3D OpenFOAM numerical model was employed to study secondary currents in this study. This model was validated by using two sets of experimental data. Two turbulence models (the standard k-ε and realizable k-ε) were applied in this study, and the following conclusions can be drawn:

- According to the results achieved by simulating the curved channel, the distribution of flow velocity in both of the examined models (standard k-ε and realizable k-ε) indicates that the maximum velocity at the beginning of the channel curve occurs at the interior bank and then moves gradually towards the exterior bank near the bend exit, as expected. The comparison between the studied numerical models and the experimental and other numerical data showed good agreements between the experimental and numerical data. However, near the bend exit there is a slight variation in the two models, particularly at the inner bank, due to the change from a curved to a straight channel, which makes the flow features in this region complex and not easy to capture, showing the weaknesses of the two models in this area. For all the sections of the bend, when examining the flow velocity, the standard k-ε model performed better.
- The higher velocity in the confluent channel diverts from the branch channel towards the outer bank of the main channel, which is observed in both models and is in agreement with the laboratory observations. Regarding the flow velocity distribution, both numerical models (standard k-ε, and realizable k-ε) showed almost the same results, and both achieved good agreement with the experimental data. However, there was some variation for the cross-sections immediately after the junction. The sudden change in flow direction, from straight to curved, could be the main reason behind this variation, which leads to difficulty in determining the flow features in this area, or it may be because of a weakness of the two models at this area. In terms of preference, the realizable k-ε model is better.

Chapter 5. Numerical Simulation of Turbulent Flow in Bends and Confluences Considering Free Surface Changes Using the Volume of Fluid Method

Abstract

The impact of secondary flows on the flow velocity in open channel bends and confluences was simulated using three-dimensional (3D) numerical models. The Reynolds-averaged Navier– Stokes equation system was utilized as the governing equations and two different turbulence models were employed in this study: the standard k-ε model and the realizable k–ε model. In a recent study by the authors, the rigid lid approach was used, which does not allow for vertical displacement of the water surface. In this study, the simulation of free surface displacements was simulated using the volume of fluid free-surface tracking method. The numerical models were evaluated and validated by using the experimental data of a sharply curved channel and a confluent channel. The accuracies of the two turbulence models were evaluated and discussed. This study found that both models can satisfactorily reproduce the experimental data. However, the standard k–ε model performed better for the curved channel case while the Realizable k–ε model performed better for the confluent channel case.

Keywords: secondary flow; Free Surface Model; standard k–ε; realizable k–ε; OpenFOAM

---

[5] This chapter has been published as Rawaa Shaheed, Abdolmajid Mohammadian, and Xiaohui Yan (2022) Numerical Simulation of Turbulent Flow in Bends and Confluences Considering Free Surface Changes Using the Volume of Fluid Method. Water journal, 14, 1307. https://doi.org/10.3390/w14081307.

5.1. Introduction

The flow pattern in curved rivers and confluences is fairly complex due to the high turbulence and the three-dimensional (3D) flow characteristics. The flow in such areas is affected by the centrifugal force that results in a lateral gradient on the water's surface, which leads to a lateral pressure gradient at the cross-section. The interaction between the centrifugal force and the lateral pressure gradients due to the lateral slope of the water's surface results in the generation of secondary flow in the transverse direction of the bend. The helical motion of the secondary flow causes the particles near the bed to move inwards, and those near the water's surface to move outwards (Figure 5.1). Considering the impact of the secondary flow and velocity distribution on the flow pattern of open channel curves is of high significance due to its effect on erosion and sedimentation patterns in rivers, and transport of the pollutants.

The flow in curved rivers and confluences have been significantly studied in recent decades. Due to the merits of low-cost and high-efficiency, numerical modeling techniques have been widely adopted. The flow in curved rivers has been studied numerically by numerous studies using different kinds of numerical models due to the intricacy of flow features in this field. Some of these studies are described below.

The flow in rotating annular flumes at a mildly-curved 180° bend and a mildly curved river was measured and simulated by Booij (2003a) through the use of Large Eddy Simulation (LES) and Reynolds-Averaged Navier-Stokes (RANS) (standard k-ε) models. He concluded that the main features of the main flow and the secondary flow can be produced by the RANS model, but it failed to satisfactorily reproduce the complicated secondary flow fields in both curved flows. The pattern of the secondary flow computed by LES hardly deviated from the measured flow pattern in the rotative annular flume, and the turbulence was reproduced correctly. The main and secondary flow fields were reproduced well by LES for the slightly curved river. The second, counter-rotating, secondary flow cell along the upper external riverbank was yielded by LES computations, which contrasts with RANS computations.

The secondary flows in a spacious curved channel were studied by Huang et al. (2009) using a 3-D free-surface turbulence model with two turbulence closure schemes using two pressure solution methods. The turbulence closure schemes included a mixing-length model and the standard k-ε model, and the pressure solution methods included hydrostatic presumptions and dynamic pressure treatments. A similar pattern of secondary flow was produced by the mixing length model with

static and dynamic pressure treatments, and the center-region cell of the secondary flow could be predicted as well. In addition, a similar pattern of secondary flow was generated by the standard k-ε model with either static or dynamic pressure treatments, and the presence of the outer-bank cell and the center-region cell of secondary flows could also be predicted.

Detached Eddy Simulation (DES) was used by Constantinescu et al. (2010) to calculate the turbulence structure and the flow in an open channel 193° bend of very high curvature. The experimental data of Blanckaert (2003) was used to apply the model and compare the three-dimensional velocity distributions predicted by DES. The predicted results by DES to capture the distribution of the streamwise velocity in the mean flow, and the streamwise vorticity distribution in relevant cross-sections were satisfactory. Furthermore, the simulations indicated that DES is considerably more successful than Reynolds Averaged Navier Stokes (RANS) in forecasting the velocity redistribution in the channel.

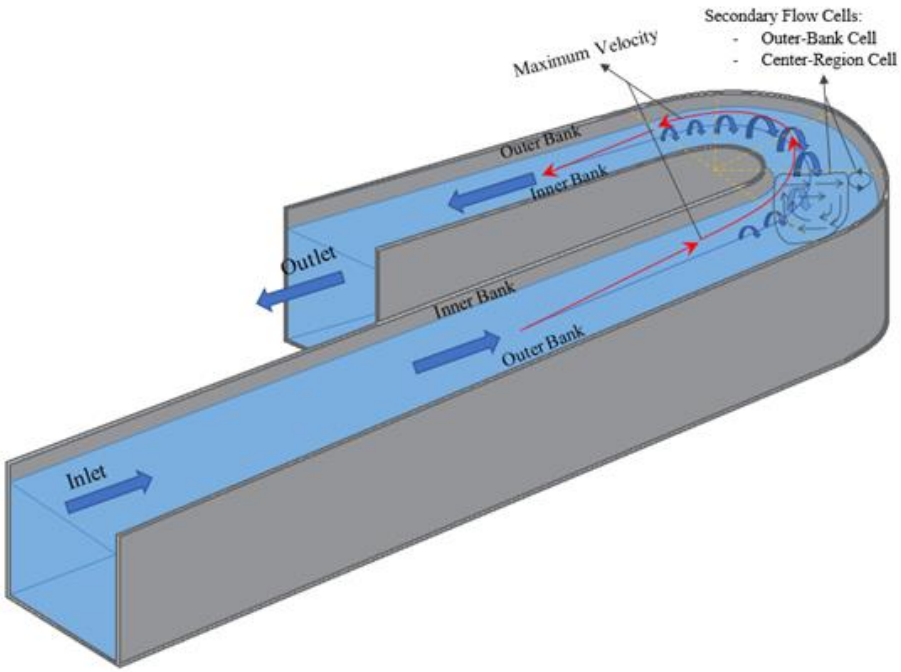

Figure 5.1: Flow pattern in a curved channel

The experimental data of Blanckaert was used by van Balen et al. (2010) to detect the characteristics of the main and secondary flow by applying and comparing large-eddy simulations (LES) and Reynolds-averaged numerical simulations (RANS) in a curved open channel. The strength of

secondary flow depends significantly on the turbulence in river bends which in turn plays a significant role in the substantial processes in natural rivers and especially in the flow areas close to the banks. The intensity of the center region cell was under anticipated by the RANS model and well anticipated by the LES model. The outer-bank cell of secondary flow was resolved accurately by LES, while RANS was unable to reproduce this process. The bed shear stress was overestimated by RANS as compared with LES. Consequently, overall friction losses that were measured experimentally over the bend were reproduced properly by LES, while they were overestimated by RANS.

The pattern of the flow in a 90° bend was studied empirically and numerically by Abhari et al. (2010) using the Sediment Simulation In Intakes with Multiblock (SSIIM 1.1) numerical model. The turbulence was expected by k-ε model, and the pressure was computed by the Semi-Implicit Method for Pressure Linked Equations (SIMPLE) method. A comparison of the results between the numerical model and the experimental data indicated the capability of SSIIM-1.1 in simulating the flow pattern accurately.

The flow patterns in a highly bent 90° open channel curve were studied experimentally and numerically by Gholami et al. (2014). The water-free surface was simulated using the volume of fluid (VOF) method and the turbulence was predicted by the k-ε (RNG) model. The results indicated that the higher flow velocity occurred close to the interior wall along the bend, and the influence of the secondary flows was not limited to the sections within the bend. Additionally, the k-ε (RNG) model and VOF methods have the capability to simulate the flow pattern in the strongly curved bends.

The experimental data of Blanckaert (2003) was also used by Abdou et al. (2021) to study the flow features in a strongly-curved open channel using the LES turbulence model. They concluded that the LES model had the capability to predict the produced super-elevation, stream and transverse velocities, and the two secondary circulation cells (main and outer bank cells).

The free surface flow in a steeply curved open channel with a 30° bend was studied numerically by Seyedashraf and Akhtari (2017). The experimental data of a sharp 90° bend was used to authorize the simulation results of the numerical model in a sharp 30° bend. The standard k-ε turbulence model and volume of fluid free-surface tracking method were used for the air-water interactions and turbulence closure. The results showed that the intensity of secondary flow in a 30° bend is

minor compared to the 90° bend. However, in these curves, the tendency toward flow separation is more intense because of the momentum of the liquid molecules passing the bend.

The experimental data of Rozovskii (1961) that includes a 180° sharply curved channel was used by Shaheed et al. (2018) to evaluate the Rigid Lid Model in the simulation of flow in curved channels. Two turbulence models (standard k-ε and realizable k-ε) were applied in this study. The results showed that both two models simulated the flow in the curved channel well. However, the standard k-ε model performed better than the realizable k-ε model.

The other common phenomenon in natural rivers is open-channel confluences that play an important role in hydraulic engineering works due to the complex interaction between the main channel and tributary flows. This complex interaction generates complex turbulent structures and leads to the evolution of six distinct zones (Best, 1987) (Figure 5.2): stagnation zone, deflection zone, separation zone, shear layers zone, extreme velocity zone, and recovery zone. Several variables could affect these turbulent structures like the discharge of the two channels, the junction angle, and the geometry of the channel. Thus, studying the features of this flow in such areas is not an easy matter and requires an important tool such as numerical simulation (Brito et al., 2014). In channel confluences, there are two counter-rotating helical cells: the secondary flow of the branch channel near the inner bank downstream of the main channel, and the secondary flow of the main channel near the outer bank downstream of the major channel (Figure 5.2). Because of the fluid viscosity, the two secondary flows fade gradually downstream of the main channel (Song et al., 2012). The complex flow characteristics in confluent channels have been studied numerically by many researchers using different kinds of numerical models. Some of these studies are described below.

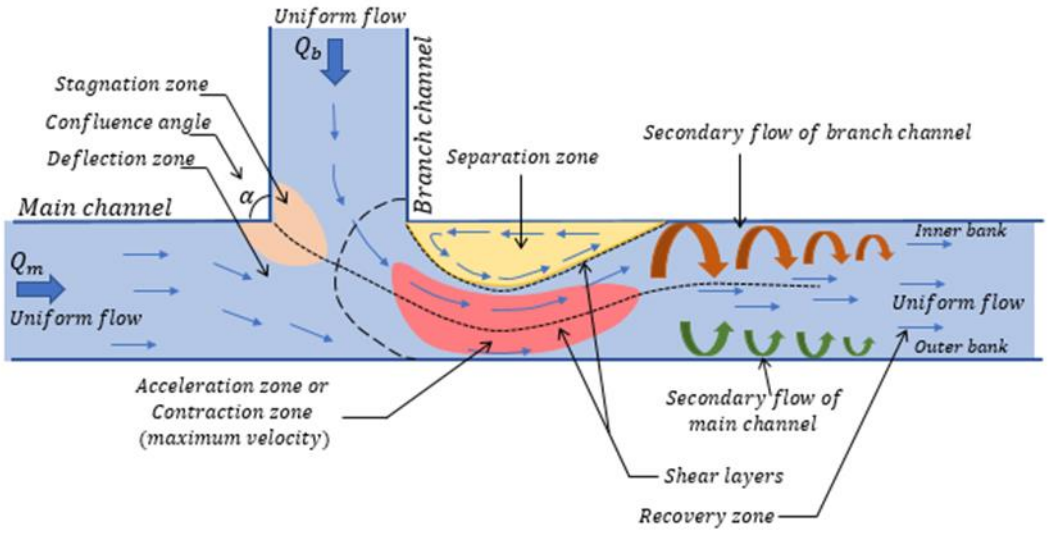

Figure 5.2: Flow pattern in a confluent channel (based on Shakibaeinia et al. (2010), from Best (1987)) , and secondary flow structure in a confluent channel (based on Song et al. (2012) after Weber (2001), (developed from Shaheed et al. (2021))

The flow in a 90° open channel junction was studied by Huang et al. (2002) using a three-dimensional numerical model. Reynolds-averaged Navier–Stokes (RANS) equations with incompressible and steady-state assumptions were employed, and the k–ω model of Wilcox (1993) was selected for this study. The experimental data of Shumate (1998) was used to validate the model with two distinctive flow discharges. Then, the influence of varying junction angles on flow characteristics was studied by applying this model. Consequently, they found that the significant hydrodynamic features of the flow in the junction were all reproduced by the developed 3D model, with a favorable agreement with the experimental data.

The flow structure in channel confluences was studied by Shakibaeinia et al. (2010) using a three-dimensional numerical model (SSIIM2.0) developed by Olsen (2006) and based on a finite volume discretization of Reynolds averaged Navier Stokes equations. The Re-Normalization Group RNG form of the k-ε turbulence model was practiced. The numerical model was first validated by comparing the simulated results with the experimental data of Shumate and Weber (1998), and then it was applied to examine secondary flows, velocity distribution, flow separation, and elevation of water surface under various circumstances. The results showed that a strong tributary helical cell occurred in the post confluence channel due to the flow deflection. There was also a weaker helical

cell created by the main flow, which rotates against the tributary helical cell. The results also showed that the confluence angle, discharge, width ratio, and Froude number significantly affected the flow structure and water surface variation because of their impact on flow deflection, secondary flows, and separation zone.

The experimental data of Weber et al. (2001) was used by Yang et al. (2013) to simulate the flow numerically in a right angle confluence open channel with the dynamic mesh technique. ANSYS FLUENT and three numerical models including standard k-ε, realizable k-ε, and k-ω were used to conduct the simulation. The surface position was tracked using three types of surface treatment methods: rigid lid, volume of fluid (VOF), and self-proposed codes with dynamic mesh technique. The results showed that the accuracy of the simulation was impacted greatly by the method of surface treatment for the same adopted turbulence models. The free surface was treated as an assumed surface in the method of the rigid lid, and a large error was generated when the actual surface differed greatly. The precision of the VOF method was better than the rigid lid process as it captured the free surface via a multi-phase model. However, for the shallow water flow, the accuracy was still poor. The dynamic mesh technique showed a good agreement with the experimental data, and turbulence models showed little effect on water level tracking. The k-ω model was preferable for the distribution of velocity in the confluence flow simulation.

The flow at a 70° open-channel confluence was studied by Brito et al. (2014) using a 3D numerical simulation. The simulation was conducted using Reynolds-averaged Navier-Stokes (RANS) equations and five turbulence closure models including: k-ε, RNG k-ε, k-ω, SST k-ω, and Explicit Algebraic Reynolds Stress Models (EARSM). The interaction between the air and water at the free surface was modeled by the volume of fluid (VOF) method as well. The results of the simulation were compared with the experimental data of Birjukova et al. (2014), which demonstrated that simple two-equation turbulence models are insufficient to obtain an accurate flow field description in confluences due to the complexity of flows at such areas. The EARSM showed a reasonably good representation for the separation zone while it underestimated the time-averaged streamwise velocity in the maximum velocity zone.

The experimental data of Shumate (1998) that includes a 90° angle confluent channel was used by Shaheed et al. (2018) to evaluate the Rigid Lid Model in the simulation of flow in confluent channels. Two turbulence models (standard k–ε and realizable k–ε) were applied in this study. The

results showed that both of the two models simulated the flow in the confluent channel well. However, the realizable k–ε model performed better than the standard k–ε model.

However, there is a gap in the literature about the performance of different turbulence models in predicting the secondary flow in channel bends and confluences while simulating free surface displacements. In (Shaheed et al., 2018) a rigid lid approach was used prohibited vertical motions of the free surface. This study employed two turbulence models to simulate the dynamics of free surface displacement, the volume of fluid methods is used. Therefore, the primary aim of this study is to comprehend what range of selected turbulence models can model the flow field in open channel curves and confluences. In view of this, two commonly used effective turbulence models (standard k–ε and realizable k–ε) were selected to evaluate their performance in such simulations.

5.2. Numerical Modeling

Numerical modeling has recently become one of the widely used methods in studying river flows, and in this study, the OpenFOAM (Open Field Operation and Manipulation) model was utilized in this study to simulate the flow in curved rivers and confluences. OpenFOAM uses the finite volume method and contains different numerical schemes that are employed for both time and space integration. More information about OpenFOAM has been well documented in the user manual (OpenFOAM, 2015). InterFoam solver is used in this study, which is usually utilized for incompressible and turbulent flows in the cases of open channels (also referred to as the Free Surface Model). The free water surface was simulated using the volume of fluid (VOF) method and the turbulence was predicted using standard k–ε and realizable k–ε turbulence models. The basic concept of the VOF technique is to define functions to represent the volume fraction (relative proportion of volume) of water and air in the model area. In each cell, the sum of the volume fractions of water and air is 1. For a computing cell, there are three situations:

$\alpha = 1$ means that the cell is filled with water, $\alpha = 0$ means that the cell is filled with air, and $0 < \alpha < 1$ means that the cell has a water-air interface.

The 3D Reynolds–Averaged Navier–Stokes equations (RANS) for mass and momentum conservation can be expressed as follows:

Continuity:

$$\frac{\partial}{\partial x}\left(u_x\right)+\frac{\partial}{\partial y}\left(u_y\right)+\frac{\partial}{\partial z}\left(u_z\right)=0 \tag{5-1}$$

Momentum in the x-direction:

$$\frac{\partial(\rho u_x)}{\partial t}+\frac{\partial}{\partial x}(\rho u_x u_x)+\frac{\partial}{\partial y}\left(\rho u_y u_x\right)+\frac{\partial}{\partial z}(\rho u_z u_x) = -\frac{\partial p}{\partial x}+\frac{\partial \tau_{xx}}{\partial x}+\frac{\partial \tau_{yx}}{\partial y}+\frac{\partial \tau_{zx}}{\partial z}+\rho g_x \tag{5-2}$$

Momentum in the y-direction:

$$\frac{\partial\left(\rho u_y\right)}{\partial t}+\frac{\partial}{\partial x}\left(\rho u_x u_y\right)+\frac{\partial}{\partial y}\left(\rho u_y u_y\right)+\frac{\partial}{\partial z}\left(\rho u_z u_y\right) = -\frac{\partial p}{\partial y}+\frac{\partial \tau_{xy}}{\partial x}+\frac{\partial \tau_{yy}}{\partial y}+\frac{\partial \tau_{zy}}{\partial z}+\rho g_y \tag{5-3}$$

Momentum in the z-direction:

$$\frac{\partial(\rho u_z)}{\partial t}+\frac{\partial}{\partial x}(\rho u_x u_z)+\frac{\partial}{\partial y}\left(\rho u_y u_z\right)+\frac{\partial}{\partial z}(\rho u_z u_z) = -\frac{\partial p}{\partial z}+\frac{\partial \tau_{xz}}{\partial x}+\frac{\partial \tau_{yz}}{\partial y}+\frac{\partial \tau_{zz}}{\partial z}+\rho g_z \tag{5-4}$$

where ρ is the density; t is the time, u_x, u_y, and u_z are the velocity components in the x, y, and z directions respectively; p is the pressure; τ_{ij} denotes a stress in the j-direction exerted on a plane perpendicular to the i-axis; g_x, g_y, and g_z are the gravitational acceleration components in the x, y, and z directions respectively (Wendt, 2008).

The OpenFOAM numerical model solves the Navier Stokes equations with the two models on a three-dimensional grid. The continuity equation and the Reynolds averaged Navier-Stokes equations are solved to determine the flow field for three-dimensional geometry. The turbulence model's objective is to close the RANS equations and to compute the Reynolds stresses. Standard k–ε (Launder and Spalding, 1972) and realizable k–ε (Shih et al., 1995) turbulence models are two-equation models. Two extra transport equations are included in these models to represent the turbulent flow properties. The first transport variable is turbulent kinetic energy, k, and the second is the turbulent dissipation, ε.

The standard k–ε model can be written as:

$$\frac{\partial k}{\partial t}+\frac{\partial k u_i}{\partial x_i}-\frac{\partial}{\partial x_i}\left(D_{keff}\frac{\partial k}{\partial x_i}\right)=G-\varepsilon \tag{5-5}$$

$$\frac{\partial \varepsilon}{\partial t}+\frac{\partial \varepsilon u_i}{\partial x_i}-\frac{\partial}{\partial x_i}\left(D_{\varepsilon eff}\frac{\partial \varepsilon}{\partial x_i}\right)=c_{1\varepsilon}\frac{\varepsilon}{k}G-c_{2\varepsilon}\frac{\varepsilon^2}{k} \tag{5-6}$$

$$D_{keff}=\nu_t+\nu \tag{5-7}$$

$$D_{\varepsilon eff}=\frac{\nu_t}{\sigma_\varepsilon}+\nu \tag{5-8}$$

$$\nu_t=c_\mu\frac{k^2}{\varepsilon} \tag{5-9}$$

$$G=2\nu_t S_{ij}S_{ij} \tag{5-10}$$

$$S_{ij}=\frac{1}{2}\left(\frac{\partial u_j}{\partial x_i}+\frac{\partial u_i}{\partial x_j}\right) \tag{5-11}$$

where σ_ε, $c_{1\varepsilon}$, $c_{2\varepsilon}$, c_μ are model constants equal to 1.3, 1.44, 1.92, and 0.09, respectively; k is the turbulent kinetic energy; ε is the turbulent energy dissipation rate; u_i is the instantaneous velocity component in the direction xi; Dkeff and Dεeff are the effective diffusivity for k and ε, respectively; νt is the turbulent kinematic viscosity; ν is the kinematic viscosity; G is the production of turbulence due to shear; Sij is the strain-rate tensor; dev denotes the deviatoric component.

The Realizable k–ε model employed in the present study can be expressed as:

$$\frac{\partial k}{\partial t}+\frac{\partial k u_i}{\partial x_i}-\frac{\partial}{\partial x_i}\left(D_{keff}\frac{\partial k}{\partial x_i}\right)=G-\varepsilon \tag{5-12}$$

$$\frac{\partial \varepsilon}{\partial t}+\frac{\partial \varepsilon u_i}{\partial x_i}-\frac{\partial}{\partial x_i}\left(D_{\varepsilon eff}\frac{\partial \varepsilon}{\partial x_i}\right)=\sqrt{2}c_{1\varepsilon}S_{ij}\varepsilon-c_{2\varepsilon}\frac{\varepsilon^2}{k+\sqrt{\nu\varepsilon}} \tag{5-13}$$

$$D_{keff}=\frac{\nu_t}{\sigma_k}+\nu \tag{5-14}$$

$$D_{\varepsilon eff}=\frac{\nu_t}{\sigma_\varepsilon}+\nu \tag{5-15}$$

$$\nu_t=C_{\mu r}\frac{k^2}{\varepsilon} \tag{5-16}$$

$$C_{\mu_r} = \frac{1}{A_0 + A_s U_s \frac{k}{\varepsilon}} \tag{5-17}$$

$$A_s = \sqrt{6}\cos\varphi_s \tag{5-18}$$

$$\varphi_s = \frac{1}{3} arccos\{min[max(\sqrt{6}W, -1), 1]\} \tag{5-19}$$

$$W = \frac{2\sqrt{2}S_{ij}S_{jk}S_{ki}}{S_{mag}S_2} \tag{5-20}$$

$$S_{mag} = \sqrt{S_2} \tag{5-21}$$

$$S_2 = 2\left(dev(S_{ij})\right)^2 \tag{5-22}$$

$$S_{ij} = \frac{1}{2}\left(\frac{\partial u_j}{\partial x_i} + \frac{\partial u_i}{\partial x_j}\right) \tag{5-23}$$

$$U_s = \sqrt{\frac{S_2}{2} + \Omega_{ij}\Omega_{ij}} \tag{5-24}$$

$$\Omega_{ij} = \frac{1}{2}\left(\frac{\partial u_j}{\partial x_i} - \frac{\partial u_i}{\partial x_j}\right) \tag{5-25}$$

$$G = \nu_t S_2 \tag{5-26}$$

$$c_{1\varepsilon} = max\left(\frac{\eta}{5+\eta}, 0.43\right) \tag{5-27}$$

$$\eta = S_{mag}\frac{k}{\varepsilon} \tag{5-28}$$

where Ωij is the vorticity (spin) tensor; σ_k, σ_ε, A_0, $c_{2\varepsilon}$ are model constants equal to 1, 1.2, 4, and 1.9 respectively.

The boundary of the flow inlet was set as a velocity inlet condition which was (0.265 m/s) for the curved channel and (0.628) for the confluent channel, and the flow outlet was set as a zero-gradient boundary condition. The boundary of the free surface was set as an atmospheric boundary condition. The standard wall functions (Launder and Spalding, 1974) were used for the sidewalls and bed. The free surface was modeled using the volume of method (VOF) according to the following equation:

$$\frac{\partial \alpha}{\partial t} + \frac{\partial(\alpha x)}{x} + \frac{\partial(\alpha y)}{y} + \frac{\partial(\alpha z)}{z} = 0 \qquad (5\text{-}29)$$

5.3. Verification of Numerical Model

5.3.1. Curved Channel

One of the previous experimental studies on curved channels is the experimental study of Rozovskii (1961) who reported the results of velocity fields and water surface in a 180-degree sharp curved channel. The numerical model was utilized to simulate the experiment of Rozovskii, the channel setup of which is demonstrated in Figure 5.3. This channel consisted of a straight channel in a 6 m length followed by a 180° curve with a mean radius of 0.8 m and then the outlet in a 3 m straight channel length. The cross-section was a 0.8 m wide rectangle, and the whole channel was set on a horizontal bed (Song et al., 2012). The channel's characteristics and some hydraulic data gained from Rozovskii's experiment are shown in Table 5.1.

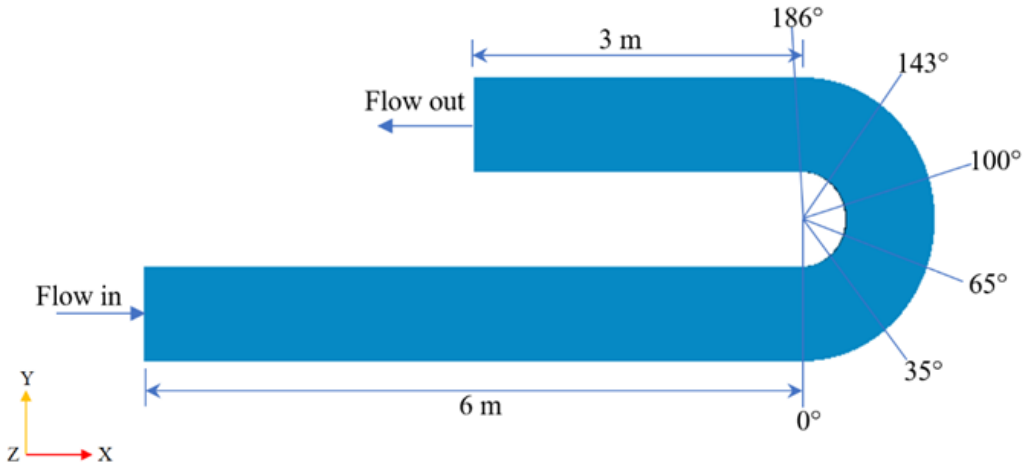

Figure 5.3: Rozovskii's experimental data (Shaheed et al., 2018)

Table 5.1: The flow conditions and dimensions of the curved channel (Rozovskii, 1961)

Variable	Symbol	Value
Upstream discharge	Q	0.0123 m3/s
Downstream water depth	h	0.058 m
Channel width	B	0.8 m
Bend angle	θ	180º
Internal radius of curvature	r_i	0.4 m
Mean radius of curvature	r_c	0.8 m
Mean radius to width ratio	r_c/B	1.0
Che'zy factor	C	60
Mean velocity at downstream	U_∞	0.265 m/s
Tailwater Froude number	Fr_d	0.35

5.3.1.1. Boundary Conditions and Mesh Generation

The model of the curved channel includes four different boundaries as shown in Figure 5.4: the inlet, the outlet, the walls (sidewalls and bottom), and the channel surface (atmosphere). The mesh that was used in the simulation is shown in Figure 5.5 and it was refined to better resolve the velocity, especially at the curve which is the study area and near the two banks of the channel. The mesh resolution was determined based on mesh sensitivity analyses: the results obtained by the current mesh and those provided by a finer mesh were almost identical. The flow was discharged with a primary velocity of U_0. The boundary conditions were chosen as: $u_x = U_0$; $u_y = u_z = 0$; $k = 0.06u2$; and $\varepsilon = 0.06u3D$, where D is the average water depth. The Courant number in all cases was kept below 0.9.

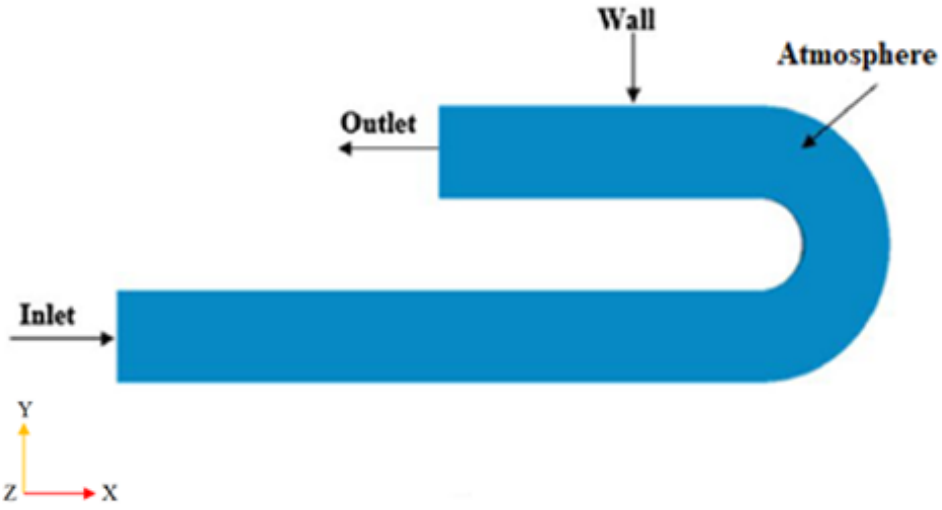

Figure 5.4: Boundary conditions

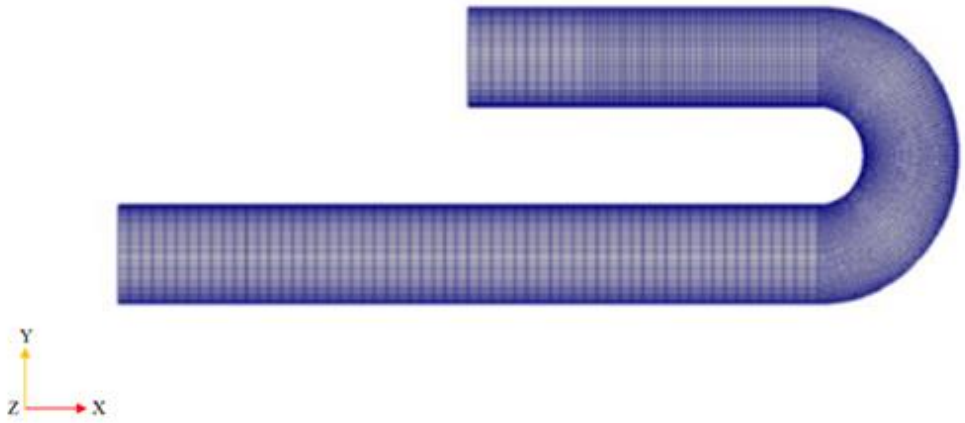

Figure 5.5: The refined mesh

5.3.2. Results of Curved Channel

5.3.2.1. Velocity Distribution

The velocity distribution of the curved open channel is shown in Figure 5.6 and Figure 5.7 for the two numerical models. It appeared that the maximum velocity moved from the internal bank at the start of the curve to the external bank near the exit of the bend, which is consistent with previous experimental and numerical studies for bend flow (Yan et al., 2020; Shaheed et al., 2018).

Figure 5.6: The distribution of water surface velocity (Standard k-ε)

Figure 5.7: The distribution of water surface velocity (Realizable k-ε)

5.3.2.2. Longitudinal Velocity Distribution

The simulated longitudinal velocity of the curved open channel for the two numerical models was compared with the experimental data of Vaghefi et al. (2015), who performed their experiment in a 180° curved open channel with some difference in dimensions from the experiment of Rozovskii (1961). The simulated longitudinal velocity at the section close to the water surface agreed well with the experimental data, as shown in Figure 5.8.

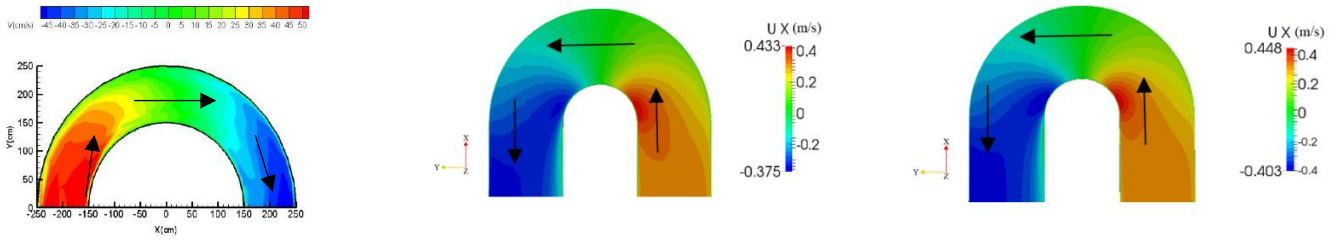

(**a**) (**b**) (**c**)

Figure 5.8: Longitudinal velocity contours. (a) contours of longitudinal velocity in the plan views- experiment (Mohammad Vaghefi et al., 2015); (b) contours of longitudinal velocity in the plan views- simulated (Standard k-ε); (c) contours of longitudinal velocity in the plan views- simulated (Realizable k–ε)

5.3.2.3. Properties of Flow Velocity

Figure 5.9 shows the depth-averaged velocity across the width of the channel, where: U is the depth averaged velocity magnitude; and $u, v,$ and w are the longitudinal, vertical, and lateral velocity averaged over depth, respectively. Note that the depth-averaged velocity is represented by the vertical axis and is non-dimensionalized by U_1, which is the downstream mean velocity. The horizontal axis represents the radial distance $(r - r_i)/B$, non-dimensionalized by the channel

width; where B is the channel width and r and r_i are the radius of curvature for the outer and inner banks, respectively. The velocity of the flow at the bend area was examined by taking some cross-sections at different locations of the bend including (0°, 35°, 65°, 100°, 143°, and 186°), as shown in the figure. The two numerical models were compared with the experimental data Rozovskii (1961) and other models of other researchers (Lien et al., 1999; Yeh and Kennedy, 1993; Johannesson, 1988; Shaheed et al., 2018) in these sections as well. It is clear from these cross-sections that the velocity of the flow increased near the interior bank at the beginning of the bend and then moved towards the exterior bank near the exit of the bend. Both numerical models performed well with some minor differences, especially near the two-channel banks. The flow near the banks is subjected to the effects of anisotropy, so it is quite common that a numerical model performed relatively worse in these regions.

To further assess the performance of the numerical models, the index root-mean-squared error (RMSE) was used to quantify the agreement between the two models and the experiment.

$$\mathrm{RMSE} = \sqrt{\sum_{i=1}^{n} \frac{(\hat{y_i} - y_i)^2}{n}} \tag{5-30}$$

where n is the number of observations, and $\hat{y}_i$ are predicted values, y_i is observed values.

Table 5.2 shows the sectional RMSE of the resultant velocity for each model. Considering the average RMSE calculations and despite the convergence of the results, the standard k-ε model of closed channel or Rigid Lid Model (RLM) was better than the Standard k-ε model of open channel or Free Surface Model (FSM), while the realizable k-ε model of the open channel (FSM) was better than the realizable k-ε model of the closed channel (RLM).

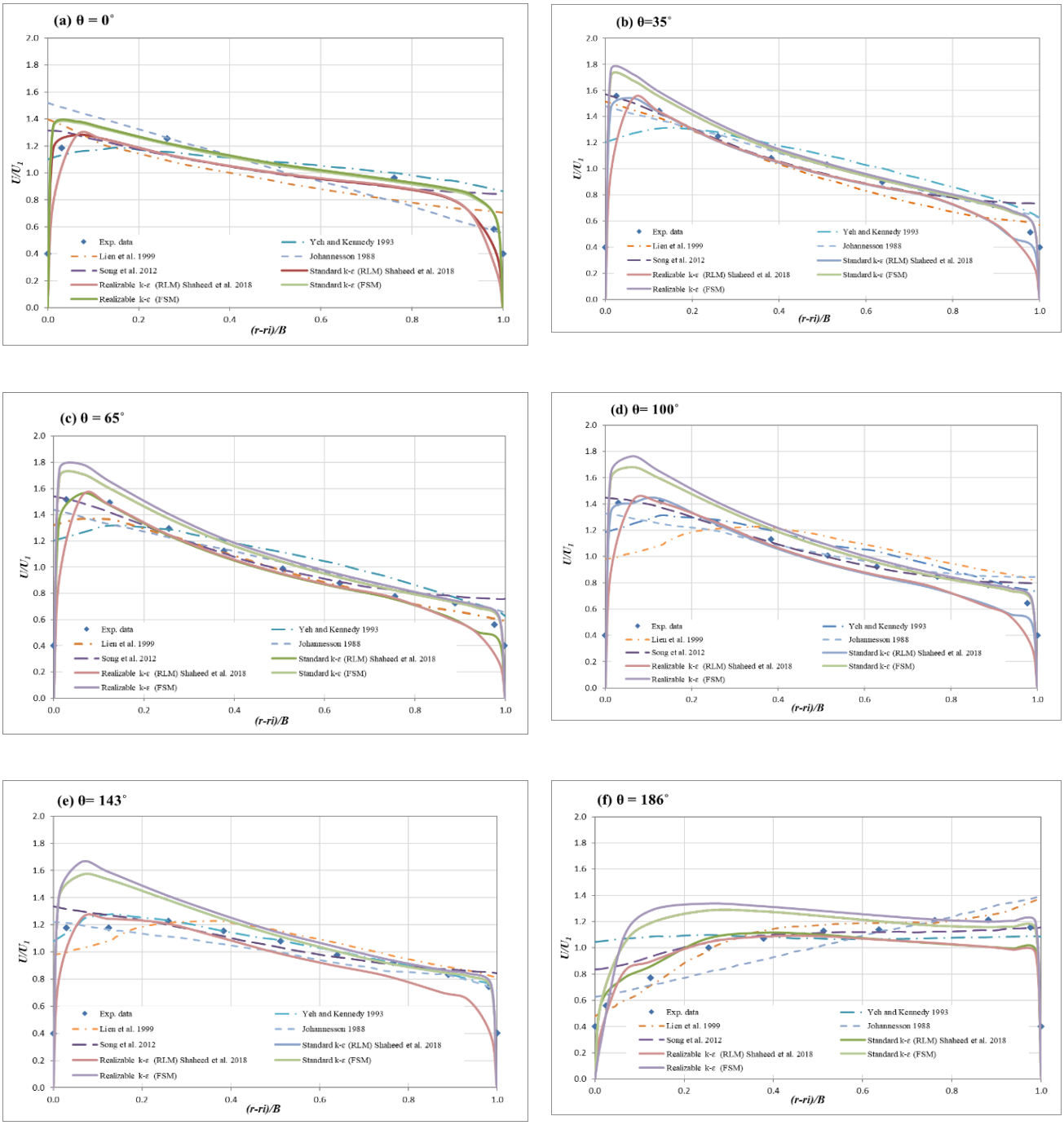

Figure 5.9: The resultant velocities comparison across the dimensionless channel width: (a) at θ=0°; (b) at θ=35°; (c) at θ=65°; (d) at θ=100°; (e) at θ=143°; and (f) at θ=186°

Although the values of R^2 as shown in Table 5.3 for the two models of the open channel or Free Surface Model (FSM) were similar to each other and similar to the R^2 values of the closed channel or Rigid Lid Model (RLM), these values were small at the start of the curve and smaller at the end

of the bend, which means that the two models were weak at this area when the direction of the flow changed from straight to curved and vice versa. In addition, this could be attributed to the complexity of flow features for these areas, which makes it not easy to be captured by numerical models. Accordingly, it could be concluded that the RLM was better at the start and end of the curve, while FSM was better at the middle of the bend. For RLM, the standard k-ε model reduced the averaged RMSE by about 42.9% and increased the averaged R^2 value by more than 10.5% compared to the realizable k-ε model. For FSM, the standard k-ε model reduced the averaged RMSE by about 18.3% but increased the averaged R^2 value by approximately 0.1% compared to the realizable k-ε model.

Table 5.2: RMSE estimation for resultant velocities in Figure 5.9

θ (°)	Models							
	Yeh and Kennedy	Lien et al.	Johannesson	Song et al.	Standard k-ε model (RLM)	Realizable k-ε model (RLM)	Standard k-ε model (FSM)	Realizable k-ε model (FSM)
0	0.1515	0.1462	0.1663	0.1555	0.0972	0.1706	0.0848	0.0869
35	0.1790	0.1163	0.0782	0.1026	0.0757	0.1741	0.0718	0.0948
65	0.1771	0.1063	0.1070	0.0963	0.0733	0.1668	0.0846	0.1174
100	0.1287	0.1020	0.1339	0.0731	0.0855	0.1635	0.1063	0.1388
143	0.0476	0.1255	0.0866	0.0887	0.0975	0.1574	0.1618	0.1903
186	0.2838	0.0978	0.1682	0.1514	0.1183	0.1262	0.1917	0.2297
Mean RMSE	0.1613	0.1157	0.1234	0.1112	0.0912	0.1597	0.1168	0.1429

Table 5.3: R^2 values of resultant velocities in Figure 5.9

θ (°)	R^2 values			
	Standard k-ε model (RLM)	Realizable k-ε model (RLM)	Standard k-ε model (FSM)	Realizable k-ε model (FSM)
0	0.9668	0.9272	0.8939	0.8994
35	0.9895	0.8383	0.9897	0.99
65	0.9892	0.8575	0.994	0.9922
100	0.9948	0.8677	0.993	0.9916
143	0.9637	0.884	0.8859	0.8956
186	0.7494	0.7406	0.5116	0.5062

5.3.2.4. Helical Path

The helical path of the fluid particles could be represented by the vectors at the section in the middle of the bend shown in Figure 5.10 for the standard k-ε model and Figure 5.11 for the Realizable k-ε

model. The vectors are more numerous and larger close to the internal bank of the curve, as the maximum velocity occurred in this area.

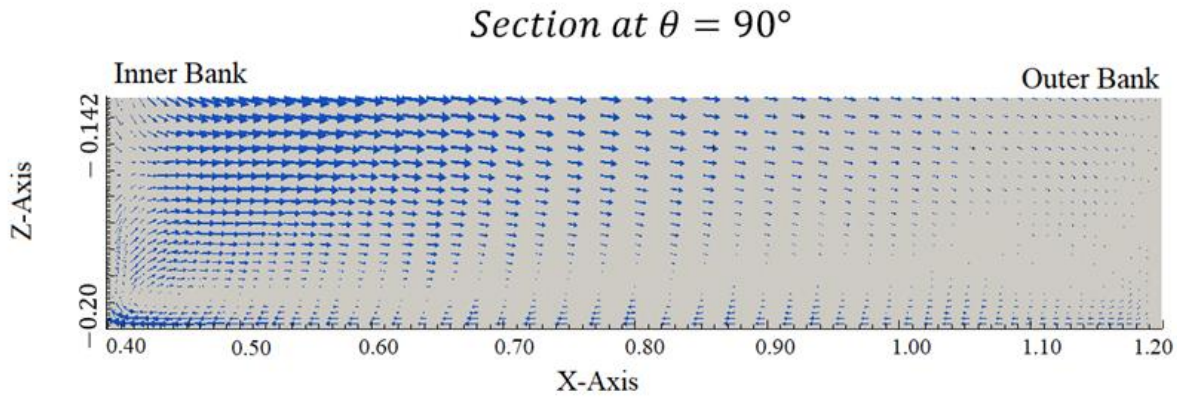

Figure 5.10: The velocity vectors at θ=90° (Standard k-ε)

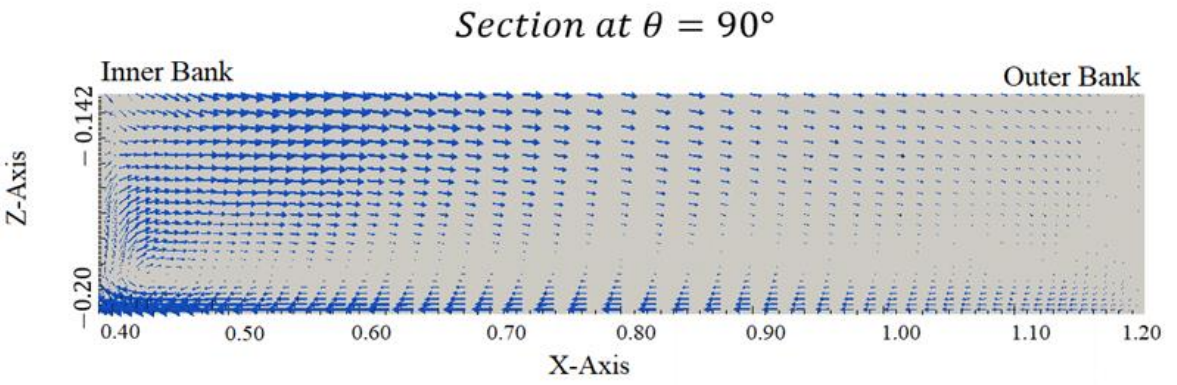

Figure 5.11: The velocity vectors at θ=90° (Realizable k-ε)

5.3.3. Confluent Channel

The open channel confluence flow experiment of Shumate (1998) was used to apply the model of the confluent channel. In this experiment, a branch channel joins with the main channel at a 90° angle as shown in Figure 5.12. The information on the channel and flow parameters is shown in Table 5.4.

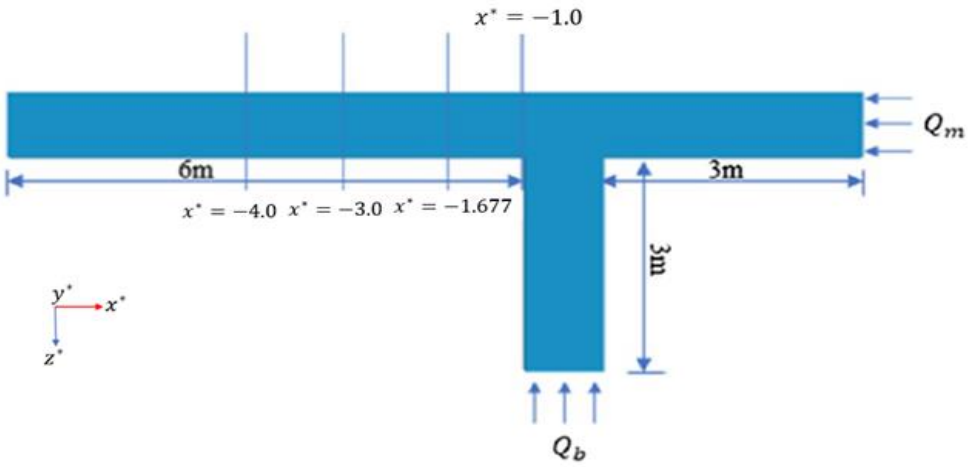

Figure 5.12: The confluent channel model (Shaheed et al., 2018)

Table 5.4: The flow conditions and dimensions of the confluent channel (developed from Shumate)

Variable	Symbol	Value
Main channel discharge	Q_m	0.043 m^3/s
Branch channel discharge	Q_b	0.127 m^3/s
Downstream water depth	h	0.296 m
Channel width	B	0.914 m
Che'zy factor	C	60
Mean velocity at downstream	U_∞	0.628 m/s
Tailwater Froude number	Fr_d	0.37

5.3.3.1. Boundary Conditions and Mesh Generation

Figure 13 shows the confluent channel boundary conditions. They are similar to those of the curved channel mentioned previously in Section 3.1.1 because of the boundary's identical nature. The mesh is shown in Figure 14, and it was also refined for a better resolution.

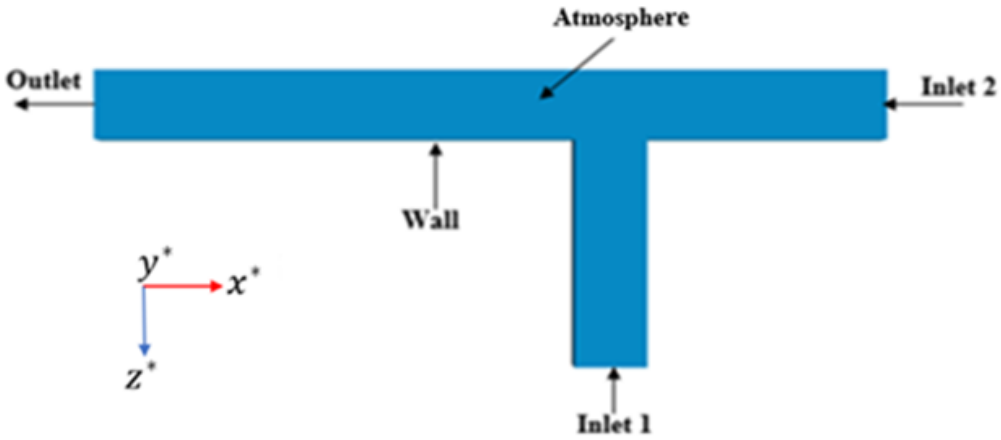

Figure 5.13: Boundary conditions for open channel

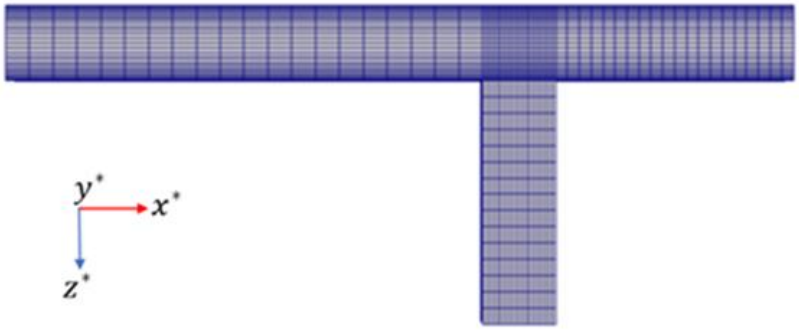

Figure 5.14: The refined mesh

5.3.4. Results of Confluent Channel

5.3.4.1. Velocity Distribution

The velocity distribution of the curved open channel is shown in Figure 5.15 and Figure 5.16 for the two numerical models. The differences in the distribution of water surface velocity obtained by the two models were insignificant. It appeared that the maximum velocity moved towards the outside bank of the main channel.

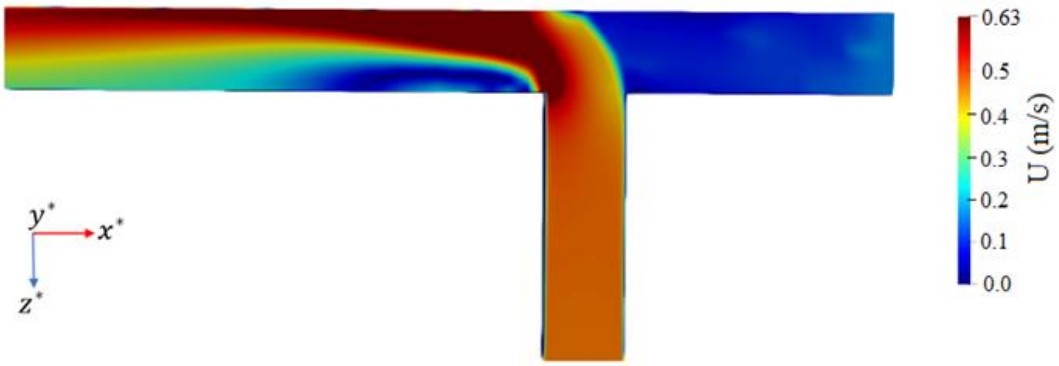

Figure 5.15: The distribution of water surface velocity (Standard k-ε)

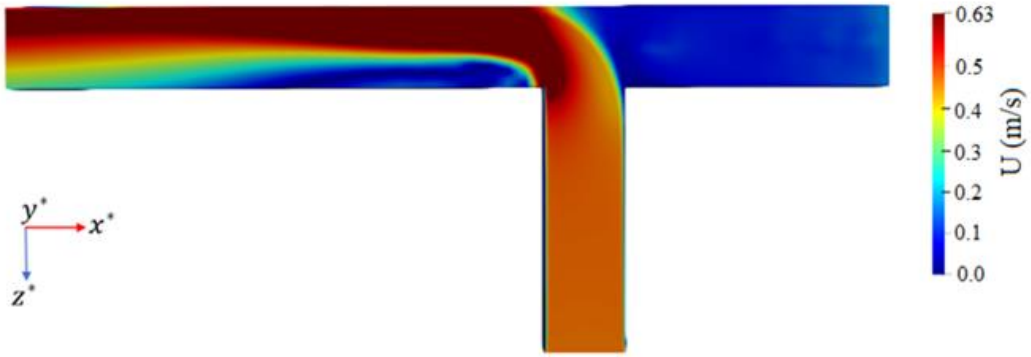

Figure 5.16: The distribution of water surface velocity (Realizable k-ε)

5.3.4.2. Properties of Flow Velocity

Figure 5.17 shows the depth-averaged velocity across the width of the channel, where: U is the depth-averaged velocity magnitude, which is non-dimensionalized by U_1 (the downstream mean velocity); $x^* = x/B$, with the x coordinate non-dimensionalized by the channel width; $z^* = z/B$, with the z coordinate non-dimensionalized by the channel width; and B is the channel width. The obtained results indicate that the distribution of the flow velocity for the two numerical models is somewhat similar. The higher velocity moved from the branch channel as the secondary flow entered the main channel towards the outside bank of the main channel. Some cross-sections were taken at the main channel immediately after the convergence and afterward to study the velocity curve in this area (see Figure 5.12). The simulated results of the numerical models were compared with the experimental data (Shumate, 1998) and the agreement of both models was reasonable. However, for the first section, the experiment was underestimated by the two numerical models, while for the other three sections, the simulated results were close to the experimental results near

the inside bank but underestimated the experimental results near the outside bank. A possible reason for the underestimation is that the non-homogeneity and anisotropy of turbulence near the outside bank were more significant, and it is typical that a RANS model cannot well predict the non-homogeneity and anisotropy of turbulence. Referring to the RMSE values of the two models shown in Table 5.5, the mean RMSE of the realizable k-ε model had the lowest value, which means it performed better. However, the difference between the two models was not significant.

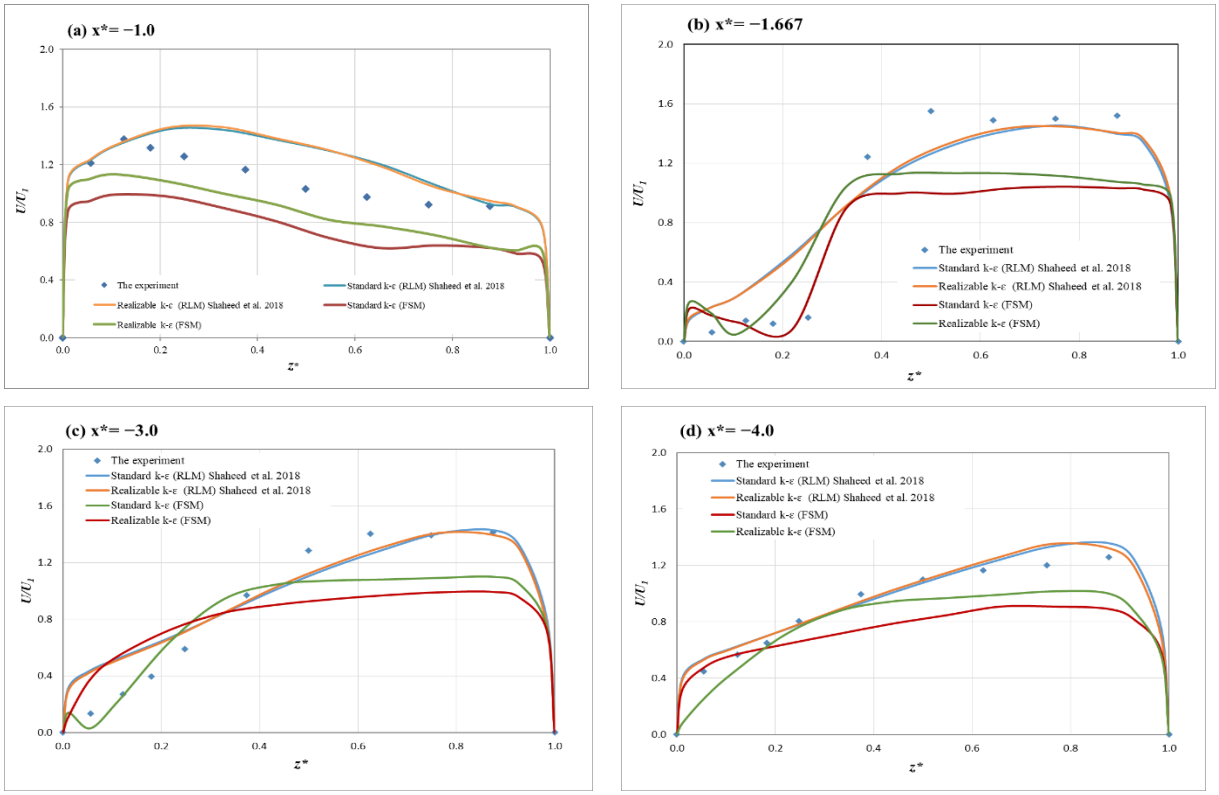

Figure 5.17: Resultant velocities across dimensionless transverse distance for confluent channel (a) at x* = -1.0 (b) at x* = -1.667 (c) at x* = -3.0 (d) at x* = -4.0

Table 5.5: RMSE estimation for the resultant velocities in Figure 5.17

Cross-Sections	Models			
	Standard k-ε Model (RLM)	Realizable k-ε Model (RLM)	Standard k-ε Model (FSM)	Realizable k-ε Model (FSM)
−1.0	0.1775	0.1798	0.3110	0.2075
−1.667	0.2688	0.2610	0.3518	0.3182
−3.0	0.1795	0.1700	0.3199	0.2051
−4.0	0.0708	0.0687	0.2271	0.1543
Mean RMSE	0.1741	0.1698	0.3024	0.2212

The values of R^2 shown in Table 5.6 indicate that both numerical models achieved high values of R^2 and were close to those values of the closed channel or RLM.

Table 5.6: R^2 values of the resultant velocities in Figure 5.17

Cross Sections	R^2			
	Standard k-ε model (RLM)	Realizable k-ε model (RLM)	Standard k-ε model (FSM)	Realizable k-ε model (FSM)
−1.0	0.5872	0.6081	0.9612	0.9293
−1.667	0.9231	0.9301	0.9773	0.9148
−3.0	0.9583	0.9707	0.925	0.9176
−4.0	0.9578	0.9647	0.9806	0.943

5.3.4.3. Helical Path

The helical path of the fluid particles can be represented by the vectors in two sections, one of them at x* = −1.667 and the other at x* = −3.0 as shown in Figure 5.18 and Figure 5.19 for the standard k-ε model, respectively. Figure 5.20 and Figure 5.21 represent the same sections for the realizable k-ε model, respectively.

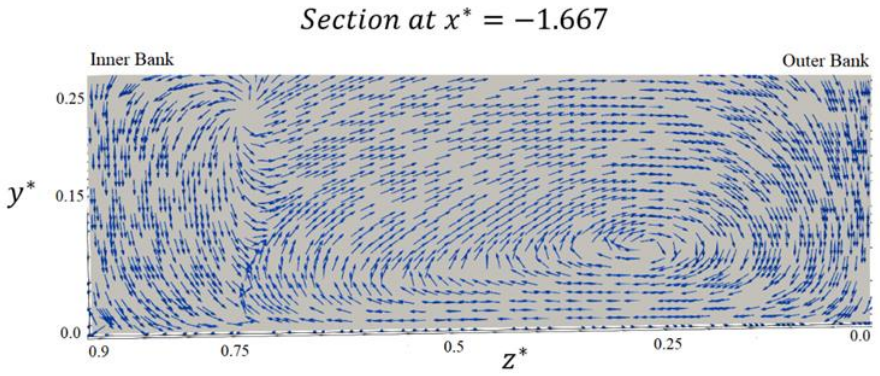

Figure 5.18: The vectors of velocity at section x*= -1.667 (Standard k-ε)

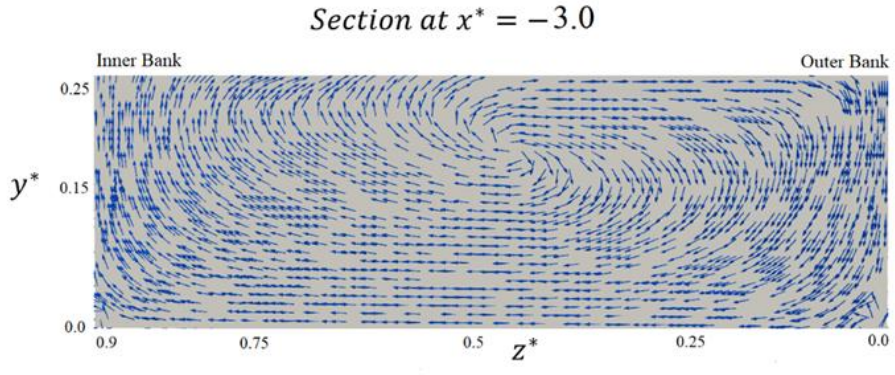

Figure 5.19: The vectors of velocity at section x*= -3.0 (Standard k-ε)

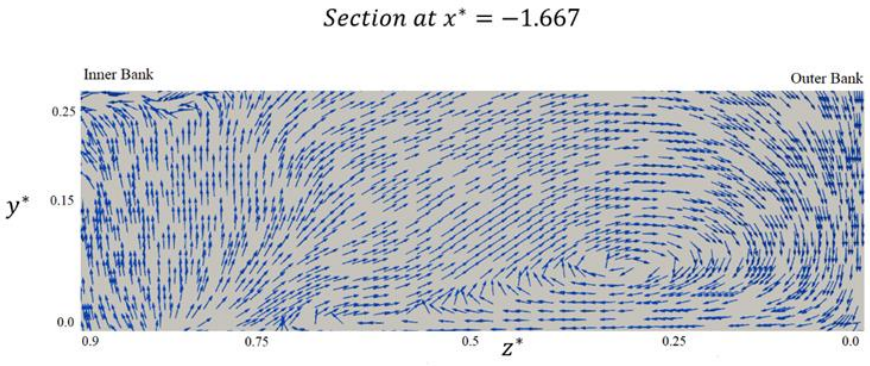

Figure 5.20: The vectors of velocity at section x*= -1.667 (Realizable k-ε)

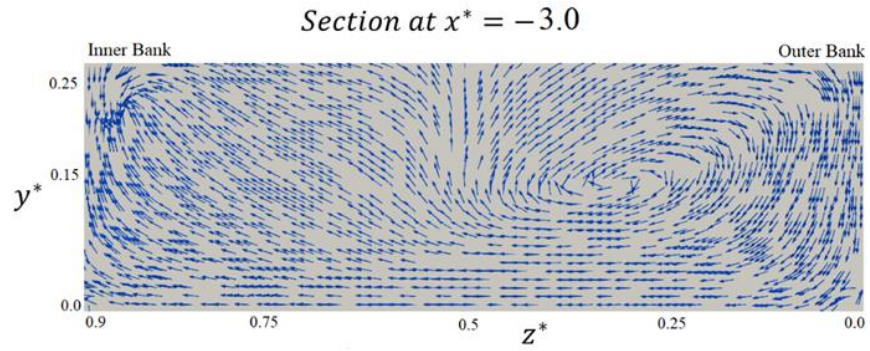

Figure 5.21: The vectors of velocity at section x*= -3.0 (Realizable k-ε)

5.3.4.4. Longitudinal Velocity Distribution

The simulated results for longitudinal velocity distribution were compared with the experimental data of Weber et al. (2001) as shown in Figure 5.22 which represents a longitudinal section close to the water surface, and the results seem reasonable. Immediately below the channel junction and along the wall adjacent to the junction there was a zone of low velocity which represents the separation zone. Rotation within the separation region is shown as a region with positive velocity. The highest velocities occur downstream of the junction towards the outer bank of the main channel as clarified by section x* = −2.0 (Figure 5.23). The velocity patterns near the surface were distinctly different from the longitudinal velocity contours near the bed. Additionally, the separation zone near the surface was larger in length and width. The size of the separation zone is different as well from top to bottom due to the branch channel flow entry angle. In the area near the surface, more recirculation occurred inside the separation zone. The higher velocities immediately downstream of the junction occurred near the bed which could be attributed to the entrance angle of the lateral flow. However, the maximum velocities are readjusted to be near the surface as the contracted zone is passed (Weber et al., 2001).

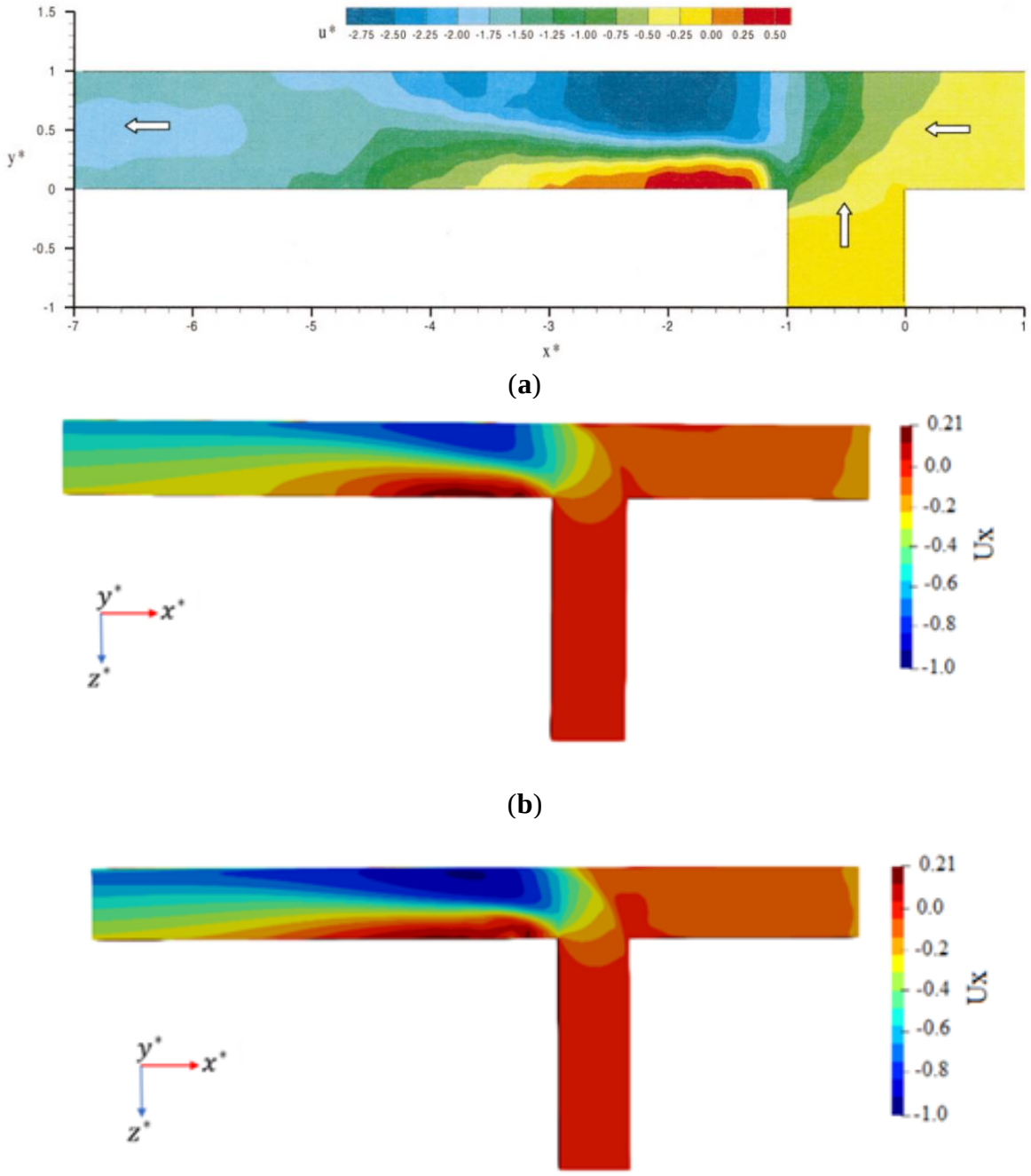

Figure 5.22: Comparison between experimental data and simulated results for longitudinal velocity. (a) Longitudinal velocity contour- experiment (Weber et al., 2001); (b) Longitudinal velocity contour for open confluent channel (Standard k-ε)- Simulated; (c) Longitudinal velocity contour for open confluent channel (Realizable k-ε)- Simulated

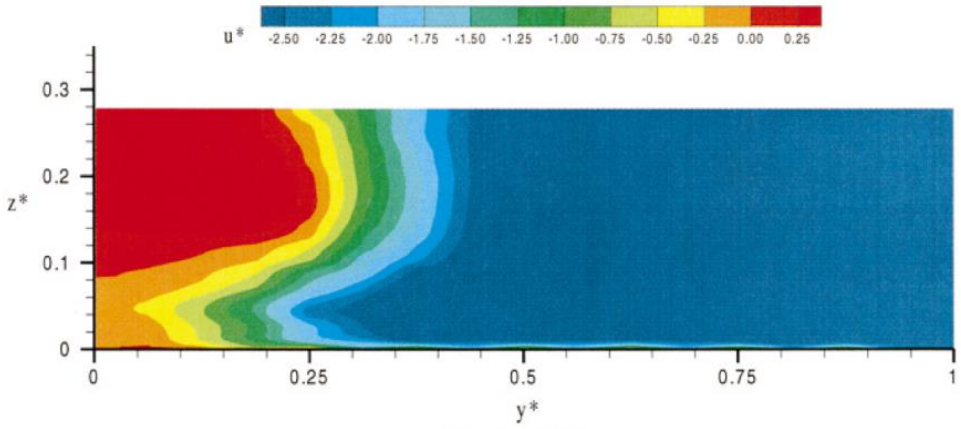

(**a**)

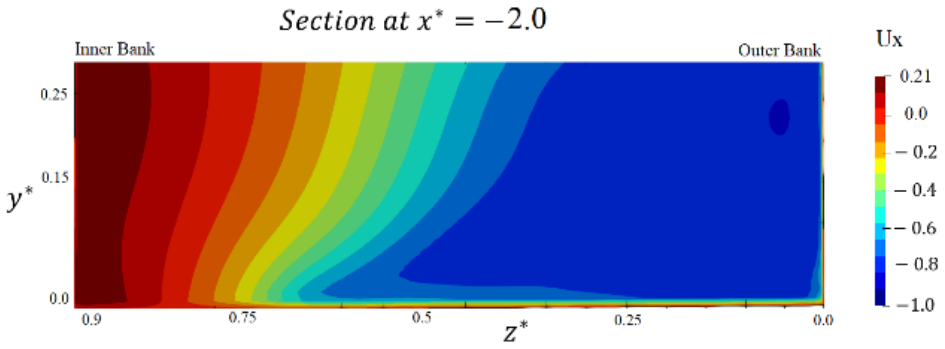

(b)

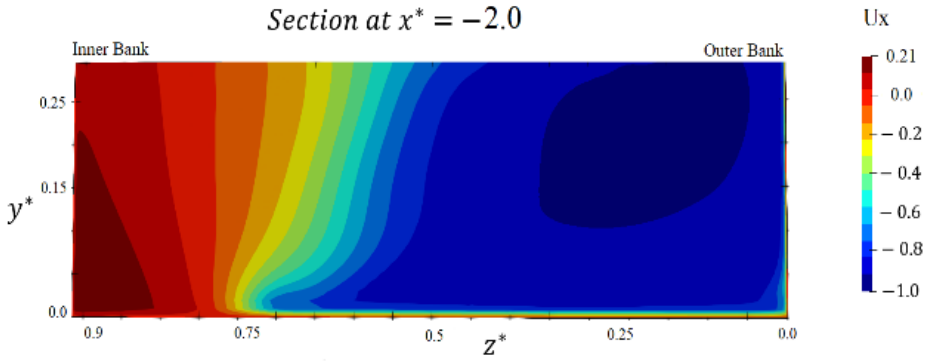

(**c**)

Figure 5.23: Comparison between experimental data and simulated results for longitudinal velocity contours. (a) Longitudinal Velocity Contours at Cross-Section x* = -2.00 – experiment (Weber et al., 2001); (b) Longitudinal Velocity Contours at Cross-Section x* = -2.00 - (Standard k-ε)- Simulated; (c) Longitudinal Velocity Contours at Cross-Section x* = -2.00 - (Realizable k-ε)- Simulated

5.3.4.5. Turbulent Kinetic Energy (k)

The comparison between the experimental data of Weber et al. (2001) and the simulated result for turbulent kinetic energy is shown in Figure 5.24. It could be seen from the figure that the area of high turbulence occurred along the boundary of the passing flow and the lower part of the separation zone. It is important to note that there was no significant mixing between the branch channel flow and the main channel flow during the passing through the channel junction. However, as the mixing of the main channel's high-velocity flow and the branch channel's low-velocity flow began in the separation zone below the junction, considerable turbulence happened. The relative location of the extreme turbulent kinetic energies with respect to the separation zone was comparable for all flow situations (Weber et al., 2001).

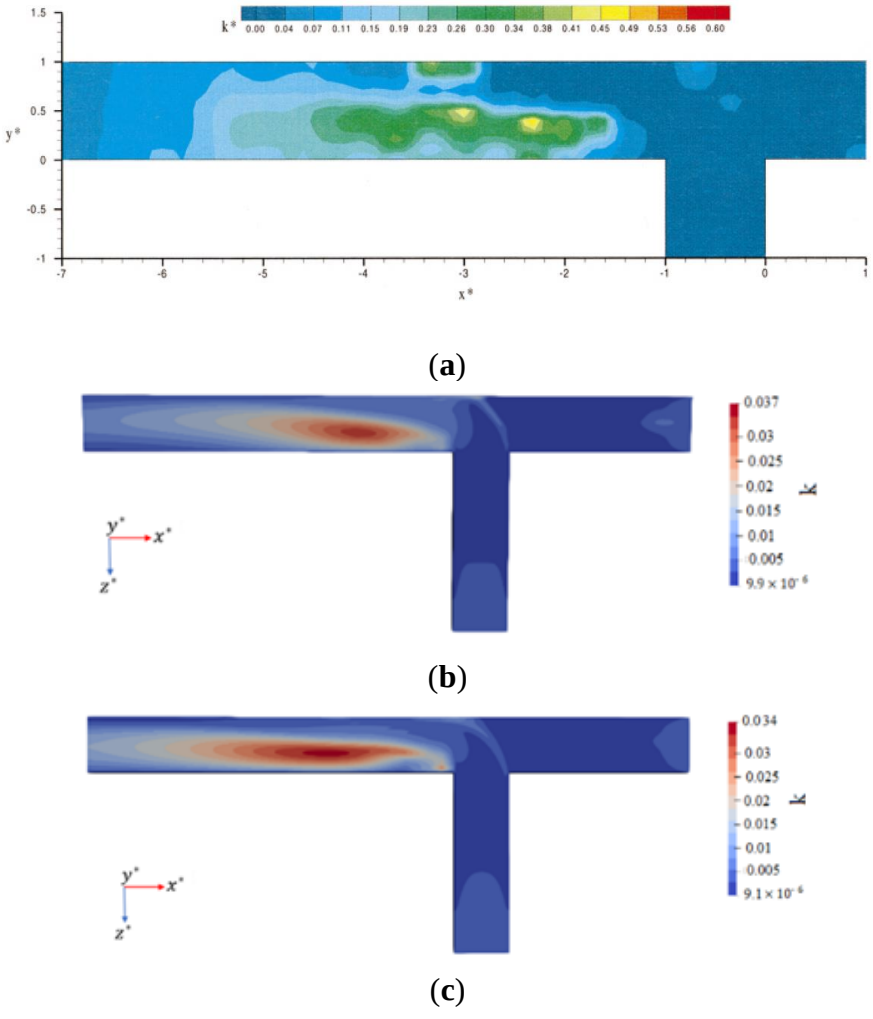

Figure 5.24: Turbulent kinetic energy distribution. (a) Dimensionless turbulent kinetic energy- experiment (Weber et al., 2001); (b) Dimensionless turbulent kinetic energy- simulated (Standard k-ε); (c) Dimensionless turbulent kinetic energy- simulated (Realizable k-ε)

5.4. Discussion and Future Works

Numerical models are considered one of the important tools for predicting flow in a curved channel, allowing for various environmental studies, such as sediment transport and pollutant dispersion (Shaheed et al., 2021). In this paper, the secondary flow in two types of open channels (including a 180-degree curved channel and a right-angle confluent channel) was studied using three-dimensional numerical models. The two channels were simulated using the standard k–ε and realizable k–ε turbulence models and the results were compared with the experimental data of Rozovskii (1961) for the curved channel and Shumate (1998) for the confluent channel. The performance of the two turbulence models was evaluated using the depth-averaged velocity across the width of the channel as shown in Figure 5.9 for curved channels and Figure 5.17 for confluent channels. In addition, RMSE and R^2 were also calculated for a further quantitative evaluation of the model performance. The higher velocity for the simulation of the open curved channel was close to the inner bank of the channel at the beginning of the bend and then it headed towards the outer bank near the bend exit. This was consistent with the observations obtained from the experiment. However, in most sections, the experimental data was overestimated by the two models near the inner bank, while both models performed well near the outer bank. In the last section and near the bend exit, there was a slight difference between the two numerical models and the experimental data which could be attributed to the change in the fluid direction in this area, making its characteristics very complex and difficult to capture, or it could be attributed to the weakness of these two models to capture or simulate these areas. Accordingly, it could be said that the difference between FSM and RLM was not significant, and the RLM was better at the start and end of the curve while the FSM was better at the middle of the bend. For the simulation of the open confluent channel, the higher velocity headed towards the outer bank of the main channel as the flow entered the main channel. Despite the difference between the simulated results of the two models and the experimental data seen in Figure 5.17 and Table 5.5 for RMSE, both models predicted the main characteristics of the flow reasonably well, which can be seen in the results of R^2 as shown in Table 6. Accordingly, it could be said that FSM is good but not as good as RLM.

A limitation of the widespread usage of 3D numerical models in practical applications was the high computational costs. However, the current simulations were conducted using a parallel computing technique on a high-performance device, and thus the computational costs were no longer a significant issue. The computational costs varied with the simulated cases, the computing device,

and the status of the device. In general, it has been noticed that the computational costs of FSM were slightly higher than those of RLM simulations, and the Realizable k–ε models were more computationally expensive than the standard k–ε models.

The present study demonstrated the performance of the standard and Realizable k–ε models in predicting the flow in a channel bend and in a confluent bend and provide user experience in handling the viscosity treatments. In future studies, the validated model can be further applied to carry out additional computations to investigate how varying channel configurations affect the flow characteristics.

5.5. Conclusions

Secondary flows are one of the phenomena that occur in river curves and confluences due to the curved directions that the flow takes in such areas. The flow in these types of channels is affected significantly by the secondary flows, and its features become very complicated and are not easy to accurately capture and determine by numerical models. Unlike Shaheed et al. (2018) which used a rigid lid approach, which implied no vertical displacement of the water surface, in the present study, the volume of fluid method was used to simulate the free surface displacements. This study employed two turbulence models to simulate the flow in a sharply curved channel and vertical angle confluent channel. The key conclusions of this study are concise as follows:

- For the curved channel, the two models successfully captured the general velocity distribution pattern, i.e., the higher velocity occurred near the inner bank at the start of the curve and near the outer bank at the end of the curve. In addition, both models performed reasonably well in reproducing the experimental data. For all the sections of the curve, when assessing the flow velocity, the standard k–ε model performed relatively better.
- For the confluent channel, the two models captured the main velocity characteristics correctly, i.e., the higher velocity occurred near the inner bank of the main channel as the flow entered the main channel. Moreover, both models performed reasonably well in predicting the experimental data. For all the sections taken after the junction, when assessing the flow velocity, the Realizable k–ε model performance was better.
- The current work focused on validating the numerical models and investigating the flow characteristics in some benchmark cases. In future studies, the validated model can be

employed to assess the influence of different channel configurations, including the aspect ratio, the curvature, and the geometry of the confluences.

Chapter 6. Conclusions and future work

6.1. Conclusions

Due to the large existence of river curvature and confluences and their major impact on river engineering issues, studying the characteristics of the flow in river bends and confluences might be considered as one of the essential jobs in river engineering. However, due to the complexity of the flow features in this area, which makes it challenging to be captured and identified, evaluating the dynamic of the flow in river bends and confluences is a difficult work. One of the flow features of curved and confluent rivers is secondary flow. In this study, a 3D OpenFOAM numerical model was used to analyze secondary currents. The finite volume method (FVM), which contains numerous numerical techniques developed for both time and space integration, is the foundation upon which OpenFOAM is built. The suggested model was verified using two sets of experimental data. InterFoam, a solver for open channel flow (Free Surface Model), and PisoFoam, a solver for closed channel flow (Rigid-Lid Model), were both employed. In the numerical model of this work, two turbulence models (standard k-ε, and realizable k-ε) are used.

6.1.1. Curved channel

- In curved open channel, the two models accurately represented the general velocity distribution pattern, i.e., the higher velocity occurred near the inner bank at the start of the curve and near the outer bank at the curve's end. Additionally, both models reproduced the experimental data fairly well. The standard k-ε model performed relatively better when determining the flow velocity for each part of the curve.
- In curved closed channel, the distribution of flow velocity in both of the examined models (standard k–ε and realizable k–ε) indicates that the maximum velocity at the beginning of the channel curve occurs at the interior bank and then moves gradually towards the exterior bank near the bend exit, as expected, according to the results obtained by simulating the curved channel. The examined numerical models and the experimental and other numerical data were compared, and it was found that there was good agreement between the two sets of experimental and numerical data. However, due to the change from a curved to a straight channel at the bend exit, there is a little variation in the two models, especially at the inner bank, making the flow features in this region complex and difficult to capture,

demonstrating the inadequacies of the two models in this area. The standard k–ε model performed better for all the bend's portions when analyzing flow velocity.

- In curved open and closed channel, the secondary flows are present at the beginning of the curve, rise to a peak value roughly in the middle of the bend, and then progressively fall approaching the bend exit.
- In curved open and closed channel, the presence of secondary flows in the acute bend is indicated by the flow lateral velocity component's negative values close to the channel bottom and positive values close to the water's surface.
- In curved open and closed channel, secondary flows are present in the sharp bend as evidenced by the flow vertical velocity component's negative values near the outer bank and its positive values near the inner bank.

6.1.2. Confluent channel

- In confluent closed channel, according to both models and the laboratory data, the higher velocity diverts from the branch channel and moves to the main channel's outer bank. Both the standard k-ε model and the realizable k-ε model produced nearly identical findings in terms of the flow velocity distribution, and both models were in good agreement with the experimental data. The cross-sections immediately following the junction, however, showed some variance. This variation, which makes it difficult to identify the flow features in this area, may be caused by a weakness in one of the two models at this location or by an abrupt change in flow direction from straight to curved. The realizable k–ε model performs better in terms of preference.
- In confluent open channel, the two models accurately represented the basic characteristics of velocity, i.e., the flow entered the main channel with a higher velocity near the inner bank. Additionally, both models were able to predict the experimental results fairly well. When determining the flow velocity for all of the sections taken after the junction, the realizable model performed better.
- In confluent open and closed channel, the branch channel's secondary flow, which happens close to the inner bank of the main channel, and the main channel's secondary flow, which occurs close to the outer bank of the main channel, are the two secondary flows that may be seen in the main channel. The two channels' secondary flows rotate in different directions

and fade progressively in the main channel's direction. The branch secondary flow is stronger than the main channel.

- In confluent open and closed channel, the presence of secondary flows is indicated by the fact that the lateral velocities of the main channel are positive near the channel bed and negative near the water's surface.

6.2. Suggestions for future work

Based on the findings of this research, the following can be recommended:

- The implementation of OpenFOAM to simulate the flow in channels with abrupt curves was the main goal of this work. Therefore, it is advised that future research take different kinds of curved channels, like those with moderate and mild curvature, into account. In order to analyze the effects of secondary flows and their impact on the design of river engineering works, different degrees of curvature and cross flows should also be taken into consideration.
- This study's analysis of the confluent channel was focused on asymmetrical confluent channels. It is therefore strongly advised to research additional confluent channel types, such as symmetrical confluent channels or confluent channels of various degrees. To gather more precise data for such circumstances, more field and experimental research are also required.
- It is crucial to run simulations for curved channels with various cross sections, such as circular and trapezoidal, because the primary and secondary flow are affected by the form of the curved channel.
- A significant consideration in curved and confluent channels is bed topography. Examining how a distorted and sloped substrate affects the main flow, secondary flow, and ultimately the channel is crucial.
- Two turbulence models were employed in OpenFOAM to simulate the two instances that were the subject of this study. To broaden the scope of comparison between the models and field data, more turbulence models might be used. In order to generate findings with a higher level of accuracy, the simulation could also make use of higher resolution, a finer grid, parallel simulation, domain decomposition, and alternative wall Functions.

- Based on the validation performed in this study it is recommended to use the model for parametric studies. Also, it should be noted that this result has been obtained based on a single experimental case and further studies are needed to confirm these results and more cases are needed to draw more conclusions.

References

Abdou, S. S., ElMoustafa, A. M., & Samy, M. (2021). Assessing Flow Bends in Open Channels. *International Research Journal of Advanced Engineering and Science*, *6*(2), 49–54.

Abhari, M. N., Ghodsian, M., Vaghefi, M., & Panahpura, N. (2010). Experimental and numerical simulation of flow in a 90, bend. *Flow Measurement and Instrumentation*, *21*, 292_298.

Alizadeh, L., & Fernandes, J. (2021). Turbulent Flow Structure in a Confluence: Influence of Tributaries Width and Discharge Ratios. *Water*, *13*(465). https://doi.org/doi.org/10.3390/w13040465

Almeida, J. R. M. de, & Ota, J. J. (2020). Comparative study between turbulence models in curved channels. *Brazilian Journal of Water Resources*, *25*(21).

Baghlani, A., & Talebbeydokhti, N. (2013). Hydrodynamics of Right-Angled Channel Confluences by a 2D Numerical Model. *IJST, Transactions of Civil Engineering*, *37*(C2), 271–283.

Barkdoll, B. (2003). Discussion of "Experiments on Flow at a 90-Degree Open-Channel Junction by Larry J. Weber, Eric D. Schumate, and Nicola Mawer,. *Journal of Hydraulic Engineering*, *129*(2), 165–166.

Bathurst, J. ., Thorne, C. ., & Hey, R. D. (1977). Direct measurements of secondary currents in river bends. *Nature*, *269*, 504–506.

Best, J. (1987). Flow dynamics at river confluences: Implications for sediment transport and bed morphology. *The Society of Economic Paleontologists and Mineralogists (SEPM) Recent Developments in Fluvial Sedimentology*, *SP39*, 27–35.

Best, JL., & Reid, I. (1984). Separation zone at open-channel junctions. *J Hydraul Eng.*, *110*(11), 1588–1594.

Bilal, A., Xie, Q., & Zhai, Y. (2020). Flow, Sediment, and Morpho-Dynamics of River Confluence in Tidal and Non-Tidal Environments. *J. Mar. Sci. Eng.*, *8*(591). https://doi.org/10.3390/jmse8080591

Birjukova, O., Guillen, S., Alegria, F., & Cardoso, A. (2014). Three dimensional flow field at confluent fixed-bed open channels. In *River Flow 2014 – Schleiss et al. (Eds)*. © 2014 Taylor & Francis Group, London.

Biron, P., Best, J. L., & Roy, A. G. (1996). Effects of bed discordance on flow dynamics at open channel confluences. *Journal of Hydraulic Engineering*, *122*(12), 676–682.

Biron, P. M., Ramamurthy, A. S., & Han, S. (2004). Three-dimensional numerical modeling of mixing at River confluences. *Journal of Hydraulic Engineering*, *130*(3), 243–253.

Biron, P. M., Richer, A., Kirkbride, A. D., Roy, A. G., & Han, S. (2002). Spatial patterns of water surface topography at a river confluence. *Earth Surface Processes and Landforms*, *27*(9), 913–928.

Biron, P. M., Roy, A. G., Best, J. L., & Boyer, C. J. (1993). Bed morphology and sedimentology at the confluence of unequal depth channels. *Geomorphology*, *8*, 115–129.

Biron, P., Roy, A. G., & Best, J. L. (1996). Turbulent flow structure at concordant and discordant open-channel confluences. *Exp. Fluids*, *21*, 437–446.

Blanckaert, K. (2003). *Flow and turbulence in sharp openchannel bends*. Ecole Polytechnique Fédérale Lausanne, Switzerland.

Blanckaert, K. (2009). Saturation of curvature-induced secondary flow, energy losses, and turbulence in sharp open-channel bends: Laboratory experiments, analysis, and modeling. *Journal of Geophysical Research – Earth Surface*, *114*(F03015. doi:10.1029/2008 JF001137.).

Blanckaert, K. (2010). Topographic steering, flow circulation, velocity redistribution and bed topography in sharp meander bends,. *Water Resour. Res.*, *46*(doi:10.1029/2009WR008303).

Blanckaert, K. (2011). Hydrodynamic processes in sharp meander bends and their morphological implications. *Journal of Geophysical Research: Earth Surface*, *116*, F1003. https://doi.org/10.1029/2010JF001806

Blanckaert, K., & De Vriend, H. (2010). Meander dynamics: a nonlinear model without curvature restrictions for flow in open-channel bends. *J Geophys Res*, *115*, F04011.

Blanckaert, K., & De Vriend, H. J. (2004). Secondary flow in sharp open-channel bends. *Journal of Fluid Mechanics*, *498*, 353–380. https://doi.org/10.1017/S0022112003006979

Blanckaert, K., & Graf, W. H. (2001). Mean flow and turbulence in open-channel bend. *J. Hydraulic Eng.*, *127*(10), 835–847.

Blanckaert, K., & Graf, W. H. (2004). Momentum transport in sharp open-channel bends. *Journal of Hydraulic Engineering*, *130*(3), 186–198.

Blanckaert, K., Schnauder, I., Sukhodolov, A., van Balen, W., & Uijttewaal, W. S. J. (2009). Meandering: field experiments, laboratory experiments and numerical modeling. *River, Costal and Estuarine Morphodynamics (RCEM), Santa Fe, Argentina*.

Bodnar, T., & Prihoda, J. (2006). Numerical simulation of turbulent free-surface flow in curved channel. *Flow Turbulence Combust*, *76*, 429–442.

Booij, R. (1992). *Turbulentie in de waterloopkunde*.

Booij, R. (2003a). Measurements and Large Eddy Simulations of the flows in some curved flumes. *Journal of Turbulence*, *4*(8), 1–17.

Booij, R. (2003b). Modeling the Flow in Curved Tidal Channels and Rivers. *International Conference on Estuaries and Coasts , Hangzhou, China*.

Booij, R., & Tukker, J. (1996). 3-Dimensional Laser-Doppler Measurements in a Curved Flume. *In: Adrian R.J., Durão D.F.G., Durst F., Heitor M.V., Maeda M., Whitelaw J.H. (Eds) Developments in Laser Techniques and Applications to Fluid Mechanics.*

Boon, P. J. (1992). Essential elements in the case for river conservation. In Boon, P.J., Calow, P. and Petts, G.E. (eds), River conservation and management. In *River conservation and management* (pp. 11–33). Chichester: Wiley.

Boxall, J. B., Guymer, I., & Marion, A. (2003). Transverse mixing in sinuous natural open channel flows. *Journal of Hydraulic Research*, *41*, 153–165.

Boyer, C., Roy, A. G., & Best, J. L. (2006). Dynamics of a river channel confluence with discordant beds: Flow turbulence, bed load sediment transport, and bed morphology. *JOURNAL OF GEOPHYSICAL RESEARCH*, *111*(F4). https://doi.org/10.1029/2005JF000458

Bradbrook, K. F., Biron, P. M., Lane, S. N., Richards, K. S., & Roy, A. G. (1998). Investigation of controls on secondary circulation in a simple confluence geometry using a three-dimensional numerical model. *Hydrol. Process.*, *12*, 1371–1396.

Bradbrook, K. F., Lane, S. N., & Richards, K. S. (2000a). Numerical simulation of three-dimensional, time-averaged flow structure at river channel confluences,. *Water Resources Research*, *36*(9), 2731–2746.

Bradbrook, K. F., Lane, S. N., Richards, K. S., Biron, P. M., & Roy, A. . (2000b). Large Eddy Simulation of periodic flow characteristics at river channel confluences. *Journal of Hydraulic Research*, *38*(3), 207–215.

Bradbrook, K. F., Lane, S. N., Richards, K. S., Biron, P. M., & Roy, A. G. (2001). Role of bed discordance at asymmetrical river confluences. *J. Hydraul. Eng.*, *127*, 351–368.

Bradshaw, P. (1987). Turbulent secondary flows. *Annual Review of Fluid Mechanics*, *19*, 53–74. https://doi.org/org/10.1146/annurev.fl.19.010187.000413

Bristow, C. S., Best, J. L., & Roy, A. G. (1993). Morphology and facies models of channel confluences. In Marzo, M. and Puigdefabregas, C. (eds), Alluvial sedimentation. In *Alluvial sedimentation* (Blackwell, pp. 91–10).

Brito, M., Canelas, O., Leal, J., & Cardoso, A. (2014). 3D numerical simulation of flow at a 70º open-channel confluence. *V Conferência Nacional de Mecânica Dos Fluidos, Termodinâmica e Energia*.

Bryan, R. B., & Kuhn, N. J. (2002). Hydraulic conditions in experimental rill confluences and scour in erodible soils. *Water Resources Research*, *38*(5), 211–214.

Bulat, M. P., & Bulat, P. (2013). Comparison of turbulence models in the calculation of supersonic separated flows. *World Applied Sciences Journal*, *27*(10), 1263–1266.

C.R.Thorne, L.W.Zevenbergen, J.C.Pitlick, S.Rais, J.B.Bradley, & P.Y.Julien. (1985). *Direct measurement of secondary currents in a mendering sand bed river*. *315*.

Cable, M. (2009). *An Evaluation of Turbulence Models for the Numerical Study of Forced and Natural Convective Flow in Atria by A thesis submitted to the Department of Mechanical and Materials* (Issue May). Queen's University, Kingston, Ontario, Canada.

Caboussat, A. (2003). *ANALYSIS AND NUMERICAL SIMULATION OF FREE SURFACE FLOWS*. *2893*, 150.

Cameron, H., & Bauer, B. (2014). *RIVER BANK EROSION PROCESSES ALONG THE LOWER SHUSWAP RIVER*.

Cebeci, T., & Bradshaw, P. (1977). *Momentum transfer in boundary layer*. Hemisphere, Washington, D.C.

Chang, H. H. (1988). *Fluvial processes in river engineering*. Krieger Publishing Company, Malabar, FL.

Chang, Y. C. (1971). *Lateral mixing in meandering channels.* Univ. of Iowa, Iowa City, Iowa.

Cheng, Z., & Constantinescu, G. (2020). Stratification effects on hydrodynamics and mixing at a river confluence with discordant bed. *Environmental Fluid Mechanics*, *20*, 843–872.

Church, M., Biron, P. M., & Roy, A. G. (2012). *Gravel-Bed Rivers: Processes, Tools, Environments*. Copyright © 2012 John Wiley & Sons, Ltd.

Colombini, M. (1993). Turbulence-driven secondary fows and formation of sand ridges. *J Fluid Mech*, *254*(1), 701–7019.

Constantinescu, G., Koken, M., & Zeng, J. (2010). Simulation of flow in an open channel bend of strong curvature using Detached Eddy Simulation. *River Flow, Dittrich, Koll, Aberle and Geisenhainer (Eds):*, 1527–1534.

Constantinescu, G., Miyawaki, S., Rhoads, B., & Sukhodolov, A. (2012). Numerical analysis of the e ect of momentum ratio on the dynamics and sediment-entrainment capacity of coherent flow structures at a stream confluence. *J. Geophys. Res. Earth Surf.*, *117*, 1–12.

Constantinescu, G., Miyawaki, S., Rhoads, B., Sukhodolov, A., & Kirkil, G. (2001). Structure of turbulent flow at a river confluence with momentum and velocity ratios close to 1: Insight provided by an eddy-resolving numerical simulation. *Water Resour. Res.*, *47*(W05507). https://doi.org/10.1029/2010WR010018

Dabaghi, F., Kacimi, A. El, Kloucha, C. K., & Mezali, F. (2005). *Numerical Modelling and Analysis of Water Free Surface Flows*. *2005*, 563–567.

Davidson, L. (2011). *An introduction to turbulence models.* Chalmers University of Technology, Sweden.

Davidson, Lars. (2015). An Introduction to Turbulence Models. *CHALMERS*, *97*(2).

De Serres, B., Roy, A. G., Biron, P. M., & Best, J. L. (1999). Three-dimensional structure of flow at a confluence of river channels with discordant beds. *Geomorphology*, *26*, 313–335.

De Vriend, H. (1977). A mathematical model of steady flow in curved shallow channel. *J. Hydraul. Res.*, *15*((1)), 37–54.

De Vriend, H. (1979). *Flow measurements in a curved rectangular channel.*

De Vriend, H. (1980). Velocity redistribution in curved rectangular channels. *J. Fluid Mech.*, *107*, 423–439.

De Vriend, H. J., & Geldof, H. J. (1983). Main flow velocity in short river bends. *Journal of Hydraulic Engineering*, *109*(7), 991–1011.

Demuren, A. O., & Rodi, W. (1986). Calculation of flow and pollutant dispersion in meandering channels. *J . Fluid Mech.*, *172*, 63–92.

Demuren, A., & Rodi, W. (1984). Calculation of turbulence-driven secondary motion in non-circular ducts. *Journal of Fluid Mechanics*, *140*, 189–222.

Dietrich, W. E., & Whiting, P. J. (1989). Boundary Shear Stress and Sediment Transport in River Meanders of Sand and Gravel. In S. Ikeda & G. Parker (Eds.), *River Meandering, Volume 12* (pp. 1–50). American Geophysical Union (AGU).

Dordevica, D., & Stojnic, I. (2016). Numerical simulation of 3D flow in right-angled confluences with bed elevation discordance in both converging channels. *12th International Conference on Hydroinformatics, HIC 2016*, 1026 – 1033.

Duan, G., Wang, S. S. Y., & Jia, Y. (2001). The applications of the enhanced CCHE2D model to study the alluvial channel migration processes. *J. Hydraul. Res.*, *39*, 469–480.

Duan, J. G. (2004). Simulation of Flow and Mass Dispersion in Mendering Channels. *J. Hydraulic Eng. © ASCE*, *October*, 964–976.

Duchêne, V. (2014). On the Rigid-Lid Approximation for Two Shallow Layers of Immiscible Fluids with Small Density Contrast. *Journal of Nonlinear Science*, *24*(4), 579–632. https://doi.org/10.1007/s00332-014-9200-2

Einstein, H., & Li, H. (1958). Secondary currents in straight channels. *Trans Am Geophys Union*, *39*(6), 1058–1088.

Engelund, F., & Skovgaard, O. (1973). On the origin of meandering and braiding in alluvial streams. *J. Fluid Mech*, *57*, 289–302.

Falcon, M. (1984). Secondary flow in curved open channels. *Ann.Rev.Fluid Mech.*, *16*(1), 179–193.

Farhadia, A., Arno, M., Trittharta, M., Martin, G., & Habersacka, H. (2017). Accuracy and comparison of standard k-ε with two variants of k-ω turbulence models in fluvial applications. *Engineering Applications of Computational Fluid Mechanics*, *12*(1), 216–235.

Ferguson, R., & Hoey, T. (2008). *Effects of Tributaries on Main-Channel Geomorphology*. JohnWiley & Sons, Ltd.: Chichester, UK.

Fischer, H. B. (1969). The effects of bends on dispersion in streams. *Water Resour. Res.*, *5*(2), 496–506.

Fraga, B., Cea, L., & Peña, E. (2012). Comparison between standard and non-linear k-ε turbulence models for three-dimensional simulation of turbulent flow in a meandering open channel. *River Flow 2012 - Proceedings of the International Conference on Fluvial Hydraulics*, 1161–1168.

Germanoski, D., & Ritter, D. F. (1988). Tributary response to local base level lowering below a dam. In *Regulated Rivers: Research and Management* (2nd ed., pp. 11–24).

Ghaneeizad, S. M., Jovein, E. B., & Abrishami, J. (2010). An Investigation of Turbulence Models In Flow Treatment Simulation in Strongly Curved Bends. *9th International Conference on Hydroinformatics HIC*.

Ghanmi, A. (1999). Modeling of flows between two consecutive reverse curves. *J. Hydraul. Res.*, *37*(1), 121–135.

Ghobadian, R., & Mohammadi, K. (2011). Simulation of subcritical flow pattern in 180° uniform and convergent open-channel bends using SSIIM 3-D model. *Water Science and Engineering*, *4*(3), 270–283. https://doi.org/10.3882/j.issn.1674-2370.2011.03.004

Gholami, A., Akhtari, A. A., Minatour, Y., Bonakdari, H., & Javadi, A. A. (2014). Experimental And Numerical Study on Velocity Fields and Water Surface Profile in a Strongly-Curved 90º Open Channel Bend. *Engineering Applications of Computational Fluid Mechanics*, *8*(3), 447–461.

Gildeh, H. K. (2013). *Numerical Modeling of Thermal / Saline Discharges in Coastal Waters*. University of Ottawa, Ottawa, Canada.

Gökçen, B. (2015). Hydrodynamics and Morphodynamics of River Confluences. *4th International Workshop on "River and Reservoir Hydrodynamics Ans Morphodynamics" & Summer School in "Measuring Techniques for Turbulent Open Channel Flows."*

Graf, W. H., & Blanckaert, K. (2002). Flow Around Bends in Rivers. *2nd International Conference New Trends in Water and Environmental Engineering for Safety and Life: Eco-Compatible Solutions for Aquatic Environments*.

Guymer, I. (1998). Longitudinal Dispersion in Sinuous Channel with Changes in Shape. *Journal of Hydraulic Engineering*, *124*(1), 33–40.

Herreras, N., & Izarra, J. (2013). Two-Phase pipeflow simulations with OpenFoam. *Master's Thesis, June*.

Hjertager, B. (2009). *Lecture Notes in OpenFOAM - MSK 600*.

Hodskinson, A., & Ferguson, R. I. (1998). Numerical modeling of separated flow in river bends: Model testing and experimental investigation of geometric controls on the extent of flow separation at the concave bank. *Hydrological Processes*, *12*(8), 1323–1338.

Holley, E. R., & Abraham, G. (1973). Field tests of transverse mixing in rivers. *J. Hydraul. Div., Am. Soc. Civ. Eng.*, *99*(12), 2313–2331.

Horna-Munoz, D., Constantinescu, G., Rhoads, B., Lewis, Q., & Sukhodolov, A. (2020). Density Effects at a Concordant Bed Natural River Confluence. *Water Resources Research*, *56*(4).

Hsieh, T. Y., & Yang, J. C. (2003). Investigation on the suitability of two-dimensional depth-averaged models for bend-flow simulation. *J. Hydraul. Eng.*, *129*(8), 597–612.

Huang, J., Weber, L. J., & Lai, Y. G. (2002). Three-dimensional numerical study of flows in open-channel junctions. *Journal of Hydraulic Engineering*, *128*(3), 268–280.

Huang, S., Jia, Y., Chan, H.-C., & Wang, S. S. Y. (2009). Three-Dimensional Numerical Modeling of Secondary Flows in a Wide Curved Channel. *Journal of Hydrodynamics*, *21*(6), 758–766.

Ikeda, S., & Nishimura, T. (1986). Flow and bed profile in meandering sand-silt rivers. *J. Hydraul. Eng.*, *112*(7), 562–579.

Iliescu, T., & Fischer, P. (2004). Backscatter in the rational LES model. *Computers & Fluids*, *33*, 783–790.

Jamieson, E. C., Post, G., & Rennie, C. D. (2010). Spatial variability of three-dimensional Reynolds stresses in a developing channel bend. *Earth Surface Processes and Landforms*, *35*(9), 1029–1043.

Jansen, P. P. (1994). *Principles of river engineering*.

Jian, Y. &, & McCorquadale, J. A. (1998). Simulation of curved open channel flows by 3D hydrodynamic model. *Journal of Hydraulic Engineering*, *124*(7), 687–698.

Jing, H., Guo, Y., Li, C., & Zhang, J. (2009). Three-dimensional numerical simulation of compound meandering open channel flow by the Reynolds stress model. *Int. J. Numer. Meth. Fluids*, *59*, 927–943.

Jing, Hefang, Li, C., Guo, Y., & Xu, W. (2011). Numerical simulation of turbulent flows in trapezoidal meandering compound open channels. *Int. J. Numer. Meth. Fluids*, *65*, 1071–1083.

Johannesson, H. (1988). *Theory of river meanders*. University of Minnesota, Minnesota, MN, USA.

Jongbloed, J. (1996). *Three-dimensional modelling of secondary flow in river bends*. Delft University of Technology/Netherlands.

Kang, H., & Choi, S. (2006). Reynolds stress modelling of rectangular open-channel flow. *Intl. J. Num. Meth. Fluids*, *51*(11), 1319–1334.

Kean, J. W., Kuhnle, R. A., Smith, J. D., Alonso, C. V., & Langendoen, E. J. (2009). Test of a method to calculate nearbank velocity and boundary shear stress. *Journal of Hydraulic Engineering*, *135*, 591–601.

Kennedy, B. A. (1984). On Playfair's law of accordant junctions, Earth Surf. *Earth Surf. Process. Landf.*, *9*(2), 153–173.

Kheirkhah Gildeh, H Mohammadian, A., Nistor, I., & Qiblawey, H. (2014a). Numerical modelling of 30° and 45° inclined dense turbulent jets in stationary ambient. *J Environ Fluid Mech*, *15*(3), 537–562.

Kheirkhah Gildeh, H Mohammadian, A., Nistor, I., & Qiblawey, H. (2014b). Numerical modelling of turbulent buoyant wall jets in stationary ambient water. *J Hydraul Eng*, *140*(6), 04014012.

Kheirkhah Gildeh, H Mohammadian, A., Nistor, I., Qiblawey, H., & Xiaohui, Y. (2015). CFD modelling and analysis of the behavior of 30° and 45° inclined dense jets; new numerical insights. *J Appl Water Eng Res.*, *4*(2), 112–127.

Khosronejad, A., Rennie, C. D., Neyshabouri, S. A. A. S., & Townsend, R. D. (2007). 3D numerical modeling of flow and sediment transport in laboratory channel bends. *J. Hydraulic Eng.*, *133*(10), 1123–1134.

Kinghton, D. (1998). *Fluvial Forms and Processes: A New Prespective.* Hodder Arnold.

Lambert, R. J. (2012). *Development of a numerical wave tank using openFOAM*. University of Coimbra, Coimbra, Portugal.

Lane, S. N. (1998). `Hydraulic modelling in hydrology and geomorphology: a review of high resolution approaches'. *Hydrol. Process., 12, ., 12*, 1131-1150 (this issue).

Lane, S. N., Bradbrook, K. F., Richard, K. S., Biron, P. M., & Roy, A. G. (2000). Secondary circulation cells in river channel confluences: measurement artefacts or coherent flow structures? *Hydrological Processes*, *14*(11–12), 2047–2071.

Lane, S. N., Bradbrook, K. F., Richards, K. S., Biron, P. A., & Roy, A. G. (1999). The application of computational fluid dynamics to natural river channels: three-dimensional versus two-dimensional approaches. *Geomorphology*, *29*(1–2), 1–20.

Launder, B. E., Reece, G. J., & Rodi, W. (1975). Progress in the development of a Reynolds-stress turbulence closure. *Journal of Fluid Mechanics*, *68*(3), 537–566.

Launder, B. E., & Rodi, W. (1981). The turbulent wall jet. *Progress in Aerospace Sciences*, *19*, 81–128.

Launder, B. E., & Spalding, D. B. (1972). *Mathematical models of turbulence*. Academic Press.

Launder, B. E., & Spalding, D. B. (1974). The numerical computation of turbulent flows. *Computer Methods in Applied Mechanics and Engineering*, *3*(2), 269–289.

Leite Ribeiro, M., Blanckaert, K., Roy, G., & Schleiss, A. J. (2012). Flow and sediment dynamics in channel confluences. *Journal of Geophysical Research*, *117*(F01035).

Leopold, L. B., & Wolman, M. G. (1957). River channel patterns: Braided, meandering and straight. *Professional Paper 282-B, U.S., Geologic S*, 37–86.

Leschziner, M. A., & Rodi, W. (1979). Calculation of strongly curved open channel flow. *Journal of the Hydraulics Division*, *105*(10), 1297–1314.

Lien, H. C., Hsieh, T. Y., Yang, J. C., & Yeh, K. C. (1999). Bend-Flow Simulation Using 2D Depth-Averaged Model. *Journal of Hydraulic Engineering*, *125*(10), 1097–1108.

Liu, H., Zhou, J. G., & Burrows, R. (2009). Multi-block lattice Boltzmann simulations of subcritical flow in open channel junctions. *Computers & Fluids*, *38*(6), 1108–1117.

Liu, X., Li, L., Hua, Z., Tu, Q., Yang, T., & Zhang, Y. (2019). Flow Dynamics and Contaminant Transport in Y-Shaped River Channel Confluences. *Int. J. Environ. Res. Public Health*, *16*(572).

Lu, W., Zhang, W., Cui, C., & Leung, A. (2004). A numerical analysis of free-surface flow in curved open channel with velocity - pressure - free - surface correction. *Computational Mechanics*, *33*, 215–224.

Ludeña, G. (2015). *Hydro-morphodynamics of open-channel confluences with low discharge ratio and dominant tributary sediment supply*. University of Lisbon, Portugal.

Luo, H., Fytanidis, D. K., Schmidt, A. R., & García, M. H. (2018). Comparative 1D and 3D numerical investigation of open-channel junction flows and energy losses. *Advances in Water Resources*, *117*, 120–139.

Luo, J., & Razinsky, E. H. (2009). Analysis of turbulent flow in 180 deg turning ducts with and without guide vanes. *J. Turbomachinery*, *131*(2), 021011.

Manual Trisula. (1994).

Marion, A., & Zaramella, M. (2006). Effects of velocity gradients and secondary flow on the dispersion of solutes in curved channels. *Journal of Environmental Engineering*, *132*, 1295–1302.

Marriott, M. J. (1999). The effect of overbank flow on the conveyance of the inbank zone in meandering compound channels. *28th IAHR Congress*.

Matsuura, T. (2004). *Stream-bank protection in narrow channel bends using 'barbs'-A laboratory study*. Univ. of Ottawa, Ottawa.

Mcguirk, J. J., & Rodi, W. (1977). *The Calculation of Three-Dimensional Turbulent Free Jets*.

Melaaen, M. C. (1990). *Analysis of curvilinear non orthogonal coordinate for numerical calculation of fluid flow in complex geometries*. The Norwegian Institute of Technology, Trondheim, Norway.

Menter, F. R. (1994). Two-equation eddy-viscosity turbulence models for engineering applications. *AIAA Journal, 32*(8).

Mohammadiun, S., Salehi Neyshabouri, S. A. A., Naser, G., Parhizkar, H., & Vahabi, H. (2015). Effects of Open-Channel Geometry on Flow Pattern in a 90° Junction. *Iranian Journal of Science and Technology-Transactions of Civil Engineering*, *39*, 559–573.

Molls, T., & Chaudhry, M. H. (1995). Depth-averaged open-channel flow model. *J. Hydraul. Eng.*, *121*(6), 453–465.

Mosley, M. P. (1976). An experimental study of channel confluences. *Journal of Geology*, *84*(5), 535–562.

Mosonyi, E., & Gotz, W. (1973). Secondary currents in subsequent model bends. *Proceedings of the International Association for Hydraulic Research International Symposium on River Mechanics*, 191–201.

NajiAbhari, M., Ghodsian, M., Vaghefi, M., & Panahpur, N. (2010). Experimental and numerical simulation of flow in a 90^{o} bend. *Flow Measurement and Instrumentation*, *21*(3), 292–298.

Nash, J. E., & Sutcliffe, J. V. (1970). River flow forecasting through conceptual models. Part I - a discussion of principles. *Journal of Hydrology*, *10*(3), 282–290.

Nezu, I., & Nakagawa, H. (1993). *Turbulence in open-channel flows.* A.A.Balkema.

Odgaard, A. J., & Bergs, M. A. (1988). Flow processes in a curved alluvial channel. *Water Resour. Res.*, *24*(1), 45–56.

Olsen, N. R. B. (2000). *CFD algorithms for hydraulic engineering*. The Norvegian University of Science and Technology.

Olsen, N. R. B. (2006). *SSIIM users' manual*. The Norwegian University of Scince and Technology.

OpenFOAM The Open Source CFD Toolbox Programmer's Guide, Version 3.0.1. (2015).

Parsons, D. R., Best, J. L., Lane, S. N., Kostaschuk, R. A., Hardy, R. J., Orfeo, O., Amsler, M. L., & Szupiany, R. N. (2008). *Large river channel confluences. In River Confluences, Tributaries and the Fluvial Network.* JohnWiley & Sons: Chichester, UK.

Penna, N., De Marchis, M., B. Canelas, O., Napoli, E., Cardoso, A. H., & Roberto, G. (2018). Effect of the Junction Angle on Turbulent Flow at a Hydraulic Confluence. *Water*, *10*(4), 469. https://doi.org/org/10.3390/w10040469

Pezzinga, G. (1990). Applicazione del modello K-e non lineare alio studio di circolazioni secondarie. *Atti Del XXII Convegno Di Idraulica e Costruzioni Idrauliche*, *2*, 125–139.

Pilechi, A., Mohammadian, A. M., & Rennie, C. (2011). Experimental and numerical study of turbulent wall jets. *In: 20th Canadian Hydrotechnical Conference*.

Pouchoulin, S., Ramos, P. X., Emmanuel, M., Schindfessel, L., Tom, D. M., & Riviere, N. (2018). Discussion of "Tang, H., Zhang, H., & Yuan, S. (2018). Hydrodynamics and contaminant transport on a degraded bed at a 90-degree channel confluence. Environmental Fluid Mechanics, 18(2), 443–463." *Environmental Fluid Mechanics*, *18*, 1293–1295.

Poungkrajorn, T. (2015). *Assuring asset integrity through improving the accuracy of leakage source identification of a permanently installed subsea leak detection system using artificial neural networks* (Issue June).

Qin, C., Shao, X., & Xiao, Y. (2019). Secondary Flow E ects on Deposition of Cohesive Sediment in a Meandering Reach of Yangtze River. *Water*, *11*(1444). https://doi.org/10.3390/w11071444

Ramón, C. L., Prats, J., & Rueda, F. J. (2015). Simulation of Turbulent Flows in River Confluences and Meandering Channels with a Cartesian 3D Free Surface Hydrodynamic Model. *International Journal of Computational Methods*, *12*(6), 1550035.

Ramos, P. X., Schindfessel, L., Pêgo, J. P., & De Mulder, T. (2019). Flat vs. curved rigid-lid LES computations of an open-channel confluence. *Journal of Hydroinformatics*, *21*(2), 318–334.

Reinauer, R., & Hager, W. H. (1997). Supercritical bend flow. *J. Hydraulic Eng.*, *123*(3), 208–218.

Rhoads, B. L. (1996). *Mean structure of transport-effective flows at an asymmetrical confluence when the main stream is dominant, in Coherent Flow Structures in Open Channels, edited by P. J. Ashworth, S. J. Bennett, J. L. Best, and S. J. McLelland, pp. 491–517*. John Wiley, New York.

Rhoads, B. L., & Kenworthy, S. T. (1995). Flow structure at an asymmetrical stream confluence. *Geomorphology*, *11*(4), 273–293.

Rhoads, B. L., & Kenworthy, S. T. (1998). Time-averaged flow structure in the central region of a stream confluence. *Earth Surf. Processes Landforms*, *23*, 171–191.

Rhoads, B. L., & Sukhodolov, A. N. (2001). Field investigation of three-dimensional fow structure at stream confuluance:1 thermal mixing and time-averaged velocities. *Water Resour Res*, *7*(9), 2393–2410.

Riesterer, J., Wenka, T., Brudy-Zippelius, T., & Nestmann, F. (2016). Bed load transport modeling of a secondary fow infuenced curved channel with 2D and 3D numerical models. *Journal of Applied Water Engineering and Research*, *4*(1), 54–66. https://doi.org/org/10.1080/23249676.2016.1163649

Riley, J. (2013). *The Fluvial Dynamics Of Confluent Meander Bends*.

Riley, J. D., & Rhoads, B. L. (2012). Flow structure and channel morphology at a natural confluent meander bend. *Geomorphology*, *163–164*, 84–98. https://doi.org/doi.org/10.1016/j.geomorph.2011.06.011

Riley, J. D., Rhoads, B. L., Parsons, D. R., & Johnson, K. K. (2015). Influence of junction angle on three-dimensional flow structure and bed morphology at confluent meander bends during di erent hydrological conditions. *Earth Surf. Process. Landf.*, *40*, 252–271.

Roca, M., Martin Vide, J. P., & Blanckaert, K. (2007). Reduction of bend scour by an outer bank footing: Footing design and bed topography. *J. Hydraulic Eng.*, *133*(2), 139–147.

Rodi, W. (1984). *Turbulence models and their application in hydraulicsA state of art review, 2nd Ed., Int.* Assoc. for Hydr. Res., Delft, The Netherlands.

Rodi, W. (1993). *Turbulence models and their applications in hydraulics.''* (3rd Ed.). IAHR Monograph, Balkema.

Rowinski., P. ., Guymer., I., & Kwiatkowski., K. (2008). Response to the slug injection of a tracer – large scale experiment in a natural river. *Hydrological Sciences Journal*, *53*, 1300–1309.

Rozovskii, I. (1961). *Flow of water in bends of open channels*. Academy of Sciences of the Ukrainian SSR, i.e. Jerusalem : Israel Program for Scientific Translations.

Rutherford, J. C. (1994). *River Mixing*. Chichester, John Wiley & Sons, Ltd.

Sadrehaghighi, I. (2020). *Turbulence Modeling*. A NNAPOLIS, MD.

Safarzadeh Gandoshmin, A., & Salehi Neishbouri, A. (2005). *Numerical simulation of flow structure in lateral intake on 180 degree bend*. Tarbiat Modarress University.

Schindfessel, L., Creëlle, S., & De Mulder, T. (2017). How Different Cross-Sectional Shapes Influence the Separation Zone of an Open-Channel Confluence. *J. Hydraul. Eng.*, *143*(9), 04017036.

Schindfessel, L., Creëlle, S., & Mulder, T. De. (2015). Flow Patterns in an Open Channel Confluence with Increasingly Dominant Tributary Inflow. *Water*, *7*, 4724–4751.

Schneider, G. E., & Zedan, M. (1981). A Modified Strongly Implicit Procedure for the Numerical Solution of Field Problems. *Numerical Heat Transfer*, *4*(1), 1–19.

Schumm, S. A., & Hadley, R. F. (1957). Arroyos and the semi-arid cycle of erosion. *American Journal of Science*, *255*, 161–174.

Seminara, G. (2006). Meanders. *J Fluid Mech*, *554*, 271–297.

Seyedashraf, O., & Akhtari, A. A. (2017). Three-dimensional CFD Study of Free-Surface Flow in a Sharply Curved 30° Open- Channel Bend. *Engineering Science and Technology Review*, *10*(3), 85–89.

Shaheed, R., Mohammadian, A., & Gildeh, H. K. (2018). A comparison of standard k–ε and realizable k–ε turbulence models in curved and confluent channels. *Environmental Fluid Mechanics*, *19*, 543–568.

Shaheed, R., Mohammadian, A., & Yan, X. (2021). A Review of Numerical Simulations of Secondary Flows in River Bends. *Water*, *13*(7), 884. https://doi.org/https://doi.org/10.3390/w13070884

Shakibaeinia, Ahmad, Tabatabai, M. R. M., & Zarrati, A. R. (2010). Three-dimensional numerical study of flow structure in channel confluences. *Canadian Journal of Civil Engineering*, *37*(5), 772–781.

Shams, M., Ahmadi, G., & Smith, D. H. (2002). Computational modeling of flow and sediment transport and deposition in meandering rivers. *Advances in Water Resources*, *25*(6), 689–699.

Shao, D., & Law, A. W.-K. (2009). Turbulent mass and momentum transport of a circular offset dense jet. *Journal of Turbulence*, *10*(40), 1–24.

Shih, T., Zhu, J., & Lumley, J. (1995). A new Reynolds stress algebraic equation model. *Computer Methods in Applied Mechanics and Engineering*, *125*(1–4), 287–302.

Shimizu, Y., Yamaguchi, H., & Itakura, T. (1990). Three-dimensional computation of flow and bed deformation. *J. Hydraul. Eng.*, *116*(9), 1090–1108.

Shumate, E. D. (1998). *Experimental description of flow at an open-channel junction*. Univ. of Iowa, Iowa.

Shumate, E. D., & Weber, L. J. (1998). Experimental description of combining flows at an open channel junction. *In Proceeding of the ASCE Water Resources Engineering Confluences*, 1679–1684.

Shur, M., Strelets, P. R., Spalart, M., & Travin, A. (1999). Detached-eddy simulation of an 902 airfoil at high angle of attack. In: Rodi, W., Laurence, D. (Eds.), Engineering 903 Turbulence Modelling and Measurements, vol. 4. *Proceedings of the 4th International Symposium on Engineering Turbulence Modelling and Measurements*, 669–678.

Siebert, W. (1982). *Stroemungscharakteristiken in einen Kanal mit 180-Kruemmungen, Mitteilungen 168.* Theodor-Rehbock Flusslaboratorium.

Sivakumar, M., Dissanayake, K., & Godbole, A. (2004). Numerical modeling of flow at an open-channel confluence. *Environmental Engineering Research Event.*, 97–106.

Song, C. G., Seo, I. W., & Kim, Y. Do. (2012). Analysis of secondary current effect in the modeling of shallow flow in open channels. *Advances in Water Resources*, *41*, 29–48. https://doi.org/10.1016/j.advwatres.2012.02.003

Stoesser, T., Ruether, N., & Olsen, N. R. B. (2010). Calculation of primary and secondary flow and boundary shear stresses in a meandering channel. *Advances in Water Resources*, *33*(2), 158–170.

Sukhodolov, A. N., Krick, J., Sukhodolova, T. A., Cheng, Z., Rhoads, B. L., & Constantinescu, G. S. (2017). Turbulent flow structure at a discordant river confluence: Asymmetric jet dynamics with implications for channel morphology. *Journal of Geophysical Research: Earth Surface*, *122*, 1278–1293.

Sun, S., Yan, H., & Kouyi, G. L. (2014). Artificial neural network modelling in simulation of complex flow at open channel junctions based on large data sets. *Environmental Modelling & Software*, *62*, 178–187.

Tajnesaie, M., Nodoushan, E., Barati, R., & Moghadam, M. (2018). Performance comparison of four turbulence models for modeling of secondary fow cells in simple trapezoidal channels. *ISH Journal of Hydraulic Engineering*, *26*(2), 187–197. https://doi.org/org/10.1080/09715010.2018.1469053

Talebpour, M. (2016). *Numerical investigation of turbulent-driven secondary fow*. The Pennsylvania State University.

Talebpour, M., & Liu, X. (2018). Numerical investigation on the suitability of a fourth-order nonlinear k–ω model for secondary current of second type in open-channels. *J Hydraul Res.*, *57*(1), 1–12. https://doi.org/org/10.1080/00221686.2018.1444676

Tang, H., Zhang, H., & Yuan, S. (2018). Hydrodynamics and contaminant transport on a degraded bed at a 90-degree channel confluence. *Environ. Fluid Mech.*, *18*, 443–463.

Tawekal, J. R. (2015). *CFD Simulation of the Flow over a 2-Dimensional Pipe and Vortex Induced Vibration of the Pipe with 1 Degree of Freedom*.

Termini, D., & Piraino, M. (2011). Experimental analysis of cross-sectional flow motion in a large amplitude meandering bend. *Earth Surf Process Landforms*, *36*, 244–256.

Thanh, M., Kimura, I., Shimizu, Y., & Hosoda, T. (2010). Depth-averaged 2D models with effects of secondary currents for computation of flow at a channel confluence. *Proceedings of the River Flow 2010*, 137–44.

Tominaga, A., & Nagao, M. (2000). Secondary flow structure in bends of narrow open channels with various cross sections. *4th Intl. Conf. Hydro-Science and Engineering.*

Tuan, D. H., Quoc, Y. N., & Xuan, L. L. (2017). Study of Secondary Flow and Sediment Transport in a Laboratory-scale Model of a Meandering River. *Advanced Experimental Mechanics*, *2*, 65–70.

Vaghefi, M., Akbari, M., & Fiouz, A. (2015). Experimental Investigation of the Three-dimensional Flow Velocity Components in a 180-Degree Sharp Bend. *World Applied Programming*, *5*(9), 125–131.

van Balen, W., Blanckaert, K., & Uijttewaal, W. S. J. (2010). Analysis of the role of turbulence in curved open-channel flow at different water depths by means of experiments, LES and RANS. *Journal of Turbulence*, *11*(12), 1–34.

van Balen, W., Uijttewaal, W. S. J., & Blanckaert, K. (2009). Large eddy simulation of a mildly curved open-channel flow. *J. Fluid Mech.*, *630*, 413–442.

van Balen, W., Uijttewaal, W. S. J., & Blanckaert, K. (2010). Large-Eddy Simulation of a Curved Open-Channel Flow over Topography. *Physics of Fluids*, *22*(7), 075108.

Van Balen, Wim. (2010). *Curved open-channel flows : A numerical study*.

Vanoni, V. A. (1946). Transportation of suspended sediment by water. *Transactions of the American Society of Civil Engineers*, *111*, 67–133.

Versteeg, H. K., & Malalasekera, W. (1995). *An introduction to computational fuid dynamics, The finite volume method*. Longman Science & Technical, Harlow.

Versteeg, H. K., & Malalasekera, W. (2007). *An Introduction to Computational Fluid Dynamics.*

Wang, S. S., & Hu, K. (1990). Improved methodology for formulating finite element hydrodynamic models. *Finite Elements in Fluids, T. Chung, Ed.*, *8*.

Wang, X., & Yan, Z. (2007). Three-Dimensional Simulation for Effects of Bed Discordance on Flow Dynamics At Y-Shaped Open Channel Confluences. *Journal of Hydrodynamics*, *19*(5), 587–593.

Wang, Z.-Q., & Cheng, N.-S. (2006). Time-mean structure of secondary flows in open channel with longitudinal bedforms. *Advances in Water Resources*, *29*(11), 1634–1649.

Weber, L. J., Schumate, E. D., & Mawer, N. (2001). Experiments on Flow at a 90° Open-Channel Junction. *J. Hydraul. Eng.*, *127*(5), 340–350.

Weerakoon, S. B. (1990). *Flow structure and bed topography in river confluences*. University of Tokyo.

Weerakoon, S. B., Kawahara, Y., & Tamai, N. (1991). Three-dimensional flow structure in channel confluences of rectangular section. *Proceedings of the 25th IAHR Congress A. IAHR, Madrid.*, 373–380.

Weerakoon, S. B., & Tamai, N. (1989). Three-dimensional calculation of flow in river confluences using boundary fitted coordinates. *J. Hydrosci. Hydraul. Engng.*, *7*, 51–62.

Wendt, J. (2008). *Computational fluid dynamics: an introduction*. Springer.

Wilcox, D. C. (1993). *Turbulence modeling for CFD, 1st Ed.* DCW Industries, Inc.

Wilcox, D. C. (1998). *Turbulence modeling for CFD, 2nd Ed.* DCW Industries, La Canada, Ca.

Wu, W., Rodi, W., & Wenka, T. (2000). 3D numerical modeling of flow and sediment transport in open channels. *Journal of Hydraulic Engineering, ASCE*, *126*(1), 4–15.

Yakhot, V., Orzag, S. A., Thangam, S., Gatshi, T. B., & Speziale, C. G. (1992). Development of a turbulence model for shear flow by a double expansion technique. *Phys. Fluids A*, *4*(7), 1510–1520.

Yan, X., Rennie, C. D., & Mohammadian, A. (2020). A three-dimensional numerical study of flow characteristics in strongly curved channel bends with different side slopes. *Environmental Fluid Mechanics*, *20*, 1491–1510.

Yang, Qingyuan, Sun, Y., Wang, X., Lu, W., & Wang, X. (2011). Effects of Turbulence Models on the Numerical Simulation of Flow in Open Channel Junction. *Mechanics of Advanced Materials and Structures*, *18*, 566–571. https://doi.org/10.1080/15376494.2011.621800

Yang, QY, Liu, T., Lu, W., & Wang, K. (2013). Numerical Simulation of Confluence Flow in Open Channel with Dynamic Meshes Techniques. *Advances in Mechanical Engineering*, *5*. https://doi.org/http://dx.doi.org/10.1155/2013/860431

Yeh, K., & Kennedy, J. (1993). Moment model of nonuniform channel-bend flow. I: Fixed beds. *J Hydraul Eng*, *119*(7), 776–795.

Zaji, A. H., & Bonakdari, H. (2015). Efficient methods for prediction of velocity fields in open channel junctions based on the artifical neural network. *Engineering Applications of Computational Fluid Mechanics*, *9*(1), 220–232.

Zeng, C., & Li, C. W. (2010). A hybrid RANS-LES model for combining flows in open-channel T-junctions. *Journal of Hydrodynamics*, *22*(5), 154–159.

Zeng, J., Constantinescu, G., Blanckaert, K., & Weber, L. (2008). Flow and bathymetry in sharp open-channel bends: Experiments and predictions. *Water Res. Res.*, *44*(9), W09401,doi:10.1029/2007WR006303.

Zhou, G., Wang, H., Shao, X., & Jia, D. (2009). 2-D numerical simulation of flow in a curved open channel. *Advanced in Water Resources and Hydraulic Engineering*, 871–876.

Appendix A

A.1. Results and Discussions in open and closed curved channel

In order to understand the behaviour of the flow in channel bends, some turbulence models were studied in this research. An evaluation for each model will be done based on velocity parameters. The results of the velocities across dimensional channel width that obtained from these models will be compared with Rozovskii experimental data (Rozovskii 1961). In addition, three-dimensional velocity components will be studied to highlight the reasons behind the variation in these velocities. Finally, each model will be evaluated depending on the results obtained from simulation outputs to choose the best one for each case. This thesis focuses on shallow river bends based on experimental data for a depth of only 6cm. Re number is large and Froude scaling is used. Because the straight channel before the bend is relatively long, the flow can be assumed to be fully developed before entering the bend. Deep river is more difficult than shallow river because of corner cells which are hard to simulate. The superelevation is small in shallow river. The largest discrepancies were close to the side walls because of the inaccuracy in calculating the effect of shear stress at the wall.

A.1.1. Velocity distribution in open and closed curved channel

The velocity pattern of the curved channel surface is shown in Figure A.1. At the beginning of the bend, the maximum velocity moves towards the inner bank of the channel, and then changes direction towards the outer bank near the bend exit. The behavior of the velocity distribution agrees with the study of De Vriend & Geldof (1983) who studied the flow velocity in river bends in a field investigation on the Dommel River (in the Netherlands) and also performed a numerical simulation of the flow. The river section was in the form of two consecutive curves, both of 90 degrees and in the same direction, with a short straight connection between them. The maximum velocity according to the results occurred at the beginning of the bend near the inner bank of the river, while at the end of the bend it tended to be oriented toward the outer bank of the river, which agrees with the results of the present study. Also, the velocity distribution agrees with the study of Vaghefi et al. (2015) who conducted an experimental investigation of the three-dimensional flow velocity components in a 180 degree sharp bend.

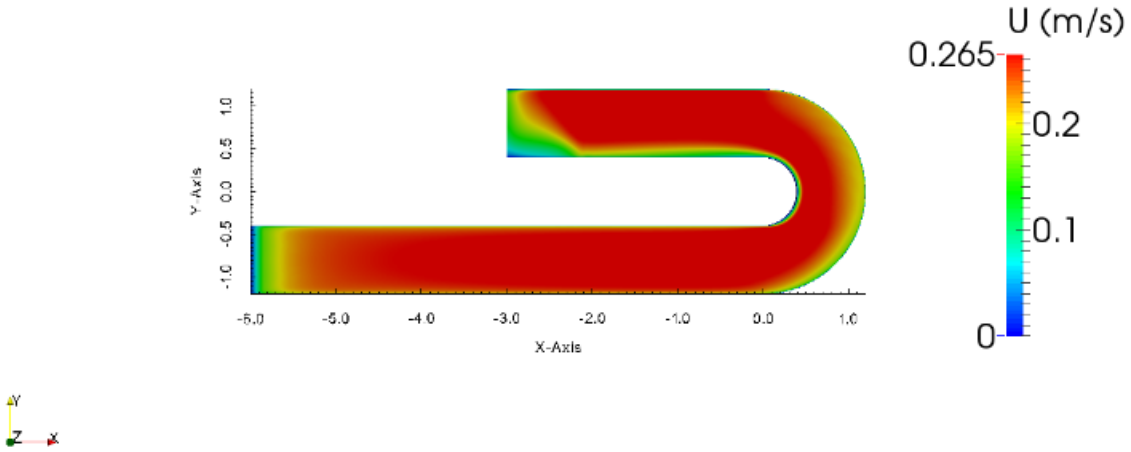

a. k-ε model in curved open channel

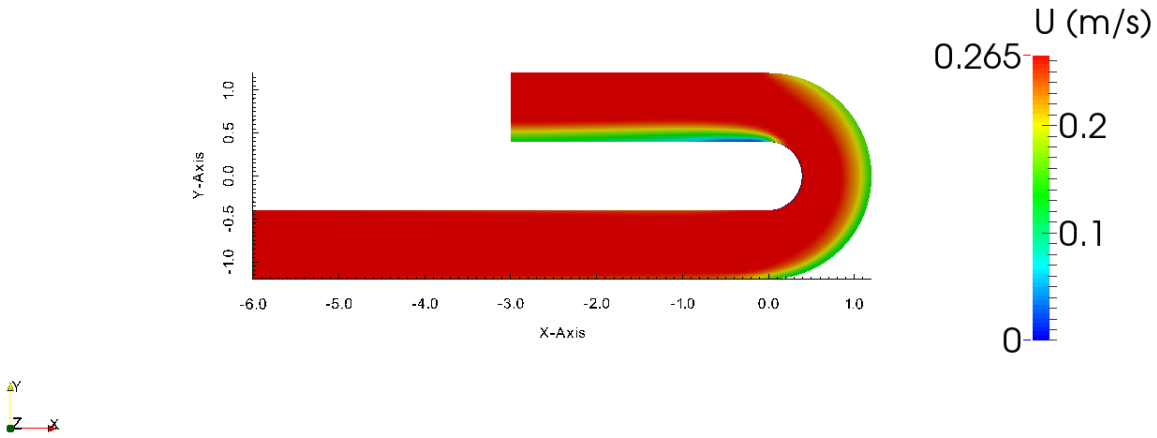

b. k-ε model in curved closed channel

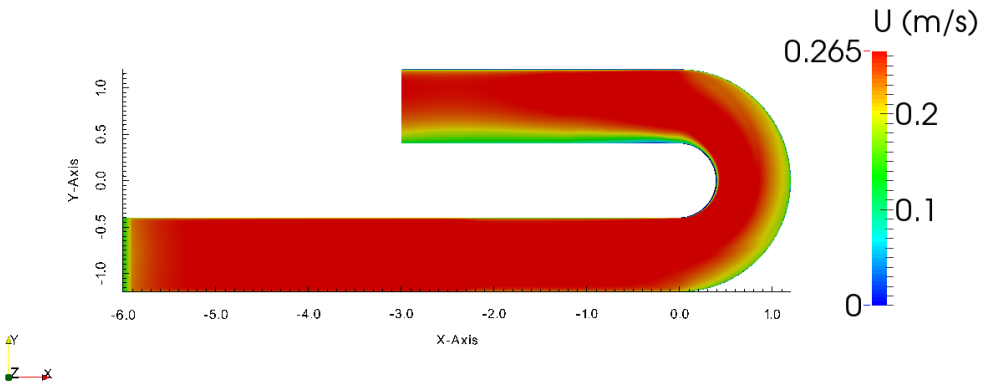

c. Realizable k-ε model in curved open channel

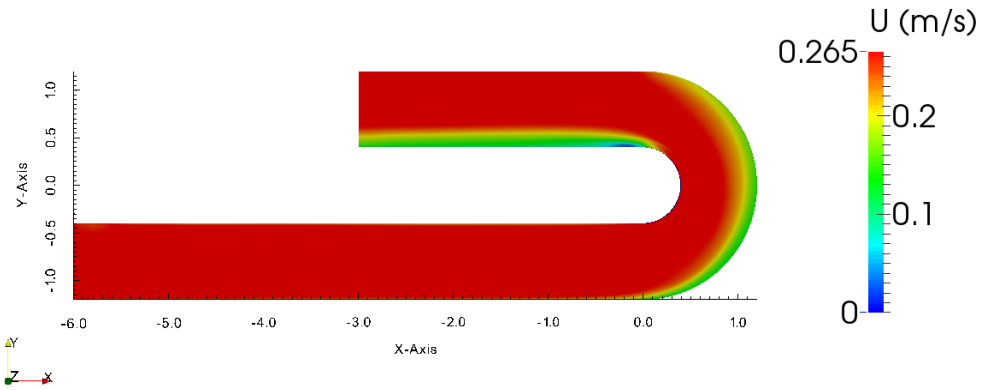

d. Realizable k-ε model in curved closed channel

Figure A.1: Velocity distribution in river bend

The contours of velocity distribution are clarified in Figure A.2 blew for closed channel and different types of numerical models. The helical path of the flow is clear at the bend for all the two numerical models.

a. k-ε model in curved closed channel

b. Realizable k-ε model in curved closed channel

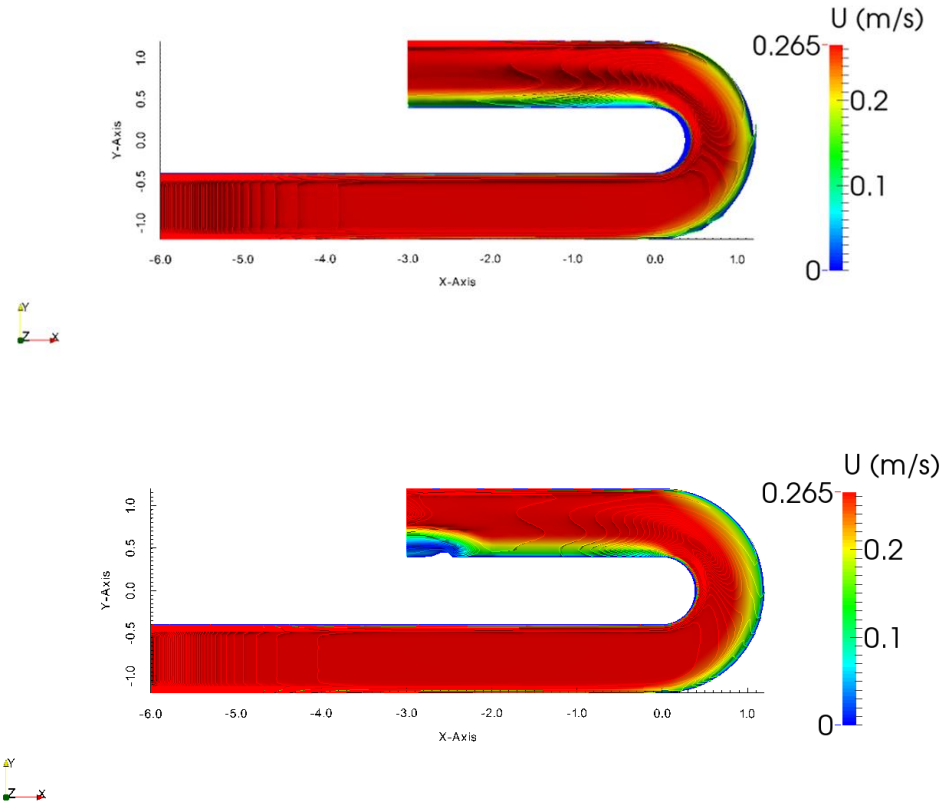

Figure A.2: contours of velocity distribution in curved closed channel

A.1.1.1. Longitudinal Velocity Distribution

The distribution of the longitudinal velocity is shown in Figure A.3 below and it could be explained as follows:

- The maximum velocity moves towards the inner bank at the beginning of the bend, and this is mainly because of the longitudinal pressure gradients that exist close to the inner bank in sharp curve channel. The longitudinal pressure gradients appear due to the changing in the channel from straight to curved causing the same change in the flow. Thereafter, the longitudinal velocity reaches its the maximum value at the middle of the bend affected by the secondary flow. Then, the longitudinal velocity decreases gradually towards the bend exit.
- At 0-degree cross section, the maximum velocity occurs near the water surface because of the flow at upstream straight route.
- The helical path of the secondary flow exists, and it reaches its highest strength at a 90-degree cross-section and results in the formation of a vortex in this cross-section.
- The comparison between the experimental data and simulated results for longitudinal velocity contours is shown in Figure A.3 and there is a good agreement between them.
- Most of the results agrees with Vaghefi et al. (2015).

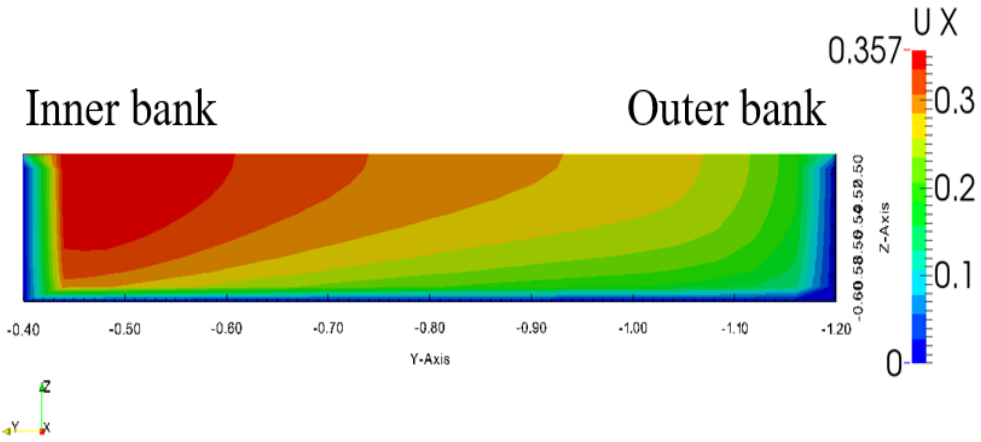

a. Section at 0 degree

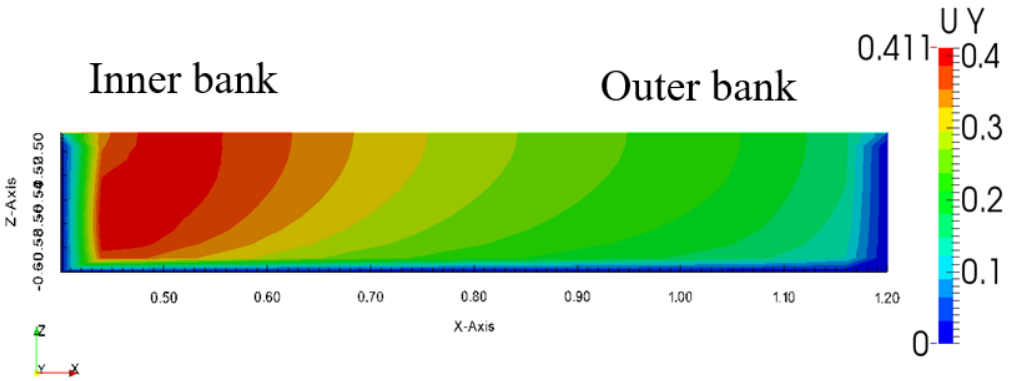

b. Section at 90 degree

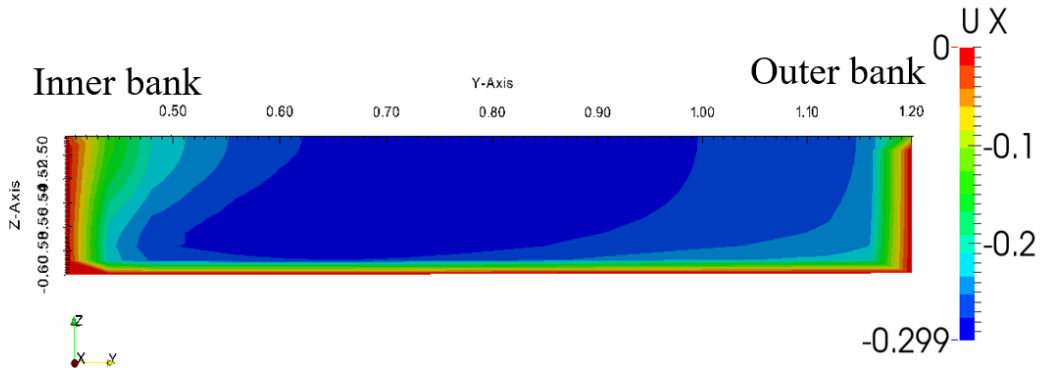

c. Section at 180 degree

Figure A.3: Longitudinal velocity distribution in curved closed channel

A.1.1.2. Vertical Velocity Distribution

The distribution of the longitudinal velocity is shown in Figure A.4 below and it could be explained as follows:

- At 90-degree cross section, the vertical velocity reaches to the maximum value near the inner bank of the channel and then it decreases towards the bend exit.
- Two types of circulation appear in the cross sections of vertical velocity; the first strong one is rotating clockwise, close to the inner bank of the channel, and reach to its maximum value

at the middle of the bend; the second weak one is rotating counterclockwise, close to the outer bank of the channel, and also reach to its maximum value at the middle of the bend. These two circulations could be the secondary flow cells and the outer bank cells due to the big similarity in the features.

- The results agree with Vaghefi et al. (2015).

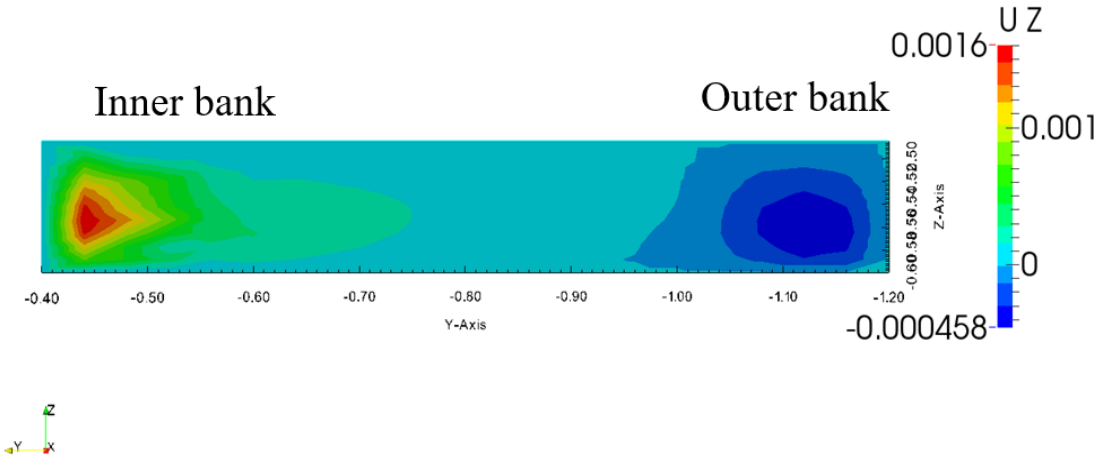

a. Section at 0 degree

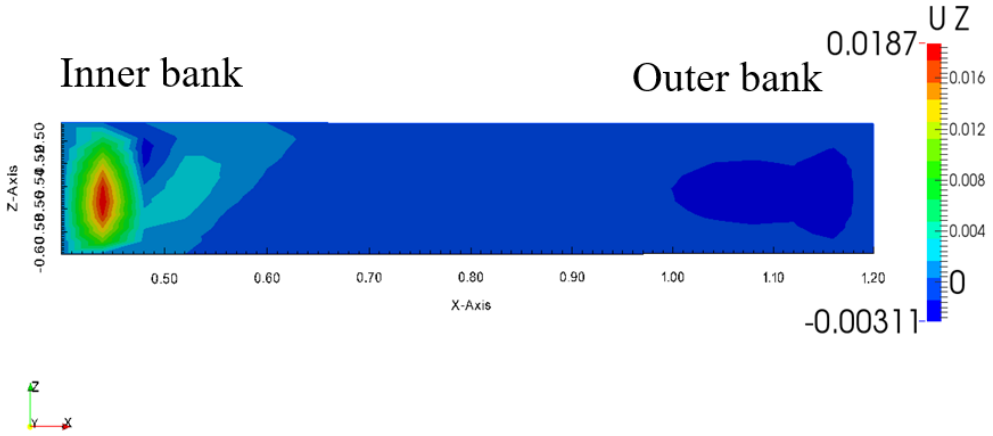

b. Section at 90 degree

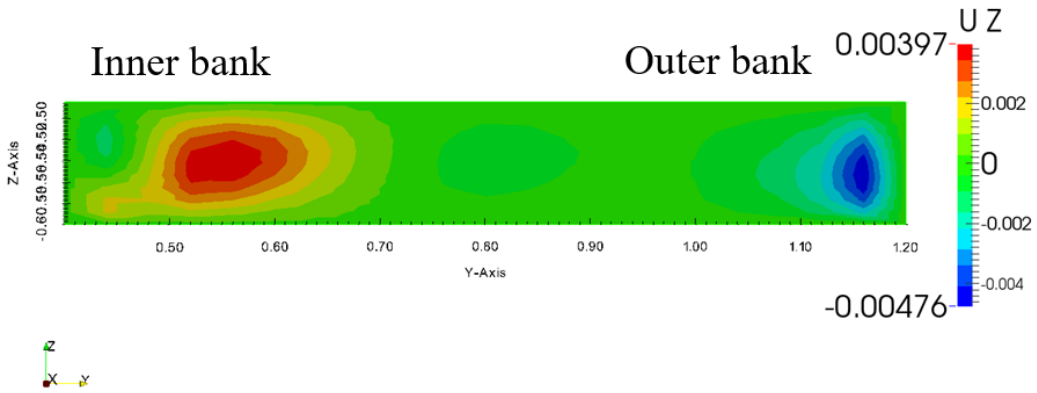

c. Section at 180 degree

Figure A.4: Vertical Velocity Distribution in curved closed channel

A.1.1.3. Lateral Velocity Distribution

The distribution of the longitudinal velocity is shown in Figure A.5 below and it could be explained as follows:

- The negative values of the flow velocity component near the channel bed, and its positive values near the water surface indicate the existence of the secondary flows in the sharp bend.
- The value of lateral velocity at the beginning of the bend is very small because of the strong longitudinal pressure gradients at this area. Then, the lateral velocity increases towards the middle of the bend and the bend exit as well. It reaches to the maximum value, and consequently the secondary flows, at the bend center near the inner bank.
- When the flow has passed the middle of the bend and reaches the bend exit, the lateral velocity values decrease for the longitudinal pressure gradients gain strength to a large extent at the end of the route.
- Most of the results agree with Vaghefi et al. (2015).
- If there is an iced cover on a 90-degree Confluence, the velocity below the ice will be zero.

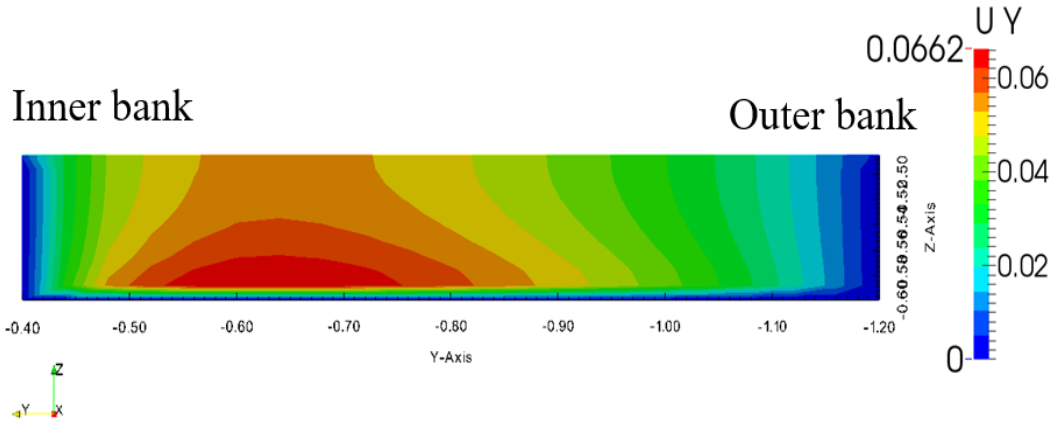

a. Section at 0 degree

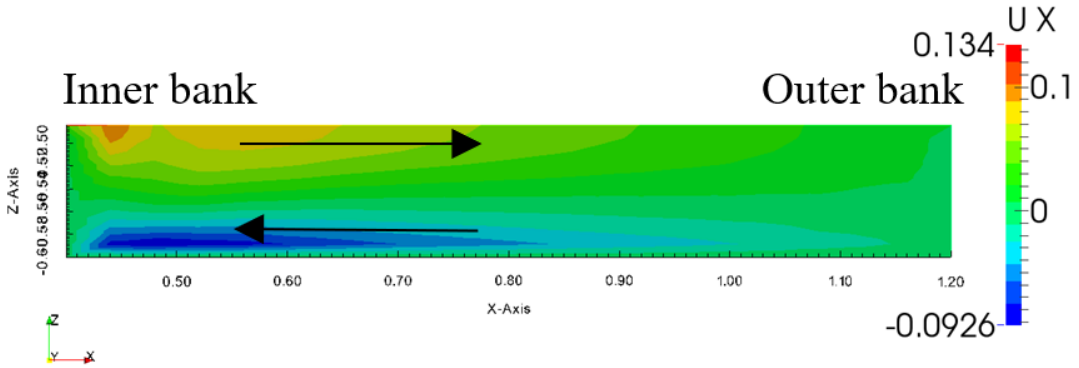

c. Section at 90 degree

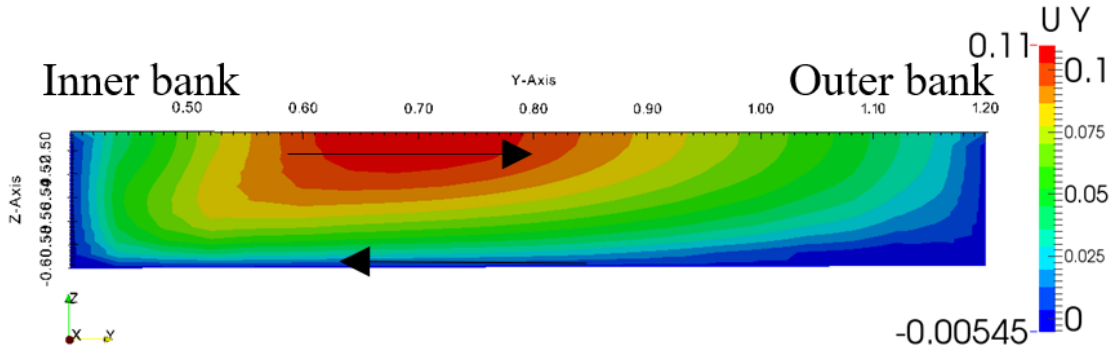

d. Section at 180 degree

Figure A.5: Lateral Velocity Distribution in curved closed channel

A.2. Results and Discussions in closed confluent channel

Due to the complexity of flow features in river confluences and its importance in river engineering, several studies were reviewed to better understand these features. In this study, the velocity

parameters were used to evaluate the models because of its capability on visualizing the flow characteristics. The results of the velocities across dimensional channel width that obtained from the different models were compared with Shumate experimental data (1998). Also, the components of the velocity in three dimensions were studied, and reasons behind the difference in each velocity were examined. Finally, the best model for each case was selected after evaluating the results of each model.

A.2.1. Velocity distribution

Both of the two numerical models gave almost the same results for the distribution of the flow velocity. The maximum velocity moves from the branch channel towards the outer bank of the main channel as shown in Figure A.6. The two models standard k-ε and realizable k-ε achieved a very good agreement with the experiment.

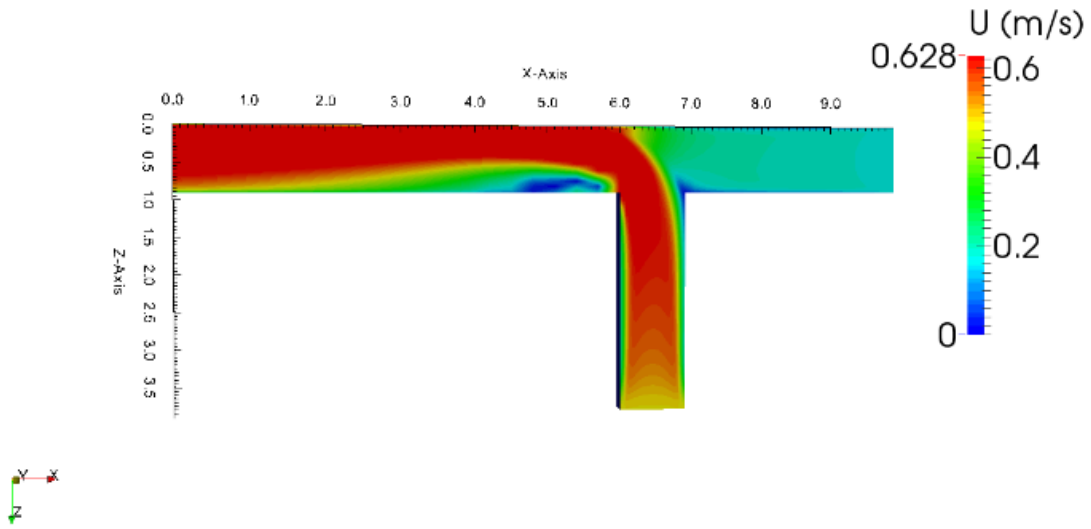

Velocity distribution at simulated k-ε model

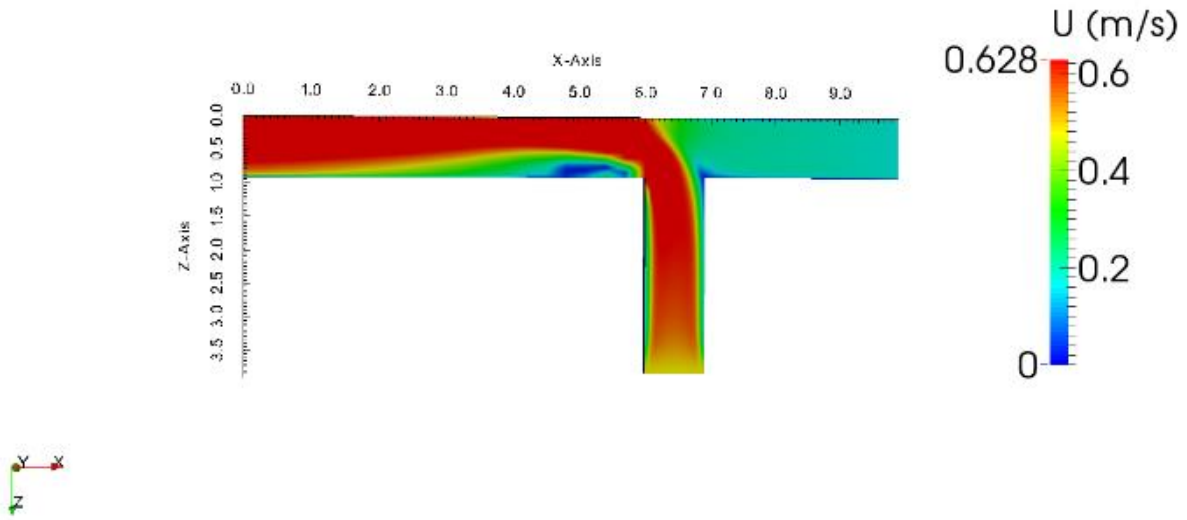

Velocity distribution at simulated realizable k-ε model

Figure A.6: Velocity distribution for confluent channel

The contour plot of velocity distrubution is shown in Figure A.7 where the intraction of primary flow and tributary flow can be observed.

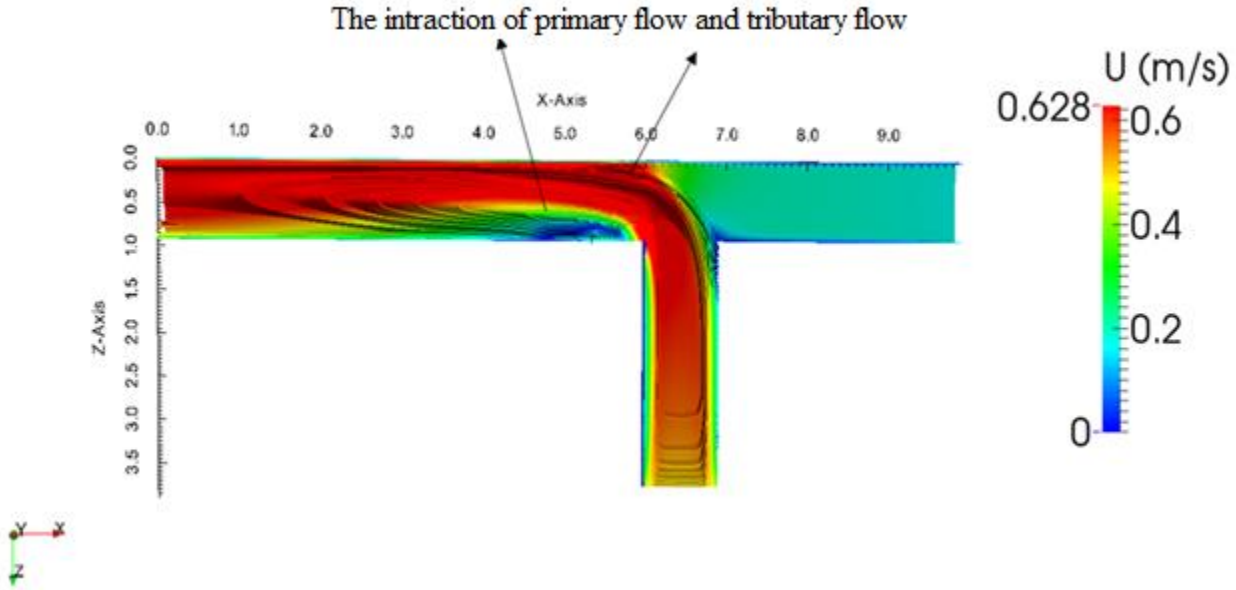

Figure A.7: The flow in closed confluent channel (k-ε model)

A.2.2. Vertical Velocity Distribution

Three types of circulation appear in the distribution of vertical velocity as shown in Figure A.8. Due to the joining of the flows of the branch and main channels, in this case, a shearing action to the main flow is set up by the tributary channel, and then two surface flows are evolved. The influences of comparative magnitudes of consolidated flows and the profile of the non-uniform vertical velocity are the reason behind the skewing of the shear plane rather than vertical. The new merged flow has features of the three-dimensionality induced by the non-uniform vertical velocity profile. Subsequently, a clockwise rotating secondary vortex could be found downstream of the main channel close to the internal bank and looking downstream. At the other bank of the main channel downstream, another secondary vortex appears and rotates against the secondary flow of the branch channel. At last, the secondary currents of the two channels fade gradually towards the direction of the river, and this takes place mainly because of the fluid viscosity.

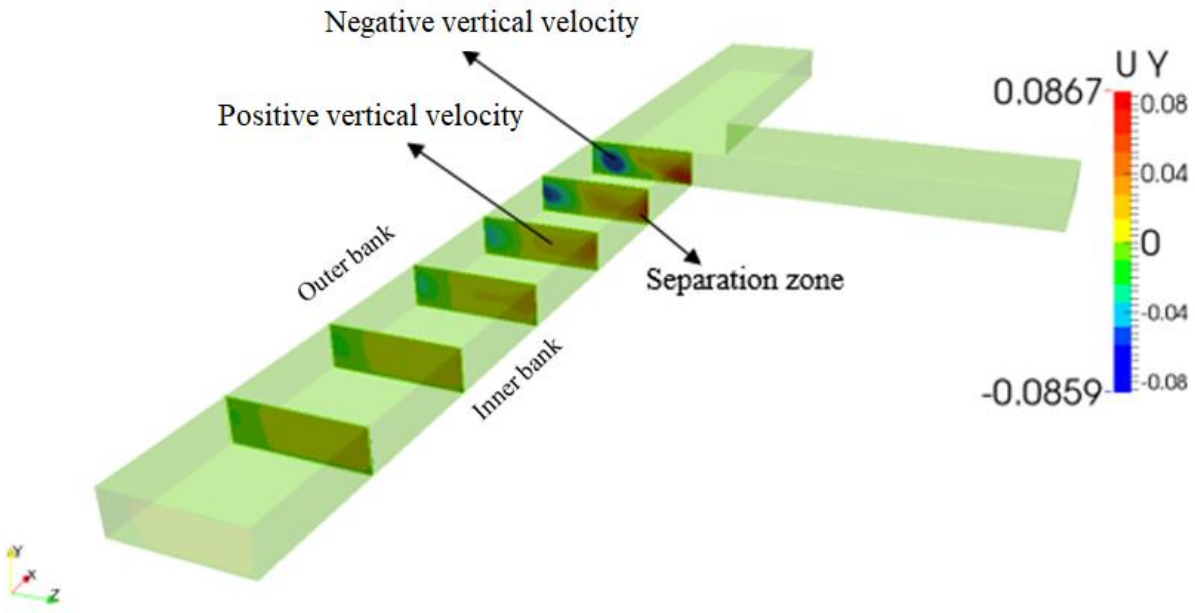

Figure A.8: Vertical velocity distribution

A.2.3. Lateral Velocity Distribution

The lateral velocity distribution as shown in Figure A.9 below is positive at the area near the bed and negative near the water surface which indicating the existence of the secondary flows. If there is an iced cover on a 90-degree Confluence, the velocity below the ice will be zero.

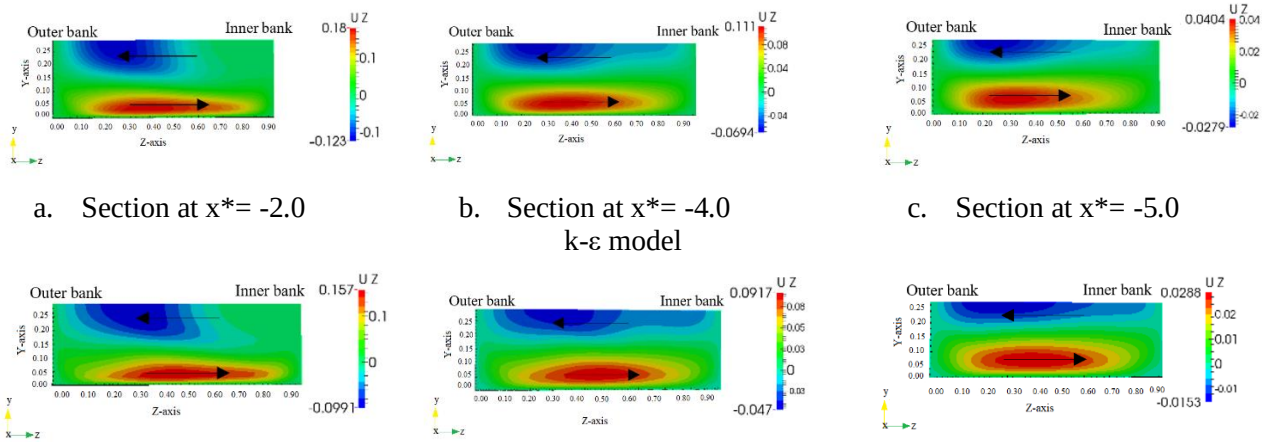

a. Section at x*= -2.0 b. Section at x*= -4.0 c. Section at x*= -5.0

k-ε model

d. Section at x*= -2.0 e. Section at x*= -4.0 f. Section at x*= -5.0

Realizable k-ε model

Figure A.9: Lateral Velocity Distribution

Appendix B

B.1. Mathematical Description of the Main Flow and Secondary Circulation

The three-dimensional fluid flow could be described by Navier-Stokes equations which in Cartesian coordinates are written as following (Bradbrook et al., 1998):

Continuity equation

$$\frac{\partial u}{\partial x}+\frac{\partial v}{\partial y}+\frac{\partial w}{\partial z}=0 \tag{B-1}$$

Momentum equations

x-direction
$$u\frac{\partial u}{\partial x}+v\frac{\partial u}{\partial y}+w\frac{\partial u}{\partial z}=-\frac{1}{\rho}\frac{\partial p}{\partial x}+\frac{1}{\rho}\left(\frac{\partial \tau_{ii}}{\partial x}+\frac{\partial \tau_{ij}}{\partial y}+\frac{\partial \tau_{ik}}{\partial z}\right) \tag{B-2}$$

y-direction
$$u\frac{\partial v}{\partial x}+v\frac{\partial v}{\partial y}+w\frac{\partial v}{\partial z}=-\frac{1}{\rho}\frac{\partial p}{\partial y}+\frac{1}{\rho}\left(\frac{\partial \tau_{ij}}{\partial x}+\frac{\partial \tau_{jj}}{\partial y}+\frac{\partial \tau_{jk}}{\partial z}\right) \tag{B-3}$$

z-direction
$$u\frac{\partial w}{\partial x}+v\frac{\partial w}{\partial y}+w\frac{\partial w}{\partial z}=-\frac{1}{\rho}\frac{\partial p}{\partial z}+\frac{1}{\rho}\left(\frac{\partial \tau_{ik}}{\partial x}+\frac{\partial \tau_{jk}}{\partial y}+\frac{\partial \tau_{kk}}{\partial z}\right) \tag{B-4}$$

where u, v and w are the time-averaged cartesian velocity components in the x, y and z directions, respectively, ρ is the density, p is the pressure,

$$\tau_{ij}=\nu\left(\frac{\partial u_j}{\partial x_i}+\frac{\partial u_i}{\partial x_j}\right)-\overline{u_i' u_j'} \tag{B-5}$$

ν is the kinematic viscosity and $\overline{u_i' u_j'}$ are the time-averaged turbulent Reynolds shear stresses (Lane, 1998) where i and j are standard tensor notation indicating two out of the three orthogonal coordinate directions.

B.2. OpenFOAM

An open source CFD model is the OpenFOAM (Open-Source Field Operation and Manipulation) programme. It has the quality of being adaptable to new developments. Users can provide fresh concepts to aid in the expansion of software functionalities. Since OpenFOAM comes with an open

C++ library, it can be used to develop applications. Additionally, it is utilised to specify solutions for Finite Volume Method (FVM)–based Continuum Mechanics issues, particularly for CFD. Solver and utility are the two parts of these applications in OpenFOAM. While the latter is frequently used to manipulate data in various formats, the former is utilised to solve partial differential equations. The fundamental benefit of OpenFOAM might be seen as the ease with which solvers can be created and customised. In order to make the syntax of the solver applications more reminiscent of the partial differential equations that are being employed, OpenFOAM classes have been introduced. The programming language must have certain characteristics like template classes, inheritance, virtual functions, and operator overloading in order to accomplish this. This could be found in a few languages, C++ being one of them. The software's ability to be customized has made it a popular option for users who want some level of control over the physics and calculation of a solution to a problem. Many times, other people can use the custom solvers and tools that are for the users of OpenFOAM. Many commercial and academic organizations, as well as many peer-reviewed research articles, use OpenFOAM (Lambert, 2012).

The Volume of Fluid method (VOF) is used in OpenFOAM for tracking the free surface movement (the air-water interface). The interFoam solver is used with free surface flow while the pisoFoam solver is used in the closed channel (no free surface). This method depends on determining the fraction of each fluid in every cell of the computational mesh (known as the volume fraction). The volume fraction equation's is:

$$\frac{\partial \alpha}{\partial t} + \nabla.(\alpha\, U) = 0 \qquad \text{(B-6)}$$

where U is the velocity field composed of u,v, and w and α are the water volume fraction and air volume fraction, respectively. The parameter α varies between 0 and 1. The case $\alpha = 1$ denotes a cell that is full of water and $\alpha = 0$ if it is full of air.

The density of the fluid inside each cell of the mesh could be determined by volume fraction, which is also known as the phase fractionα (the density that is used in solving Navier-Stokes equations). The density of the mixture is determined by:

$$\rho = \alpha\rho_w + (1 + \alpha)\rho_a \qquad \text{(B-7)}$$

where ρ_w is the density of water; and ρ_a is the density of the air.

The toolbox in OpenFOAM implements operator-based implicit and explicit second and fourth-order Finite Volume (FV) discretization in three-dimensional spaces and on a curved surface, which could be considered the most important feature to help CFD programmers.

The dimensional check is one of the important advantages that is done by OpenFOAM. The dimensions of the physical quantity's objects are referenced with the construction of these quantities, and only valid dimensional operations can be performed.

B.2.1. Model Preparation

One of the strengths of OpenFOAM is that users can develop new solvers and utilities with some prerequisite knowledge of the core method, programming skills, and physics.

Figure B.1 depicts the pre-processing and post-processing environments that have been made available in OpenFOAM. Like OpenFOAM utilities, the pre- and post-processing interface is the same. In order to provide consistent data handling across all environments. Figure B.2 depicts the general structure of OpenFOAM. This section seeks to make clear how Open Foam's current applications can be used to simulate the flow in river bends.

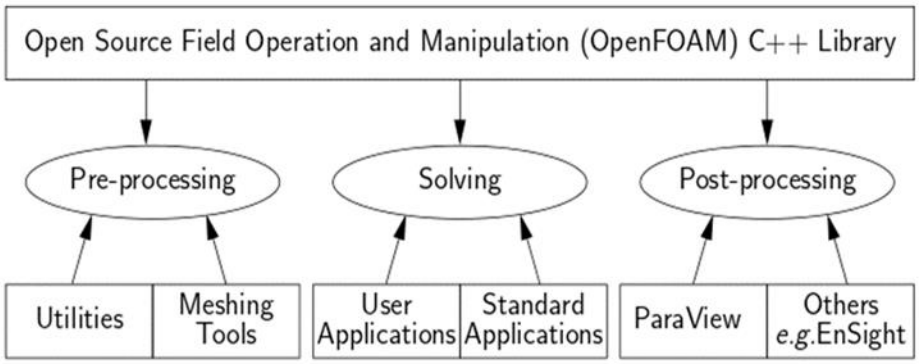

Figure B.1: The structure of OpenFOAM (Hjertager, 2009)

The case directory includes the following directories (Hjertager, 2009):

- Constant: regulates the turbulence, mesh, and material properties that are appropriate for each task.
- System: specifies solution controls, time step size, and iteration count.
- 0: establishes the boundary conditions and initial flow fields.

As was previously noted, the OpenFOAM toolbox contains a number of distinct solvers that are created to address various particular problems (Poungkrajorn, 2015). To tackle the issue pertaining to the experiment in this study, two solvers have been chosen:

InterFoam: is a transient solver for incompressible flow which is utilised in conjunction with a Free Surface Model.

PisoFoam: is a Rigid-Lid Model-compatible transient solver for incompressible flow.

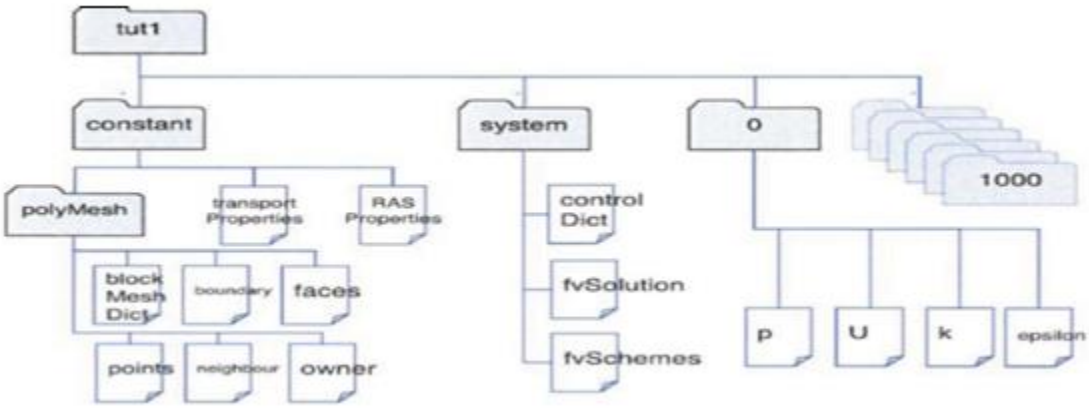

Figure B.2: OpenFOAM case structure (Hjertager, 2009)

B.2.2. Implementation of the Solvers

- InterFoam Solver

High air-water interaction is a characteristic of free surface flows. The interFoam solver, a multiphase solver from OpenFOAM, can reproduced some of these characteristics.

- PisoFoam Solver

PisoFoam is a transient solver for laminar and turbulent conditions for incompressible fluid flows. PisoFoam, which means for Pressure Implicit with Splitting of Operators, is built on the PISO algorithm. PisoFoam is a pressure-velocity computation method that has two corrector phases and one predictor step. Momentum equations are used in the predictor step for solving an intermediate pressure field, which is the concept of the SIMPLE algorithm. Two corrector stages are used to correct and check the pertinent parameters in a way that satisfies the momentum and continuity equations (Versteeg and Malalasekera, 2007). Therefore, pisoFoam also could be considered as an extension of the SIMPLE algorithm by adding corrector steps to ensure the calculated values (Poungkrajorn, 2015).

The main question to be answered from the comparing between the rigid-lid model and Free Surface Model is to know if the rigid lid which is easier and more stable can accurately solved this problem

of river bends and confluences. Taking in consideration that for the cases when the water surface variation is very large, rigid lid is not accurate.

B.3. Turbulence Modelling

Different types of turbulence models have been developed to solve the Navier Stokes equations based on a modelling strategy that uses less computational efforts and resources by averaging the flow quantities across all turbulence scales that are being modeled (Cable, 2009). Several models that are included in RANS turbulence models have been developed in increasing order of complexity, ability to model the turbulence, and cost in terms of computational work. (Lars Davidson, 2015):

- Algebraic (zero equation) models: mixing length (first-order model),
- one equation model: k-model, μt-model, Spalart-Almaras (first-order model),
- two equation models: k- ε, k-kl, k-$\omega 2$, low Re k-ε (first-order model),
- algebraic stress models: ASM (second-order model), and
- Reynolds stress models: RSM (second-order model).

A brief explanation for each group of the turbulence models is shown below:

I. Algebraic models: An algebraic equation can be used to calculate turbulent viscosity, also known as eddy viscosity. A turbulent (eddy) viscosity is the basic of eddy viscosity models.
II. One-equation models: For this type of model, the turbulent quantity (often the turbulent kinetic energy) is derived from a transport equation. Additionally, an algebraic expression for a second turbulent quantity, typically a scale of turbulent length, is solved. The turbulent viscosity is often calculated under the Boussinesq assumption.
III. Two-equation models: These models fall under the category of eddy viscosity models. The turbulent kinetic energy k and its dissipation ε are two transport equations that are derived to describe the transfer of two scalars. The Reynolds stress tensor is calculated under the presumption that it is related to the velocity gradients and an eddy viscosity. The two transported scalars are used to measure the eddy viscosity.
IV. Reynolds stress models: In this instance, the Reynolds tensor is derived from the transport equation. One more transport equation, typically the dissipation ε equation, should be included to get the length scale of the turbulence.

The general Hierarchy of Turbulence Models is shown in Figure B.3. The following sections describe the turbulence models that will be tested to determine which model gives the best results.

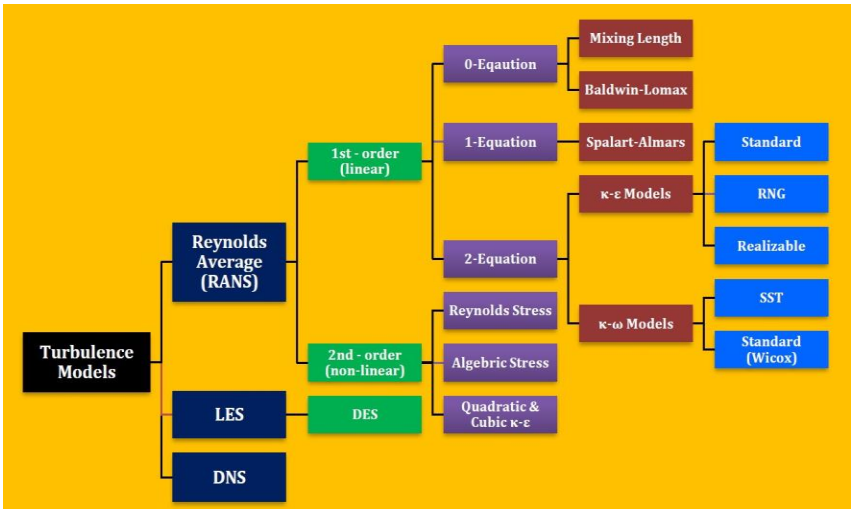

Figure B.3: The general Hierarchy of Turbulence Models (Sadrehaghighi, 2020)

B.3.1. K-Epsilon Turbulence Model

The k-ε model is one of the turbulence models that is used in Computational Fluid Dynamics (CFD). It is mainly used for developed and general turbulence. The model allows for the impact of transport of turbulence properties by convection, diffusion, and the production and destruction of turbulence. Since it is a two-equation model, the description of turbulence is given by means of two transport equations (PDEs); the turbulent kinetic energy (k), and the rate of dissipation of turbulent kinetic energy (ε). The turbulent viscosity is isotropic, and the main presumption of this model is considered according to Versteeg and Malalasekera (2007). Accordingly, the ratio between Reynold's stress and mean rate of deformation is assumed to be the same in all directions. Nevertheless, the inaccurate predictions make this assumption failing in many complex flows (Tawekal, 2015). Various turbulence models (i.e., Standard k-ε, Realizable k-ε since they are the most common models because of their simplicity, stability, accuracy, and low computational cost) are applied in the numerical model to assess the accuracy of turbulence models in predicting the behavior of the flow. The accuracy is reasonable considering the low computational cost.

- Standard K-Epsilon Turbulence Model

This concept was presented by Launder and Spalding in 1972, and it has been widely applied since since. For this model, momentum equations are used to derive the transport equation for turbulent kinetic energy (k), and physical reasoning is used to obtain the transport equation for turbulent

energy dissipation (ε), keeping in mind that it should be similar to the mathematically derived transport equation of k (Gildeh, 2013). In this model, the following equations were used to obtain the turbulent kinetic energy and its rate of dissipation:

$$\frac{\partial k}{\partial t} + \frac{\partial k u_i}{\partial x_i} = \frac{\partial}{\partial x_i}\left(D k_{eff} \frac{\partial k}{\partial x_i}\right) + G_k - \varepsilon \quad \text{(B-8)}$$

$$\frac{\partial \varepsilon}{\partial t} + \frac{\partial \varepsilon u_i}{\partial x_i} = \frac{\partial}{\partial x_i}\left(D \varepsilon_{eff} \frac{\partial \varepsilon}{\partial x_i}\right) + C_{1\varepsilon}\frac{\varepsilon}{k} G_k - C_{2\varepsilon}\frac{\varepsilon^2}{k} \quad \text{(B-9)}$$

where Gk symbolized the generation of turbulent kinetic energy due to mean velocity gradients, $Dkeff$ and $D\varepsilon eff$ are the effective diffusivity for k and ε, respectively. They are calculated as shown below:

$$D k_{eff} = v + v_t \quad \text{(B-10)}$$

$$D \varepsilon_{eff} = v + \frac{v_t}{\sigma_\varepsilon} \quad \text{(B-11)}$$

The equation of the turbulent kinematic viscosity at each point is:

$$v_t = C_\mu \frac{k^2}{\varepsilon} \quad \text{(B-12)}$$

σ_ε is turbulent Prandtl number for ε, which has been determined according to the experiment and is assumed equal to 1.3.

Furthermore, the constants $C1\varepsilon$, $C2\varepsilon$ and $C\mu$ are also determined on the light of the experiment and they have been chosen to have the following values:

$C1\varepsilon = 1.44, C2\varepsilon = 1.92, C\mu = 0.09$

G_k is the production of turbulent kinetic energy which is common in most turbulence models and is defined as:

$$G_k = -u_i' u_j' \frac{\partial u_j}{\partial x_i} \quad \text{(B-13)}$$

It also can be written as

$$G_k = 2 v_t S_{ij}^2 \quad \text{(B-14)}$$

$$S_{ij} = 0.5(\frac{\partial \mathrm{u}_j}{\partial \mathrm{x}_i} + \frac{\partial \mathrm{u}_i}{\partial \mathrm{x}_j}) \quad \text{(B-15)}$$

where $u_i{}', u_j{}'$ and S_{ij} are the fluctuating parts of velocity and strain-rate tensor respectively.

- Realizable K-Epsilon Turbulence Model

Shih et al. developed this model in 1995, and it is one of the most modern and sophisticated turbulence models in the k-ε category (Gildeh, 2013). Two significant variances from the typical k-ε model have been identified in this model. These differences are represented in using (i) a new turbulent viscosity equation, and (ii) the transport of the mean-squared vorticity fluctuation equation was utilized to derive the dissipation rate transport equation. The Realizability restrictions, the positivity of normal Reynolds stresses, and Schwartz's inequality for turbulent shear stresses served as the foundation for the eddy viscosity equations (Gildeh, 2013). The realizable k-ε model became more accurate than other models in predicting flows such discontinuous flows and flows with complex secondary flow features because of the standard k-ε model's unsatisfactory findings on this.

The transport equations become as below:

$$\frac{\partial k}{\partial t} + \frac{\partial k u_i}{\partial x_i} = \frac{\partial}{\partial x_i}\left(D k_{eff} \frac{\partial k}{\partial x_i}\right) + G_k - \varepsilon \quad \text{(B-16)}$$

$$\frac{\partial \varepsilon}{\partial t} + \frac{\partial \varepsilon u_i}{\partial x_i} = \frac{\partial}{\partial x_i}\left(D k_{eff} \frac{\partial \varepsilon}{\partial x_i}\right) + \sqrt{2} C_{1\varepsilon} S_{ij} \varepsilon - C_{2\varepsilon} \frac{\varepsilon^2}{k + \sqrt{\upsilon\, \varepsilon}} \quad \text{(B-17)}$$

The equation of the turbulent viscosity is determined by

$$\upsilon_{\mathrm{t}} = C_\mu \frac{k^2}{\varepsilon} \quad \text{(B-18)}$$

where, C_μ is computed by:

$$C_\mu = \frac{1}{A_0 + A_s \frac{k U^*}{\varepsilon}} \quad \text{(B-19)}$$

$$U^* = \sqrt{S_{ij} S_{ij} + \tilde{\Omega}_{ij} \tilde{\Omega}_{ij}} \quad \text{(B-20)}$$

$$\tilde{\Omega}_{ij} = \bar{\Omega}_{ij} - \varepsilon_{ijk}\omega_k - 2\varepsilon_{ijk}\omega_k \quad \text{(B-21)}$$

where $\bar{\Omega}_{ij}$ the mean rate of rotation tensor, and ω_k is the angular velocity.

The constants A_0 and A_s are determined as below:

$$A_0=4,\ A_s = \sqrt{6}cos\varphi \quad \text{(B-22)}$$

$$\varphi = \frac{1}{3}Arccos\ (\min\ (\max(\sqrt{6}W, -1), 1) \quad \text{(B-23)}$$

$$W = \frac{S_{ij}S_{jk}S_{ki}}{\tilde{S}^2} \quad \text{(B-24)}$$

The equation of $C_{1\varepsilon}$ is defined as below:

$$C_{1\varepsilon} = \max\ (\frac{\eta}{5+\eta}, 0.43) \quad \text{(B-25)}$$

The constants C_2, σ_k and σ_ε were specified by Shih in 1995 and they are defined as below:

$C_2 = 1.9, \sigma_k = 1.0, and \sigma_\varepsilon = 1.2$